Technische Universität München
TUM School of Natural Sciences

Multitopic Dithiocarboxylate Ligands as Linkers for Metal-Organic Coordination Polymers

Margit Aust

Vollständiger Abdruck der von der TUM School of Natural Sciences der Technischen Universität München zur Erlangung einer

Doktorin der Naturwissenschaften (Dr. rer. nat.)

genehmigten Dissertation.

Vorsitz: Prof. Dr. Klaus Köhler

Prüfende der Dissertation:

1. Prof. Dr. Roland A. Fischer
2. Prof. Dr. Torben Gädt

Die Dissertation wurde am 02.08.2024 bei der Technischen Universität München eingereicht und durch die TUM School of Natural Sciences am 14.10.2024 angenommen

In der Wissenschaft gleichen wir alle nur den Kindern, die am Rande des Wissens hie und da einen Kiesel aufheben, während sich der weite Ozean des Unbekannten vor unseren Augen erstreckt.

(Isaac Newton)

DANKSAGUNG

Allen voran möchte ich **Roland A. Fischer** danken, der mir die Forschung zu dieser Arbeit als Teil seiner Gruppe ermöglichte. Ich danke Ihnen für das entgegengebrachte Vertrauen, den respektvollen Umgang und Ihre kritischen Fragen an richtiger Stelle. Obwohl Sie mir große Freiheiten bei der Gestaltung meiner Forschung ließen, stand Ihre Tür stets offen für Diskussionen und Hilfestellungen. Sie unterstützten mich bei jedem Vorhaben und ermöglichten mir dadurch die Teilnahme an spannenden Konferenzen sowie Auslandsbesuche, die meine Zeit sehr prägten. Durch Ihre Begeisterung und vielfältigen Ideen haben Sie mich immer wieder zu einer offenen Denkweise ermutigt, wodurch ich nicht nur fachlich dazugelernt habe, sondern mich auch persönlich unglaublich weiterentwickeln konnte. Dafür danke ich Ihnen sehr.

Außerdem bedanke ich mich bei **Torben Gädt** für die Übernahme des Zweitgutachters in meiner mündlichen Prüfung.

Mein besonderer Dank gilt **Alexander Pöthig** für die vielen fachlichen Diskussionen im Rahmen der COORNETs Subgroup, deine Unterstützung beim Verfassen meiner Publikationen und die vielen unterhaltsamen Abende in unserer Lounge oder beim BBQ. Du schaffst es auch in stressigen Situationen deinen Humor nicht zu verlieren und hast mich immer wieder positiv auf meine Herausforderungen blicken lassen. Besonders unsere gemeinsame Zeit in Seattle und Eugene wird mir immer in Erinnerung bleiben.

Special thanks also go to **Julien Warnan** for your endless patience during long e-chem lab days. I am truly grateful for your guidance in understanding electrochemical fundamentals and for your help during on-site experiments. From electrode polishing to the fiddly assembly of spectro-e-chem cells, thank you for teaching me all of this.

I further thank **Dana Medina** and **Marina Schönherr** for your great support during our collaboration. With your expertise in conductivity measurements, you have significantly contributed to the success of my research through our joint publication.

Ich möchte mich bei **Jürgen Kudermann** und **Ulrike Amari** bedanken für eure tatkräftige Unterstützung beim Durchführen verschiedener Analysen. Besonders in zeitkritischen Phasen, habt ihr immer einen Weg gefunden mal eine Probe dazwischenzuschieben, und habt dabei stets eure gute Laune bewahrt.

Mein weiterer Dank gilt dem gesamten **akademischen Mittelbau** des AMC, ganz besonders **Markus Drees** sowie dem AMC Sekretariat mit **Martin Schellerer** und **Dana Weiß**. Dank

euch fand ich stets den richtigen Ansprechpartner für Fragen im wissenschaftlichen Kontext und administrativen Dschungel.
Diese Arbeit wäre nicht möglich gewesen ohne die Unterstützung einer Reihe weiterer, wundervoller Menschen. Ich möchte mich bei allen bedanken, die mir stets zur Seite standen.
Ich möchte dem gesamten **AMC Lehrstuhl** für die freundschaftliche Atmosphäre danken. Es tat gut im Laboralltag stets von hilfsbereiten Kollegen umgeben zu sein, bei denen man immer ein offenes Ohr finden konnte – egal ob bei Synthese-Fragen oder einer gemütlichen Kaffeepause.
Auch dir danke ich, **Christian**. Du hast meine Begeisterung für die Welt der MOFs geweckt. Während meiner Masterarbeit konnte ich schon unglaublich viel von dir lernen. Ein besonderes Highlight war für mich unsere gemeinsame Reise nach Livermore. Neben den unglaublich spannenden wissenschaftlichen Erfahrungen, die ich dabei sammeln konnte, hatten wir auch die Gelegenheit uns die schönsten Orte in San Francisco anzusehen. Ich danke dir für diese tolle Zeit.
Ich möchte mich bei meinen Bachelor- und Masterstudenten bedanken, mit denen ich zusammenarbeiten durfte. **Lena, Anna, Maurice und Niklas**, danke für euer Vertrauen und die gemeinsame Zeit. Auch ich konnte viel während unserer Zusammenarbeit lernen und bin sehr dankbar für eure Unterstützung.
Ich bin unglaublich froh, dass ich während dieser Zeit so vielen wundervollen Menschen begegnet bin, die für mich zu wahren Freunden geworden sind.
Schon am ersten Tag unseres Studiums sind wir uns begegnet, **Franzi**. Seitdem haben wir nicht nur 10 Semester mit unzähligen Klausuren und Praktika zusammen gemeistert, sondern auch viele weitere Dinge erlebt. Schon während dem Bachelorstudium entstand daraus eine tolle Freundschaft. Ich danke dir für deine Unterstützung, deine Ratschläge und die absolut beste Restaurantauswahl.
Ich möchte mich auch bei euch bedanken, **Pati & Sebi, Alex & Philip, Karina & Philip.** Danke für die vielen schönen Momente und Erinnerungen. Besonders die Abende mit euch haben mir nach einem anstrengenden Labortag immer sehr viel Freude gemacht, egal ob beim Feiern in der Lounge oder bei einem entspannten Bachelor-Abend.
Vor allem danke ich euch, **Pati und Alex**. Ihr seid während dieser Zeit zu meinen engsten Freunden geworden, habt mich aufgemuntert bei Rückschlägen und Erfolge mit mir gefeiert. Ihr habt mir immer das Gefühl gegeben für alles eine Lösung finden zu können,

egal wie Ausweglos eine Situation scheint. Danke, dass ihr auch außerhalb der Uni immer für mich da seid und ich euch alles anvertrauen kann.
Obwohl nicht immer alles glatt lief, würde ich es jederzeit wieder genauso machen. Denn dadurch konnte ich auch dich, **Lukas**, kennenlernen. Du bist mir immer eine Schulter zum Anlehnen und bringst mich in stressigen Zeiten zur Ruhe. Durch das viele Brainstorming beim Frühstück hast du mir geholfen wie kein anderer und bist mittlerweile selbst auch ein halber MOFler geworden. Ich bin dir unglaublich dankbar, dass ich jederzeit auf deine Unterstützung zählen kann.
Während dieser Zeit konnte ich viele tolle Menschen kennenlernen, doch ihr wart schon immer da: **Tanja & Jassi.** Danke fürs Zuhören, euer Verständnis und dafür, dass ihr immer an meiner Seite seid. Ich liebe euch dafür, dass ihr wisst, dass ich *irgendwas mit anorganischer Chemie* mache!
Zuletzt danke ich meiner Familie. In Momenten des Zweifelns sprecht ihr mir unaufhörlich Mut zu und zeigt mir immer wieder, wie sehr ihr an mich glaubt. Danke, **Mama, Papa & Stefan**, dass ihr mir immer den Rücken freihaltet und ich mich jederzeit auf euch verlassen kann. Wenn ich eines weiß, dann das: „Wie´s geht, geht's...heimkommen kann ich immer".

ABSTRACT

Sulfur-based organic ligands represent a promising avenue in coordination chemistry, offering distinct electronic advantages over nitrogen or oxygen containing ligands. The lower electronegativity of sulfur-donor atoms compared to nitrogen or oxygen allows for increased orbital overlap with central metal ions in coordination compounds. Consequently, the resulting coordination bonds exhibit enhanced covalent character, facilitating electron transport essential for functionalities like electronic communication, charge carrier mobility, and electrical conductivity.

In this work, two multitopic dithiocarboxylate ligands, benzene-1,4-di(dithiocarboxylate) (BDDTC) and benzene-1,3,5-tri(dithiocarboxylate) (BTDTC), are investigated for their potential as versatile ligands in both molecular and extended metal-organic coordination compounds.

The first study presented in this thesis involves the synthesis and in-depth characterization of the novel tritopic ligand in the form of its sodium salt Na_3BTDTC. Through synthesis of two model complexes and their comprehensive analysis, the coordination behavior of BTDTC is thoroughly studied on the molecular level. Notably, the trinuclear Cu(I) compound $[Cu(Xantphos)(MeCN)_2][PF_6]$ and the hexanuclear Mo_2(II) complex $[Mo_2(DAniF)_3]_3(BTDTC)$ reveal diverse coordination modes, including chelating and bridging coordination, laying the groundwork for the construction of extended structures such as coordination polymers (CPs) and metal-organic frameworks (MOFs). Electrochemical analysis confirms superior electronic communication in $[Mo_2(DAniF)_3]_3(BTDTC)$ compared to its carboxylate analogue, supported by computational insights indicating reduced HOMO-LUMO gaps for CS_2-based complexes.

Transitioning from molecular complexes to solid-state materials, the ditopic BDDTC ligand is utilized as linker in the construction of multidimensional CPs. Within the scope of the second study included herein, three CPs are synthesized through reaction with manganese-, zinc-, and iron-based metal nodes. Diverse coordination behavior and manifold structural motifs are evidenced by comprehensive structural analysis of $[Mn(BDDTC)(DMF)_2]$, which exhibits one-dimensional chains, and $[Zn_2(BDDTC)_3][Zn(DMF)_5(H_2O)]$, displaying two-dimensional honeycomb sheets.

Reaction with an iron-based metal precursor yields a Fe^{2+}/Fe^{3+} mixed valence coordination polymer displaying remarkable electrical conductivity of $5\cdot10^{-3}$ S cm^{-1}. Despite lacking single crystals for X-ray structural analysis, spectroscopic and magnetic

analyses elucidate a 1:1 ratio of Fe^{2+}/Fe^{3+} ions, attributing conductivity to partial oxidation during synthesis. X-ray absorption spectroscopy (XANES and EXAFS) confirms the presence of multinuclear Fe^{2+}/Fe^{3+} metal nodes, further highlighting the structural complexity of the polymer.

This dissertation underscores the potential of dithiocarboxylate ligands, including BTDTC and BDDTC, in enhancing the electronic properties of CPs and MOFs. The importance of tailored design strategies, considering both ligand and metal entity, emerges as pivotal in the development of functional electronic materials in coordination chemistry.

KURZFASSUNG

Obwohl schwefelbasierte organische Liganden innerhalb metallorganischer Koordinationsverbindungen deutlich weniger verbreitet sind als ihre Carboxylat Gegenstücke, bieten besonders CS_2 basierte Liganden deutliche Vorteile hinsichtlich elektronischer Eigenschaften im Vergleich zu Stickstoff- oder Sauerstoffliganden. Die vergleichsweise geringere Elektronegativität der Schwefel-Donor Atome führt zu einer verbesserten Orbitalüberlappung zwischen Ligand und zentralem Metallion. Der höhere kovalente Anteil der gebildeten Koordinationsbindungen erleichtert den elektronischen Transport von Ladungsträgern, wodurch sich die elektronische Kommunikation, die Ladungsträgermobilität und die elektrische Leitfähigkeit der resultierenden Materialien verbessern lassen.

In dieser Studie werden die beiden multitopischen Dithiocarboxylatliganden, Benzol-1,4-di(dithiocarboxylat) (BDDTC) und Benzol-1,3,5-tri(dithiocarboxylat) (BTDTC), hergestellt und ihr Potential als vielseitige Liganden in molekularen und mehrdimensionalen metallorganischen Koordinationsverbindungen demonstriert.

Die erste Studie, die in dieser Dissertation vorgestellt wird, befasst sich mit der Synthese und der eingehenden Charakterisierung des neuartigen tritopischen Liganden in Form seines Natriumsalzes Na_3BTDTC. Die Synthese zweier Modellkomplexe und deren umfassende Charakterisierung ermöglichen zunächst eine gründliche Untersuchung des Koordinationsverhaltens auf molekularer Ebene. Dabei lassen sich für den trinuklearen Cu(I)-Komplex $[Cu(Xantphos)(MeCN)_2][PF_6]$ und den hexanuklearen Mo_2(II)-Komplex $[Mo_2(DAniF)_3]_3$(BTDTC) verschiedene Koordinationsmodi beobachten, einschließlich chelatisierender und verbrückender Koordination. Mittels elektrochemischer Analyse lässt sich eine verbesserte elektronische Kommunikation in $[Mo_2(DAniF)_3]_3$(BTDTC) im Vergleich zu seinem Carboxylat-Analogon belegen. Theoretische Berechnungen bestätigten dies durch eine verringerte HOMO-LUMO Lücke im Falle der CS_2-basierten Komplexe.

Um diese Erkenntnisse anschließend auf mehrdimensionale metallorganische Feststoffmaterialien anzuwenden, werden im Rahmen einer zweiten Studie drei CPs aus dem ditopischen BDDTC Liganden zusammen mit mangan-, zink- oder eisenbasierten Metallkomponenten synthetisiert. Die erhaltenen kristallinen Materialien zeigen vielfältige Strukturmotive. Dies wird durch umfassende strukturelle Analyse von $[Mn(BDDTC)(DMF)_2]$ und $[Zn_2(BDDTC)_3][Zn(DMF)_5(H_2O)]$ deutlich, wobei

eindimensionale Ketten in dem Mn-Polymer, sowie eine zweidimensionale Wabenstruktur im Falle des Zn-Polymers vorzufinden sind.

Die Reaktion mit einem eisenbasierten Metallvorläufer resultiert in einem gemischtvalentes Fe^{2+}/Fe^{3+} Koordinationspolymer, das eine bemerkenswerte elektrischen Leitfähigkeit von $5 \cdot 10^{-3}$ S cm^{-1} aufweist. Spektroskopische und magnetische Charakterisierung ergeben ein Fe^{2+}/Fe^{3+} Verhältnis von 1:1, welches mit Ergebnissen der Röntgenabsorptionsspektroskopie (XANES und EXAFS) übereinstimmt.

Die vorliegende Dissertation verdeutlicht das Potenzial von Dithiocarboxylatliganden, insbesondere BTDTC und BDDTC, zur Verbesserung der elektronischen Eigenschaften von CPs und MOFs. Die Bedeutung maßgeschneiderter Designstrategien, die sowohl Liganden als auch Metallkomponenten berücksichtigen, wird als entscheidend für die Entwicklung funktionaler elektronischer Materialien in der Koordinationschemie hervorgehoben.

LIST OF ABBREVIATIONS

BDC	benzene-1,4-dicarboxylate
BDDTC	benzene-1,4-di(dithiocarboxylate)
BDT	1,4-benzenedithiolate
BET	Brunauer-Emmet-Teller
bpy	bipyridine
BTC	benzene-1,3,5-tricarboxylate
BTDTC	benzene-1,3,5-tri(dithiocarboxylate)
CAT	crystal-to-amorphous transformation
CCT	crystal-to-crystal transformation
CP	coordination polymer
CV	cyclo voltammogram
DAniF	N,N'-di(*p*-anisyl)formamidinate
DFT	density functional theory
DMBDC	2,5-dimethylbenzenedicarboxylate
DOBDC	2,5-dihydroxybenzene-1,4-dicarboxylate
DSBDC	2,5-disulfhydrylbenzene-1,4-dicarboxylate
HITP	hexaiminotriphenylene
IUPAC	International Union of Pure and Applied Chemistry
LMCT	ligand to metal charge transfer
MLCT	metal to ligand charge transfer
MOF	metal-organic framework
NIR	near infrared
pdt	2,3-pyrazinedithiolate
PSM	post synthetic modification
PTCA	perylenetetracarboxylate
SBU	secondary building unit
TCNQ	7,7,8,8-tetracyanoquinododimethane
TMA	tetramethylammonium
ZIF	zeolitic imidazolate frameworks

TABLE OF CONTENT

1. INTRODUCTION

The origins of material science can be traced back to ancient times when humans first began manipulating natural resources for practical purposes, using naturally occurring goods such as stone, wood, clay, bones, animal skin, and fur. From shaping rocks into tools in the Stone Age and the discovery of alloying copper and tin during Bronze Age, early civilizations laid the groundwork for what would later become the field of material science. However, the formal establishment of material science as a scientific discipline emerged around the 20th century, driven by an emerging demand for novel materials with specific properties. This accelerated the need for systematic investigations toward the tailored manipulation of specific materials to fulfill desired characteristics.[1-3]
In 1959, Richard P. Feynman envisioned the potential of manipulating matter at the atomic scale in his iconic speech "*Plenty of Room at the Bottom*".

> I am not afraid to consider the final question as to whether, ultimately – in the great future – we can arrange the atoms the way we want; the very *atoms*, all the way down! What would happen if we could arrange the atoms one by one the way we want them. […] What could we do with layered structures with just the right layers? What would the properties of materials be if we could arrange the atoms the way we want them? […] I can´t see exactly what would happen, but I can hardly doubt that when we have some *control* of the arrangement of things on a small scale we will get an enormously greater range of possible properties that substances can have, and of different things that we can do.

Richard P. Feynman (1960) – There's Plenty of Room at the Bottom[4]

Although, this being visionary at that time, it was during the mid-20th century when technology expanded rapidly and the need for a more comprehensive understanding of materials and the underlying structure-property relationships arose. This led to the convergence of various scientific disciplines, including physics, chemistry, engineering, and metallurgy, setting the stage for modern material science. Today, material science constitutes a diverse field exploring the interplay of materials' structures, their properties and possible manipulations across various scales – from atomic and molecular levels to

macroscopic dimensions. It encompasses a broad spectrum of materials, ranging from nanomaterials to metals, glasses, ceramics, polymers and composites.[5-6]

This evolution has been – and still is – driven by the quest for more advanced and efficient materials.

With the beginning of digitalization, the focus expanded, enabling the use of computational tools to model and predict materials' behaviors. Additionally, the principles of crystal engineering and the development of smart materials (*e.g.* thermoelectrics, shape-memory and self-healing polymers as well as electro-, thermo- and photochromic materials)[7-8] are reshaping the landscape of today´s material sciences, offering unprecedented functionalities and applications.[1-3, 5]

As a result of ongoing innovation, new classes of materials emerge, among which organic-inorganic hybrid materials have gained considerable interest. Over the last decades, particular attention has been devoted to the exploration of metal-organic coordination polymers (CPs). Combining inorganic rigidity and organic functionality, their architectural intricacies offer a toolbox for precise customization at the atomic and molecular levels. This renders metal-organic CPs a promising avenue for tailored functionalities, pushing the boundaries of material design.

1.1 Metal-Organic Coordination Polymers

Metal-organic coordination polymers (CPs) are a class of coordination compounds with extended structures in one, two, or three dimensions.[9-10] They are constructed from recurring inorganic metal nodes interconnected by coordinating organic ligands, also referred to as linkers. Besides single (transition-) metal ions, metal clusters and mono- or polynuclear metal complexes can also serve as inorganic entities.[11-12] Together with the coordinating ligator atoms from the organic components so called secondary building units (SBUs) are formed. Through bridging coordination of the linker molecules, these SBUs are connected to form an extended structure. Typically, multidentate linkers with functional groups, primarily based on N or O donor atoms, are used for the construction of metal-organic CPs. Polycarboxylates and polyamines (including pyridine, pyrazole-, or imidazole-derivatives) are commonly used as organic connectors, although nitriles, phosphonates and sulfonates are also employed.[13-16] The central metal ions within the inorganic SBUs are predominantly first row transition metals, however, investigations also include alkaline earth metals, lanthanides and late transition metals.[11, 15, 17-19]
Depending on the geometry of inorganic SBU and organic linker, multiple topologies with extension in one or multiple dimensions are possible.[14, 20-21] By definition, the degree of coordinative crosslinks in such compounds is decisive for their classification into 1D, 2D or 3D CPs. Consequently, the term *'coordination network'* is applicable only to CPs featuring coordinative crosslinks between one-dimensional substructures (e.g. single chains) or repeating coordination entities in more than one dimension. Similarly, 2D networks, where layers are connected via non-coordinative hydrogen bonds, are not classified as 3D frameworks but are instead specified as 2D hydrogen-bonded networks.[9, 17] While 1D extensions such as linear or zig-zag chains represent the simplest structures, increasing complexity can be found in 2D and 3D networks (Figure 1). To visualize the underlying topologies, they are commonly described as simplified nets with inorganic SBUs being the vertices and organic linkers the edges in the respective depiction.[11]

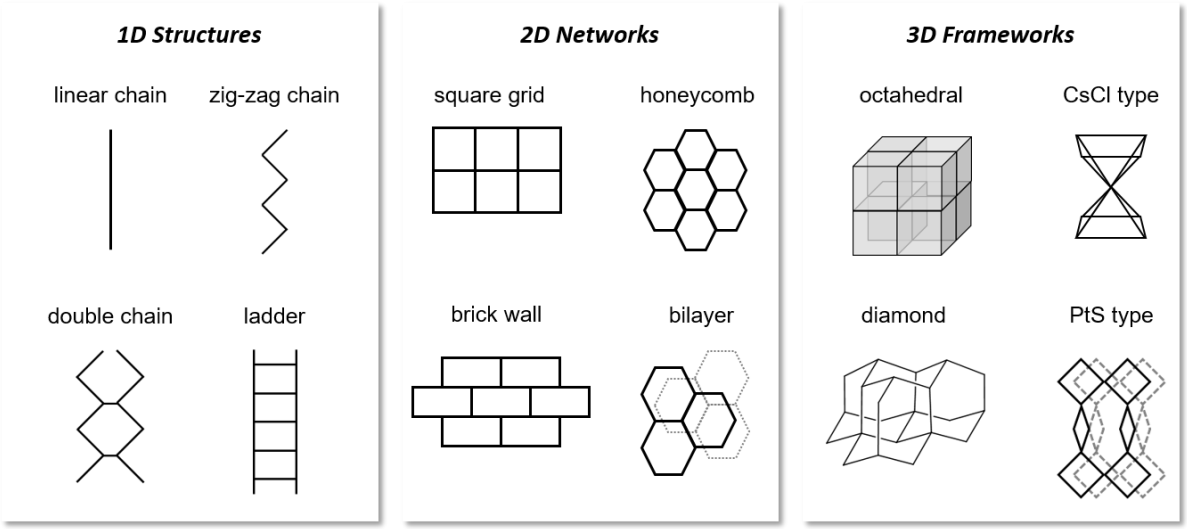

Figure 1: Selected structures for 1D (left,) 2D (middle) and 3D (right) coordination polymers.[11]

In this simplified description, both the inorganic and organic building blocks are reduced to their connectivity. While the connectivity of the linker is determined by the number of functional groups coordinating to the metal atoms, the inorganic moiety is characterized by its points of extension.[12] To consistently describe the resulting net topologies, they are assigned a three-letter designation such as **pcu** or **dia**, representing the primitive cubic lattice and the diamond structure, respectively.[22-23] Also, depending on the used building blocks and formed SBUs, CPs can include a varying number of coordination bonds being involved in the assembly of the polymeric structure (Figure 2). In particular, SBUs based on metal-oxo clusters show higher connectivity, which fosters the robustness and stability of the resulting CP.[17]

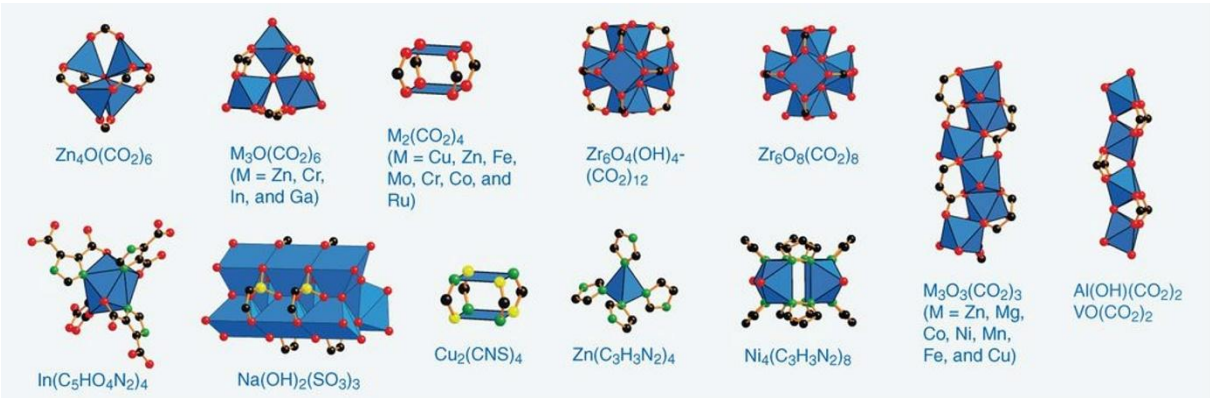

Figure 2: Selected examples for inorganic SBUs. Color code: black for C, red for O, green for N, yellow for S. Blue polyhedra represent the coordination environment around the central metal atom. From Furukawa, H.; Cordova, K. E.; O'Keeffe, M.; Yaghi, O. M., The Chemistry and Applications of Metal-Organic Frameworks. *Science* **2013,** *341* (6149), 1230444. Reprinted with permission from AAAS. Copyright (2013) American Association for the Advancement of Science.[15]

To date, most CPs are constructed using polycarboxylate or polyamine linkers. Typically, these linkers feature an aromatic backbone which enables functionalization with

additional substituents such as hydroxy, amino or nitro groups, as well as alkyl chains or halogens (Figure 3). Besides the possibility to introduce chemical moieties via functionalized linkers, it is also possible to incorporate more than one organic building block and create mixed-linker copolymers, named multivariate frameworks.[15, 24-26] Similarly, mixed-metal materials are conceivable through the introduction of multiple metal ions. While doping with a second metal enables isomorphic substitution,[27] heterogeneous core-shell structures can be achieved through subsequent formation of two different phases.[28]

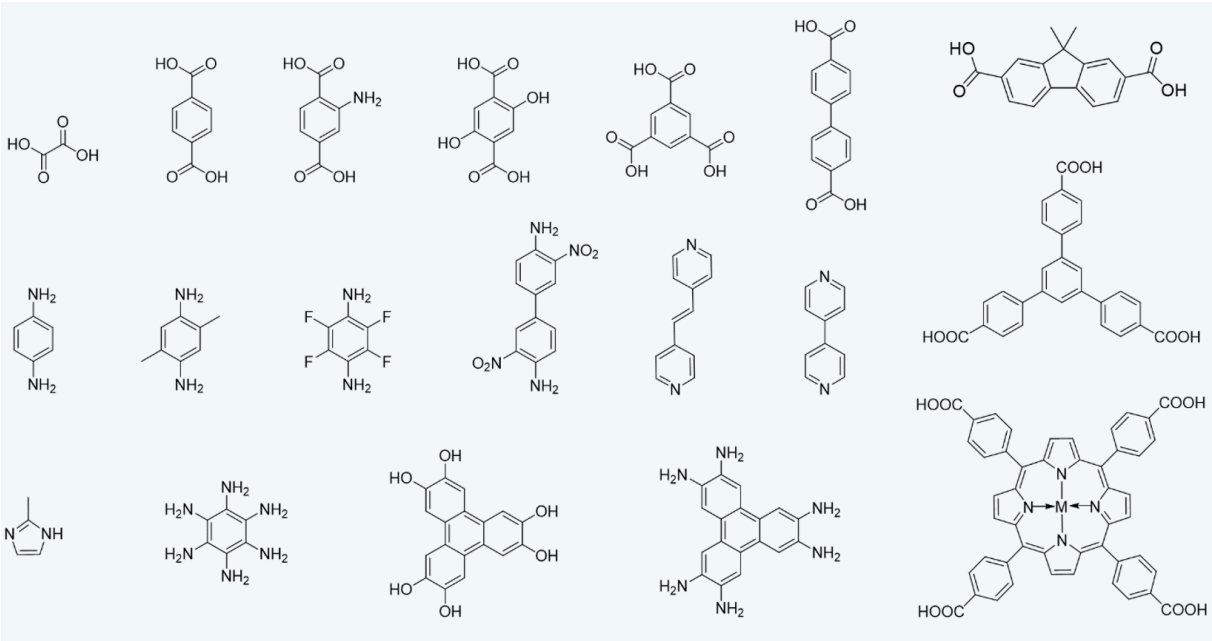

Figure 3: Exemplary structures of organic linkers which are commonly used as building blocks in CPs.

This variety of possible modifications, combined with the huge diversity of available building blocks enables the creation of countless structures. Paired with the manifold selection of substituents and functional groups, this structural tunability allows for precise tailoring of the material´s properties.[21, 29-30] Consequently, CPs are investigated for several fields of application such as gas storage and separation, catalysis, as well as optoelectronic and magnetic applications.[15, 17, 21, 30]

1.2 Metal-Organic Frameworks

Within the scope of CPs, porous CPs, also known as metal-organic frameworks (MOFs), hold particular significance in contemporary materials research. According to the International Union of Pure and Applied Chemistry (IUPAC) MOFs are defined as "*coordination network with organic ligands containing potential voids*"[9]

As a subclass of CPs, MOFs adhere to similar design principles while offering specific structural features and properties, rendering them a unique class of innovative materials. Their crystalline structure implies high regularity and rigidity, resulting in good chemical and thermal stability.[15] Additionally, the versatile interactions involved during their assembly enable structural transformability and flexibility.[31] Due to their open three-dimensional framework structure, MOFs exhibit exceptionally high porosity and unparalleled internal surface area. Observed values for their Brunauer-Emmet-Teller (BET) surface area surpassing those of traditional porous materials such as zeolites (260-590 $m^2 g^{-1}$), silica (450-1070 $m^2 g^{-1}$) and activated carbon (1250 $m^2 g^{-1}$).[32] To date, the highest reported BET surface area, reaching 7839 $m^2 g^{-1}$, was observed for $Zn_4O(BBC)_{4/3}(BCPDB)$ (DUT-60, H_3BBC = 1,3,5-tris(4'-carboxy[1,1'-biphenyl]-4-yl)benzene, H_2BCPDB = 1,4-bis-p-carboxyphenylbuta-3-diene), a mesoporous MOF constructed from $Zn_4O(CO_2)_6$ clusters and two types carboxylate linkers.[33] Typically, MOF cavities fall within the range of micro- (<2 nm)[34] or mesopores (2-50 nm)[34], enabling the incorporation of guest molecules within the framework.[15] Through strategic selection of building blocks, systematic design of pore size and functionality becomes feasible. Thus, elongation of the linker and functional group incorporation serve as powerful tools to target specific pore apertures, adjust pore volume and introduce tailored interactions. This method of customization, while maintaining the original topology, is called isoreticular synthesis and has been demonstrated on a series of isoreticular MOFs derived from the cubic structure of $Zn_4O(BDC)_3$ (MOF-5, BDC = benzene-1,4-dicarboxylate) (Figure 4).[35]

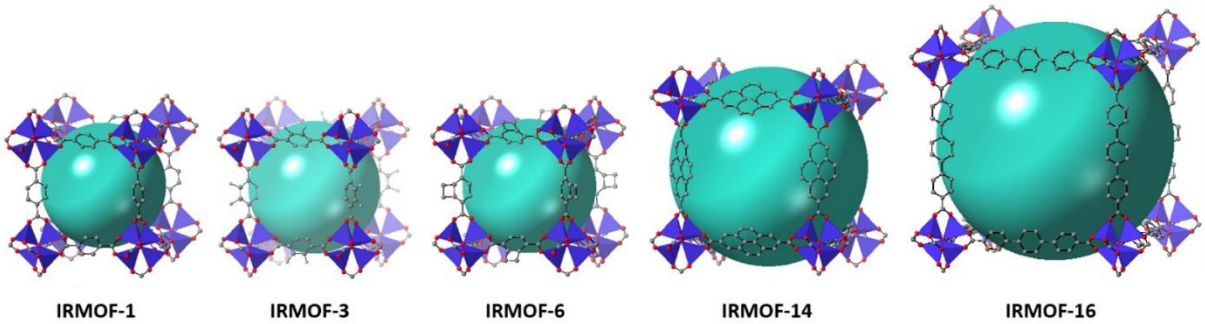

Figure 4: Single crystal X-ray structures of the isoreticular MOF series IRMOF-n (n = 1,3, 6, 14, 16). Blue tetrahedra represent the coordination environment around the Zn atoms and turquoise spheres depict the largest van der Waals spheres that would fit in the cavities. Hydrogen atoms are omitted for clarity. Color code: grey for C, red for O, blue for N.[35]

Typically, these pores are occupied by small guests such as solvent which has been incorporated during solvothermal synthesis or other compounds involved during preparation. To make the pores accessible, different routes for so-called activation have been established. While heating in vacuum is the common strategy for activating zeolites and carbon, only very stable frameworks can withstand these conditions. For most MOFs, the gradual exchange of high-boiling solvents (*e.g.* DMF) for lower-boiling solvents (*e.g.* CH_2Cl_2) is an effective approach to enable activation at milder conditions. This exchange reduces surface tension and capillary forces due to weaker intermolecular interactions, minimizing the risk of destroying the framework structure. To further support solvent removal, supercritical CO_2 extraction has been established. At high pressure, solvent molecules are exchanged for liquid CO_2 which can transition directly from the supercritical state to the gas phase after reaching the supercritical temperature. Depending on the nature of the MOF and the solvent to be removed, freeze-drying or chemical treatment (*e.g.* concentrated HCl to activate PCN-222) may also be suitable options.[36-37]

According to the behavior of the host framework during guest removal, MOFs are classified into three categories: First-generation compounds are unstable upon guest removal and lose their crystalline structure when incorporated molecules are extracted from the pores.[38] Especially, this host-guest dependence is observed for charged frameworks where guests within the cavities serve as counter ions.[39] Second-generation materials, in contrast, retain their crystallinity and enable reversible release and readsorption of guest molecules without phase transition or morphological changes. MOFs of the third generation exhibit dynamic behavior induced by external stimuli such as radiation, pressure, temperature or guest uptake/release.[38] Among these third-generation compounds different guest-induced responses are known. While crystal-to-

amorphous transformation (CAT) results in the collapse of the framework upon guest removal, the crystalline structure is restored when the guest is reintroduced. Moreover, crystal-to-crystal transformation (CCT) can cause structural shifts induced by guest exchange (CCT-I) as well as the removal or addition of guest (CCT-II). In any case, the original structure is restored when initial conditions are applied.[11] Recently, the term of '4th generation MOFs' has been introduced, referring to MOFs which can sustain post synthetic modifications (PSM).[39]

1.3 Application of Coordination Polymers and Metal-Organic Frameworks

The outstanding sorption properties of MOFs make them particularly attractive for applications in storage, transport and separation of gases. The first MOF material known for gas adsorption at ambient temperatures is $[M_2(4,4'\text{-bpy})_3(NO_3)_4]\cdot xH_2O$ (M=Co, Ni, Zn, H_2O=2, 4, bpy=bipyridine) which was reported in 1997 by Kitagawa *et al.* The 3D framework comprises channeling cavities measuring 3x6 Å, allowing for the reversible uptake of CH_4, N_2 and O_2.[40]

Addressing current challenges within the field of renewable energy, especially their capability of storing hydrogen gas and methane are of great interest to be used in fuel cells, natural gas storage and the generation of green energy.[41-44] In 2003, Yaghi *et al.* set the starting point by investigating the iconic MOF-5 and its derivatives toward their hydrogen adsorption properties. Remarkably, hydrogen uptake of 1.0 wt.-% was achieved for MOF-5 at conditions mimicking realistic pressures and temperatures for possible applications. Even though this already exceeds the adsorption capacities of active carbon (0.1 wt.-% H_2 uptake), this value was even surpassed by the isoreticular derivatives IRMOF-6 and IRMOF-8, reaching values up to 2.0 wt.-%.[45] Following on this, numerous MOFs were reported for their Hydrogen adsorption capabilities with NU-100 marking the top performer with regard to its gravimetric H_2 uptake of 13.9 wt.-%.[41, 43]

Beyond fundamental research, the concept of MOFs as structurally integrated hydrogen container has been launched by Mercedes Benz in their research car *F125!* – a visionary hydrogen-fueled vehicle advertising: "*Gigantic "inner" surfaces of up to 10,000 sq. m. per gram*".[1]

In the realm of gas adsorption, big effort has also been made in the area of demanding separation problems. MOFs have been successfully explored for selective CO_2 capture, demonstrating great potential toward environmental concerns such as air purification or reduction of emissions.[46] For instance, the two zeolitic imidazolate frameworks ZIF-95 and ZIF-100 show high affinity and storage capacity for CO_2 over CO, CH_4 and N_2. This is attributed to pore size effects and quadrupolar interactions between the adsorbent and the framework's N atoms located at the inner surface of the pores.[47-48]

[1] Mercedes Benz F125!; https://emercedesbenz.com/autos/mercedes-benz/concept-vehicles/mercedes-benz-f125-research-vehicle-technology/ (retrieved: 28. December 2023)

Besides the uptake of guest molecules for storage and subsequent release thereof, also chemical conversion can be performed within the cavities of the framework. Owing to the large number of open metal sites accessible within the pore environment of many MOFs, catalytic reactivity is another key feature provided by these compounds. Frameworks like HKUST-1 ($Cu_3(BTC)_2$; BTC = benzene-1,3,5-tricarboxylate) and MIL-101 ([$Cr_3X(H_2O)_2O(BDC)_3$; X = F, OH]; BDC = benzene-1,4-dicarboxylate) contain exposed Cu(II) and Cr(III) sites, respectively, acting as lewis acidic catalysts.[49-51] Within the scope of exploring MOF catalysts for oxidative coupling reactions and the oxidation of different alkenes and alkanes, also the oxidation of methane in vanadium-based materials was investigated. MIL-47 (VO(BDC))[52] was reported to selectively convert methane into acetic acid. The reported performance could further be improved through methyl-functionalization of the BDC linker. The derived MOF-48 (VO(DMBDC), DMBDC = 2,5-dimethylbenzenedicarboxylate) catalyzed methane oxidation to acetic acid, reaching 100 % selectivity and a turnover number of 490 in the presence of CO. These numbers outperform comparable heterogeneous systems while keeping up with the performance of homogeneous Vanadium catalysts. Notably, these compounds remain stable and retain their catalytic activity for several cycles.[53]

Besides catalytic conversion at the metal sites of the framework, also different loading approaches have been explored for designing catalytically active MOF materials. For instance, the incorporation of porphyrins during the assembly of MOFs resulted in high porphyrin loading, providing binding sites for subsequent metalation and the utilization of the loaded material for the oxidation of cyclohexane.[54] Lastly, the integration of metal nanoparticles into the pores of pre-formed MOFs (e.g. Pd nanoparticles into MIL-101) has been successfully applied to stabilize the particles and achieve narrow size distributions.[55-56]

The tailored design of dimensions, alignment and functionalities of the pores can thereby ensure the confinement of incorporated catalysts as well as the selective uptake of desired substrates and anchoring thereof. This selectivity for specific guest molecules has also been investigated toward drug delivery systems by encapsulating and precisely releasing therapeutic agents or biomolecules.[57-60]

Moreover, MOFs and CPs are also explored for their optical, magnetic and photo physical properties. Over the past years, numerous studies highlighted their application for optical materials (*e.g.* non-linear optics and multiphoton absorption)[61-63], photocatalysis (*e.g.*

light harvesting and artificial photosynthesis)[64-70] and chemical sensing (e.g. luminescence quenching or enhancement)[71-75].

In the electronic and electrochemical sectors, applications still lack behind those in the aforementioned fields due to the majority of CPs being electrically insulating. However, increasing efforts to combine structural advantages with adequate electrical conductivity have led to the development of a few exemplary materials that successfully combine both qualities. In 2017 $Ni_3(HITP)_2$ (HITP = hexaiminotriphenylene) was reported as electrode material for electrochemical double layer capacitors by Dincă *et al.* as the first example of a conductive CP representing the sole electrode material in a superconductor.[76] Following this, $M_3(HHTP)$ (M = Cu, Ni, Co; HHTP = hexahydroxytriphenylene) materials have been investigated as electrode material in Li-ion batteries, showing superb Li-ion diffusion coefficients paired with good long-term cycling stability.[77-79] Lastly, the utilization as electrode material in Na-ion batteries was reported for $[Co(L)(H_2O)]\cdot 2H_2O$ (L = 5-aminoisophthalic acid),[80] Co-HAB (HAB = Hexaaminobenzene)[81] and Zn-PTCA (PTCA = 3,4,9,10perylenetetra-carboxylate).[82] These examples demonstrate the great potential of CPs for advanced energy-storage technologies. Even though, electronic applications are still scarce, rapid progress can be expected in this highly demanded research area.

1.4 Electrical Conductivity in Metal-Organic Coordination Polymers

The growing interest in gaining in-depth understanding of the underlying principles for designing electrically conductive CPs and MOFs arises from the prospect of utilizing them as functional materials in electronic technologies, as outlined in the preceding chapter. Despite their remarkable porosity and structural versatility, most MOFs are characterized as electrical insulators owing to their inherent high resistivity. This lack of intrinsic electrical conductivity impedes their use in technologies such as fuel cells, capacitors and electrochemical sensing devices.

In a general context, electrical conductivity is determined by the density (n) of available charge carriers, comprising electrons (e) or holes(h), along with their mobility (μ) within the compound. This relationship is represented in the formula:

$$\sigma = e \cdot (n_e\mu_e + n_h\mu_h)$$

According to this equation, both a high charge carrier density and elevated charge carrier mobility are essential to achieve notable electrical conductivity. In the realm of MOFs, the introduction of charge carriers can originate from both the linker and the metal ion. The linker contributes to the electronic properties of the MOF through its conjugated structure, while the metal ions can augment the presence of charge carriers through their redox activity or electronic configuration. Particularly, high-energy electrons, such as the unpaired electron in d^9 Cu(II) or minority spin electrons, exemplified by the high spin d^6 Fe(II), are conceivable. Nevertheless, facilitating charge carrier mobility necessitates low-energy pathways, which are notably absent in the majority of MOFs. One primary explanation for the absence of these charge-transport routes lies in the highly ionic nature of the coordination bonds between the metal nodes and the organic linker. These bonds typically comprise metal–oxygen or metal–nitrogen coordination, leading to poor orbital overlap due to the combination of soft metal ions and comparatively hard ligand atoms (e.g., O or N atoms). As a result, energy barriers are formed, impeding charge transport within the material.[83-86]

Strategies to enhance the potential for charge carrier mobility and thereby increase the intrinsic electrical conductivity of the framework can be categorized into two approaches. First, the through-space approach relies on non-covalent interactions such as π-π stacking or charge hopping. This was demonstrated by a series of isostructural M_2(TTFTB) (M = Mn, Co, Zn, and Cd; $TTFTB^{4-}$ = tetrathiafulvalene tetrabenzoate) MOFs (Figure 5, left),

marking the first reported example for porous and electrically conductive 3D CPs. As the radii of the incorporated metal ions increased, a progressive enhancement in intrinsic conductivity was observed, escalating from 10^{-6} S cm^{-1} for Zn_2(TTFTB) to 10^{-4} S cm^{-1} for Cd_2(TTFTB). This observed trend is ascribed to the shorter S–S distances between adjacent TTFBT moieties, facilitating through-space charge transport.[87-88]

Conversely, following the through-bond approach, long-range charge transport is promoted via extended charge delocalization. This involves π-conjugated organic linkers as well as enhanced orbital overlap between the metal center and ligands to form more covalent bonds.[85] One of the first examples adopting this approach is $Cu[Cu(pdt)_2]$ (pdt = 2,3-pyrazinedithiolate), which consists of 2D sheets formed by pdt-bridged Cu(II) ions. The resulting square sheets are interconnected through Cu(dithiolene) units, creating a 3D cubic structure (Figure 5, middle).[89] While $Cu[Cu(pdt)_2]$ attains an electrical conductivity of $6\cdot10^{-4}$ S cm^{-1}, its subsequent mixed-metal counterpart $Ni[Cu(pdt)_2]$ displays a value of $1\cdot10^{-8}$ S cm^{-1}. Despite both compounds sharing identical structural features responsible for charge carrier mobility, a notable reduction in electrical conductivity of about four orders of magnitude was observed. Presumably, the substitution of d^9 Cu(II) with d^8 Ni(II) results in the reduction of charge carrier density, thus explaining this finding.[90]

Within the frame of through-bond charge transport, also the introduction of guests emerges as an effective alternative to enhance electrical conductivity. Allendorf *et al.* accomplished the transformation of the insulating HKUST-1 structure into a semiconducting material, elevating its electrical conductivity from 10^{-8} S cm^{-1} to $7\cdot10^{-2}$ S cm^{-1} through doping with the redox-active 7,7,8,8-tetracyanoquinododimethane (TCNQ). The inclusion of conjugated TCNQ molecules enhances electronic coupling between the Cu(II) centers by binding to open metal sites, thereby cross-linking coordinatively unsaturated Cu_2-paddlewheel nodes within the MOF (Figure 5, right). The significance of through-bond charge transport in the obtained TCNQ-doped $Cu_3(BTC)_2$ was confirmed by the inclusion of its saturated counterpart, H_4TCNQ, which failed to support resonance delocalization. However, the introduction of TCNQ within the micropores led to a significant reduction in the BET surface area from 1844 m^2 g^{-1} to 214 m^2 g^{-1}.[83, 91-94]

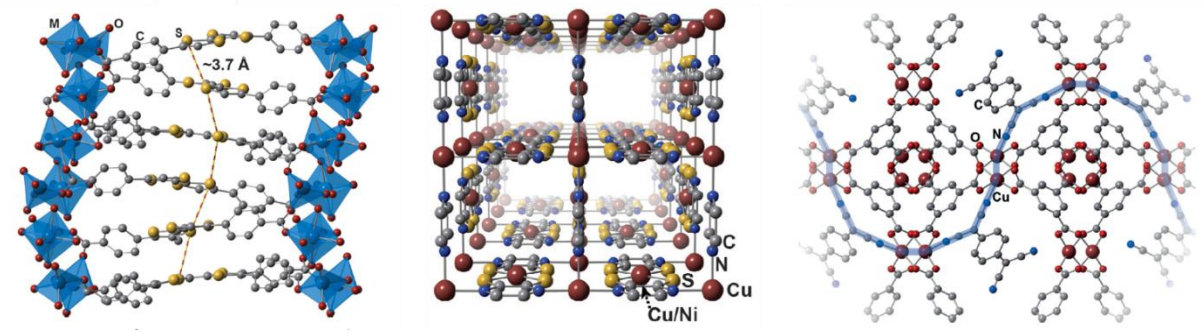

Figure 5: Approaches to introduce charge carrier mobility in MOFs: Through-space transport via π-π stacking in M_2(TTFTB) (M=Mn, Co, Zn, Cd) (left), through-bond transport through Cu(pyrazine) sheets in Cu[M(pdt)$_2$] (M=Cu, Ni) (middle) and cross-liniking of Cu_2-paddlewheels with redox-active guest in TCNQ doped HKUST-1 to achieve through-bond charge transport (right). Reprinted with permission from Sun, L.; Campbell, M. G.; Dincă, M., Electrically Conductive Porous Metal–Organic Frameworks. *Angewandte Chemie International Edition* **2016,** *55* (11), 3566-3579. Copyright (2016) Wiley-VCH.[84]

An alternative methodology known as *redox matching* aims to enhance spatial and energetic orbital overlap between organic and inorganic moieties, facilitating charge transport without compromising the framework´s surface area. Unlike the prevalent ionic character of metal–oxygen or metal–nitrogen bonds, redox matching strives for a more covalent nature of the metal-ligand coordination bond. In this regard, employing ligator atoms with lower electronegativity (*e.g.* heavier chalcogenides) represents a promising approach to enhance the covalent character of formed coordination bonds and diminish electronic barriers for charge carrier transport.[84-85]

The use of sulfur-based ligands has emerged as an auspicious strategy to realize the concept of redox matching. Sun *et al.* demonstrated this potential by replacing the bridging phenolate groups in Mn_2(DOBDC) (DOBDC = 2,5-dihydroxybenzene-1,4-dicarboxylate) with thiophenol units, resulting in the creation of the thiolated analogue Mn_2(DSBDC) (DSBDC = 2,5-disulfhydrylbenzene-1,4-dicarboxylate). The synthesized material provides a charge mobility of 0.01 $cm^2\ V^{-1}\ s^{-1}$, comparable to organic semiconductors like rubrene (0.05 $cm^2\ V^{-1}\ s^{-1}$) while maintaining unchanged porosity (BET surface area: 978 $m^2\ g^{--1}$). Despite the promising charge mobility in Mn_2(DSBDC), its electrical conductivity remained notably low ($2.5\cdot10^{-12}$ S cm^{-1} for Mn_2(DSBDC) and $3.9\cdot10^{-13}$ S cm^{-1} for Mn_2(DOBDC)), presumably due to the lack of free charge carriers.[95] To address this limitation, the respective Iron analogues Fe_2(DOBDC) and Fe_2(DSBDC) were investigated, achieving a substantial increase in electrical conductivity by six orders of magnitude, reaching values of $3.2\cdot10^{-7}$ S cm^{-1} and $3.9\cdot10^{-6}$ S cm^{-1}, respectively.[96]

Even higher values have been achieved by M_2Ni(dmit)$_2$ (dmit = 4,5-dimercapto-1,3-dithiole-2-thione, M = Cu, Ag, Au), which displayed significant conductivities ranging

from $5 \cdot 10^{-4}$ S cm^{-1} for the Cu compound to 1.6 S cm^{-1} for $Au_2Ni(dmit)_2$.[97] Additionally, the 1D-polymers $Cu_2(C_4S_6)$ and $Ni(C_4S_6)$ showcased electrical conductivities of 0.1 S cm^{-1} and 0.9 S cm^{-1}, respectively.[98] However, the conductivities of these materials were surpassed by certain two-dimensional CPs. For instance, Cu(HT) (HT = 4-hydroxythiophenolate) exhibits an electrical conductivity of 120 S cm^{-1} due to the coordination of Cu(I) ions by three sulfur atoms in a trigonal planar geometry, forming infinite 2D layers.[99]

Overall, it becomes evident that both the choice of ligands and a metal species capable of providing charge carriers are crucial. Particularly, electron-rich metals such as Mn, Fe, Co, Ni, and Cu have proven to be suitable.

1.5 Sulfur-Donor Ligands in Coordination Chemistry

In line with previous examples, sulfur-based ligands offer significant potential for implementing redox matching and provide several advantages for enhancing electronic properties. However, while N- and O-based ligands such as amines and carboxylates are prevalently used in molecular as well as extended coordination compounds, sulfur-based analogues are much less explored. Nevertheless, the family of thiols, (di-)thiocarbamates, xanthates and (di-)thiocarboxylates shows promising characteristics upon reaction with various (transition)metals.[100] The increased atomic radius of sulfur (1.84 Å) compared to oxygen (1.4 Å)[101] allows for a wide range of possible coordination patterns, including chelating and bridging motifs. Thus, structurally diverse coordination compounds have been reported, ranging from coordination complexes and metal clusters to extended CPs and MOFs. Beyond structural diversity, the introduction of sulfur-rich ligands offers auspicious features toward substantially improved electronic properties. Enhanced metal–metal interaction, facilitated charge mobility and electronic communication between inorganic moieties were observed for discrete as well as extended coordination compounds derived from S-based ligands.[100, 102] In this regard, most of to date reported examples are based on thiols whereas dithiocarboxylates – the counterpart of commonly used carboxylates – are much less investigated and especially 3D extended structures are scarce.

1.5.1 Molecular Model Complexes of Sulfur-Donor Ligands

Since the 1990s, a series of Mo_2 paddlewheel complexes has emerged as a prime examples for investigating the influence of varying bridging ligands on redox behavior and electronic properties.[103-106] Following different studies from Cotton *et al.* on O- and N-based ligands, focus has shifted toward the evaluation of S-donor ligands since 2006. Electronic properties of phenylene bridged Mo_2 dimers were investigated on a series of complexes derived from the terephthalate bridged $[Mo_2(DAniF)_3]_2(\mu\text{-}O_2CC_6H_4CO_2]$ (DAniF = N,N'-di(*p*-anisyl)formamidinate). Gradual introduction of S-ligator atoms led to the [OS–OS], $[O_2–S_2]$ and $[S_2–S_2]$ analogues (Figure 6). Due to their conjugated core, these ligands are especially promising toward the implementation of long-range charge delocalization and intramolecular electron transfer.[107]

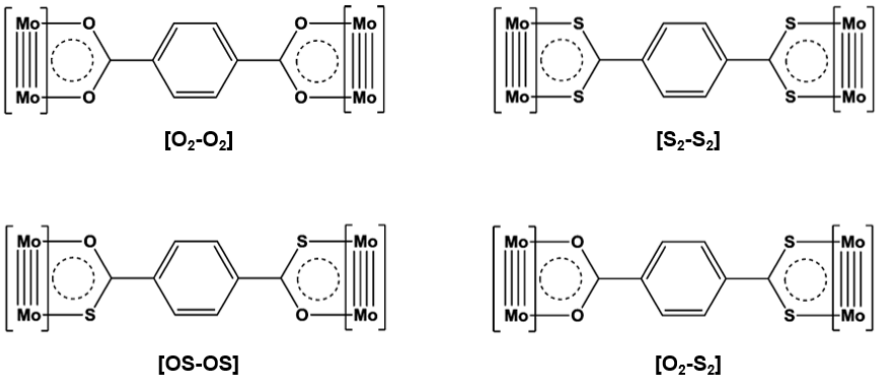

Figure 6: Mo_2-paddlewheels with varying bridging ligands. $[Mo_2] = [Mo_2(DAniF)_3]^+$ (DAniF = N,N'-di(*p*-anisyl)formamidinate). Adapted and reprinted with permission from Xiao, X.; Liu, C. Y.; He, Q.; Han, M. J.; Meng, M.; Lei, H.; Lu, X., Control of the Charge Distribution and Modulation of the Class II–III Transition in Weakly Coupled Mo2–Mo2 Systems. *Inorganic Chemistry* **2013,** *52* (21), 12624-12633. Copyright (2013) American Chemical Society.[107]

Electronic structure calculations based on density functional theory (DFT) evidenced a reduced HOMO-LUMO gap for sulfur-rich compounds compared to the $[O_2–O_2]$ counterpart as the energy of the LUMO is lowered with gradual substitution of O by S.[108] This results from the lower energy of the π^* orbital in the tetrathioterephthalate ligand (3.75 eV) compared to the terephthalate ligand (5.76 eV). Consequently, enhanced mixing with the metal δ orbitals is enabled, leading to strong metal–ligand interactions as evidenced by the smallest HOMO-LUMO gap of 1.81 eV found for $[S_2–S_2]$.[107, 109] These theoretical findings have further been experimentally confirmed by electrochemical and spectroscopic investigations. Electronic absorption spectroscopy of the four complexes revealed that stepwise thiolation leads to an enhanced intensity as well as red shift of the respective metal to ligand charge transfer (MLCT) absorption band. While $[O_2–O_2]$ shows a MLCT band at 492 nm, the band for $[S_2–S_2]$ is located at 715 nm. The mixed compounds [OS–OS] and $[O_2–S_2]$ display a similar energy (637 and 618 nm, respectively). Thereby, the observed band energies are in agreement with the calculated energies for HOMO-LUMO transitions as obtained from DFT. Electrochemical oxidation of the $Mo_2–Mo_2$ complexes resulted in successive electron removal on both Mo_2 units. In the respective cyclic voltammogram (CV) this is presented by two one-electron redox couples with a potential separation of 91 mV for $[O_2–O_2]$, 116 mV for [OS–OS] and 195 mV for $[S_2–S_2]$. The increased peak to peak separation results from enhanced electronic communication between the Mo_2 units in the case of the tetrathioterephthalate bridged dimer. Since $Mo_2–Mo_2$ distances are slightly longer in the fully thiolated complex compared to the O-based ligand and the auxiliary ligands remained unchanged, this coupling effect is ascribed to

the enhanced electronic resonance between the central metal atoms and the bridging ligand.[107-108, 110]

Subsequent studies have been performed to further expand this series of model complexes. For example, naphthalene-based ligands as well as elongated phenylene bridges with different substituents and varying auxiliary ligands were introduced to investigate other parameters (e.g. planarity and symmetry).[110-111]

This exemplary series of bridged Mo_2 dimers demonstrates the benefit of sulfur-donor ligands to introduce electronic coupling between two metal units. Following this approach, the incorporation of such motifs into extended structures would open manifold opportunities for the implementation of electron transfer into CPs and the design of conductive materials.

1.5.2 Sulfur-Based Coordination Polymers: Thiolate linkers

Lately, there has been a notable shift in considering sulfur atoms as integral components for the design of CPs. Consequently, first examples of extended materials comprising metal–sulfur coordination bonds have been reported, showcasing properties distinct from conventional metal–oxygen bonded materials. In this regard, thiols are the most widely used class of ligands when it comes to designing sulfur-based CPs. For the construction of extended structures, especially multidentate thiols are of interest due to their ability to coordinate various metal ions through their thiolate groups.

In 2019, preformed Fe_4S_4 clusters were successfully converted into a polymeric chain through bridging coordination by the 1,4-benzenedithiolate linker (Figure 7). The resulting CPs can be described with the sum formula $[(Fe_4S_4(BDT)_2](TBA)_2$ (TBA = tetra-*n*-butylammonium) and $[(Fe_4S_4(BDT)_2](TMA)_2$ (TMA= tetramethylammonium).[112]

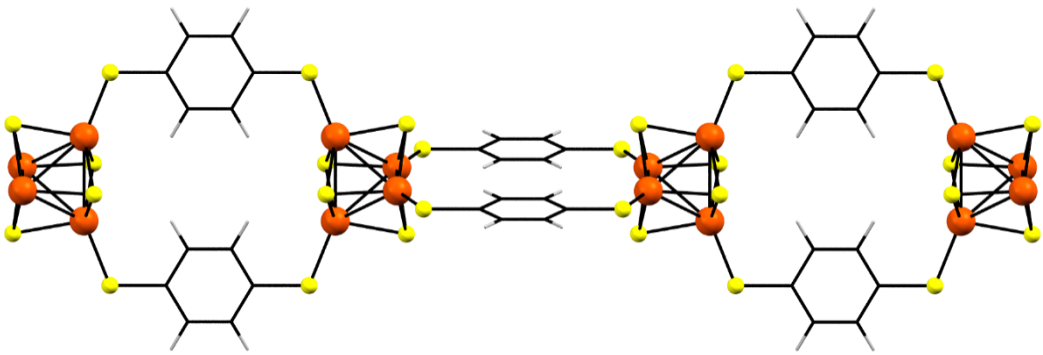

Figure 7: Solid state linear chain structure of $[(Fe_4S_s(BDT)_2][TBA]_2$ (BDT = 1,4-benzenedithiolate).[112]

UV/Vis absorption spectroscopy indicates the presence of ligand to metal charge transfer (LMCT) between the thiolate linker and the Fe atom, suggesting potential electronic transitions between organic and inorganic components. Subsequent electrochemical investigations confirmed redox activity. Two quasi-reversible reductions were observed in the CV, corresponding to the $[Fe_4S_4]^{2+}/[Fe_4S_4]^{+}$ (-1.43 V vs. $FeCp_2^{+}/FeCp_2$) and $[Fe_4S_4]^{+}/[Fe_4S_4]^{0}$ (-2.13 V vs. $FeCp_2^{+}/FeCp_2$) conversions. Moreover, an electrical conductivity of $3 \cdot 10^{-11}$ S cm^{-1} was determined. After introduction of additional charge carriers through partial reduction, this value could be enhanced by two and four orders of magnitude for the TBA and the TMA compound, respectively.[112]

In the context of multi-dimensional structures, introducing a greater number of thiol groups proved to be a promising strategy. Most intensively investigated examples of this family are the conjugated triphenylenehexathiolate (THT) and benzenehexathiol (BHT). Through reaction with different transition metals, 2D π-conjugated CPs are obtained, which are known for their outstanding electronic properties and notable electronic conductivity.

For instance, various materials within the family of $M_3(THT)_2$ (M = Fe, Co, Ni, Pt) have been intensively investigated. In 2014 the first example, $Pt_3(THT)_2$[113] has been reported, followed by isostructural materials comprising Fe,[114] Ni[115-116] and Co[116-118] metal ions. In these CPs, central metal ions are coordinated by four thiolate groups in a square planar geometry. Thus, 2D extended hexagonal sheets are formed, consisting of six metal ions which are bridged through six THT linkers (Figure 8, left). Typically, the pore diameter in these sheets is in the range of 2 nm and N_2 physisorption measurements confirmed a BET surface area of 329 m^2 g^{-1} in the case of $Pt_3(THT)_2$.[113] Because of the high density of metal-bis(dithiolene) units in these materials, especially the Ni- and Co-versions have been intensively studied for their electrocatalytic properties. The deposition of $M_3(THT)_2$ sheets onto electrode surfaces was realized either by immersing the support into the reaction mixture or by transferring the already prepared free-standing $M_3(THT)_2$ film onto the electrode. Both, $Ni_3(THT)_2$ and $Co_3(THT)_2$, showed outstanding electrocatalytic performance in the hydrogen evolution from water. Compared to molecular Ni/Co dithiolene species, enhanced stability and durability was observed which is ascribed to the stabilizing effect of the surrounding network. Further, the immobilization of active centers within the crystalline structure enables high catalyst loading which in turn leads to substantial increase of catalytic activity.[115, 117]

In addition to their electrocatalytic performance, their charge transport properties as well as electrical conductivity have been extensively studied. In 2018, Feng *et al.* reported band-like charge transport for $Fe_3(THT)_2(NH_4)_3$ with a mobility of 220 $cm^2 V^{-1} s^{-1}$ and an electrical conductivity of 0.1 S cm^{-1} at room temperature. For lower temperatures, a linear decrease of conductivity was observed down to 10^{-5} S cm^{-1} at 100 K. Charge mobility, however, remained nearly constant during varying temperatures and therefore, thermally excited charge carriers are presumably the reason for the observed temperature dependence since lower temperatures would substantially reduce such charge carrier density.[114] In contrast to this, $Co_3(THT)_2$ showed transition from semiconducting to metallic conductivity at lower temperatures. The transition temperature thereby strongly depends on the thickness of the sample. For a thin film with a thickness of 0.20 µm, for example, a room temperature conductivity of $3 \cdot 10^{-2}$ S cm^{-1} was measured with transition to metallic behavior occurring in the range between 150-170 K.[118]

These conductivity values, however, have been surpassed by 2D sheets from the M-BHT (M = Ni, Co, Cu) family. For $Ni_3(BHT)_2$ electrical conductivities of 0.15 S cm^{-1} for pelletized powder and 160 S cm^{-1} for a microflake sample are reported.[119-120] Even higher values are reached by $Cu_3(BHT)$ with an electrical conductivity of 1580 S cm^{-1} measured at room temperature on a thin-film.[121] To date, this marks the highest reported conductivity for an extended CP.

Similar to THT derived CPs, also in the case of M-BHT metal ions are coordinated in a square planar environment by four thiolate groups from two BHT ligands. Due to the smaller diameter of the BHT, dense CPs are formed with no significant surface area (Figure 8, middle).[119] In the special case of $Cu_3(BHT)$, each sulfur atom is coordinating to two copper centers, resulting in a dense topological structure. Through the additional coordination of each S atom, a continuous 2D Cu-S network is generated (Figure 8, right). Again, strong π–d interactions and enhanced charge transfer between metal and ligand are discussed to cause substantial charge delocalization through the 2D lattice, enabling this high conductivity.[121]

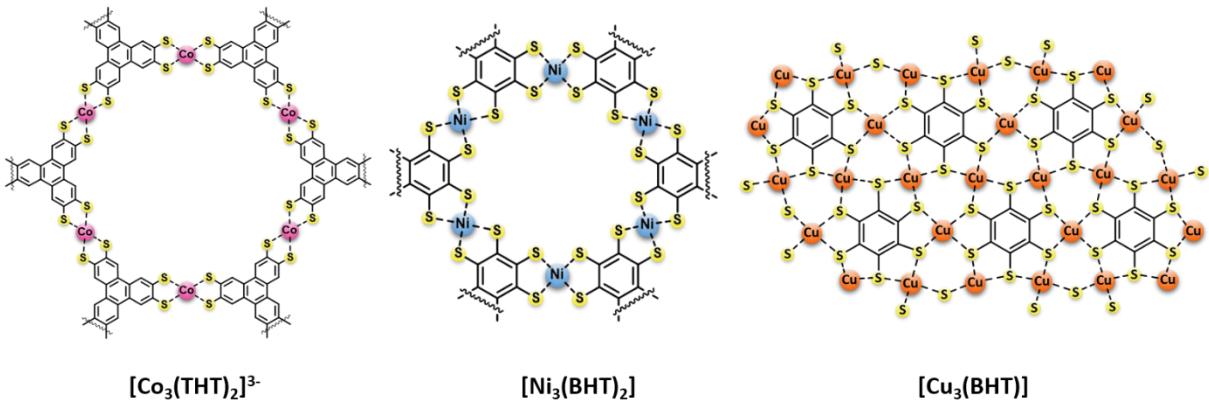

Figure 8: Schematic representation of 2D sheets in $[Co_3(THT)_2]^{3-}$ (left),[118] $[Ni_3(BHT)_2]$ (middle)[119] and $[Cu_3(BHT)]$ (right).[121]

1.5.3 Sulfur-Based Coordination Polymers: Dithiocarboxylate Linkers

Crosslinking through metal–metal interactions or hetero atoms

Compared to the extensively studied thiols, dithiocarboxylate linkers (RCS_2) have received significantly less exploration, resulting in scarce examples of derived coordination polymers. While CPs based on thiols typically create networks by utilizing the bridging coordination modes of their multi-topic linkers, most RCS_2-based CPs reported to date form polymeric structures through additional metal–metal interactions or involve the incorporation of heteroatoms such as nitrogen or halogens to establish their polymeric frameworks.

An example of this is a series of 1D polymer chains. Initial studies date back to the 1980s, when the first syntheses and structural investigations of linear $[M_2(RCS_2)_4]$ (M = Pt, Pd, Ni; R = *n*-alkane) chains have been reported.[122-125] Following that, extensive investigations were performed, focusing on partial oxidation via the introduction of halogens to form halogen-bridged 1D chains of the general formula $[M_2(RCS_2)_4X_n]$ (M = Pt, Pd, Ni; R = aliphatic group; X = Cl, Br, I; n = 1, 2).[126-129] Even though various metals and halogens have been used, $[Pt_2(CH_3CS_2)_4I]$ is the most extensively studied example. Therefore, this compound will be discussed exemplarily in the following.

Structural analysis revealed that these compounds exhibit infinite MMX chains, which are held together via bridging iodide ions on the one hand, and linkage through RCS_2 ligands on the other hand. Specifically, two Pt(II) ions are bridged by four RCS_2 ligands via μ_2-1κS^1:2κS^2 coordination of the dithiocarboxylate groups to form a neutral $Pt_2(CH_3CS_2)_4$ paddlewheel unit (Figure 9, left). After oxidative addition of iodine, the dimers are aligned along the b-axis with bridging iodide being located at the midpoints between the

$Pt_2(CH_3CS_2)_4$ paddlewheels.[130] Interestingly, adjacent chains are interconnected via weak S–S van der Waals interactions along the c-axis (Figure 9, right), contributing to increased dimensionality.[131]

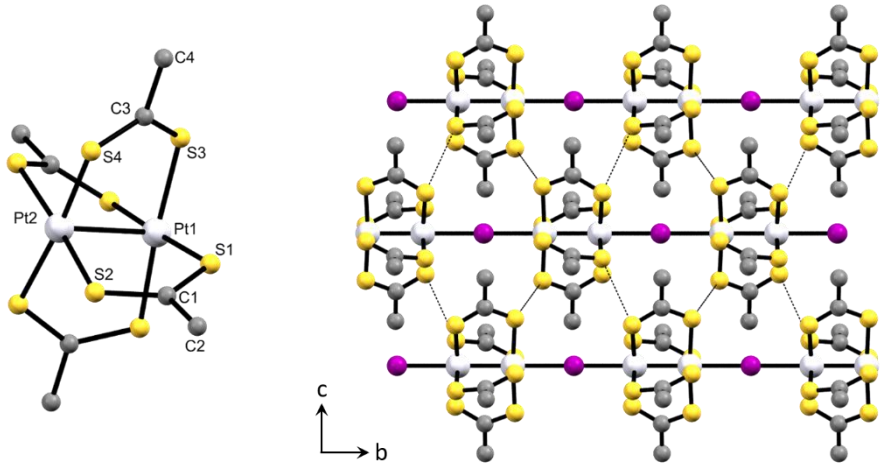

Figure 9: Solid state structure of the $[Pt_2(CH_3CS_2)_4]$ paddlewheel unit (left) and linear $[Pt_2(CH_3CS_2)_4I]$ chains with crosslinking via weak S–S van der Waal contacts (right).[127]

The introduction of iodide further lead to partial oxidation of the neutral $[Pt_2(CH_3CS_2)_4]$ chains, resulting in a mixed-valence compound with a formal oxidation state of +2.5 for each Pt atom. Metallic conductivity of 13 S cm^{-1} was observed for temperatures above 300 K, while a transition to semiconducting behavior was found below this temperature.[131] This metallic-to-semiconductor transition is ascribed to different charge-ordering modes: while an averaged valence ordering (–I–$Pt^{2.5+}$–$Pt^{2.5+}$–I–$Pt^{2.5+}$–$Pt^{2.5+}$–) is assumed for the metallic phase, a trapped-valence state (–I–Pt^{2+}–Pt^{3+}–I–Pt^{2+}–Pt^{3+}–) is considered to be present in the semiconducting phase.[130-133] Moreover, computational studies indicated a strong influence of the CH_3CS_2 ligand on the electronic structure of these chains.[134] Further investigations on the influence of the ligand chain length (e.g. *n*-propyl, *n*-butyl, *n*-pentyl) concluded that this variations mainly impact structural parameters and disorder, but do not substantially influence the electronic structure.[135]

In this series of one-dimensional MMX chains, individual units are linked via metal–metal or metal–halogen interactions, while the CS_2 ligands participate in the construction of the paddlewheel units through their bridging coordination. However, by introducing additional functional groups to the ligand, polymeric structures can also be formed through the coordination of the multitopic linker.

For example, one dimensional chains of $(CH_3)_2Sn(S_2CC_3H_2N_2)$ are built by chelating coordination, where Sn atoms are coordinated by one dithiocarboxylate S atom and one

N atom (ortho position to the CS_2 group) of the 4(5)-imidazoledithiocarboxylate linker. The coordination of the second imidazole nitrogen atom to an adjacent Sn atom leads to the formation of infinite chains. Overall, each Sn atom is in a homoleptic coordination environment consisting of two N atoms, one S atom and two methyl ligands (Figure 10).[136]

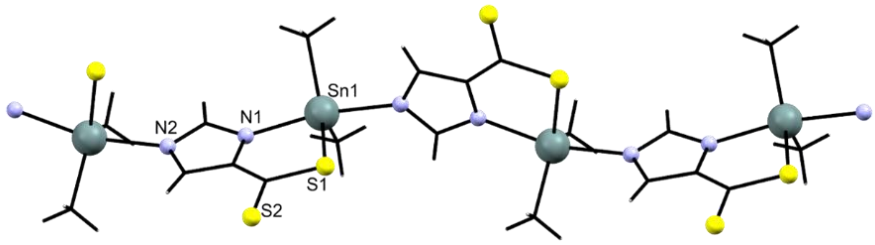

Figure 10: Linear chain structure of $(CH_3)_2Sn(S_2CC_3H_2N_2)$.[136]

Depending on the specific ligand, the construction of higher-dimensional structures can be realized as well. For instance, the para-substituted ligand pyridine-4-dithiocarboxylate was utilized to build two-dimensional sheets of [Ag(pyridine-4-dithiocarboxylate)].[137] In this polymer Ag_2 dimers are formed in which each Ag^+ ion is coordinated in a μ_2-1κS^1:2κS^2 coordination mode by two sulfur atoms of different dithiocarboxylate linkers as well as one nitrogen atom from a third linker. As a result, each Ag atom exhibits a T-shaped coordination environment and square pores are formed. In the solid state the layers are stacked in an ABAB sequence, showing additional inter-layer Ag–S interactions. The parallel alignment of the sheets leads to the formation of infinite square-shaped tubular channels along the *c*-axis (Figure 11).

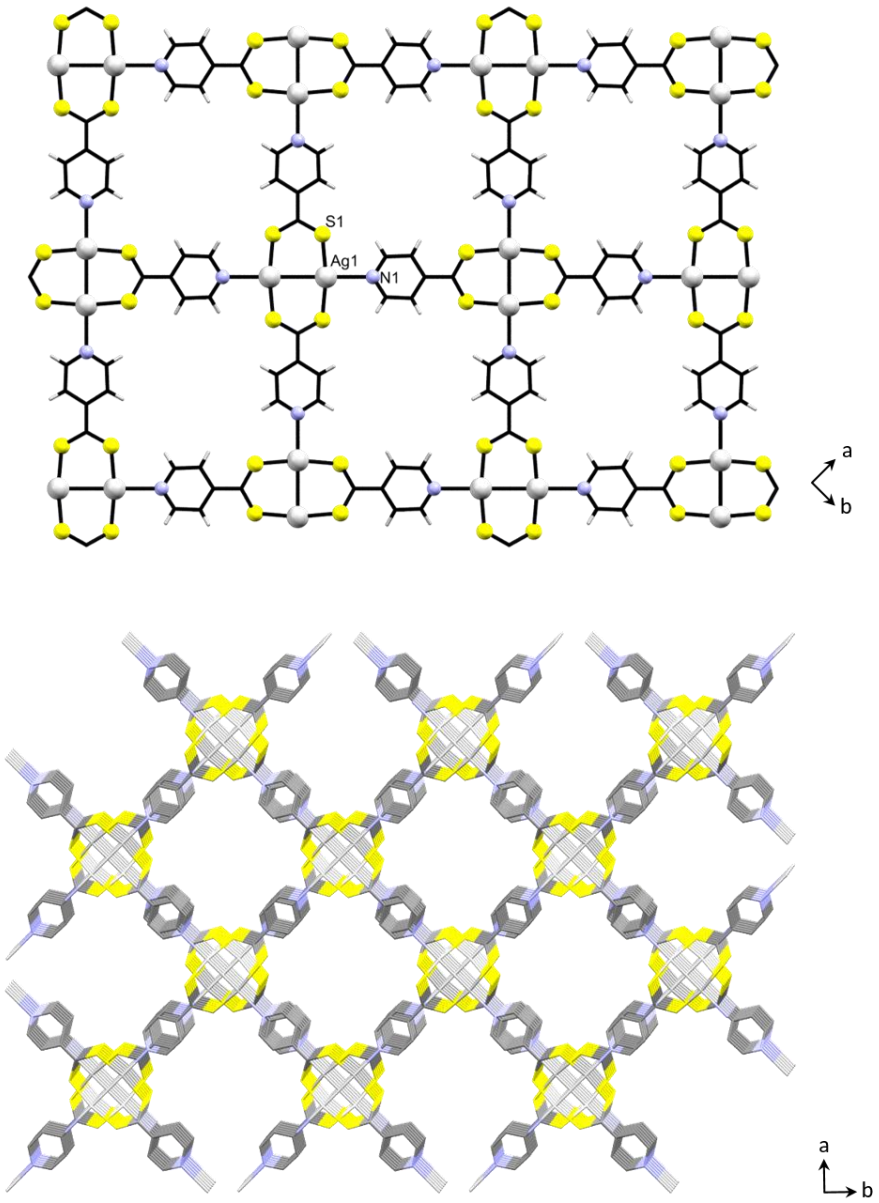

Figure 11: 2D sheet structure of [Ag(pyridine-4-dithiocarboxylate)]. Single layer (top) and packing in the solid state with tubular channels along the crystallographic *c*-axis (bottom).[137]

This CP shows strong absorption of light in the near infrared (NIR) region, indicating a small bandgap in the range of semiconductors together with possible photothermal effect under NIR radiation. Although, absorption spectroscopy as well as DFT calculations confirmed a direct band gap of 1.2 eV, a relatively low electrical conductivity of 10^{-11} S cm^{-1} was found.[137] This can be explained by the absence of free charge carrier due to the stable configuration of the d^{10} Ag^{+} ion.

Crosslinking through bridging CS_2 linker

In contrast to the linkage of inorganic units via heteroatoms or metal–metal interactions, only a few examples of CPs have been reported where the polymeric structure is

exclusively determined by the coordination of the linker. In such CPs, typically, both sulfur atoms coordinate to different metal atoms. The resulting μ_2-1κ*S*[1]:2κ*S*[2] coordination enables the linkage of neighboring metal atoms, forming extended metal–sulfur chains. For instance, in [$Au_2(CS_2$-*i*-butyl$)_2$], Au atoms are bridged via *iso*-butyldithiocarboxylate linkers, which are alternately arranged on opposite sides of the Au chain (Figure 12, left).[138] Due to the versatile coordination modes of dithiocarboxylate groups, more complex structures are also possible. In [$Ag_4(S_2C$-*o*-toluato$)_4$], two Ag atoms are coordinated by a total of four S atoms from two ligands, resulting in Ag_4L_4 (L = S_2C-*o*-toluato) subunits. By additional coordination of one S atom to the neighboreing metal, these units are linked together, leading to the formation of an extended chain structure (Figure 12, right).[139]

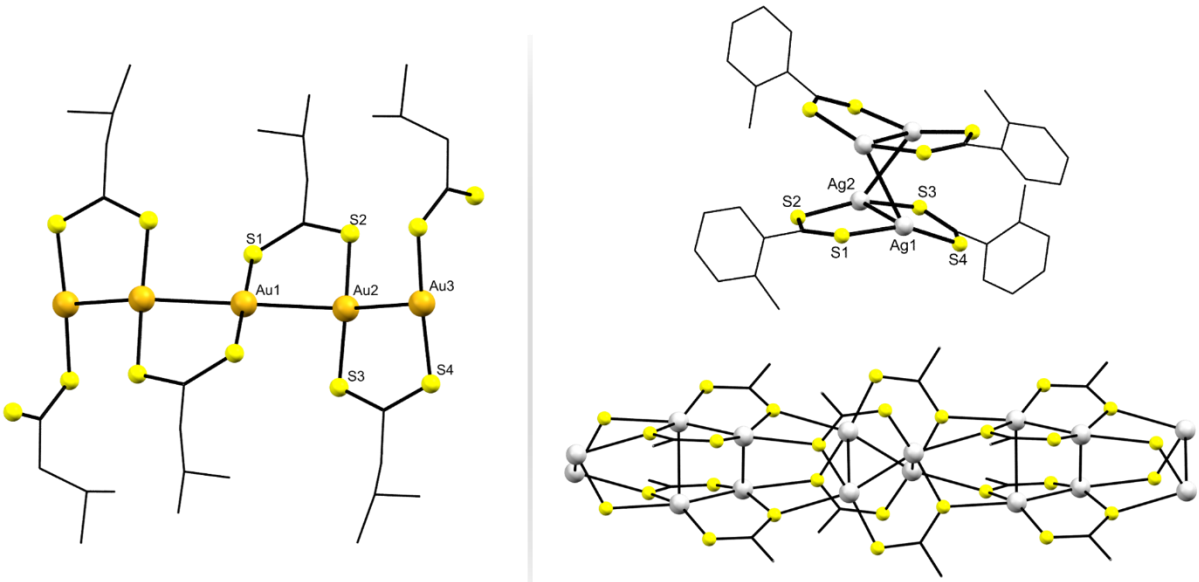

Figure 12: Chain structure of [$Au_2(CS_2$-*i*-butyl$)_2$][138] (left) and Ag_4L_4 subunit (L = S_2C-*o*-toluato) as well as polymeric structure of [$Ag_4(S_2C$-*o*-toluato$)_4$][139] (right).

Carboxylate-based CPs and MOFs, on the contrary, are typically constructed from multitopic linkers, bridging inorganic units via their multiple functional groups. In the realm of CS_2-based CPs, however, such examples are scarce. To date, there is only one example reported in the literature where a multi-dimensional structure is obtained from bridging coordination through a multitopic dithiocarboxylate linker. In this CP, infinite 1D zig-zag chains of [Zn(BDDTC)] (BDDTC = benzene-1,4-di(dithiocarboxylate)) are formed by connecting Zn^{2+} ions through the ditopic $BDDTC^{2-}$ ligand as reported in 2007.[140] Through coordination of four sulfur atoms from two linkers and two additional DMF molecules, an octahedral coordination environment is obtained for each Zn atom (Figure 13, top), giving the overall formula of [Zn(BDDTC)$(DMF)_2$]. In the solid state the chains

are running parallel along the crystallographic *a*-axis, stabilized via H–S hydrogen bonds. Along the *b*-axis, chains stack on top of each other (Figure 13, bottom) with intercalated DMF molecules in between. Additionally, the Mn counterpart is reported, for which an analogous structure is postulated based on PXRD data. Interestingly, solvent removal through thermal activation of [Zn(BDDTC)(DMF)$_2$] led to a substantial structural change as evidenced by PXRD analysis. However, after reintroduction of DMF, the initial structure is restored.[140]

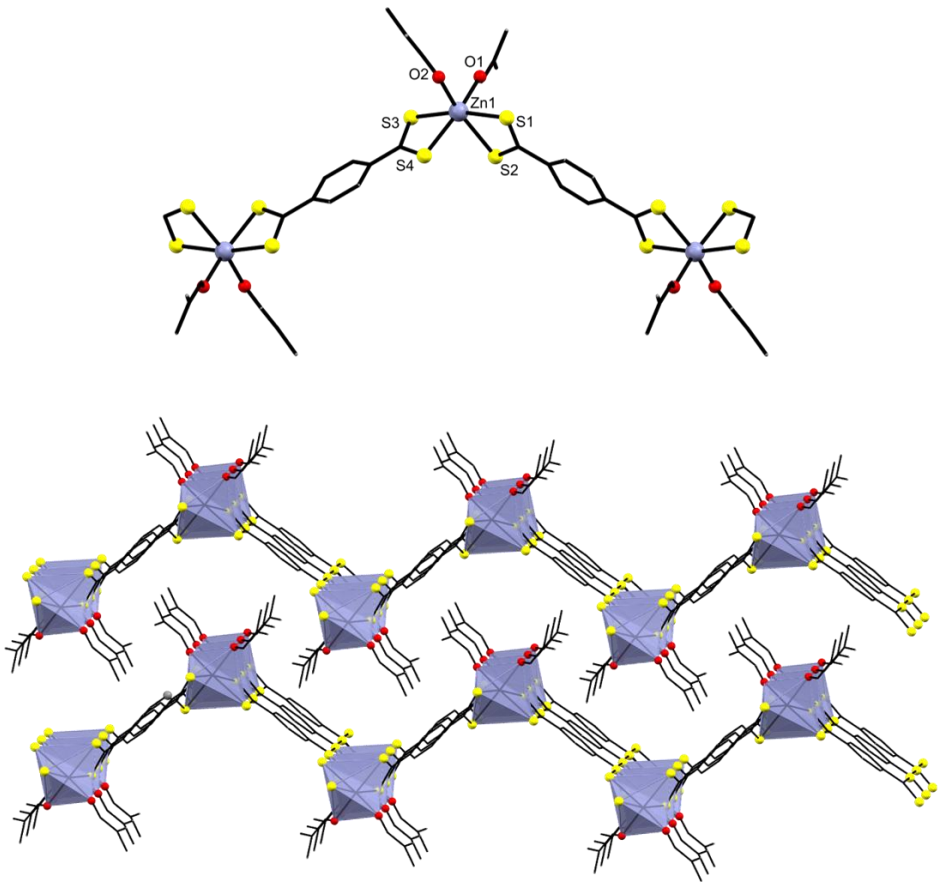

Figure 13: Coordination environment around the Zn atom (top) and crystalline arrangement of zig-zag chains (bottom) in Zn(BDDTC) as determined by single-crystal XRD. Intercalated DMF molecules and hydrogen atoms are omitted for clarity.[140]

For both CPs, electronic absorption in the UV-Vis/NIR region is reported, with absorption bands at 600 nm and 925 nm for [Zn(BDDTC)(DMF)$_2$] and [Mn(BDDTC)(DMF)$_2$], respectively. These low-energy electronic transition originate from LMCT, suggesting semiconductive behavior.[140] However, no experimental proof of this assertion has been reported.

1.6 Synthetic Challenges and Strategies Toward Sulfur-Based CPs

Despite their promising structures and properties, sulfur-based CPs have received limited attention in literature compared to their well investigated carboxylate counterparts. For the construction of CPs and MOFs, the use of sulfur-donor ligands as linkers can pose some unique challenges. Firstly, the synthesis of these compounds is challenging due to their high reactivity and potential instability. Especially dithiocarboxylates are prone to decomposition or side reactions.[141] In the presence of oxygen, dithiocarboxylates can undergo oxidation reactions, leading to the formation of disulfides (R-S-S-R) or polysulfides, sulfoxides (R-S(O)-R), sulfones (R-S(O)$_2$-R) or sulfonic acids (R-SO$_3$H). Additionally, in contact with water or moisture from air, dithiocarboxylates are easily hydrolyzed, resulting in the cleavage of the sulfur-carbon bond and the formation of corresponding thiol- or carboxylic acids along with the release of H_2S gas.[142-145] Compared to carbonyl compounds thiocarbonyl groups are less stabilized. Therefore, C=S bonds tend to rearrange to more stable C-S single bonds by forming oligomers in solution as well as in solid-state.[146] Due to their increased reactivity, dithiocarboxylate compounds necessitate production and storage under inert conditions. Moreover, most of these compounds exhibit a potent and unpleasant odor, adding complexity to their handling.[142, 147]

For their incorporation into MOFs, this also poses several challenges compared to the robust carboxylate analogs. For instance, the oxygen sensitivity only allows the use of degassed solvents, as well as the conduct of CP assembly under inert conditions. Furthermore, the solubility behavior of many dithiocarboxylates differs significantly from that of conventional RCO$_2$ linkers, rendering established synthesis protocols inapplicable. Also, the addition of further additives, such as acid-based modulators, is often not feasible due to potential side reactions. In addition to these synthetic challenges, different reactivities towards metallic building blocks need to be considered as well. The lower electronegativity of the sulfur donor atom compared to oxygen allows for better orbital interaction between the metal and linker. The formed coordination bonds thus exhibit a higher covalent character.[84, 86] While this is advantageous for achieving highly stable metal–linker connections and facilitating electron transport within the formed coordination polymer, it also presents significant challenges for the self-assembly process. Typically, the formation of crystalline CPs and MOFs proceeds under thermodynamic control, relying on the reversible attachment of the linker to the inorganic

SBU (Figure 14). For instance, elevated temperatures in the solvothermal process promote entropically driven dehydration. Through additional linker coordination to the vacant metal sites, increased connectivity and thus higher dimensionality are achieved in the thermodynamically favored framework, representing the energetic minimum.[148]
The increased covalent character of metal–sulfur bonds, however, leads to significantly reduced reversibility, resulting in predominantly kinetic reaction products. In many cases, this causes the formation of amorphous precipitates rather than the formation of the thermodynamically favored end product. In the case of crystalline end products, the rapid kinetics of the reaction often give rise to the formation of numerous small crystallization nuclei. As a consequence, the resultant materials tend to be mixtures comprising various phases rather than exhibiting phase purity. This characteristic poses challenges in terms of reproducibility and the precise control of material composition.[149]

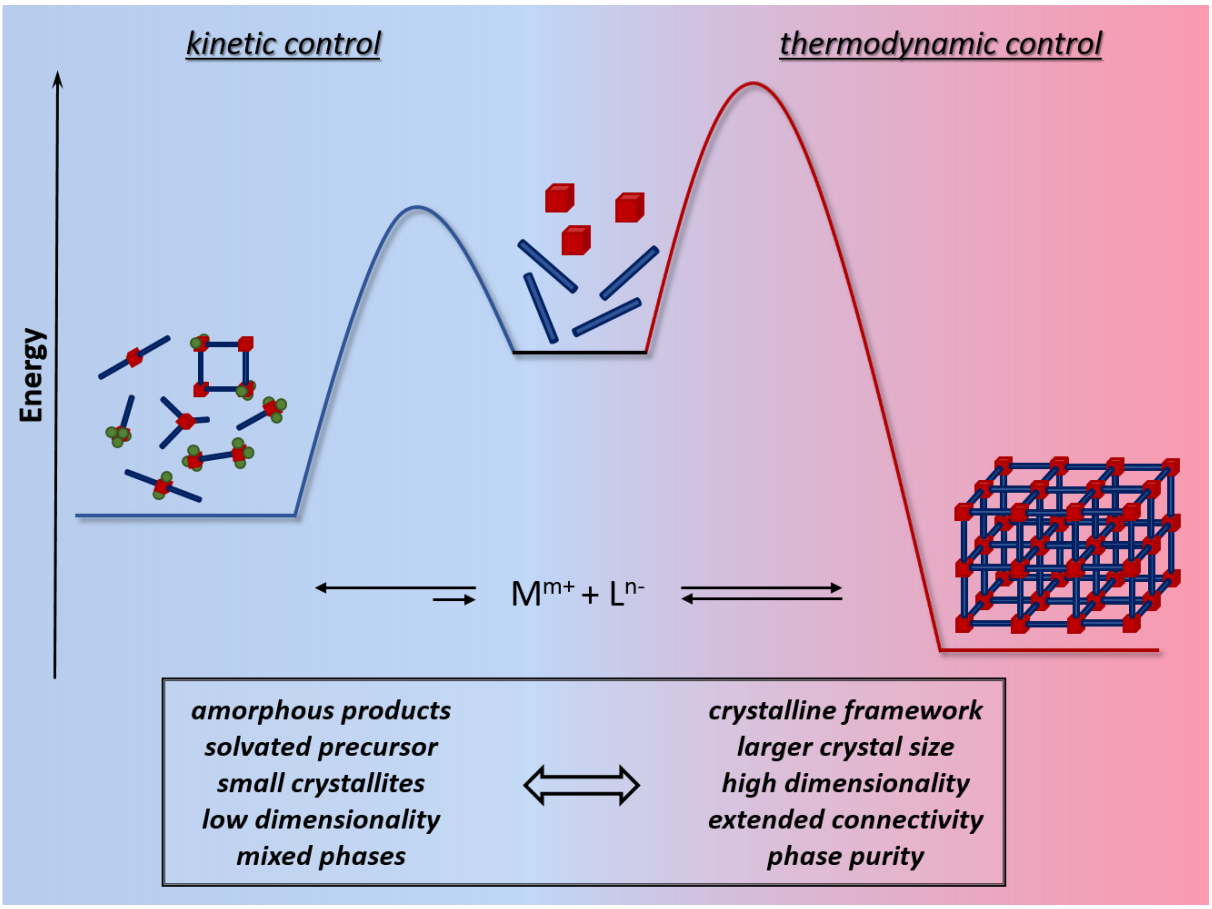

Figure 14: Thermodynamic versus kinetic control in the solvothermal synthesis of CPs and MOFs. M = transition metal, L = organic linker.

To obtain crystalline CPs based on sulfur-donor linkers, it is crucial to precisely adjust the reaction conditions, considering all the aforementioned influencing factors. In addition to the conventional solvothermal synthesis, other synthesis methods can be exploited to control reaction kinetics, thereby enabling selective and reproducible synthesis of crystalline materials.

For instance, through slow and controlled combination of organic and inorganic components low concentrations can be maintained, thus facilitating controlled crystallization. Specifically, diffusion-based techniques such as layering or crystallization in gels are conceivable in this context.[150-152] To ensure the complete separation of linker and metal salt solutions, layer-by-layer methods can be employed. This involves the sequential application of the two solutions onto a substrate, thus preventing uncontrolled bulk reactions. However, due to the fundamentally different reaction setup, a distinct set of reaction parameters must be considered, including flow velocity, residence time, concentration of injected solutions and substrate characteristics. Furthermore, this method only allows for the production of thin film materials, which imposes significant limitations on subsequent characterization.[153-158]

Traditional approaches from organic chemistry, such as the use of protecting groups, are also conceivable to gradually expose CS_2 functionalities. However, synthesizing corresponding thioesters proves challenging. Moreover, altered solubility properties, formation of by-products and stability issues need to be addressed.

2. OBJECTIVE

Even though coordination polymers and metal-organic frameworks are known for many years now, their application for electronic sectors such as electrocatalysis, electrochemical sensing or battery materials still lack behind owing to their electrically insulating properties. During the past years, different approaches to overcome this limitation have evoked. In order to maintain their high surface area while implementing electrical conductivity, especially the use of less electronegative ligator atoms such as sulfur instead of oxygen or nitrogen showed promising results in order to increase charge carrier transport and electrical conductivity in the resulting materials. However, the vast majority of CPs and MOFs is still based on well-established carboxylate linkers while the thiolated analogues, dithiocarboxylates, are much less explored.

This work presents a comprehensive study of two multitopic aromatic dithiocarboxylates which represent the sulfur-analogues to the well known BDC and BTC linkers: benzene-1,4-di(dithiocarboxylate) (BDDTC) and benzene-1,3,5-tri(dithiocarboxylate) (BTDTC).

To demonstrate the potential of this ligand class within the context of metal-organic coordination polymers, the following questions will be answered:

I) Which synthetic steps are required to ensure scalable and reproducible synthesis of these CS_2-ligands in good yield and excellent purity?

II) How can the properties of the novel BTDTC ligand be thoroughly investigated on the molecular level to gain in depth understanding of its coordination behavior and electronic effects?

III) Is it possible to transition from the molecular level to multidimensional solid-state materials and implement the advantageous properties into extended coordination polymers?

Since literature is limited to only a few synthetic protocols reporting the preparation of dithiocarboxylates, the existing procedures are reviewed and the synthesis conditions are carefully adjusted to develop an improved procedure suitable for gram-scale production. Owing to the instability of dithiocarboxylic acids in solution as well as in the solid state, both ligands are isolated in the form of their respective sodium salts Na_2BDDTC and Na_3BTDTC. The prepared ligands are fully characterized by means of structural and spectroscopic investigations. To investigate the coordination properties of the novel BTDTC ligand, two molecular coordination complexes are prepared. The compounds are

derived from mononuclear Cu(I) and dinuclear Mo_2(II) precursors with remaining coordination sites being saturated by auxiliary ligands. The resulting complexes serve as an ideal platform to demonstrate the versatile coordination behavior of BTDTC on the one hand, and its influence on electronic properties, specifically electronic coupling, on the other hand. Through comparison to the already known BTC-bridged Mo complex, superior electronic communication between the Mo-centers is evident as a consequence of S-substitution.

To pave the way for the construction of extended CS_2-based coordination polymers, the ligands are reacted with different transition metals to form coordination compounds with infinite structures. Through reaction of the BDDTC ligand with metal precursors of the form $M(OTf)_2$ (M = Mn, Zn, Fe), different coordination polymers are synthesized, characterized and compared to their carboxylate counterparts. In the case of the Fe-based polymer, the influence of the CS_2 ligand on the electrical conductivity of the polymer is also demonstrated.

Overall, the present work aims to deepen the understanding of the coordination behavior of multitopic dithiocarboxylate ligands and to demonstrate the direct impact of S-substitution on the electronic properties of the resulting complexes and polymers. In this context, it is the aim of this study to demonstrate the potential of previously underexplored dithiocarboxylates as linkers in CPs and to highlight their advantages over conventional linkers in terms of electronic applications.

3. RESULTS AND DISCUSSION

3.1 Manuscript I: Introducing Benzene-1,3,5-tri(dithiocarboxylate) as a Multidentate Linker in Coordination Chemistry

Sulfur-based organic ligands are much less explored compared to N- or O-containing ligands although they offer multiple advantages, particularly in terms of electronic properties. As a result of the relatively lower electronegativity of S-donors compared to N- or O-donor atoms, increased orbital overlap between the ligator atom of the organic ligand and the central metal ion can be achieved in derived coordination compounds. Thus, formed coordination bonds are more covalent in character and therefore facilitate electron transport which is key to enable desirable features such as electronic communication, charge carrier mobility and electrical conductivity.

In this paper the family of dithiocarboxylate ligands is extended from bis- to tris-dithiocarboxylate by synthesizing benzene-1,3,5-tri(dithiocarboxylate), the CS_2 counterpart of trimesic acid. Full characterization including structural analysis of the respective sodium salt is reported. Also, the solid-state structure of the sodium salt of the already known tetrathioterephthalate anion is included for detailed comparison. Further, two molecular coordination complexes are synthesized and characterized to investigate the effect of S-substitution with respect to structural and electronic aspects. The trinuclear Cu(I) compound $[Cu(Xantphos)(MeCN)_2][PF_6]$ and the hexanuclear Mo_2(II) complex $[Mo_2(DAniF)_3]_3(BTDTC)$ (BTDTC = benzene-1,3,5-tri(dithiocarboxylate)) are reported to serve as exemplary model compounds in line with previously reported Mo-CS_2 complexes. Single crystal X-ray diffraction analysis of the respective sodium salts Na_2BDDTC and Na_3BTDTC as well as the obtained Cu(I) and Mo_2(II) model complexes revealed possible κ^2 coordination, chelating coordination, as well as bridging coordination mode. This manifold coordination behavior allows for the formation of various configurations, paving the way for the construction of extended structures such as CPs and MOFs.

Besides full characterization and structural investigation, electronic coupling properties are investigated by electrochemical analysis. In the case of $[Mo_2(DAniF)_3]_3(BTDTC)$ superior electronic communication between the coordinated metal ions can be evidenced compared to the already known $[Mo_2(DAniF)_3]_3(BTC)$. To further confirm these findings, computational calculations are conducted, showing reduced HOMO-LUMO gaps for the

CS_2 ligands compared to their respective CO_2 counterparts. Calculated absorption spectra which were obtained by time-dependent DFT calculations, are in line with experimental spectra and therefore complement this study. In combination with their ability to bridge both mononuclear and dinuclear metal moieties, this renders them potential candidates for the construction of functional CPs with interesting electronic properties.

The paper was written by the author and all co-authors were involved during the editing process. The conceptual idea for this ligand system arose from discussions with C. Schneider. Synthesis and characterization of the ligands, including data collection and evaluation were performed by M. Aust. The Synthesis and characterization of model complexes was conducted by M. Aust in collaboration with A. J. Herold during her research internship which was supervised by the author. Acquisition and interpretation of data as well as conclusions drawn from them was carried out by the author. Electrochemical experiments and analysis of the data were performed by M. Aust with support from J. Warnan and L. Niederegger. Single crystal X-ray diffraction analysis and refinement were conducted by D. C. Mayer. Density functional theory calculations were performed by M. Drees. Drafting of the manuscript and revision thereof was implemented by M. Aust. All co-authors gave approval to the final version.

Inorganic Chemistry

pubs.acs.org/IC Article

Introducing Benzene-1,3,5-tri(dithiocarboxylate) as a Multidentate Linker in Coordination Chemistry

Margit Aust, Anna J. Herold, Lukas Niederegger, Christian Schneider, David C. Mayer, Markus Drees, Julien Warnan,* Alexander Pöthig,* and Roland A. Fischer*

Cite This: *Inorg. Chem.* 2021, 60, 19242−19252 Read Online

ACCESS | Metrics & More | Article Recommendations | Supporting Information

ABSTRACT: Benzene-1,3,5-tri(dithiocarboxylate) ($BTDTC^{3-}$), the sulfur-donor analogue of trimesate (BTC^{3-}, benzene-1,3,5-tricarboxylate), is introduced, and its potential as a multidentate, electronically bridging ligand in coordination chemistry is evaluated. For this, the sodium salt Na_3BTDTC has been synthesized, characterized, and compared with the sodium salt of the related ditopic benzene-1,4-di(dithiocarboxylate) (Na_2BDDTC). Single-crystal X-ray diffraction of the respective tetrahydrofuran (THF) solvates reveals that such multitopic aromatic dithiocarboxylate linkers can form both discrete metal complexes ($Na_3BTDTC{\cdot}9THF$) and (two-dimensional) coordination polymers ($Na_2BDDTC{\cdot}4THF$). Additionally, the versatile coordination behavior of the novel $BTDTC^{3-}$ ligand is demonstrated by successful synthesis and characterization of trinuclear Cu(I) and hexanuclear $Mo(II)_2$ paddlewheel complexes. The electronic structure and molecular orbitals of both dithiocarboxylate ligands as well as their carboxylate counterparts are investigated by density functional theory computational methods. Electrochemical investigations suggest that $BTDTC^{3-}$ enables electronic communication between the coordinated metal ions, rendering it a promising tritopic linker for functional coordination polymers.

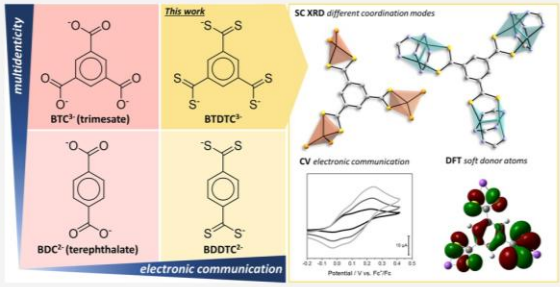

INTRODUCTION

In metal−organic coordination chemistry, the choice and design of suitable ligands are crucial for attaining specific features and properties of the resulting coordination compound. To date, carboxylate-based ligands (RCO_2^-) are some of the most prevalent ligands due to their well-known reaction and coordination behavior. Many carboxylate ligands are easily accessible, relatively stable and offer a variety of possible coordination modes, such as monodentate, chelating, and bridging.[1] This renders them versatile ligands for the synthesis of molecular complexes [e.g., $M_2(OAc)_4$, where M = Cu(II), Rh(II), Cr(II), or Mo(II)] as well as extended coordination polymers (CPs) {e.g., $[ZnO_4(BDC)_3]$ (BDC^{2-} = benzene-1,4-dicarboxylate) or $[Cu_3(BTC)_2]$ (BTC^{3-} = benzene-1,3,5-tricarboxylate)}.[2,3] While acetate and oxalate ligands are typically used to create discrete coordination complexes, aromatic bis- and tris-carboxylates, such as terephthalate (BDC^{2-}) and trimesate (BTC^{3-}), are commonly used for the construction of extended metal−organic CPs.[4] These organic−inorganic hybrid materials, consisting of inorganic metal units interconnected by organic ligands, allow for tailored properties as a result of their structural tunability.[5,6] However, when it comes to electronic features, such as charge mobility or electronic coupling, carboxylate-based CPs are strongly limited because of insufficient charge transport properties. This is caused by the ionic character of the coordination bonds formed between O ligator atoms and the metal centers.[7,8] The use of less electronegative ligator atoms (e.g., heavier chalcogenides) is an auspicious strategy for increasing the covalent character of the coordination bonds and for reducing electronic barriers. Several examples of both molecular and extended structures have shown that especially the exchange of oxygen for sulfur allows for improved charge mobility and electronic communication between the inorganic moieties as well as enhanced metal−metal interactions.[9−14]

Among sulfur-based ligands, dithiocarboxylates (RCS_2^-) are of special interest due to their structural analogy to widely used carboxylate compounds. However, they have been much less explored than other sulfur-based ligands (such as dithiocarbamates or thiols), which is due to some synthetic difficulties.[5] Their potential has been demonstrated by the bidentate tetrathioterephthalate anion ($tttp^{2-}$), the sulfur analogue of BDC^{2-}, displaying enhanced electronic communication in

Received: September 29, 2021
Published: December 6, 2021

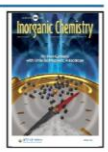

https://doi.org/10.1021/acs.inorgchem.1c03045
Inorg. Chem. 2021, 60, 19242−19252

coupling two bridged Mo_2 moieties compared to that of the carboxylate counterpart.[9,15,16] In addition to this molecular example, the use of the $tttp^{2-}$ anion for the construction of extended CPs has been demonstrated by a one-dimensional Zn-CP in which Zn centers are bridged by $tttp^{2-}$ ligands to form extended chains.[6] To date, this is the only example of a structurally characterized CP constructed from a bridging dithiocarboxylate ligand. In addition, examples of extended structures are scarce and mostly limited to monoperiodic extension, whereas additional ligator atoms other than S are used to achieve higher dimensionalities.[5,17]

Here, we further extended the breadth of aromatic CS_2-based ligands from bis- to tris-dithiocarboxylates by synthesizing and characterizing the sulfur analogue of BTC^{3-}, benzene-1,3,5-tri(dithiocarboxylate) ($BTDTC^{3-}$), as the first tridentate aromatic dithiocarboxylate ligand (Figure 1). Analogous to

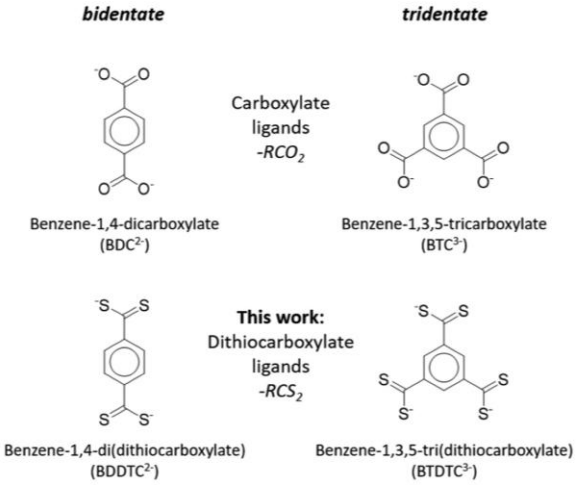

Figure 1. Overview of the well-established carboxylate ligands (top) and the analogous dithiocarboxylate ligands (bottom) investigated in this paper.

BTC^{3-}, which is widely used as a linker for the construction of CPs, the dithiocarboxylate-based counterpart $BTDTC^{3-}$ can serve as a tritopic linker while providing the advantages mentioned above.

To further investigate the coordination behavior and electronic properties with special regard to electronic coupling as well as metal−metal interactions, we synthesized two coordination complexes in which $BTDTC^{3-}$ serves as a linker to bridge three Cu(I) or $Mo(II)_2$ moieties. Copper−sulfur coordination compounds, on one hand, are known for their high conductivity and charge mobility due to strong metal−ligand coordination bonds.[18] On the other hand, Mo_2 paddlewheels have already been used to investigate electronic coupling in CS_2-bridged complexes.[9] Both metal precursors can be prepared in good yields following well-established literature procedures. The good stability of the resulting complexes in the solid state and in solution enables comprehensive analysis and characterization.

■ EXPERIMENTAL SECTION

Materials. Starting materials 1,4-di(chloromethyl)benzene and 1,3,5-tri(chloromethyl)benzene were prepared according to a literature procedure and purified by sublimation *in vacuo* (10^{-3} mbar, 60 °C) before further use.[19] *N,N′*-Di-*p*-anisylformamidine (DAniF) was prepared according to a reported procedure.[20] All other chemicals were purchased commercially and used as received. Methanol was dried from magnesium methoxide, degassed, and stored under argon over 3 Å activated molecular sieves. All other solvents were dried with an M. Braun solvent purification system and degassed prior to use. The preparation of compounds **1−6** was performed under an inert argon atmosphere using standard Schlenk techniques or in an argon-filled glovebox.

Instrumentation and Methods. Nuclear magnetic resonance (NMR) spectra were recorded at room temperature on a Bruker AV-400 spectrometer and referenced against the residual signal of the deuterated solvent. Solid state attenuated total reflection infrared spectroscopy (ATR-IR) spectra were recorded at room temperature with an FTIR spectrometer from PerkinElmer equipped with a germanium crystal. High-resolution ESI/LIFDI MS measurements were carried out with a Thermo Fisher Scientific Exactive Plus orbitrap mass spectrometer equipped with a heated ESI source from Thermo Fisher and a LIFDI ion source from Linden CMS. Electronic absorption spectra were recorded at room temperature on an Agilent Cary 60 spectrophotometer in the range of 200−1000 nm. Elemental analysis was performed by the microanalytical laboratories at the Technical University of Munich.

Electrochemical Characterization. Electrochemical investigations were carried out under an inert argon atmosphere with an Interface 1010 potentiostat from Gamry. All measurements were conducted at a concentration of 1 mM in CH_2Cl_2 with 0.1 M NBu_4PF_6 as the supporting electrolyte and using glassy carbon and Pt wire as the working and counter electrodes, respectively, as well as a Ag^+/Ag pseudoreference system. Reported potentials are referenced against the oxidation of ferrocenium/ferrocene (Fc^+/Fc) under the same conditions [$E_{1/2}(Fc^+/Fc) = 0.234$ V]. Cyclic voltammetry (CV) experiments were performed at different scan rates between 15 and 200 mV/s. Differential pulse voltammetry (DPV) was performed under the same conditions with the following parameters: step size of 5 mV, pulse size of 15 mV, pulse time of 0.2 s, and sample period of 1 s.

Single-Crystal X-ray Diffraction (SC-XRD). Data were collected on a Bruker D8 Venture single-crystal X-ray diffractometer equipped with a CMOS detector (Bruker Photon-100), a TXS rotating anode with Mo Kα radiation (λ = 0.71073 Å), and a Helios optic using the APEX3 software package.[21] Measurements were performed on single crystals coated with perfluorinated ether. The crystals were fixed on top of a kapton micro sampler and frozen under a stream of cold nitrogen. A matrix scan was used to determine the initial lattice parameters. Reflections were corrected for Lorentz and polarization effects, scan speed, and background using SAINT.[22] Absorption correction, including odd and even ordered spherical harmonics, was performed using SADABS.[22] Space group assignments were based upon systematic absences, *E* statistics, and successful refinement of the structures. The structures were determined using SHELXT with the aid of successive difference Fourier maps and were refined against all data using SHELXL in conjunction with SHELXLE.[23−25] Hydrogen atoms were calculated in ideal positions as follows. Methyl H atoms were refined as part of rigid rotating groups, with a C−H distance of 0.98 Å and $U_{iso}(H) = 1.5U_{eq}(C)$. Non-methyl H atoms were placed in calculated positions and refined using a riding model, with methylene, aromatic, and other C−H distances of 0.99, 0.95, and 1.00 Å, respectively, and $U_{iso}(H) = 1.2U_{eq}(C)$. Non-hydrogen atoms were refined with anisotropic displacement parameters. Full-matrix least-squares refinements were carried out by minimizing $\sum w(F_o^2 - F_c^2)^2$ with the SHELXL weighting scheme.[24] Neutral atom scattering factors for all atoms and anomalous dispersion corrections for the non-hydrogen atoms were taken from the International Tables for Crystallography.[26] Images of the crystal structures were generated with Mercury.[27] PLATON SQUEEZE[28] was applied in one case (CCDC 2105959) to account for residual electron density of disordered solvent molecules, which could not be modeled otherwise. CCDC 2105874, 2105875, 2105958, and 2105959 contain the supplementary crystallographic data for this paper. These data are

https://doi.org/10.1021/acs.inorgchem.1c03045
Inorg. Chem. 2021, 60, 19242−19252

provided free of charge by The Cambridge Crystallographic Data Centre.

Computational Details. The Gaussian 16.B.01 suite of software[29] was used for the density functional theory (DFT) calculations. The level of theory was adapted from the literature[10] and contains the functional O3LYP[30] and 6-31G*[31−34] basis sets for H, C, and N, the aug-cc-pVDZ[35−37] basis set for S and O, and the SDD ECP[38] basis set for Mo. PCM solvent calculations[39] were applied for acetonitrile. Excitations were simulated with time-dependent DFT[40,41] as implemented in Gaussian16. All optimized structures were identified as ground states by having no negative frequencies.

Synthesis. *Sodium Benzene-1,4-di(dithiocarboxylate) (Na_2BDDTC) (1).* A modified procedure from the literature was followed.[42] A sodium methoxide solution was prepared by dissolving elemental sodium (0.14 g, 6.2 mmol, 4 equiv) in dry methanol (20 mL). Sulfur powder (0.20 g, 6.2 mmol, 4 equiv) was suspended in this solution while it was being vigorously stirred. After reflux for 12 h, the sulfur was nearly completely dissolved and a dark brown solution was obtained. To this solution was added 1,4-di(chloromethyl)-benzene (0.27 g, 1.5 mmol, 1 equiv) as a solution in dry methanol (10 mL) over a period of 2 h through a syringe pump. The resulting mixture was then refluxed for an additional 12 h. The dark red solution was cooled to room temperature, and the solvent was evaporated *in vacuo*. The residue was dissolved in tetrahydrofuran (THF, 10 mL) and then filtered. After the addition of hexane (3 mL) to the filtrate, a red suspension was formed, which was then cooled to −30 °C for 12 h. **1** was collected by filtration as a red solid, washed with hexane, and dried *in vacuo* (yield, 0.31 g, 71%). Single crystals for X-ray diffraction were obtained as dark red blocks after slow diffusion of hexane into a NMR tube containing a THF solution of **1**. ^{1}H NMR (400 MHz, 298 K, DMSO-d_6): δ 7.89 (s, 4H, Ar-H).

Sodium Benzene-1,3,5-tri(dithiocarboxylate) (Na_3BTDTC) (2). **2** was prepared by improving the procedure used for the synthesis of **1**. The NaOMe solution (0.5 M in MeOH, 116 mL, 58 mmol, 7 equiv) and methanol (50 mL) were placed in a Schlenk flask. Elemental sulfur (1.78 g, 55 mmol, 6.2 equiv) was added, and the mixture was refluxed for 3 days under strong stirring until the sulfur was nearly completely dissolved and a red-brown solution was obtained. After the mixture had cooled to 50 °C, a solution of 1,3,5-tri(chloromethyl)-benzene (2.00 g, 8.9 mmol, 1 equiv) in methanol (50 mL) was added dropwise over a period of 3 h through an addition funnel, which resulted in a red solution with some solid suspended. The mixture was refluxed for an additional 18 h. The solvent was evaporated, and the remaining red solid dissolved in THF. After filtration, the dark red solution was left overnight and the formation of orange precipitate was observed. The solution was filtered again, and the solvent evaporated. The residue was dissolved in acetonitrile and filtered, and the solvent removed under reduced pressure to yield **2** as a dark red solid (yield, 1.62 g, 48%). Single crystals for X-ray diffraction were obtained as dark red blocks after slow diffusion of hexane into a NMR tube containing a THF solution of **2**. ^{1}H NMR (400 MHz, 298 K, DMSO-d_6): δ 8.52 (s, 3H, Ar-H). ^{13}C NMR (400 MHz, 298 K, DMSO-d_6): δ 252.28 (s, CCS_2), 150.98 (s, CCS_2), 125.92 (s, CCH). Anal. Found (%): C, 29.61; H, 1.22; N, 0.73; S, 49.95; Na, 18.30. Calcd for $C_{9.5}H_{3.75}N_{0.25}S_6Na_3$ ($Na_3BTDTC{\cdot}0.25MeCN$) (%): C, 29.81; H, 0.99; N, 0.91; S, 50.26; Na, 18.03. ATR-IR (cm^{-1}): 1560 (w), 1405 (w), 1126 (m), 1046 (m), 975 (s), 885 (m), 687 (vs). HR-ESI(−)-MS: [$Na_2C_9H_3S_6^-$] m/z 348.8358 (calcd m/z 348.8360, error of 0.6 ppm). UV−vis: λ_{max} (nm) [ε (M^{-1} cm^{-1})] 523 (1.3 × 10^3), 358 (44 × 10^3), 289 (64 × 10^3).

[Cu(Xantphos)(MeCN)$_2$][PF$_6$] (3). Xantphos (0.25 g, 0.4 mmol, 1 equiv) was dissolved in dichloromethane (5 mL), and this solution added dropwise to a solution of [Cu(MeCN)$_4$][PF$_6$] (0.16 g, 0.4 mmol, 1 equiv) in dichloromethane (10 mL). The colorless solution was stirred for 90 min in the dark. After evaporation of the solvent and washing with hexane, **3** was obtained as a white powder (yield, 0.31 g, 81%).[43] ^{1}H NMR (400 MHz, 298 K, CD_2Cl_2): δ 7.65 (d, 2H, CH_{ar}), 7.38 (t, 4H, CH_{Ph}), 7.30−7.25 (m, 16H, CH_{Ph}), 7.19 (t, 2H, CH_{ar}), 6.68−6.65 (m, 2H, CH_{ar}), 2.04 (s, 6H, -NCCH_3), 1.67 (s, 6H, CH_3). ^{31}P NMR (162 MHz, 298 K, CD_2Cl_2): δ −14.78 (s), −144.51 (quint, PF_6).

[Cu(Xantphos)]$_3$[BTDTC] (4). **2** (0.01 g, 0.038 mmol, 1 equiv) was dissolved in acetonitrile (3 mL) to give a dark red solution. Upon addition of this solution to a solution of **3** (0.10 g, 0.114 mmol) in acetonitrile (5 mL), the formation of a yellow precipitate was observed. To complete the reaction, the mixture was stirred for 45 min in the dark. After filtration, the yellow solid was washed with acetonitrile and diethyl ether and dried *in vacuo* (yield, 0.07 g, 83%). Single crystals for structural analysis were obtained in the shape of yellow blocks by slow diffusion of diethyl ether into a solution of **4** in dichloromethane. ^{1}H NMR (400 MHz, 298 K, $CDCl_3$): δ 9.46 (s, 3H, CH_{BTDTC}), 7.55 (d, 6H, CH_{Ar}), 7.39 (q, 24H, CH_{Ph}), 7.2−7.16 (m, 36H, CH_{Ph}), 7.09 (t, 6H, CH_{Ar}), 6.58−6.54 (m, 6H, CH_{Ar}), 1.68 (s, 18H, CH_3). ^{13}C NMR (400 MHz, 298 K, $CDCl_3$): δ 246.75 (CS_2), 155.52 ($C_{Ar}O$), 145.30 (CCS_2), 134.06, 133.90, 133.37, 131.36, 129.80, 128.75, 126.71, 124.70, 122.04, 36.31 (CH_3), 28.15 (CCH_3). Anal. Found (%): C, 65.82; H, 4.44; S, 8.41; P, 7.95; Cu, 8.0. Calcd for $C_{126}H_{99}O_3Cu_3P_6S_6$ (%): C, 67.86; H, 4.47; S, 8.63; P, 8.33; Cu, 8.55. ^{31}P NMR (162 MHz, CD_2Cl_2): δ −12.05. HR-LIFDI(+)-MS: [$C_{126}H_{99}O_3Cu_3P_6S_6$] m/z 2230.1960 (calcd m/z 2230.2248, error of 13 ppm). UV−vis: λ_{max} (nm) [ε (M^{-1} cm^{-1})] 396 (33 × 10^3), 289 (91 × 10^3).

Mo_2(DAniF)$_3$(OAc) (5). **5** was prepared according to a literature procedure by reacting DAniF (1.79 g, 7.0 mmol, 3 equiv) with $Mo_2(OAc)_4$ (1.00 g, 2.3 mmol, 1 equiv).[44] The commercially purchased $Mo_2(OAc)_4$ was recrystallized from hot THF prior to use (yield, 1.54 g, 65%). ^{1}H NMR (400 MHz, 298 K, CD_2Cl_2): δ 8.50 (s, 2H, -NC*H*N-), 8.40 (s, 1H, -NC*H*N-), 6.65 (d, 8H, CH_{ar}), 6.50 (d, 8H, CH_{ar}), 6.43 (d, J = 8.8 Hz, 4H, CH_{ar}), 6.22 (d, 4H, CH_{ar}), 3.71 (s, 12H, OCH_3), 3.63 (s, 6H, OCH_3), 2.60 (s, 3H, CH_3).

[Mo_2(DAniF)$_3$]$_3$(BTDTC) (6). A solution of **2** (0.005 g, 0.013 mmol, 1 equiv) in acetonitrile (3 mL) was added dropwise to a solution of **5** (0.041 g, 0.04 mmol, 3 equiv) in acetonitrile (5 mL) causing a change in color to green. After the mixture had been stirred for 2 h at room temperature, an intensively blue colored suspension was obtained. The solid was collected by filtration over a glass filter frit in an argon-filled glovebox and washed with acetonitrile to obtain **6** as dark blue powder. Single crystals suitable for X-ray diffraction were obtained as dark blue rods by slow diffusion of diethyl ether into a dichloromethane solution of **6**. ^{1}H NMR (400 MHz, 298 K, CD_2Cl_2): δ 9.17 (s, 3H, CH_{BTDTC}), 8.50 (s, 3H, -NC*H*N-), 8.34 (s, 6H, -NC*H*N-), 6.60 (q, 48H, -CH_{ar}), 6.40 (d, 12H, -CH_{ar}), 6.06 (d, J = 8.8 Hz, 12H, -CH_{ar}), 3.66 (s, 36H, -OCH_3), 3.64 (s, 18H, -OCH_3). ^{13}C NMR (400 MHz, 298 K, $CDCl_3$): δ 157.34 (NCN), 156.68 (OC_{Ar}), 156.46 (OC_{Ar}), 143.51 (NC_{Ar}), 142.70 (NC_{Ar}), 123.58 ($C_{Ar,DAniF}$), 123.38 ($C_{Ar,DAniF}$), 114.81 ($C_{Ar,DAniF}$), 114.55 ($C_{Ar,DAniF}$), 55.82 (OCH_3), 55.76 (OCH_3). Anal. Found (%): C, 53.27; H, 4.40; N, 7.84; S, 6.10; Mo, 17.66. Calcd for $C_{144}H_{138}Mo_6N_{18}O_{18}S_6$ (%): C, 54.44; H, 4.38; N, 7.94; S, 6.06; Mo, 18.12. HR-LIFDI(+)-MS: [$C_{144}H_{138}Mo_6N_{18}O_{18}S_6$] m/z 3177.3215 (calcd m/z 3177.3146, error of 2.2 ppm). UV−vis: λ_{max} (nm) [ε (M^{-1} cm^{-1})] 624 (43 × 10^3), 382 (2.3 × 10^3), 285 (155 × 10^3).

[Mo_2(DAniF)$_3$]$_3$(BTC) (7). A solution of Na_3BTC (0.03 g, 0.1 mmol, 1 equiv) in dry methanol (50 mL) was added to a solution of **5** (0.30 g, 0.29 mmol, 3 equiv) in acetonitrile (100 mL). The resulting orange solution was stirred for 48 h at room temperature, and the formation of an orange precipitate was observed. After filtration through a glass filter frit in an argon-filled glovebox, the isolated solid was washed with acetonitrile and dried *in vacuo* to give the product as an orange powder (yield, 0.21 g, 71%). ^{1}H NMR (400 MHz, 298 K, CD_2Cl_2): δ 9.19 (s, 3H, CH_{BTDTC}), 8.50 (s, 3H, -NC*H*N-), 8.40 (s, 6H, -NC*H*N-), 6.62 (d, 24H, -CH_{ar}), 6.48 (d, 24H, -CH_{ar}), 6.44 (d, 12H, -CH_{ar}), 6.25 (d, 12H, -CH_{ar}), 3.65 (s, 18H, -OCH_3), 3.50 (s, 36H, -OCH_3). ^{13}C NMR (400 MHz, 298 K, $CDCl_3$): δ 157.19 (NCN), 156.46 (OC_{Ar}), 143.53 (NC_{Ar}), 143.12 (NC_{Ar}), 123.32 ($C_{Ar,DAniF}$), 123.17 ($C_{Ar,DAniF}$), 114.71 ($C_{Ar,DAniF}$), 114.56 ($C_{Ar,DAniF}$), 55.81 (OCH_3), 55.66 (OCH_3).

https://doi.org/10.1021/acs.inorgchem.1c03045
Inorg. Chem. 2021, 60, 19242−19252

Inorganic Chemistry pubs.acs.org/IC Article

RESULTS AND DISCUSSION

Synthesis and Characterization of the Ligand Salts 1 and 2. Na_2BDDTC (**1**) and Na_3BTDTC (**2**) were synthesized from a modified literature procedure reported for Na_2BDDTC.[42] A solution of the corresponding benzyl di- or trichloride in methanol was reacted with elemental sulfur in the presence of sodium methoxide (Scheme 1). While

Scheme 1. Synthesis of 2

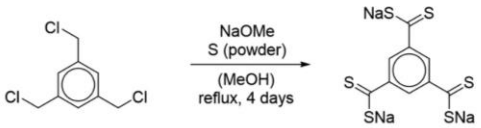

Na_2BDDTC can be isolated via precipitation from a THF solution upon addition of hexane, an improved workup procedure was established to isolate the tritopic analogue Na_3BTDTC. Both compounds were handled exclusively under inert conditions and stored in an argon-filled glovebox due to their sensitivity to air. The bis- and tris-dithiocarboxylate show good solubility in polar solvents such as CH_3CN and MeOH, while moderate solubility has been observed in THF. In nonpolar solvents such as hexane, $CHCl_3$, or toluene, they remain insoluble.

The purity of both compounds was verified by NMR spectroscopy, and chemical shifts were found to be in good agreement with the literature values (for NMR spectra, see Figures S1–S5).[45] The ^{1}H NMR spectra of **1** and **2** show residual solvent signals (0.5 equiv of THF for **1**, 0.25 equiv of MeCN for **2**) that could not be removed despite intense drying, suggesting chemically bound THF/MeCN, probably coordinating to the Na^+ ions. As the first reported aromatic tri(dithiocarboxylate), Na_3BTDTC was characterized in detail. High-resolution ESI MS confirmed the successful isolation of **2** as the signal for Na_2BTDTC^- could be detected at m/z 348.8358 as the major peak with an isotopic pattern fitting the calculated one (Figure S19). The ^{13}C NMR spectrum shows the characteristic signal of the CS_2 carbon atom at a very high chemical shift (δ 252.58) in addition to two signals (δ 150.98 and 124.36) corresponding to the carbon atoms of the aromatic ring. The CS_2 groups were further observed by ATR-IR (Figure 2) with the IR spectrum of **2** displaying an intense absorption band at 975 cm^{-1} ascribed to the stretching vibrations of the CS_2 groups.[6,45,46] Additionally, aromatic ring stretching vibrations ($\nu_{C=C}$) and deformation vibrations (δ_{C-H} and γ_{C-H}) are observed (for the full range spectrum, see Figure S22).

Thermogravimetric analysis (TGA) measurements indicate thermal stability up to 370 °C (Figure 2), which is lower than that reported for the carboxylate analogue sodium terephthalate (500 °C).[45] An initial weight loss of 3% can be observed due to the removal of residual acetonitrile. After the first decomposition step, 83% of the initial sample mass remains, which can be assigned to the loss of one NaS unit, yielding $Na_2C_9H_3S_5$ (M = 317.4 g mol^{-1}). If the procedure is performed in the presence of oxygen, an increase in sample weight is observed after 320 °C (Figure S23), ascribed to chemical reactions of the CS_2 groups to form, e.g., disulfides, sulfoxides, or sulfones.[47] The electronic UV–vis absorption spectrum of **2** (Figure 2) shows two intense bands at 289 and 358 nm with molar absorption coefficients of 64 × 10^3 and 44 × 10^3 M^{-1} cm^{-1}, respectively, in the range of π–π^* transitions. The intensity of the absorption band at 523 nm is lower (1.3 × 10^3 M^{-1} cm^{-1}), which is characteristic of n–π^* transitions. Comparison to the calculated absorption spectra (Figure S31) and involved molecular orbitals (Figure S32) confirms that the absorption at 523 nm is characteristic for the CS_2 group. The changing of all bands after exposure to air, particularly the decrease in CS_2-related absorption, highlights the sensitivity to oxygen of this compound.

The HOMO/LUMO electronic density obtained from DFT calculations indicates that S substitution provides beneficial effects for electronic communication and charge mobility. While the density for the sulfur-based ligands shows an increased level of delocalization through the whole molecule, the orbitals of the carboxylate ligands are more localized. The comparison of the calculated orbital energies and the resulting HOMO–LUMO gap shows that in Na_3BTDTC the energy of the LUMO is reduced while the energy of the HOMO is increased compared to those of Na_3BTC, resulting in a reduced HOMO–LUMO gap (Figure 3).

Next, we investigated the crystal structure of compound **1** or **2** by growing single crystals via slow diffusion of hexane into a THF solution of Na_2BDDTC or Na_3BTDTC, respectively.

Crystallographic Analysis. For compound **2**, the assumed molecular structure is confirmed. The compound crystallizes in the trigonal crystal system in space group *R*3*c*. The asymmetric unit contains two aromatic carbon atoms and one CS_2 group. The angle between the CS_2 group and the plane of the aromatic ring is 29.6(4)°. The other two dithiocarboxylate

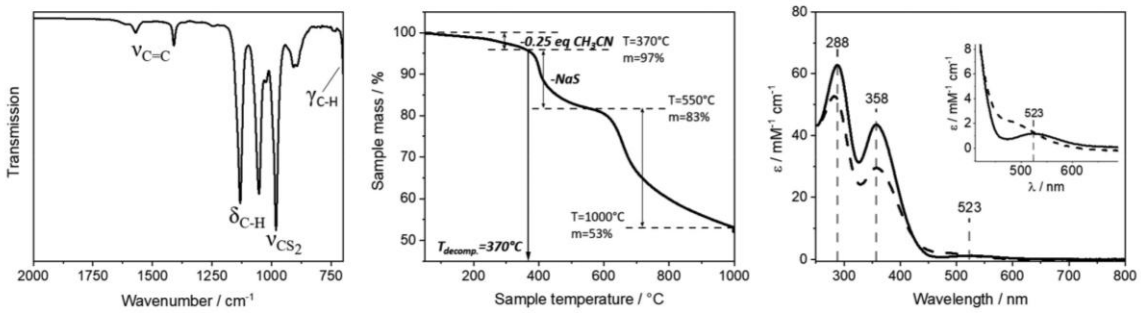

Figure 2. ATR-IR spectrum (left), TGA curve (middle), and electronic absorption spectrum in CH_3CN (right) of sodium salt **2**. TGA was performed under a N_2 gas flow in the range of 35–1000 °C with steps of 10 °C min^{-1}. The UV–vis spectrum was recorded under inert conditions (solid line) and after exposure to air for 10 h (dashed line).

https://doi.org/10.1021/acs.inorgchem.1c03045
Inorg. Chem. 2021, 60, 19242–19252

Inorganic Chemistry pubs.acs.org/IC Article

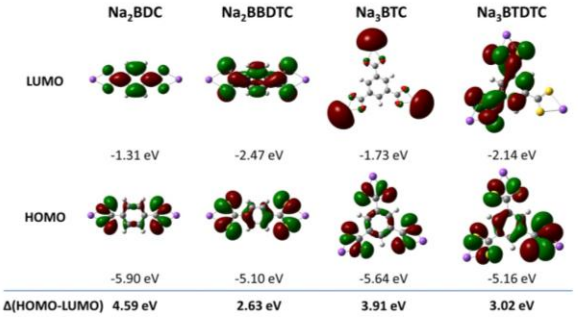

Figure 3. Computed Kohn–Sham orbitals of the sodium salts Na_2BDC, Na_2BDDTC (**1**), Na_3BTC, and Na_3BTDTC (**2**) with an isocontour value of 0.02. Orbital energies and calculated HOMO–LUMO gaps were obtained from DFT calculations at the O3LYP/6-31G*-aug-cc-pVDZ level of theory, including PCM solvent calculations for acetonitrile.

groups are symmetry-generated. Both S atoms are coordinated to one sodium ion in a $1\kappa S^1{:}1\kappa S^2$ coordination mode. The remaining coordination sites are saturated by three THF molecules, resulting in a 5-fold coordination around the sodium ion (Figure 4a). The carbon–sulfur distances [C1–S1, 1.690(3) Å; C1–S2, 1.688(3) Å] are of equal length within the confidence interval, which indicates an extended delocalized system. A closer inspection of the packing shows that the molecules are located at Wyckoff position 6*a*, on a 3-fold rotation axis in the *c*-direction with a multiplicity of 6, leading to an overall number of six Na_3BTDTC molecules in the unit cell. Hereby, the individual layers of the molecules perpendicular to the *c*-axis are separated from each other by 11.608 Å. Following the 3-fold rotational symmetry, the Na_3BTDTC molecules of neighboring layers are rotated by 60° along the *c*-axis, resulting in a staggered packing and enabling a maximization of the intermolecular distance of the sterically demanding THF ligands (Figure 4b,c).

For reasons of comparison, the crystal structure of **1** is also discussed. Although this compound has been synthesized before, no structural analysis has been reported.[42,48] Compound **1** crystallizes in the monoclinic crystal system in space group $P2_1/c$. The asymmetric unit consists of three aromatic carbon atoms and one CS_2 group that is twisted by 35.01° (rotation around the C1–C2 axis) compared to the plane of the aromatic ring, while the second functional group is symmetrically generated (Figure 4d). In contrast to previously discussed **2**, each CS_2 group contains one monodentate S-donor atom as well as one bridging S-donor atom, coordinating to two sodium ions. The overall coordination mode can therefore be described as $1\kappa S^1{:}1\kappa S^2{:}2\kappa S^2$. Thus, each sodium ion is coordinated by three S atoms and two additional THF molecules to obtain 5-fold coordination, similar to that in **2** (Figure 4e,f). The carbon–sulfur bond distances are equal within the statistical error and relatively short [C1–S1, 1.688(3) Å; C1–S2, 1.683(3) Å]. The observed bridging coordination behavior leads to extended sodium–sulfur chains with aromatic rings being alternatingly arranged on opposite sides of this chain. This connection of separate BDDTC

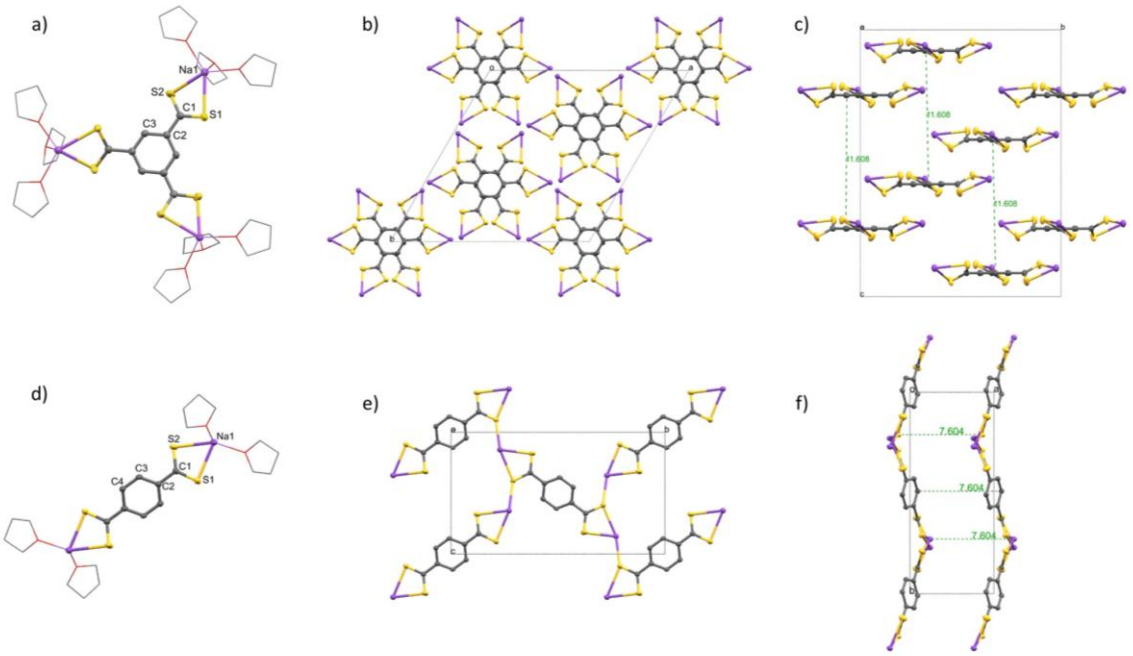

Figure 4. Solid state structures of THF solvates of **1** and **2** as determined by SC-XRD. Ellipsoids are shown at the 50% probability level. For the sake of clarity, hydrogen atoms have been omitted and THF molecules have been depicted as wireframes. Color code: gray for C, yellow for S, red for O, and purple for Na. (a) Molecular structure of $Na_3BTDTC{\cdot}9THF$. Selected bond distances: C1–S1, 1.691(3) Å; C1–S2, 1.689(3) Å; S1–Na1, 2.8793(15) Å; S2–Na1, 2.8153(16) Å. (b) Molecular packing of $Na_3BTDTC{\cdot}9THF$ along the *c*-axis. (c) Molecular packing of $Na_3BTDTC{\cdot}9THF$ along the *a*-axis. (d) Molecular structure of $Na_2BDDTC{\cdot}4THF$. Selected bond distances: C1–S1, 1.688(3) Å; C1–S2, 1.683(3) Å; S1–Na1, 2.8488(14) Å; S2–Na1, 2.9327(15) Å. (e) Polymeric structure of $Na_2BDDTC{\cdot}4THF$ along the *a*-axis. (f) Polymeric structure of $Na_2BDDTC{\cdot}4THF$ along the *c*-axis with a distance of 7.604 Å.

https://doi.org/10.1021/acs.inorgchem.1c03045
Inorg. Chem. 2021, 60, 19242–19252

Inorganic Chemistry pubs.acs.org/IC Article

Scheme 2. Preparation of Derived Cu and Mo_2 Complexes 4 and 6

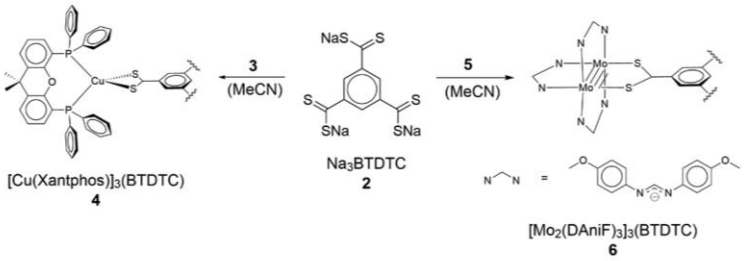

moieties results in two-dimensionally extended zigzag sheets that are perfectly stacked along the *a*-axis with a distance of 7.604 Å.

A detailed list of bond lengths and angles for both dithiocarboxylate compounds is provided in Table S1. Observed C−S distances are in the range of typical bond lengths in dithiocarboxylate compounds, which was verified through comparison to C−S distances obtained from the Cambridge Crystallographic Data Centre (CCDC). Summarized bond distances for different dithiocarboxylate compounds are listed in Figure S30.

This is the sole example of a two-dimensionally extended coordination polymer exclusively linked via CS_2 groups, which also proves that extended structures can be accessed by using the investigated linkers. Comparison to monoperiodic transition metal dithiocarboxylate polymers from the literature, i.e., $Ni(S_2CC_6H_4CO_2)_3Zn_2(DMSO)_6$[46] and $[Zn(S_2CC_6H_4CS_2)(DMF)_2]\cdot DMF$,[6] revealed similar parameters. Observed S−S distances for **1** and **2** (2.959 and 2.976 Å, respectively) conform to distances found in metal−organic Zn- and Ni-centered CS_2 polymers (2.917 and 2.886 Å, respectively)[6,46] and coordination angles around the metal centers. This points toward a future potential to build versatile coordination polymers with extended structures in one, two, or three dimensions.

Coordination Behavior of 2. To further explore the coordination properties of the new tritopic ligand, **2** was reacted in a straightforward approach with two transition metal [Cu(I) and $Mo(II)_2$] precursors in a 1:3 molar ratio (Scheme 2) to form complexes in which either single metal ions or dimetal paddlewheels are interconnected through coordination of the three CS_2 groups. While copper is known for its high thiophilicity, molybdenum has been used before to probe electronic communication in similar compounds. Complexes **4** and **6** were isolated in high yields and purity by using $Cu(Xantphos)(MeCN)_2$ (**3**) and $Mo_2(DAniF)_3(OAc)$ (**5**) as metal precursors, respectively. Both starting materials contain easily exchangeable MeCN/OAc ligands, facilitating quantitative ligand exchange upon reaction with sodium salt **2**, while the remaining coordination sites of the metal unit are saturated by the Xantphos and DAniF ligands, respectively. In the case of precursor **3**, the bulky Xantphos ligand was chosen to ensure efficient formation of a stable complex and to favor crystallization. The DAniF co-ligands in **5** were selected in analogy to the already known ditopic $[Mo_2(DAniF)_3]_2(BDDTC)$ complex reported by Liu and co-workers[9] to ensure comparability with complex **6**. Since some coordination complexes using the $BDDTC^{2-}$ anion have already been reported in the literature,[5,9] this work is confined to the investigation of complexes obtained from the tritopic $BTDTC^{3-}$ ligand.

The composition and purity of the isolated complexes have been verified by NMR spectroscopy (spectra are provided in Figures S6−S16). ^1H NMR spectra for **4** and **6** show a ratio of 1:3 with respect to the $BTDTC^{3-}$ protons and the signal of the residual ligands surrounding the metal ion. Together with the changes in chemical shifts, compared to the metal precursors, one can conclude that all three sodium ions have been replaced with Cu or Mo_2 centers, verifying the sum formulas for complex **4** and **6** that are given in Scheme 2. In the ^{13}C NMR spectra, selected Xantphos carbon atoms as well as the CS_2 carbon atom can be assigned for **4**. In the case of **6**, only the DAniF carbon atoms were assigned as the intensity of the signals for the carbon atoms of the $BTDTC^{3-}$ linker was too low. High-resolution mass spectrometry further confirmed the structure of complexes **4** and **6** as depicted in Scheme 2 (Figures S20 and S21). Detected m/z values and the isotopic pattern are in agreement with the calculated pattern and molar masses for $[Cu(C_{39}H_{32}OP_2)]_3[C_9H_3S_6]$ (2230 g mol^{-1}) and $[Mo_2(C_{15}H_{15}N_2O_2)_3]_3[C_9H_3S_6]$ (3176 g mol^{-1}). TGA was performed for both complexes (Figures S24 and S25) and revealed thermal stability up to 340 and 350 °C for **4** and **6**, respectively. The coordination of the CS_2 groups was further monitored by UV−vis spectroscopy (Figures S27 and S28). For complex **4** in a dichloromethane solution, the CS_2-related absorption at 523 nm was not observed in line with the coordination of the CS_2 group to the spectroscopically inactive d^{10} copper(I) center. By contrast, complex **6** exhibits a shoulder at 382 nm as well as an intense absorption maximum at 624 nm (ε values of 2.3×10^3 and 43×10^3 M^{-1} cm^{-1}, respectively). While the first is most likely related to transitions within the Mo_2 moiety (i.e., $\delta-\delta^*$), the second can be attributed to a metal-to-ligand charge transfer (MLCT) $\delta-\pi^*$ transition between the Mo_2 paddlewheel and the dithiocarboxylate group.[44,49,50] Time-dependent DFT computations show that excitations from the metal-centered HOMO−2, HOMO−1, or HOMO to the ligand-centered LUMO, LUMO+1, or LUMO+2 (Figure 5) contribute to this absorption band, confirming its MLCT nature (for the simulated UV−vis absorption spectrum, see Figure S37).

Crystallographic Analysis of Complexes 4 and 6. Structural investigation of complexes **4** and **6** confirmed three metal ions coordinated by one $BTDTC^{3-}$ linker molecule in both cases (Figure 6). SC-XRD revealed that complex **4** crystallizes in triclinic space group *P*1. For the three CS_2 groups, a $1\kappa S^1{:}1\kappa S^2$ coordination mode is observed, which results in a distorted tetrahedral coordination geometry around the Cu(I) center. The observed C−S bond length [1.674(7)−1.700(7) Å] and Cu−S distances [2.337(2)−2.413(2) Å] are

https://doi.org/10.1021/acs.inorgchem.1c03045
Inorg. Chem. 2021, 60, 19242−19252

Inorganic Chemistry pubs.acs.org/IC Article

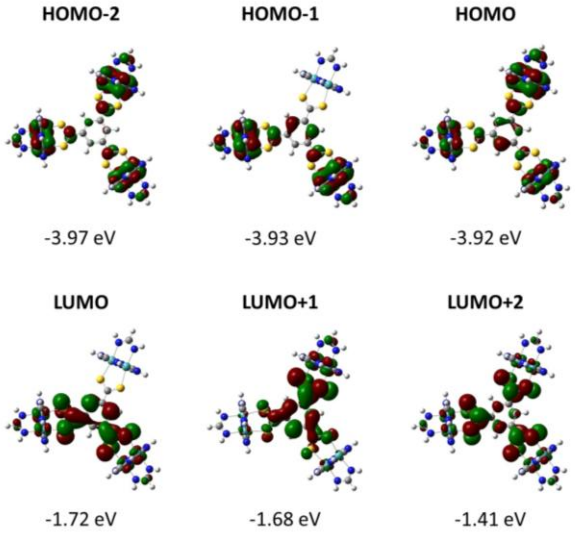

Figure 5. Computed Kohn–Sham orbitals of $[Mo_2(DAniF)_3]_3$-(BTDTC) (**6**) with an isocontour value of 0.02. Orbital energies were obtained from DFT calculations at the O3LYP/6-31G* level of theory for C, H, and N and the SDD ECP level of theory for Mo. PCM solvent calculations for acetonitrile were included.

slightly shorter than those of Na_3BTDTC. Again, all CS_2 groups are rotated out of the plane of the aromatic ring potentially to reduce the steric hindrance of the Xantphos ligands. Mo_2 paddlewheel complex **6** crystallizes in monoclinic space group $P2_1/c$. In contrast to **4**, a μ_2-1κS^1:2κS^2 bridging coordination mode is found in which each of the two CS_2 sulfur atoms coordinates to one Mo atom of the paddlewheel unit. The metal centers within one paddlewheel show Mo–Mo distances of 2.1287(6), 2.1273(6), and 2.1071(6) Å, which is in line with a quadruple bond length as reported for the ditopic analogue $[Mo_2(DAniF)_3]_2$(BDDTC).[10] All S–Mo distances are between 2.4200(12) and 2.4734(12) Å, and C–S distances are in the same range [1.683(5)–1.704(5) Å] as observed for **4**. The separations between the centroids of two neighboring Mo_2 paddlewheels are 10.471, 10.515, and 10.793 Å. One of the three CS_2 groups is rotated by 17.37°, whereas the other two functional groups are nearly in plane with the aromatic ring (1.73° and 4.35° rotations around the C1–C7 and C3–C8 axes, respectively).

Electrochemical Properties. In the cyclic voltammogram of **4** recorded from 0.00 to 0.85 V versus Fc^+/Fc, three irreversible oxidation processes are observed and tentatively ascribed to oxidation of the Cu(I) metal centers (Figure S38). Wave isolation did not result in recovered reversibility overall suggesting strong instability of the complex under oxidative conditions.

By contrast, cyclic voltammetry of **6** shows broad, quasi-reversible oxidation waves. Despite the high symmetry, distinct oxidation maxima are observed, inferring electronic coupling between the metal subunits. Differential pulse voltammetry revealed three overlapping processes at potential (E) values of ~0.08, ~0.19, and ~0.25 V versus Fc^+/Fc ascribed to the one-

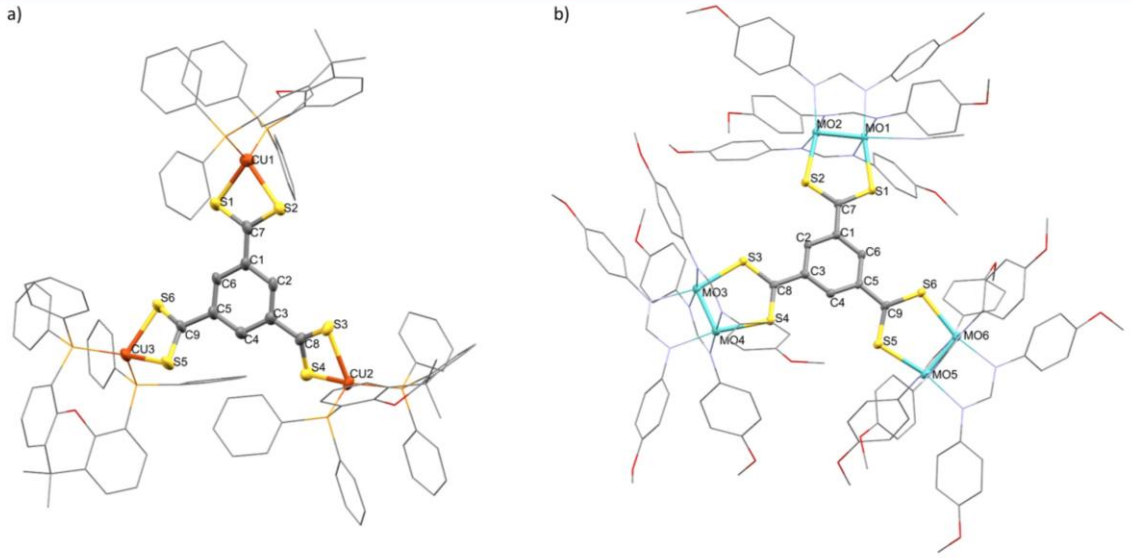

Figure 6. Molecular structures of (a) **4** and (b) **6** in the solid state as determined by SC-XRD. Ellipsoids are shown at the 50% probability level. For the sake of clarity, hydrogen atoms have been omitted and ancillary ligands have been depicted as wireframes. For compound **4**, only one of two independent molecules of the asymmetric unit is shown. Color code: gray for C, yellow for S, red for O, blue for N, light orange for P, orange for Cu, and turquoise for Mo. (a) Selected bond distances for **4** (values for the second independent molecule in brackets): C7–S1, 1.689(7) Å [C207–S7, 1.681(5) Å]; C7–S2, 1.697(6) Å [C207–S8, 1.696(5) Å]; S1–Cu1, 2.337(2) Å [S7–Cu4, 2.4111(16) Å]; S2–Cu1, 2.3898(18) Å [S8–Cu4, 2.3694(16) Å]; C8–S3, 1.699(7) Å [C209–S9, 1.693(5) Å]; C8–S4, 1.686(7) Å [C209–S10, 1.694(6) Å]; S3–Cu2, 2.4022(17) Å [S9–Cu5, 2.3741(16) Å]; S4–Cu2, 2.3728(17) Å [S10–Cu5, 2.4073(16) Å]; C9–S5, 1.700(7) Å [C208–S11, 1.693(6) Å]; C9–S6, 1.674(7) Å [C208–S12, 1.668(6) Å]; S5–Cu3, 2.413(2) Å [S11–Cu6, 2.4004(15) Å]; S6–Cu3, 2.3728(18) Å [S12–Cu6, 2.3751(16) Å]. (b) Selected bond distances for **6**: Mo1–Mo2, 2.1287(6) Å; Mo3–Mo4, 2.1273(6) Å; Mo5–Mo6, 2.1071(6) Å; C7–S1, 1.698(5) Å; C7–S2, 1.704(5) Å; S1–Mo1, 2.4734(12) Å; S2–Mo2, 2.4200(12) Å; C8–S3, 1.701(4) Å; C8–S4, 1.685(5) Å; S3–Mo3, 2.4271(12) Å; S4–Mo4, 2.4435(12) Å; C9–S5, 1.702(5) Å; C9–S6, 1.683(5) Å; S5–Mo5, 24481(12) Å; S6–Mo6, 2.4459(12) Å.

https://doi.org/10.1021/acs.inorgchem.1c03045
Inorg. Chem. 2021, 60, 19242–19252

electron oxidation of each paddlewheel moiety in line with the close energy level of the HOMO, HOMO−1, and HOMO−2 and with previous reports on bridged Mo_2 units.[9,10,51] The two first potentials are comparable to previously reported values for the corresponding, two-CS_2-bearing, 1,4-analogue $[Mo_2(DAniF)_3]_2(BDDTC)$ albeit slightly more positive.[9,10] This could originate from the lack of a mesomeric resonance effect from the relative *meta* positioning in **6** balanced by a more electron-withdrawing inductive effect of the deactivated aryl unit. Additionally, as **6** displays a Mo_2−Mo_2 distance between two neighboring paddlewheels of ∼10.6 Å, which is shorter than that observed for $[Mo_2(DAniF)_3]_2(BDDTC)$ (i.e., 12.24 Å), stronger electrostatic interactions leading to higher oxidation potentials are possibly induced.[9] Nonetheless, the small values calculated for the approximated potential separations (ΔE) of 110 and 60 mV in **6** indicate an overall modest electronic communication among the three Mo_2 moieties, lower than that observed for $[Mo_2(DAniF)_3]_2(BDDTC)$ ($\Delta E_{1/2}$ = 200 mV), highlighting that the geometry and substitution pattern strongly influence the electronic coupling properties.[9]

For the purpose of comparison, **7** was synthesized as the carboxylate counterpart of **6** and investigated under the same conditions.[52] Cyclic voltammograms revealed behavior similar to that of **6** (Figure 7), albeit with a stronger overlap between the last two one-electron oxidation processes that appeared to be less resolved in the DPV trace (Figure S40). The observed potentials are also shifted to more cathodic values with E values of ∼−0.01 and ∼0.10 V versus Fc^+/Fc (Table 1), which is in accordance with previous reports on O- versus S-based derivatives and ascribed to the impact of the chelating group of the central ligand.[10] These values are comparable to those of the previously reported terephthalate-bridged $[Mo_2(DAniF)_3]_2BDC$, indicating that *m*-tris-CO_2-aryl has an effect on the oxidation potentials similar to that of the *p*-bis-CO_2 moiety. Overall, the small ΔE (∼110 mV) and the joined second and third oxidations suggest weaker electronic communication in **7** than in **6** owing to stronger coupling among the three dimetallic sites brought by the CS_2 groups.

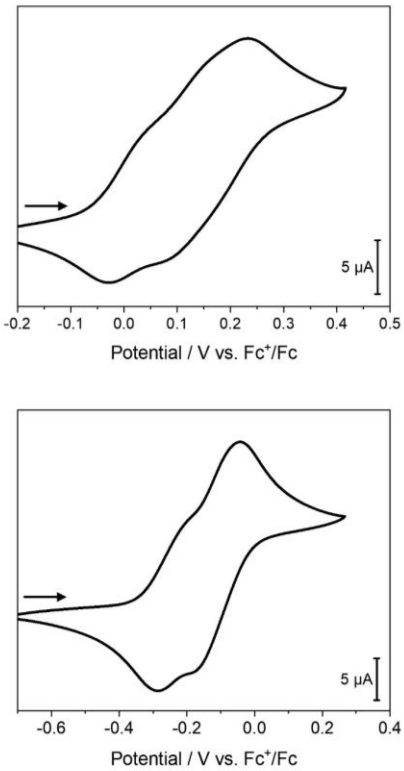

Figure 7. Cyclic voltammograms of **6** (top) and analogue carboxylate complex **7** (bottom) in a 1 mM CH_2Cl_2 solution. Measured potentials are referenced against the Fc^+/Fc couple [$E_{1/2}(Fc^+/Fc)$ = 0.234 V]. Conditions: 0.1 M NBu_4PF_6/CH_2Cl_2 electrolyte/solvent system, scan rate of 50 mV/s, glassy carbon working electrode, Pt counter electrode, and $Ag/AgNO_3$ pseudoreference electrode.

Table 1. Oxidation Potentials of Mo Paddlewheels in 6 and 7 Determined via DPV[a]

	E_1 vs Fc^+/Fc (V)	E_2 vs Fc^+/Fc (V)	E_3 vs Fc^+/Fc (V)
$[Mo_2(DAniF)_3]_3(BTDTC)$ **6**	+0.08	+0.19	+0.25
$[Mo_2(DAniF)_3]_3(BTC)$ **7**	−0.01	+0.10	–

[a]Potentials were measured in a 0.1 M NBu_4PF_6/CH_2Cl_2 electrolyte solution and referenced against the Fc^+/Fc couple, which occurred at 0.234 V under the same conditions. Glassy carbon working electrode, Pt counter electrode, $Ag/AgNO_3$ pseudoreference electrode, step size of 5 mV, pulse size of 15 mV, pulse time of 0.2 s, and sample period of 1 s.

■ CONCLUSIONS

We have synthesized and fully characterized the novel sulfur-donor ligand benzene-1,3,5-tri(dithiocarboxylate) ($BTDTC^{3-}$), which is the first aromatic tridentate CS_2-based ligand. Single-crystal X-ray analysis revealed remarkable structural features, such as high symmetry as well as similar bond lengths and angles compared to those of its well-known carboxylate analogue trimesate. Introduction of the $BTDTC^{3-}$ ligand into Cu(I) and $Mo(II)_2$ chemistry yielded coordination complexes $[Cu(Xantphos)]_3(BTDTC)$ and $[Mo_2(DAniF)_3]_3(BTDTC)$, respectively. Structural analysis of these compounds demonstrates a versatile coordination behavior, including chelating as well as bridging coordination modes. Electronic communication among the three interconnected metal units was evidenced by electrochemical investigations as well as DFT calculations.

We further investigated the structural properties of the bidentate analogue benzene-1,4-di(dithiocarboxylate) ($BDDTC^{2-}$) and found a two-dimensional polymeric structure for the corresponding sodium salt Na_2BDDTC. For the ditopic ligand, a bridging coordination mode was observed, leading to extended zigzag sheets.

From these findings, we can conclude that the novel $BTDTC^{3-}$ ligand is a promising linker motif offering great potential for the development of molecular compounds as well as extended coordination polymers with different metal centers. Further research will focus on the formation of higher-dimensional coordination polymers and investigation of their electronic properties. Preliminary experiments on the formation of extended structures mainly yielded amorphous products, presumably as a result of strong metal−sulfur coordination. Hence, precise control of the reaction parameters appears to be crucial to slow reaction kinetics and to

https://doi.org/10.1021/acs.inorgchem.1c03045
Inorg. Chem. 2021, 60, 19242−19252

enable the successful formation of crystalline materials. Nevertheless, we were able to also obtain crystalline materials in recent experiments, which are currently being investigated in our laboratory.

■ ASSOCIATED CONTENT

Supporting Information

The Supporting Information is available free of charge at https://pubs.acs.org/doi/10.1021/acs.inorgchem.1c03045.

Additional experimental spectra, electrochemical data (CV and DPV), structural details, calculated molecular orbitals, and simulated absorption spectra (PDF)

Accession Codes

CCDC 2105874−2105875 and 2105958−2105959 contain the supplementary crystallographic data for this paper. These data can be obtained free of charge via www.ccdc.cam.ac.uk/data_request/cif, or by emailing data_request@ccdc.cam.ac.uk, or by contacting The Cambridge Crystallographic Data Centre, 12 Union Road, Cambridge CB2 1EZ, UK; fax: +44 1223 336033.

■ AUTHOR INFORMATION

Corresponding Authors

Roland A. Fischer − *Chair of Inorganic and Metal−Organic Chemistry, Department of Chemistry and Catalysis Research Center, Technical University of Munich, 85748 Garching, Germany*; orcid.org/0000-0002-7532-5286; Email: roland.fischer@tum.de

Alexander Pöthig − *Chair of Inorganic and Metal−Organic Chemistry, Department of Chemistry and Catalysis Research Center, Technical University of Munich, 85748 Garching, Germany*; orcid.org/0000-0003-4663-3949; Email: alexander.poethig@tum.de

Julien Warnan − *Chair of Inorganic and Metal−Organic Chemistry, Department of Chemistry and Catalysis Research Center, Technical University of Munich, 85748 Garching, Germany*; Email: julien.warnan@tum.de

Authors

Margit Aust − *Chair of Inorganic and Metal−Organic Chemistry, Department of Chemistry and Catalysis Research Center, Technical University of Munich, 85748 Garching, Germany*

Anna J. Herold − *Chair of Inorganic and Metal−Organic Chemistry, Department of Chemistry and Catalysis Research Center, Technical University of Munich, 85748 Garching, Germany*

Lukas Niederegger − *Assistant Professorship of Bioinorganic Chemistry, Catalysis Research Center, Technical University of Munich, 85748 Garching, Germany*

Christian Schneider − *Chair of Inorganic and Metal−Organic Chemistry, Department of Chemistry and Catalysis Research Center, Technical University of Munich, 85748 Garching, Germany*; orcid.org/0000-0001-7231-3266

David C. Mayer − *Chair of Inorganic and Metal−Organic Chemistry, Department of Chemistry and Catalysis Research Center, Technical University of Munich, 85748 Garching, Germany*

Markus Drees − *Chair of Inorganic and Metal−Organic Chemistry, Department of Chemistry and Catalysis Research Center, Technical University of Munich, 85748 Garching, Germany*

Complete contact information is available at: https://pubs.acs.org/10.1021/acs.inorgchem.1c03045

Notes

The authors declare no competing financial interest.

■ ACKNOWLEDGMENTS

The authors acknowledge the German Research Foundation (DFG) for funding this research as a part of the COORNETs program (SPP-1928) and the TUM Graduate School for financial support. The authors thank Christian Jandl (TUM) for conducting single-crystal X-ray diffraction experiments. Leibniz Rechenzentrum der Bayerischen Akademie der Wissenschaften (LRZ) is gratefully acknowledged for providing computing capacity.

■ REFERENCES

(1) Corrêa, C. C.; Scaldini, F. M.; Machado, F. C.; Pinheiro, C. B. Study of the supramolecular interactions of carboxylic acids used as versatile ligands in coordination chemistry. *J. Struct. Chem.* **2016**, *57* (6), 1235−1242.

(2) Goura, J.; Chandrasekhar, V. Molecular Metal Phosphonates. *Chem. Rev.* **2015**, *115* (14), 6854−6965.

(3) Zhang, W.-X.; Liao, P.-Q.; Lin, R.-B.; Wei, Y.-S.; Zeng, M.-H.; Chen, X.-M. Metal cluster-based functional porous coordination polymers. *Coord. Chem. Rev.* **2015**, *293−294*, 263−278.

(4) Batten, S. R.; Neville, S. M.; Turner, D. R. *Coordination Polymers: Design, Analysis and Application*; 2009.

(5) Mensforth, E. J.; Hill, M. R.; Batten, S. R. Coordination polymers of sulphur-donor ligands. *Inorg. Chim. Acta* **2013**, *403*, 9−24.

(6) Neofotistou, E.; Malliakas, C. D.; Trikalitis, P. N. Novel Coordination Polymers Based on the Tetrathioterephthalate Dianion as the Bridging Ligand. *Inorg. Chem.* **2007**, *46* (21), 8487−8489.

(7) Sun, L.; Campbell, M. G.; Dincă, M. Electrically Conductive Porous Metal-Organic Frameworks. *Angew. Chem., Int. Ed.* **2016**, *55* (11), 3566−3579.

(8) Nidamanuri, N.; Maity, K.; Saha, S. Electrically Conductive Metal-Organic Frameworks. In *Elaboration and Applications of Metal-Organic Frameworks*; World Scientific, 2017; Vol. 2, pp 655−686.

(9) Han, M. J.; Liu, C. Y.; Tian, P. F. Enhanced Electronic Coupling in a Molecular Pair of Dimolybdenum Units Bridged by a Tetrathioterephthalate Dianion. *Inorg. Chem.* **2009**, *48* (14), 6347−6349.

(10) Xiao, X.; Liu, C. Y.; He, Q.; Han, M. J.; Meng, M.; Lei, H.; Lu, X. Control of the Charge Distribution and Modulation of the Class II-III Transition in Weakly Coupled Mo2-Mo2 Systems. *Inorg. Chem.* **2013**, *52* (21), 12624−12633.

(11) Sun, L.; Miyakai, T.; Seki, S.; Dincă, M. Mn2(2,5-disulfhydrylbenzene-1,4-dicarboxylate): A Microporous Metal-Organic Framework with Infinite (-Mn-S-)∞ Chains and High Intrinsic Charge Mobility. *J. Am. Chem. Soc.* **2013**, *135* (22), 8185−8188.

(12) Huang, X.; Sheng, P.; Tu, Z.; Zhang, F.; Wang, J.; Geng, H.; Zou, Y.; Di, C.-a.; Yi, Y.; Sun, Y.; Xu, W.; Zhu, D. A two-dimensional π-d conjugated coordination polymer with extremely high electrical conductivity and ambipolar transport behaviour. *Nat. Commun.* **2015**, *6*, 7408.

(13) Clough, A. J.; Skelton, J. M.; Downes, C. A.; de la Rosa, A. A.; Yoo, J. W.; Walsh, A.; Melot, B. C.; Marinescu, S. C. Metallic Conductivity in a Two-Dimensional Cobalt Dithiolene Metal-Organic Framework. *J. Am. Chem. Soc.* **2017**, *139* (31), 10863−10867.

(14) Takaishi, S.; Hosoda, M.; Kajiwara, T.; Miyasaka, H.; Yamashita, M.; Nakanishi, Y.; Kitagawa, Y.; Yamaguchi, K.; Kobayashi, A.; Kitagawa, H. Electroconductive Porous Coordination Polymer Cu[Cu(pdt)2] Composed of Donor and Acceptor Building Units. *Inorg. Chem.* **2009**, *48* (19), 9048−9050.

(15) Kang, M. T.; Meng, M.; Tan, Y. N.; Cheng, T.; Liu, C. Y. Tuning the Electronic Coupling and Electron Transfer in Mo2 Donor-Acceptor Systems by Variation of the Bridge Conformation. *Chem. - Eur. J.* **2016**, *22* (9), 3115−3126.

(16) Gao, H.; Mallick, S.; Cao, L.; Meng, M.; Cheng, T.; Chen, H. W.; Liu, C. Y. Electronic Coupling and Electron Transfer between Two Mo2 Units through meta- and para-Phenylene Bridges. *Chem. - Eur. J.* **2019**, *25* (15), 3930−3938.

(17) Li, M.-Q.; Zhao, M.; Bi, L.-Y.; Hu, Y.-Q.; Gou, G.; Li, J.; Zheng, Y.-Z. Two-Dimensional Silver(I)-Dithiocarboxylate Coordination Polymer Exhibiting Strong Near-Infrared Photothermal Effect. *Inorg. Chem.* **2019**, *58* (10), 6601−6608.

(18) Pathak, A.; Shen, J.-W.; Usman, M.; Wei, L.-F.; Mendiratta, S.; Chang, Y.-S.; Sainbileg, B.; Ngue, C.-M.; Chen, R.-S.; Hayashi, M.; Luo, T.-T.; Chen, F.-R.; Chen, K.-H.; Tseng, T.-W.; Chen, L.-C.; Lu, K.-L. Integration of a (-Cu-S-)n plane in a metal-organic framework affords high electrical conductivity. *Nat. Commun.* **2019**, *10* (1), 1721.

(19) Miura, Y.; Onogi, S.; Fukuda, T. Syntheses of sulfo-glycodendrimers using click chemistry and their biological evaluation. *Molecules* **2012**, *17* (10), 11877−11896.

(20) Chen, M.; Moerdyk, J. P.; Blake, G. A.; Bielawski, C. W.; Lee, J. K. Assessing the Proton Affinities of N,N'-Diamidocarbenes. *J. Org. Chem.* **2013**, *78* (20), 10452−10458.

(21) *APEX 3*, ver. 2015.5-2; Bruker AXS Inc.: Madison, WI, 2015.

(22) *SAINT*, ver. 7.56a, and *SADABS*, ver. 2008/1; Bruker AXS Inc.: Madison, WI, 2008.

(23) Hübschle, C. B.; Sheldrick, G. M.; Dittrich, B. ShelXle: a Qt graphical user interface for SHELXL. *J. Appl. Crystallogr.* **2011**, *44* (6), 1281−1284.

(24) Sheldrick, G. M. *SHELXL-2014/7: program for the solution of crystal structures*; University of Göttingen: Göttingen, Germany, 2014.

(25) Sheldrick, G. M. *SHELXL-97*, release 97-2; University of Göttingen: Göttingen, Germany, 1998.

(26) Wilson, A. J. C., Prince, E., Ed. International Tables for Crystallography, Vol. C. *Mathematical, Physical and Chemical Tables*; 1992.

(27) Macrae, C. F.; Bruno, I. J.; Chisholm, J. A.; Edgington, P. R.; McCabe, P.; Pidcock, E.; Rodriguez-Monge, L.; Taylor, R.; Van de Streek, J.; Wood, P. A. Mercury CSD 2.0 - new features for the visualization and investigation of crystal structures. *J. Appl. Crystallogr.* **2008**, *41* (41), 466−470.

(28) Spek, A. L. PLATON SQUEEZE: a tool for the calculation of the disordered solvent contribution to the calculated structure factors. *Acta Crystallogr., Sect. C: Struct. Chem.* **2015**, *71* (C71), 9−18.

(29) Frisch, M. J.; Trucks, G. W.; Schlegel, H. B.; Scuseria, G. E.; Robb, M. A.; Cheeseman, J. R.; Scalmani, G.; Barone, V.; Petersson, G. A.; Nakatsuji, H.; Li, X.; Caricato, M.; Marenich, A. V.; Bloino, J.; Janesko, B. G.; Gomperts, R.; Mennucci, B.; Hratchian, H. P.; Ortiz, J. V.; Izmaylov, A. F.; Sonnenberg, J. L.; Williams Ding, F.; Lipparini, F.; Egidi, F.; Goings, J.; Peng, B.; Petrone, A.; Henderson, T.; Ranasinghe, D.; Zakrzewski, V. G.; Gao, J.; Rega, N.; Zheng, G.; Liang, W.; Hada, M.; Ehara, M.; Toyota, K.; Fukuda, R.; Hasegawa, J.; Ishida, M.; Nakajima, T.; Honda, Y.; Kitao, O.; Nakai, H.; Vreven, T.; Throssell, K.; Montgomery, J. A., Jr.; Peralta, J. E.; Ogliaro, F.; Bearpark, M. J.; Heyd, J. J.; Brothers, E. N.; Kudin, K. N.; Staroverov, V. N.; Keith, T. A.; Kobayashi, R.; Normand, J.; Raghavachari, K.; Rendell, A. P.; Burant, J. C.; Iyengar, S. S.; Tomasi, J.; Cossi, M.; Millam, J. M.; Klene, M.; Adamo, C.; Cammi, R.; Ochterski, J. W.; Martin, R. L.; Morokuma, K.; Farkas, O.; Foresman, J. B.; Fox, D. J. *Gaussian 16*, rev. C.01; Gaussian Inc.: Wallingford, CT, 2016.

(30) Cohen, A. J.; Handy, N. C. Dynamic correlation. *Mol. Phys.* **2001**, *99* (7), 607−615.

(31) Ditchfield, R.; Hehre, W. J.; Pople, J. A. Self-Consistent Molecular-Orbital Methods. IX. An Extended Gaussian-Type Basis for Molecular-Orbital Studies of Organic Molecules. *J. Chem. Phys.* **1971**, *54* (54), 724.

(32) Hehre, W. J.; Ditchfield, R.; Pople, J. A. Self—Consistent Molecular Orbital Methods. XII. Further Extensions of Gaussian—Type Basis Sets for Use in Molecular Orbital Studies of Organic Molecules. *J. Chem. Phys.* **1972**, *56* (5), 2257−2261.

(33) Hariharan, P. C.; Pople, J. A. The influence of polarization functions on molecular orbital hydrogenation energies. *Theoretica chimica acta* **1973**, *28* (3), 213−222.

(34) Francl, M. M.; Pietro, W. J.; Hehre, W. J.; Binkley, J. S.; Gordon, M. S.; DeFrees, D. J.; Pople, J. A. Self-consistent molecular orbital methods. XXIII. A polarization-type basis set for second-row elements. *J. Chem. Phys.* **1982**, *77* (7), 3654−3665.

(35) Dunning, T. H. Gaussian basis sets for use in correlated molecular calculations. I. The atoms boron through neon and hydrogen. *J. Chem. Phys.* **1989**, *90* (2), 1007−1023.

(36) Woon, D. E.; Dunning, T. H. Gaussian basis sets for use in correlated molecular calculations. III. The atoms aluminum through argon. *J. Chem. Phys.* **1993**, *98* (2), 1358−1371.

(37) Kendall, R. A.; Dunning, T. H.; Harrison, R. J. Electron affinities of the first-row atoms revisited. Systematic basis sets and wave functions. *J. Chem. Phys.* **1992**, *96* (9), 6796−6806.

(38) Andrae, D.; Häußermann, U.; Dolg, M.; Stoll, H.; Preuß, H. Energy-adjustedab initio pseudopotentials for the second and third row transition elements. *Theoretica chimica acta* **1990**, *77* (2), 123−141.

(39) Tomasi, J.; Mennucci, B.; Cammi, R. Quantum Mechanical Continuum Solvation Models. *Chem. Rev.* **2005**, *105* (8), 2999−3094.

(40) Adamo, C.; Jacquemin, D. The calculations of excited-state properties with Time-Dependent Density Functional Theory. *Chem. Soc. Rev.* **2013**, *42* (3), 845−856.

(41) Stratmann, R. E.; Scuseria, G. E.; Frisch, M. J. An efficient implementation of time-dependent density-functional theory for the calculation of excitation energies of large molecules. *J. Chem. Phys.* **1998**, *109* (19), 8218−8224.

(42) Chalkov, N. O.; Cherkasov, V. K.; Abakumov, G. A.; Romanenko, G. V.; Ketkov, S. Y.; Smolyaninov, I. V.; Starikov, A. G.; Kuropatov, V. A. Compactly Fused o-Quinone-Extended Tetrathiafulvalene-o-Quinone Triad - a Redox-Amphoteric Ligand. *Eur. J. Org. Chem.* **2014**, *2014* (21), 4571−4576.

(43) McCullough, B. J.; Neyhouse, B. J.; Schrage, B. R.; Reed, D. T.; Osinski, A. J.; Ziegler, C. J.; White, T. A. Visible-Light-Driven Photosystems Using Heteroleptic Cu(I) Photosensitizers and Rh(III) Catalysts To Produce H2. *Inorg. Chem.* **2018**, *57* (5), 2865−2875.

(44) Cotton, F. A.; Liu, C. Y.; Murillo, C. A.; Villagrán, D.; Wang, X. Modifying Electronic Communication in Dimolybdenum Units by Linkage Isomers of Bridged Oxamidate Dianions. *J. Am. Chem. Soc.* **2003**, *125* (44), 13564−13575.

(45) Zhao, H.; Wang, J.; Zheng, Y.; Li, J.; Han, X.; He, G.; Du, Y. Organic Thiocarboxylate Electrodes for a Room-Temperature Sodium-Ion Battery Delivering an Ultrahigh Capacity. *Angew. Chem., Int. Ed.* **2017**, *56* (48), 15334−15338.

(46) Paital, A. R.; Zhan, J.; Kim, R.; Kampf, J.; Collins, P.; Coucouvanis, D. Synthesis and structures of perthio- and polymeric metal complexes with the tetrathio- and dithioterephthalate ligands. *Polyhedron* **2013**, *64*, 328−338.

(47) Grote, J.; Friedrich, F.; Berthold, K.; Hericks, L.; Neumann, B.; Stammler, H.-G.; Mitzel, N. W. Dithiocarboxylic Acids: An Old Theme Revisited and Augmented by New Preparative, Spectroscopic and Structural Facts. *Chem. - Eur. J.* **2018**, *24* (11), 2626−2633.

(48) Ueno, Y.; Bahry, M.; Okawara, M. Tetrathioquinodimethane chemistry. A new approach to the preparation of charge-transfer complex by lithium iodide reduction. *Tetrahedron Lett.* **1977**, *18* (52), 4607−4610.

(49) Köberl, M.; Cokoja, M.; Bechlars, B.; Herdtweck, E.; Kühn, F. E. Dicarboxylate-bridged (Mo2)n (n = 2, 3, 4) paddle-wheel complexes: potential intermediate building blocks for metal-organic frameworks. *Dalton Trans.* **2011**, *40* (43), 11490−11496.

(50) Chisholm, M. H.; Patmore, N. J. Electronic coupling in 1,4-(COS)2C6H4 linked MM quadruple bonds (M = Mo, W): the influence of S for O substitution. *Dalton Trans.* **2006**, No. 26, 3164−3169.

https://doi.org/10.1021/acs.inorgchem.1c03045
Inorg. Chem. 2021, 60, 19242−19252

(51) Cotton, F. A.; Donahue, J. P.; Murillo, C. A. Polyunsaturated Dicarboxylate Tethers Connecting Dimolybdenum Redox and Chromophoric Centers: Syntheses, Structures, and Electrochemistry. *J. Am. Chem. Soc.* **2003**, *125* (18), 5436−5450.

(52) Albert Cotton, F.; Daniels, L. M.; Lin, C.; Murillo, C. A. A molecular propeller with three quadruply-bonded blades. *Inorg. Chem. Commun.* **2001**, *4* (3), 130−133.

https://doi.org/10.1021/acs.inorgchem.1c03045
Inorg. Chem. 2021, 60, 19242−19252

3.2 Manuscript II: Benzene-1,4-Di(dithiocarboxylate) Linker-Based Coordination Polymers of Mn^{2+}, Zn^{2+}, and Mixed-Valence $Fe^{2+/3+}$

After the successful synthesis of di- and tritopic dithiocarbixylate ligands $BDDTC^{2-}$ and $BTDTC^{3-}$ and their implementation into exemplary molecular coordination complexes, the auspicious structural and electronic properties of these ligands need to be transferred into solid state materials. The utilization of these ligands as linker in extended CPs or MOFs represents the next step toward the design of functional materials which exhibit advanced electronic properties such as electrical conductivity and good charge carrier mobility.

In this manuscript, the synthesis and characterization of three coordination polymers constructed from the 1,4-di(dithiocarboxylate) ($BDDTC^{2-}$) linker – the sulfur analogue of terephthalate – and Mn-, Zn- and Fe-based inorganic metal nodes. Full characterization of the synthesized materials including different crystal structures for two coordination polymers based on Mn^{2+} and Zn^{2+} nodes are reported. Structural analysis revealed versatile coordination behavior uncovering one-dimensional chains for $[Mn(BDDTC)(DMF)_2]$ as well as two-dimensional honeycomb sheets in the case of $[Zn_2(BDDTC)_3][Zn(DMF)_5(H_2O)]$. For the latter, two polymorphs were found which result from different coordination modes of the ditopic CS_2-linker.

In addition, a mixed valence Fe-based coordination polymer was synthesized, however, no single crystals suitable for X-ray analysis were obtained. To shed light on the composition, structure and properties of the obtained Fe-based material, comprehensive investigations were conducted. By thorough spectroscopic and magnetic analysis of its electronic properties, a 1:1 ratio of Fe^{2+}/Fe^{3+} was found which can be traced back to partial oxidation during synthesis and work up. The induced mixed valency is accompanied by strong antiferromagnetic coupling, giving rise to a remarkably high electrical conductivity of $5 \cdot 10^{-3}$ S cm^{-1}. Complementary investigations by means of elemental analysis and thermal gravimetric analysis enabled the establishment of the empirical formula $[Fe_2(BDDTC)_2(OH)]$. Due to the lack of single crystals suitable for X-ray analysis, X-ray absorption spectroscopy (XANES and EXAFS) were performed to detect iron atoms in close proximity. The determined Fe–Fe distance of 3.16 Å leads to the conclusion that multinuclear $Fe^{2+/3+}$ metal nodes are present in the polymer.

Overall, this study demonstrates the potential of dithiocarboxylate linkers to introduce beneficial electronic properties to derived CPs or MOFs. The fact that electrical conductivity could only be observed for the $Fe^{2+/3+}$ mixed-valent material, whereas compounds with fully (Zn^{2+}) or half-filled (Mn^{2+}) d-orbitals resulted in non-conductive CPs, emphasizes that the nature of the inorganic metal entity is equally important and needs to be considered when designing such materials.

The development and conceptual design of the research project was established by M. Aust. Experimental design and implementation, including the preparation of the ligand and the coordination polymers, was performed by the author of this work. Conductivity measurements were carried out by M. Aust in collaboration with M. I. Schönherr and analyzed with the help of D. D. Medina. Single crystal X-ray diffraction measurements and refinement were conducted by T. Pickl and S. N. Deger. X-ray absorption spectroscopy was performed by M. Aust with support from M. Z. Hussain and A. Jentys. R. Bühler supported with the experimental realization of magnetic measurements. Z. Zhang and K. Meyer performed ^{57}Fe Mössbauer spectroscopy and provided the associated figures, data analysis and experimental details. M. Kuhl and J. Eichhorn carried out high resolution X-ray photoelectron spectroscopy including data interpretation and the preparation of related figures. X band EPR measurements were carried out by O. Storcheva and evaluated with the help of D. Halter. D. Halter also supported the interpretation of SQUID and XAS data. All remaining characterizations were carried out and evaluated by the author. Gathered data were evaluated and brought into context by M. Aust. Drafting of the original manuscript was performed by the author of this paper. All co-authors contributed critically to the discussion of the results and gave approval to the final version. The implementation of remarks during the reviewing process and finalization for re-submission were realized by L. Schröck.

Inorganic Chemistry

pubs.acs.org/IC Article

Benzene-1,4-Di(dithiocarboxylate) Linker-Based Coordination Polymers of Mn^{2+}, Zn^{2+}, and Mixed-Valence $Fe^{2+/3+}$

Margit Aust, Marina I. Schönherr, Dominik P. Halter, Lena Schröck, Thomas Pickl, Simon N. Deger, Mian Z. Hussain, Andreas Jentys, Raphael Bühler, Zihan Zhang, Karsten Meyer, Matthias Kuhl, Johanna Eichhorn, Dana D. Medina, Alexander Pöthig,* and Roland A. Fischer*

Cite This: *Inorg. Chem.* 2024, 63, 129−140 Read Online

ACCESS | Metrics & More | Article Recommendations | Supporting Information

ABSTRACT: Three new coordination polymers (CPs) constructed from the linker 1,4-di(dithiocarboxylate) ($BDDTC^{2-}$)—the sulfur-analog of 1,4-benzenedicarboxylate (BDC^{2-})—together with Mn-, Zn-, and Fe-based inorganic SBUs are reported with description of their structural and electronic properties. Single-crystal X-ray diffraction revealed structural diversity ranging from one-dimensional chains in $[Mn(BDDTC)(DMF)_2]$ (**1**) to two-dimensional (2D) honeycomb sheets observed for $[Zn_2(BDDTC)_3][Zn(DMF)_5(H_2O)]$ (**2**). Gas adsorption experiments confirmed a 3D porous structure for the mixed-valent material $[Fe_2(BDDTC)_2(OH)]$ (**3**). **3** contains a 1:1 ratio of $Fe^{2+/3+}$ ions, as evidenced by ^{57}Fe Mössbauer, X-band EPR, and X-ray absorption spectroscopy. Its empirical formula was established by elemental analysis, thermal gravimetric analysis, infrared vibrational spectroscopy, and X-ray absorption spectroscopy in lieu of elusive single-crystal X-ray diffraction data. In contrast to the Mn- and Zn-based compounds **1** and **2**, the $Fe^{2+/3+}$ CP **3** showed remarkably high electrical conductivity of 5×10^{-3} S cm^{-1} (according to van der Pauw measurements), which is within the range of semiconducting materials. Overall, our study confirms that sulfur derivatives of typical carboxylate linkers (e.g., BDC) are suitable for the construction of electrically conducting CPs, due to acceptedly higher covalency in metal−ligand bonding compared to the electrically insulating carboxylate CPs or metal-organic frameworks. At the same time, the direct comparison between insulating CPs **1** and **2** with CP **3** emphasizes that the electronic structure of the metal is likewise a crucial aspect to construct electrically conductive materials.

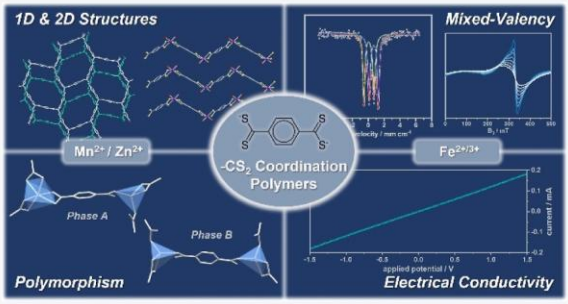

INTRODUCTION

Metal-organic frameworks (MOFs) and coordination polymers (CPs) have gained significant attention due to their characteristic properties such as high crystallinity, good stability, and exceptional tunability.[1] These organic-inorganic hybrid materials are constructed from inorganic joints, which are connected by multidentate organic ligands, also called linkers.[2,3] Particularly CPs with permanent porosity, also referred to as MOFs, are intensively investigated for applications in the fields of gas storage or separation, as well as energy storage, catalysis, and sensing.[4−6] However, for their utilization in electronic devices, advanced electronic properties such as electrical conductivity and good charge carrier mobility are required. This represents a long-standing challenge, since most MOFs behave as electrical insulators with conductivity values below 10^{-10} S cm^{-1}.[7] The reason is that the vast majority of MOFs are built from aromatic multitopic carboxylate linkers such as benzene-1,4-dicarboxylate (BDC^{2-}) or benzene-1,3,5-tricarboxylate (BTC^{3-}), featuring ionic metal−ligand coordination bonds. Softer donor atoms enhance the covalent character of the coordination bond and are thus beneficial in introducing long-range charge delocalization to create electron transport pathways.[8−11] In this context, CPs with sulfur-donor ligands, such as thiols and thiocarbamates, have gained rising interest. Especially 2D materials obtained from benzenehexathiol (BHT) or triphenylenehexathiol (THT) show promising features such as good charge mobility and high electrical conductivity.[12−15] To date, the highest conductivity for CPs was reported for $[Cu_3(BHT)]$, which exhibited an electrical conductivity of 1580 S cm^{-1} measured on a thin film.[16] In contrast to such thiols, dithiocarboxylate linkers (RCS_2^-)—the sulfur analogs to establish carboxylates—are much less explored and examples of derived CPs are scarce.[17] While

Received: July 19, 2023
Revised: October 19, 2023
Accepted: October 20, 2023
Published: December 18, 2023

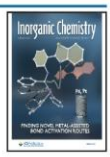

thiol-based CPs typically build networks through bridging coordination modes of their multitopic linkers, most of RCS_2^- compounds reported till date form polymeric structures through metal–metal interactions.[18–22] Additionally, hybrid linkers also containing other coordinating atoms such as nitrogen or halogens have been reported, for example, CS_2-substituted pyrazine-,[23] imidazole-[24] and pyridine-based[25,26] linkers were used to form extended CPs. Further, a series of halogen-bridged linear $M_2(RCS_2)_4X$ (M = Pt, Ni; X = Cl, Br, I) CPs was intensively studied to demonstrate their potential with regard to magnetic and electronic properties.[27] Metallic conductivity was reported for $Pt_2(MeCS_2)_4I$ (13 S cm^{-1}),[28] $Pt_2(EtCS_2)_4I$ (5–30 S cm^{-1}),[29] and $Pt_2(nBuCS_2)_4I$ (17–83 S cm^{-1}).[30] However, in contrast to these, there are only few CPs reported which are exclusively constructed from bridging coordination of the RCS_2 linker.[31–33] In fact, there are only two structures reported in which the inorganic units are exclusively connected via the bridging coordination mode of a ditopic dithiocarboxylate-based linker. The first example is $[Zn(S_2CC_6H_4CS_2)_2]$, with mononuclear metal nodes consisting of Zn^{2+} ions that are bridged by the benzene-1,4-di(dithiocarboxylate) ($BDDTC^{2-}$) linker, the all-sulfur analog of terephthalate (BDC^{2-}), to form one-dimensional (1D) zigzag chains.[34] In the same publication, the Mn^{2+} analog of $[Zn(S_2CC_6H_4CS_2)_2]$ was proposed to have the same chain structure,[34] however without confirmation from single-crystal X-ray diffraction (SC-XRD). The other example is the polymeric structure of sodium salt Na_2BDDTC, which was reported by our group very recently. In this case, additional cross-linking via Na–S coordination can be observed, which results in an extended 2D sheet structure.[35]

Herein, we investigate a series of CPs built from three different transition metals coordinated by the ditopic $BDDTC^{2-}$ linker. The crystalline materials $[Mn(BDDTC)(DMF)_2]$ (**1**), $[Zn_2(BDDTC)_3][Zn(DMF)_5H_2O]$ (**2**), and $[Fe_2(BDDTC)_2(OH)]$ (**3**) built with Mn, Zn, and Fe inorganic building units were obtained by solvothermal synthesis and subsequently characterized. Comprehensive structural analysis by SC-XRD was performed for **1** and **2**. Hereby, the previously proposed 1D periodic linear chain structure was confirmed for **1**. In contrast, in the case of **2**, a 2D periodic sheet structure was obtained. The latter is built up by an anionic network consisting of hexagonally arranged honeycomb-like $[Zn_2BDDTC_3]^{2-}$ subunits with an underlying **hcb** topology. To achieve charge neutrality, we found $[Zn(DMF)_5(H_2O)]^{2+}$ complexes to be intercalated between the sheets of the network. Finally, electrical conductivity measurements were performed to investigate the potential of the $BDDTC^{2-}$ linker toward the formation of conductive CPs. While **1** and **2** were found to behave as electrical insulators, an electrical conductivity of 5×10^{-3} S cm^{-1} was observed for **3**, most likely induced by metal-provided mobile electrons as charge carriers. To shed light on the origin of the conductivity, an additional analysis is provided. By investigating the magnetic and electronic properties of **3** we were able to show that $Fe^{2+/3+}$ mixed-valency is most likely contributing to the conductive behavior. Moreover, antiferromagnetic coupling was detected by SQUID magnetization, influencing the electronic communication between Fe metal centers. Overall, this demonstrates the great potential of CS_2-based CPs to provide charge carrier transport pathways for the construction of electrically conductive CPs.

EXPERIMENTAL SECTION

Materials. The sodium salt of the dithiocarboxylate linker $Na_2(BDDTC)$ was prepared according to a previously published procedure.[35] Triflate metal precursors were purchased from STREM Chemicals Inc. ($Fe(OTf)_2$) and Sigma-Aldrich ($(Zn(OTf)_2$ and $Mn(OTf)_2$) and used as received. Anhydrous MeOH and dimethylformamide (DMF) (Sigma-Aldrich) were degassed prior to use and stored in an argon-filled glovebox over activated molecular sieves (3 Å). All other solvents were dried through an MBraun solvent purification system and degassed prior to use. The preparation of all compounds was performed under an inert argon atmosphere by using standard Schlenk techniques or in an argon-filled glovebox. CPs **1–3** were transferred to the glovebox after workup in air and stored under inert conditions. Vacuum treatment for **1–3** was performed for 10 h at room temperature.

Instrumentation and Methods. The nuclear magnetic resonance (NMR) spectrum of the organic linker was recorded at room temperature on a Bruker AV-400 spectrometer and referenced against the residual signal of the deuterated solvent. Solid-state attenuated total reflection infrared spectroscopy (ATR-IR) spectra were recorded at room temperature with a Spectrum 3 MIR FT-IR Spectrometer from PerkinElmer Frontier, equipped with a ZnSe/diamond crystal in the range between 4000 and 650 cm^{-1}. Observed vibration bands were characterized according to their intensity: weak (w), medium (m), strong (s), and very strong (vs). Thermogravimetric analysis (TGA) was performed with a TGA/DSC 3+ STAR^e System from Mettler Toledo under a constant flow of synthetic air. Heating was applied in the temperature range between 30 and 1000 °C with a heating rate of 10 °C min^{-1}. Elemental analysis (EA) was performed by the microanalytical laboratories at the Technical University of Munich. Powder X-ray diffraction (PXRD) under air was performed on a Rigaku MiniFlex 600-C diffractometer equipped with a D/teX Ultra silicon strip detector and a 600 W X-ray tube (Cu-K_α emitter λ = 1.54 Å). Diffraction data were collected in the 2θ range between 2 and 40° from samples placed on silicon sample holders. Scanning electron microscopy (SEM) images were recorded with a TM-1000 tabletop microscope from Hitachi. Backscattered electrons were induced by a 15 keV electron beam. Porosity measurements were recorded on a 3Flex Physisorption instrument from Micromeritics Instrument Corp. The samples were prepared for measuring at room temperature for 10 h under dynamic vacuum using a SmartVac Prep by Micromeritics Instrument Corp. Nitrogen physisorption isotherms were measured with N_2 (99.999 vol %) at 77 K. Based on the N_2 isotherms, apparent surface areas were determined using the Brunauer–Emmett–Teller (BET) model. The isotherms are given as adsorption information files in the Supporting Information. The conversion of measurement files was performed using an open-access web application (https://clownfish-app-lzoex.ondigitalocean.app). Solid-state UV/VIS-NIR electronic absorption spectra were recorded by using a Perkin Elmer UV/VIS-NIR Lambda 1050 spectrophotometer equipped with a 150 mm InGaAs integrating sphere. Diffuse reflectance spectra were collected with a Praying Mantis (Harrick) accessory and referenced to barium sulfate powder. $I-V$ curves were obtained from two-probe measurements of crystalline pellets, which were performed with a Metrohm Autolab PGStat302N equipped with an in-house-built DC conductivity cell. $I-V$ curves were recorded in a voltage range between −1.5 and +1.5 V. The distance between the electrodes is equivalent to the pellet thickness (about 150 μm). The curves were fitted by a linear regression of the $I-V$ curves of **1** (slope: 1.26×10^{-11}, **2** (slope: 7.21×10^{-12}), and **3** (slope: 1.20×10^{-4}). Van der Pauw measurements were conducted by an ECOPIA Model HMS-5300 Hall measurement setup at room temperature. Gold contact electrodes were placed on pressed pellets of the crystalline samples in a square geometry with distances of about 2.4 mm. Pellet thicknesses were measured to be about 150 μm. Pellets with 1 cm diameter were fabricated from 100 mg of the respective bulk material of the CPs with a pressure of 45 kg cm^2 in a Paul-Weber KBr press. X-band EPR spectroscopy in perpendicular mode was performed on a Jeol JES-FA 200 spectrometer at 293 K and the data were simulated

https://doi.org/10.1021/acs.inorgchem.3c02471
Inorg. Chem. 2024, 63, 129–140

using the program W95EPR.[36] Samples were measured as a solid powder in a 4 mm quartz EPR tube. Zero-field ^{57}Fe Mössbauer spectra were recorded on a WissEl Mössbauer spectrometer (MRG-500) at a temperature of 77 K in constant acceleration mode. ^{57}Co/Rh was used as the γ-radiation source. WinNormos for Igor Pro software was used for the quantitative evaluation of the spectral parameters (least-squares fitting to Lorentzian peaks). The minimum experimental line width was determined at 0.21 mm s^{-1} (full width at half-maximum, FWHM). The temperature of the sample was controlled by an MBBC-HE0106 Mössbauer He/N_2 cryostat with an accuracy of ±0.3 K. Least-square fitting of the Lorentzian signals was carried out with the "Mfit" software, developed by Dr. Eckhard Bill (MPI CEC, Mülheim/Ruhr).[37,38] The isomer shifts were reported relative to an α-iron reference at 300 K. Magnetic measurements were performed on a Quantum Design MPMS XL5 SQUID magnetometer using 10 mg of the sample in a gelatin capsule. Data were corrected for diamagnetic contributions of the core electrons (Pascal's constants). Field-dependent magnetization was measured between −50 and +50 kOe at 300 K. The magnetic susceptibility was measured at 1000 kOe from 300 to 2 K. X-ray absorption spectra (XAS) were measured on a lab-scale easyXAFS300+, using a spherically bent Si(531) Bragg crystal analyzer as a monochromator. The X-ray tube was operated at 40 kV and 25 mA. An amount of sample was selected to obtain an absorption of 1.5 at the Fe K-edge and diluted with cellulose to obtain a homogeneous sample. The pellets were sealed with Kapton tape and measured at room temperature. The XAS of the samples and references were recorded at the Fe K-edge by adding 10 scans of 45 min each. Fe K-edge (7111 eV) of an Fe-foil was used to calibrate the energy. Edge height normalization and background subtraction as well as EXAFS fitting were performed using the Larch program.[39] For the EXAFS analysis, the oscillations were weighted with k^2 and the Fourier-transformation as well as the fitting in k-space was performed in the range 2.8−9.3 Å^{-1} using single scattering contributions of Fe−S, Fe−O, and Fe−Fe calculated with FEFF8L (included in the Larch software). Multiple scattering contributions as well as contributions at distances above 3.5 Å were not included during the structure determination.

Single-crystal X-ray diffraction (SC-XRD) data were collected on a Bruker D8 Venture single-crystal X-ray diffractometer equipped with Bruker Photon III CPAD detector, a TXS rotating anode with Mo-K$_\alpha$ radiation (λ = 0.71073 Å), and a Helios optic using the APEX3 software package.[40] Measurements were performed on single crystals coated with perfluorinated ether. The crystals were fixed on top of a Kapton microsampler and frozen under a stream of cold nitrogen. A matrix scan was used to determine the initial lattice parameters. Reflections were corrected for Lorentz and polarization effects, scan speed, and background using SAINT.[41] Absorption correction, including odd and even ordered spherical harmonics, was performed using SADABS.[41] Space group assignments were based on systematic absences, E statistics, and successful refinement of the structures. The structures were solved using SHELXT with the aid of successive difference Fourier maps, and were refined against all data using SHELXL in conjunction with SHELXLE.[42−44] Hydrogen atoms were calculated in ideal positions; namely, methyl H atoms were refined as part of rigid rotating groups, with a C−H distance of 0.98 Å and $U_{iso}(H) = 1.5 \cdot U_{eq}(C)$. Nonmethyl H atoms were placed in calculated positions and refined using a riding model, with methylene, aromatic, and other C−H distances of 0.99 0.95, and 1.00 Å, respectively, and $U_{iso}(H) = 1.2 \cdot U_{eq}(C)$. Non-hydrogen atoms were refined with anisotropic displacement parameters. Full-matrix least-squares refinements were carried out by minimizing $\Sigma w(F_o^2 - F_c^2)^2$ with the SHELXL weighting scheme.[43] Neutral atom scattering factors for all atoms and anomalous dispersion corrections for the non-hydrogen atoms were taken from International Tables for Crystallography.[45] Images of the crystal structures were generated with mercury.[46] For two of the structures (CCDC 2249204 and 2249205), cocrystallized H_2O molecules, and some DMF molecules were disordered and modeled using free variables in conjunction with SIMU, RIGU, SADI, SAME, FLAT, and/or DFIX restraints as implemented in the DSR plugin in SHELXLE.[47,48] PLATON SQUEEZE was applied in one case (CCDC 2249204) to account for residual electron density of disordered solvent molecules (MeCN) which could not be modeled reasonably and was treated as a diffuse contribution to the overall scattering without specific atom positions.[49] CCDC 2249203 (CP **1**), 2249204 (CP **2b**), and 2249205 (CP **2a**) contain the supplementary crystallographic data for this paper, which are provided free of charge by the Cambridge Crystallographic Data Centre.

Syntheses. *[Mn(BDDTC)(DMF)$_2$]·0.9 DMF (**1**).* Separate solutions of Mn(OTf)$_2$ (127 mg, 0.36 mmol) and Na_2BDDTC (100 mg, 0.36 mmol) were prepared in 20 mL of DMF each and combined in a 100 mL screw cap bottle. The closed bottle was placed in a preheated oven at 60 °C for solvothermal reaction. After a reaction time of 48 h, black crystals of **1** were formed on the walls of the glass bottle. The crystals were collected by centrifugation, washed three times with DMF (3 × 15 mL) and Et_2O (3 × 15 mL) and dried in air (yield: 155.5 mg, 0.31 mmol, 86%).

Anal. Found (%): C, 40.58; H, 4.85; N, 8.25; S, 25.94. Calcd for [$MnC_{14}H_{18}S_4N_2O_2$], 0.9 DMF (%): C, 40.50; H, 4.95; N, 8.20; S, 25.89. ATR-IR (cm^{-1}): 2931 (w), 1638 (vs), 1492 (w), 1433 (m), 1381 (s), 1251 (m), 1203 (s), 1110 (m), 995 (s), 907 (s), 855 (s), 674 (m).

*[Zn$_2$(BDDTC)$_3$][Zn(DMF)$_5$H$_2$O]·2.5 DMF (**2**).* Zn(OTf)$_2$ (130.4 mg, 0.38 mmol) was dissolved in DMF (20 mL) and divided into four 20 mL screw cap vials. A solution of Na_2BDDTC (100 mg, 0.36 mmol) in DMF (20 mL) was equally distributed into the vials to form an orange-red precipitate. The resulting mixtures were reacted under solvothermal conditions in a preheated oven at 60 °C for 24 h. Afterward, the crystalline powder was collected by centrifugation and washed three times with DMF (3 × 15 mL) and Et_2O (3 × 15 mL). After drying in air, **2** was obtained as a red powder (yield: 143.8 mg, 0.1 mmol, 28%).

Anal. Found (%): C, 38.82; H, 4.51; N, 7.36; S, 26.33. Calcd for [$Zn_2(C_{24}H_{12}S_{12})$][$Zn(C_{15}H_{37}N_5O_6)$], 2.5 DMF (%): C, 38.59; H, 4.63; N, 7.26; S, 26.58. ATR-IR (cm^{-1}): 2927 (w), 1641 (vs), 1492 (w), 1433 (m), 1372 (s), 1210 (s), 1110 (m), 1005 (s), 897 (s), 847 (s), 680 (m).

*[Fe$_2$(BDDTC)$_2$(OH)]·5 DMF (**3**).* Fe(OTf)$_2$ (127 mg, 0.36 mmol) was dissolved in 20 mL of DMF and 300 μL of H_2O. A solution of Na_2BDDTC (100 mg, 0.36 mmol) in DMF (20 mL) was added, giving a dark brown suspension. The mixture was placed in a 100 mL screw cap bottle and reacted under solvothermal conditions at 60 °C for 24 h. The microcrystalline powder was collected by centrifugation of the hot mixture and washed with DMF (3 × 15 mL) and Et_2O (3 × 15 mL) three times. After drying in air for 15 min, **3** was obtained as a black powder (yield: 156.6 mg, 0.35 mmol, 97%).

Anal. Found (%): C, 39.10; H, 4.50; N, 7.35; S, 27.19; Fe, 11.76. Calcd for [$Fe_2C_{16}H_9S_8O$]·5 DMF (%): C, 39.16; H, 4.66; N, 7.37; S, 26.97; Fe, 11.75. ATR-IR (cm^{-1}): 2931 (w), 2857 (w), 1649 (vs), 1564 (w), 1493 (w), 1385 (s), 1255 (s), 1147 (m), 1090 (s), 984 (s), 944 (s), 837 (m), 658 (s).

■ RESULTS AND DISCUSSION

Synthesis and Characterization of CPs 1−3. The CPs **1−3** were synthesized by reacting the sodium salt of the linker Na_2BDDTC with the respective metal triflate precursor M(OTf)$_2$ (M = Mn, Zn, Fe) under solvothermal conditions in DMF. Workup was performed in air for all materials. While **1** and **2** remained stable in air according to PXRD analysis (vide infra), **3** showed decomposition over time in the presence of air and was therefore transferred to an argon-filled glovebox directly after workup. For all materials, first, the integrity of the BDDTC^{2-} linker was verified by IR vibrational spectroscopy. The characteristic vibrational bands of the linker in the range between 840 and 1500 cm^{-1} were maintained in the IR spectra of the obtained materials (Figures S1−S3). Especially the characteristic band around 1000 cm^{-1}, which corresponds to the stretching mode of the CS_2 group, can be observed in all spectra.

https://doi.org/10.1021/acs.inorgchem.3c02471
Inorg. Chem. 2024, 63, 129−140

Inorganic Chemistry pubs.acs.org/IC Article

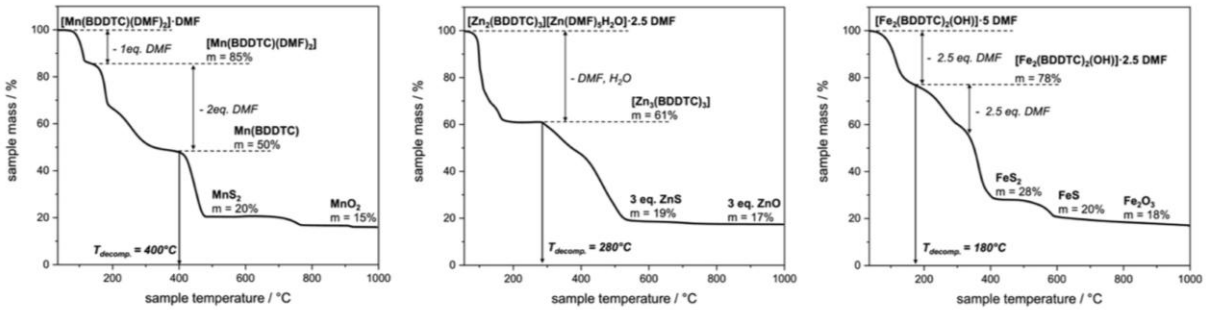

Figure 1. Thermogravimetric analysis of CPs **1** (left), **2** (middle), and **3** (right) in the range between 30 and 1000 °C. Measurements were performed with a constant flow of synthetic air and a heating rate of 10 °C min^{-1}.

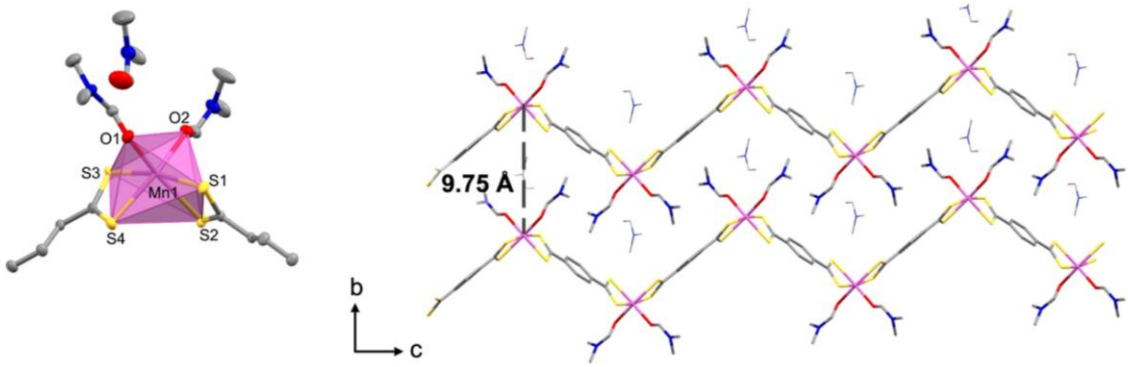

Figure 2. Solid-state structure of **1** as determined by SC-XRD. Asymmetric unit of **1** (left) shows the octahedral coordination environment around the Mn atom. Ellipsoids are shown at the 50% probability level. Packing of **1** (right) viewed along the crystallographic *a*-axis is represented as capped sticks. Parallel arrangement of zigzag chains is displayed with a metal−metal distance of 9.753 Å. For clarity, hydrogen atoms are omitted. Color code: gray for C, yellow for S, red for O, blue for N, and magenta for Mn.

Further, the composition and purity of the obtained materials were examined by elemental analysis. The obtained values agree with the calculated percentages. As suggested, a 1:1 ratio between the metal and ligand was observed for all compounds to achieve charge neutrality of the resulting polymers. In all as-synthesized samples, residual DMF was detected. In the case of compounds **1** and **2** this is, to some extent, caused by structurally incorporated solvent molecules as confirmed by SC-XRD (vide infra). For **1** two equivalents of coordinating DMF were found while **2** showed a more complex structure with incorporated complexes $[Zn(DMF)_5(H_2O)]^{2+}$. The single-crystal structures are discussed in detail in the crystallographic section below.

TGA (Figure 1) showed a high temperature stability for all CPs. **1** exhibited the highest decomposition temperature at 400 °C whereas compounds **2** and **3** started to decompose at 280 and 180 °C, respectively. All three CPs showed several decomposition steps, starting around 100 °C with the release of DMF. For **1** and **2**, a plateau was reached at 50 and 61% residual sample mass, respectively. These plateaus can be attributed to the respective solvent-free species [Mn(BDDTC)] and $[Zn_3(BDDTC)_3]$. In contrast, no plateau was observed in the case of **3**, indicating gradual decomposition of the framework accompanied by the release of DMF. After decomposition of the frameworks, the metal sulfides MnS_2, ZnS, and FeS were obtained, which are further converted to the respective metal oxides (MnO_2, ZnO and Fe_2O_3) above 800 °C.

Crystallographic Analysis. Single crystals suitable for SC-XRD analysis of **1** and **2** were obtained directly after solvothermal synthesis (note: even though **1** was reported before,[34] a SC-XRD structure was previously not available). For compound **3**, a fine powder consisting of agglomerated microcrystals was obtained, which was not suitable for SC-XRD structural analysis. CP **1** crystallizes as dark red block-like crystals in the triclinic space group $P\bar{1}$. The asymmetric unit comprises one Mn^{2+} ion, two independent halves of the $BDDTC^{2-}$ linker, and three cocrystallized DMF molecules. The Mn^{2+} ions are coordinated by the bidentate CS_2 groups of two independent $BDDTC^{2-}$ linkers in a $1\kappa S^1{:}1\kappa S^2$ coordination mode and two cis-positioned O atoms from coordinating DMF molecules, which resulted in a distorted octahedral coordination environment (Figure 2 left). The observed Mn−S distances are in the range between 2.5601(12) Å (Mn1−S1) and 2.6638(12) Å (Mn1−S2) and therefore are slightly longer compared to reported values for Mn−S bonds in molecular complexes (2.3483(5)-2.3891(8) Å)[50,51] as well as the analog Zn-polymer (Zn1−S1 2.430(2) Å, Zn1−S2 2.648(2) Å).[34] For all other relevant geometric parameters concerning CP **1** see Table 1.

The bridging coordination mode of the ditopic linker leads to the formation of one-dimensionally extended zigzag chains, which are arranged parallel along the crystallographic *b*-axis with a metal−metal separation of 9.753 Å (Figure 2 right). Similar distances of neighboring chains are reported for the Zn analogue (9.716 Å along the *b*-axis). Overall, this confirms the

https://doi.org/10.1021/acs.inorgchem.3c02471
Inorg. Chem. 2024, 63, 129−140

Table 1. Selected Parameters of Relevant Crystal Data for CP 1

space group	$P\bar{1}$
volume/Å^3	1142.08(17)
manganese−sulfur	**length/Å**
Mn1−S1	2.5601(12)
Mn1−S2	2.6638(12)
Mn1−S3	2.6002(12)
Mn−S4	2.5691(12)
Mn−O1	2.130(3)
Mn−O2	2.176(3)
sulfur−manganese−sulfur	**angles/°**
S1−Mn1−S2	68.52(4)
S3−Mn1−S4	69.37(4)

previously suggested structure, which was anticipated from comparison to the isostructural $[Zn(S_2CC_6H_4CS_2)(DMF)_2](DMF)$.[34]

In contrast to **1**, CP **2** forms a two-dimensionally extended sheet structure. SC-XRD revealed two crystalline phases (**2a**, **2b**) in the monoclinic space group $P2_1/n$ that show a different coordination environment around the Zn atoms. For all relevant geometric parameters for CP **2** see Table 2.

Table 2. Selected Parameters of the Relevant Crystal Data for CP 2

phase **2a**		phase **2b**	
space group	$P2_1/n$	space group	$P2_1/n$
volume/Å^3	7522(4)	volume/Å^3	6851(5)
zinc−sulfur	**length/Å**	**zinc−sulfur**	**length/Å**
Zn1−S1	2.4352(16)	Zn2−S7	2.287(5)
Zn1−S2	2.4338(17)	Zn2−S10	2.296(5)
Zn1−S4	2.2821(16)	Zn2−S11	2.436(5)
Zn1−S5	2.2914(16)	Zn2−S12	2.418(5)
Zn2−S7	2.3003(16)	Zn3−S1	2.494(5)
Zn2−S9	2.3038(16)	Zn3−S2	2.536(5)
Zn2−S11	2.4231(16)	Zn3−S3	2.521(6)
Zn2−S12	2.4338(16)	Zn3−S4	2.464(5)
		Zn3−S5	2.529(5)
		Zn3−S6	2.519(5)
sulfur−zinc−sulfur	**angles/°**	**sulfur−zinc−sulfur**	**angles/°**
S1−Zn1−S2	74.04(5)	S7−Zn2−S10	121.7(2)
S4−Zn1−S5	127.08(5)	S11−Zn2−S12	74.59(18)
		S1−Zn3−S2	71.05(16)
		S3−Zn3−S4	72.05(17)
		S5−Zn3−S6	70.83(17)

In phase **2a**, all Zn^{2+} metal ions are tetrahedrally coordinated by three $BDDTC^{2-}$ ligands. One CS_2 group is coordinated in a bidentate fashion while the two other linkers are coordinated through only one sulfur atom (Figure 3). For monodentate coordination, shorter Zn−S distances are found, whereas bidentate interactions result in slightly longer Zn−S coordination bonds. Overall, the observed distances are shorter compared to the reported Zn−S distances of the one-dimensional $Zn(S_2CC_6H_4CS_2)_2$, ranging up to 2.648(2) Å.[34] Linkage of six ZnS_4^{2-} nodes through six bidentate $BDDTC^{2-}$ linkers leads to the formation of distorted hexagons with distances between opposite sides of 16.8, 21.0 and 21.4 Å, respectively (Figure 3). Since each metal atom located at the corners of the hexagons can be accounted for 1/3 and each linker at the edges of the hexagons for 1/2, subunits with the general formula $[M_2L_3]^{2-}$ ($M = Zn^{2+}$, $L = BDDTC^{2-}$) can be derived. Therefore, two negative charges remain for each subunit. To counterbalance the negative charge of these $[M_2L_3]^{2-}$ units, solvated $[Zn(DMF)_5(H_2O)]^{2+}$ complexes are incorporated between every second layer of the framework. In the second phase **2b**, each $[M_2L_3]^{2-}$ subunit consists of three tetrahedrally coordinated Zn ions and three which are octahedrally coordinated by three bidentate CS_2 groups (Figure 3). Bond lengths for mono- and bidentate CS_2 coordination are comparable to those observed in phase **2a**.

In the solid state, sheets are arranged in an ABB'A' sequence. Adjacent layers are rotated 180° and stacked in a staggered conformation with an interlayer distance of 4.72 Å. Due to the incorporation of the solvated $[Zn(DMF)_5(H_2O)]^{2+}$ complexes amidst every second layer, an increased distance of 6.62 Å can be observed (Figure 4).

The experimental PXRD patterns for **1** and **2** are in good agreement with the predicted patterns calculated from the respective single crystal structure (Figure 5). In the case of **2**, it can be shown by comparison to the pattern obtained from phase **2a** and **2b** that phase **2b** (octahedral and tetrahedral coordination) is the predominant phase in the bulk material. While **1** does not exhibit any reflections at 2θ angles lower than 10°, characteristic reflections can be observed in the 2θ range between 5 and 10° for **2**. This is in accordance with the larger cell volume of 6851 Å^3, which was observed for phase **2b** (7522 Å^3 for **2a**), compared to 1142 Å^3 for **1** as determined from SC-XRD. Both materials retain their crystallinity upon vacuum treatment. While the structure of **2** remains unchanged, changes in the XRD pattern were observed for **1**. This indicates a phase transition, probably due to the removal of coordinating DMF molecules.

By contrast, the PXRD pattern of **3** (Figure 6) shows fewer reflections, with a sharp reflection around a 2θ angle of 5° indicating a relatively big unit cell in the range of a CP; thus, excluding molecular Fe−S species. Further, the material exhibits good stability upon a vacuum treatment. However, in the presence of air, **3** decomposes over time as evidenced by the loss of long-range order. This pronounced air sensitivity was not observed for CPs **1** and **2** (Figure S7), which is in accordance with the lower decomposition temperature of **3** observed in TGA.

While structural analysis revealed dense 1D and 2D structures for **1** and **2**, respectively, it was not possible to conclude on the porosity of **3** due to the lack of structure solution by means of SC-XRD analysis. Furthermore, the quality of the PXRD data was not sufficient to substantiate a structural model determined by Rietveld refinements. Standard N_2 physisorption measurements were performed for **3** to reveal a BET surface area of 237 m^2 g^{-1}, therefore confirming the porosity of **3**. Further adsorption at higher relative partial pressure, as seen in the isotherm (Figure 7) might be traced back to condensation processes.

Characterization of Electrical Conductivity and Electronic Properties. In addition to structural analysis, $I-V$ curves were recorded on pressed pellets using a two-probe setup to determine the electrical conductivity of the prepared CPs. The curves were fitted by a linear regression, and the slope of the linear function for **1** and **2** yielded an electrical conductivity typical for insulation materials of 2×10^{-12} S cm^{-1}. Contrarily, CP **3** shows an increased electrical conductivity of about 7 orders of magnitude

https://doi.org/10.1021/acs.inorgchem.3c02471
Inorg. Chem. 2024, 63, 129−140

Inorganic Chemistry pubs.acs.org/IC Article

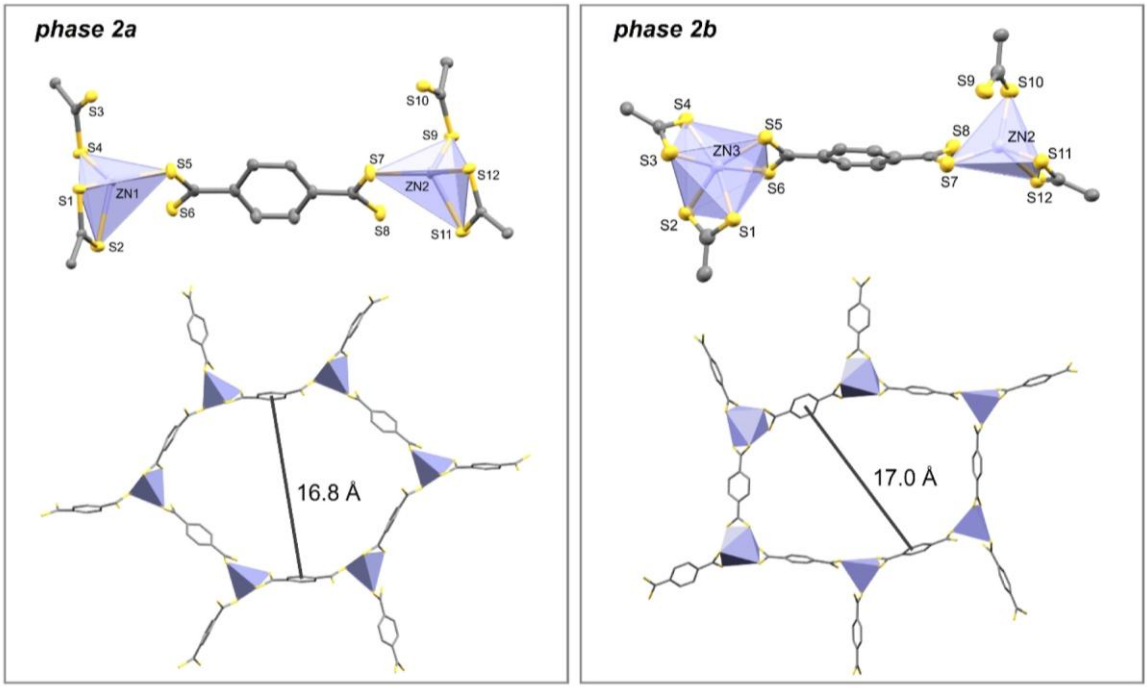

Figure 3. Solid-state structure of the two phases (**2a** and **2b**) found for **2** as determined by SC-XRD analysis, showing the local coordination environment around the Zn atoms (top) and hexagonal $[M_2L_3]^{2-}$ subunits (bottom). In phase **2a** (left) all Zn atoms are tetrahedrally coordinated while in phase **2b** (right) equal amounts of tetrahedrally and octahedrally coordinated Zn atoms are present. Hydrogen atoms and DMF solvent molecules have been omitted for clarity. Blue polyhedra represent the coordination environment around the Zn^{2+} cations. Color code: gray for C, yellow for S, and blue for Zn. The distances between opposite sides of the distorted hexagons were determined as centroid−centroid separations, without considering the van der Waals radii of the respective opposing phenyl rings.

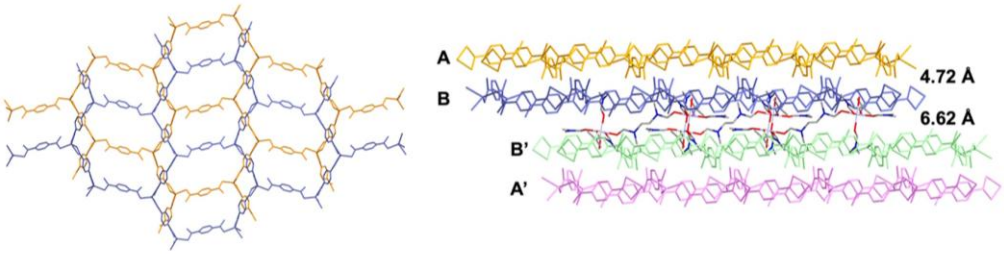

Figure 4. Solid-state packing of **2a** as determined by SC-XRD analysis. Display of two layers (A and B) (left) depicted in orange and blue along the crystallographic *a*-axis. Arrangement of four layers (right) in an ABB'A' sequence along the crystallographic *b*-axis with interlayer distances of 4.72 Å are displayed (orange-blue/green-purple) and 6.62 Å (blue-green), respectively. $[Zn(DMF)_5(H_2O)]^{2+}$ complexes are intercalated for charge neutrality of the framework. Ellipsoids are shown at the 50% probability level. Interlayer distances were determined by planes defined through six corner zinc atoms that construct a honeycomb ring. For the sake of clarity, hydrogen atoms and free DMF solvent molecules are omitted. Color code: gray for C, red for O, and blue for N.

compared to **1** and **2**, corresponding to an electrical conductivity of 2×10^{-5} S cm^{-1} (Figure 8).

After general assessment of the samples for being conductive or insulating materials, for the most promising sample **3**, the electrical conductivity was additionally determined by the van der Pauw method. There, the same pelletized crystalline samples of **3** gave an average electrical conductivity value of 5×10^{-3} S cm^{-1}. The relatively high conductivity of **3** (see Table S4) demonstrates the ability of the $BDDTC^{2-}$ linker to promote mobile charge carriers while this set of frameworks also highlights that the type of metal nodes is highly relevant for obtaining electrical conductivity, similar to observations in other MOF series. In the family of MOF-74, replacement of Mn^{2+} to Fe^{2+} leads to 6 orders of magnitude higher electrical conductivity for the iron analog.[52] The unique electrical properties of iron-based MOFs are found in various MOFs of different connectivity and composition and can often be attributed to high-spin Fe^{2+} or mixed-valent $Fe^{2+/3+}$ systems.[53] A CP containing Fe^{2+} ions with d^6 electron count in high-spin configuration may rationalize a high charge carrier mobility; for instance, the minority-spin electron in an octahedral high spin configuration might serve as mobile charge carrier.[54] Given that single crystals of material **3** were not accessible to shed light on the origin of its desirably high conductivity, further analysis was performed.

https://doi.org/10.1021/acs.inorgchem.3c02471
Inorg. Chem. 2024, 63, 129−140

Inorganic Chemistry pubs.acs.org/IC Article

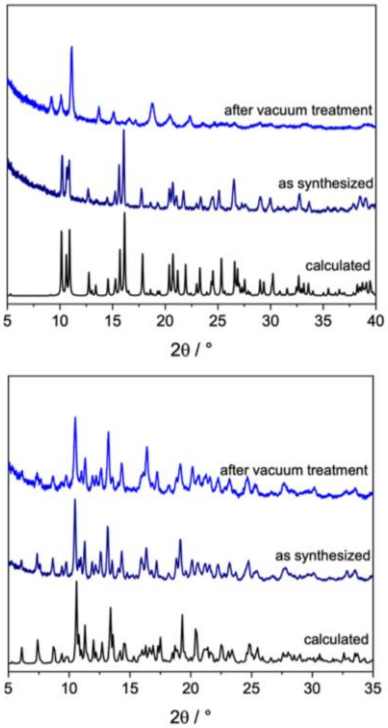

Figure 5. PXRD pattern of **1** (top) and **2** (bottom) as calculated (phase **2b** for CP **2**) from the single-crystal structure, experimentally obtained after synthesis and after vacuum treatment at room temperature.

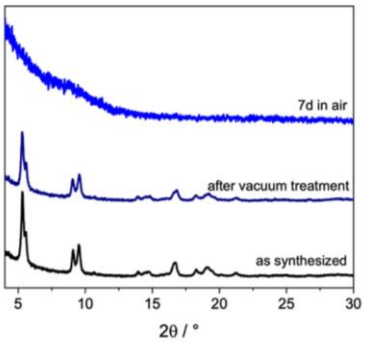

Figure 6. PXRD pattern of **3** as obtained from the as-synthesized material, after vacuum treatment at room temperature and after 1 week in air.

Solid-state UV/VIS-NIR (Figures S10−13) electronic absorption spectroscopy showed broad absorption bands with maximum at 380, 375, and 350 nm for **1**, **2**, and **3**, respectively. These bands in the UV/VIS region are most likely attributed to ligand-based $\pi-\pi^*$ transitions while no d−d transitions were observed, in line with the virtually absent charge carrier mobility across the CP's metal nodes observed in the form of low electrical conductivity. Compared with the absorption spectra of **1** and **2**, compound **3** features an additional broad absorption band centered at 725 nm, clearly indicating differences in electronic structure that may rationalize differences in conductivity. Principally, d−d transitions

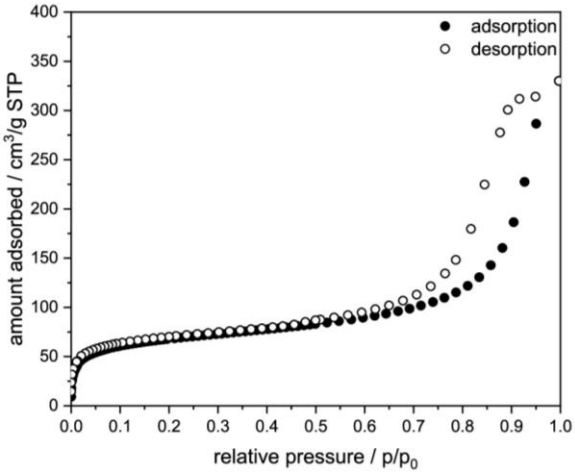

Figure 7. N_2 isotherm of **3** measured at 77 K.

can be observed in this spectral range, but the very high intensity of the absorption band renders this hypothesis unlikely. An explanation that unites the broadness of the absorption at 725 nm with its high intensity could be, to ascribe this spectral feature to an intervalence charge transfer (IVCT) band. This would be possible under the assumption that CP **3** with an unknown geometric structure is constructed from both Fe^{2+} and Fe^{3+} ions due to partial oxidation of the Fe^{2+} starting material during solvothermal synthesis in the presence of H_2O. This hypothesis is further corroborated by famous examples of mixed-valent $Fe^{2+/3+}$ compounds, such as Prussian blue and its analogs,[55−58] which show their intense IVCT band also in the range of 700 nm. The presence of such mixed-valent $Fe^{2+/3+}$ centers could make an additional contribution to the enhanced electrical conductivity of CP **3** with respect to the other materials **1** and **2**.[59] As a next step to assess a possible mixed-valent character in **3**, EPR spectroscopic characterization was therefore performed.

The fact that Fe^{2+} precursor $Fe(OTf)_2$ was employed for the synthesis of **3** under solvothermal conditions in the presence of H_2O raised the question of whether Fe^{2+} was in situ oxidized during the formation of **3**. EPR signals for non-Kramer's doublet Fe^{2+} ions cannot be observed at ambient temperature in X-band perpendicular mode, since strong spin−orbit coupling effects typically result in short spin−lattice relaxation times, thus broadening any signal beyond detection.[60] Conversely, Fe^{3+} ions are straightforwardly detected by X-band EPR spectroscopy, sometimes even at room temperature. Accordingly, we considered room temperature EPR spectroscopy to be a suitable method to detect any Fe^{3+} in samples of **3**. Indeed, a prominent EPR signal was observed (Figure 9), confirming the assumption that Fe^{3+} ions had formed in situ during the synthesis of **3**. The spectrum appears isotropic at first sight but was clearly fitted best as a slightly rhombic spectrum with $g_1 = 2.32$, $g_2 = 1.99$, and $g_3 = 1.86$ and line widths of $W_1 = 35.5$ mT, $W_2 = 6.1$ mT, and $W_3 = 28.6$ mT.

Since EPR experiments confirmed the presence of Fe^{3+} ions in **3**, ^{57}Fe Mössbauer spectroscopy was employed to reveal whether the CP was constructed exclusively from only one type or from multiple different types of iron centers and to elucidate their relative ratio. A Mössbauer spectrum recorded on a solid sample of **3** at 77 K (Figure 10) revealed a signal

https://doi.org/10.1021/acs.inorgchem.3c02471
Inorg. Chem. 2024, 63, 129−140

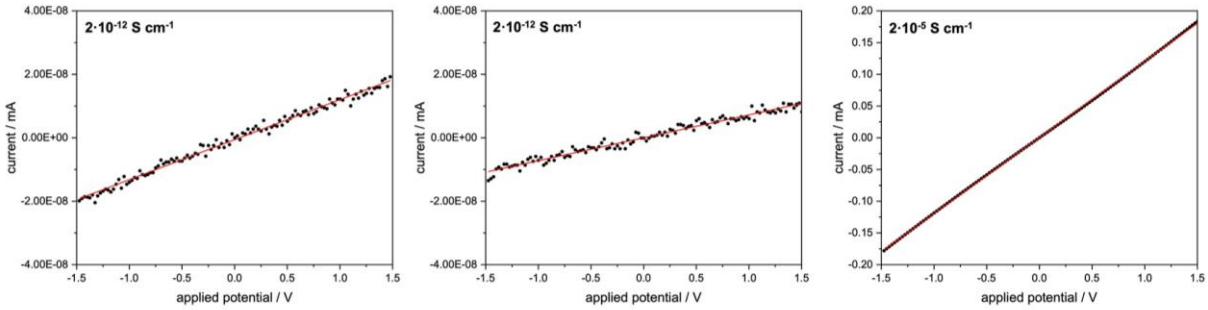

Figure 8. $I-V$ curves of CPs **1** (left), **2** (middle), and **3** (right) recorded in the potential range between −1.5 V and +1.5 V. Measurements were performed at room temperature on pressed pellets in a two-probe setup with a potential scan rate of 0.1 V s^{-1} and a step size of 0.025 V. The curves were fitted by a linear function shown in red. Note: for CP **3** additional van der Pauw measurements yielded an average electrical conductivity of 5×10^{-3} S cm^{-1}.

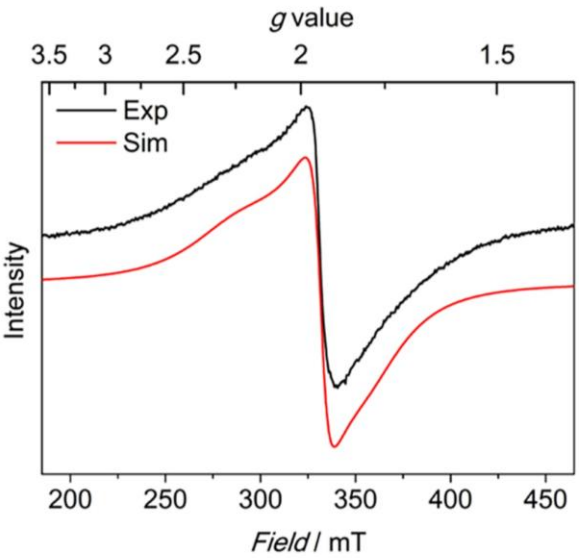

Figure 9. X-Band EPR spectrum recorded on a powder sample of **3** (ν = 9.267 GHz, P = 5.0 mW, modulation width = 0.4 mT, and T = 293 K). The experimental data (black) were best fitted (red) with g_1 = 2.32, g_2 = 1.99, g_3 = 1.86 and line widths of W_1 = 35.5 mT, W_2 = 6.1 mT, and W_3 = 28.6 mT.

pattern that was best fitted with two independent iron sites in a 1:1 ratio. The sharp lines indicate a well-defined coordination environment around each iron center. The convoluted spectrum was fitted with the one Fe-site possessing an isomer shift of δ = 0.09 mm s^{-1}, a quadrupole splitting of ΔE_Q = 1.27 mm s^{-1}, and a relative content of 48%. The other Fe-site was fitted with an isomeric shift of δ = 0.70 mm s^{-1}, a quadrupole splitting of ΔE_Q = 1.14 mm s^{-1}, and a relative content of 52%. Alternatively, an equally good fit to the experimental Mössbauer spectrum is obtained with two species, also in a 1:1 ratio, and isomer shifts of δ = 0.36 mm s^{-1} and δ = 0.43 mm s^{-1} with ΔE_Q values of 1.81 and 0.61 mm s^{-1} and almost identical line widths. Thus, the precise electronic structure cannot be unambiguously revealed by zero-field ^{57}Fe Mössbauer spectroscopy. Regardless, in combination with the magnetization measurements (vide infra) both sets of parameters are in agreement with a mixed-valent $Fe^{2+/3+}$ system, in which the Fe sites are confined within a well-defined, sulfur-based ligand environment.[61−64]

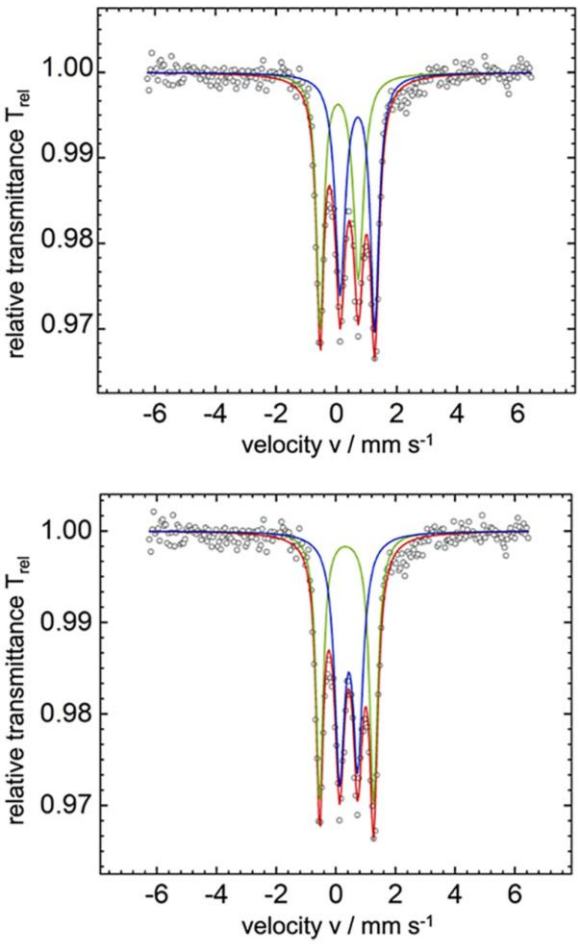

Figure 10. Zero-field ^{57}Fe Mössbauer spectrum of a solid sample of **3**, recorded at 77 K. First simulation with ΔE_Q values of 1.27 mm s^{-1} and of 1.14 mm s^{-1} (top), second simulation with ΔE_Q values of 1.81 and 0.61 mm s^{-1} (bottom) are displayed. In both cases, the red trace represents the best fit obtained with the parameters given in the text, the green trace represents the best fit of the first given Fe species, and the blue trace represents the best fit of the second Fe species in the sample; both species are in a 1:1 ratio.

https://doi.org/10.1021/acs.inorgchem.3c02471
Inorg. Chem. 2024, 63, 129−140

Inorganic Chemistry pubs.acs.org/IC Article

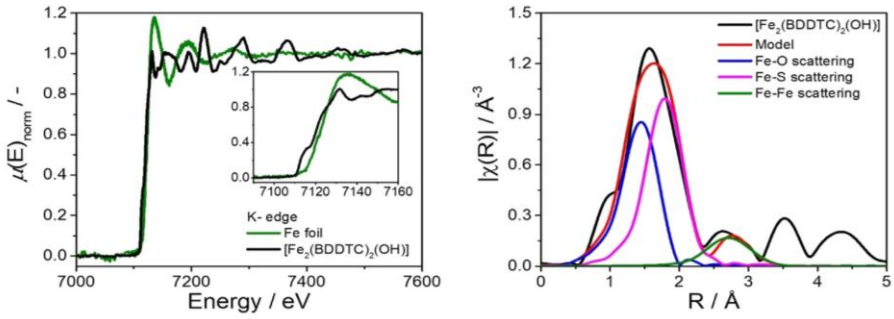

Figure 11. XAS spectra of **3**. XANES region (left) showing the Fe K-edge of the reference Fe foil and sample $Fe_2(BDDTC)_2(OH)$ (inset shows the pre-edge). Magnitude of the Fourier-transform EXAFS is displayed (right).

The mixed-valent character of **3** is expected to contribute to the experimentally observed high electric conductivity. Additionally, XPS measurements also confirmed the presence of Fe^{2+} and Fe^{3+} in **3** (Figure S18).

Magnetometric analysis of **3** with a stoichiometric sample composition of $[Fe_2(BDDTC)_2(OH)]\cdot 5$ DMF according to elemental analysis and TGA (vide supra) showed a room temperature magnetic moment of μ_{eff} = 8.1 μB per formula unit (Figure S14). According to the spin-only formula, this accounts for a total of 7 unpaired electrons per formula unit that contains two iron centers. A 1:1 ratio of Fe^{2+} and Fe^{3+} ions as found in the Mössbauer spectroscopy suggests a total of 9 unpaired electrons per formula unit, assuming both ions are in high-spin configuration. The experimentally found lower magnetic moment may be rationalized by the coupling effects or intermediate spin states of the metal ions. While intermediate spin states are not trivial to elucidate in this complicated sample, the notable decrease in the magnetic moment at low temperatures below 150 K is indicative of antiferromagnetic coupling, which is further visualized in the $\chi_m \cdot T$ vs T plot (Figure S15). Also, the plot of magnetization vs applied field (Figure S16) shows a nonlinearity, which excludes pure paramagnetism and further confirms the antiferromagnetic coupling observed in **3**.[65−67] Together, the magnetochemical characterization data, obtained from EPR, Mössbauer, and SQUID magnetization, suggest that coupling effects between the iron centers influence the intricate electronic structure and electrical conductivity of **3**.

Considering the Fe centers in **3** as nonisolated spin systems raises the question of whether the bridging nodes of CP **3** are mononuclear with coupling facilitated through covalently bound $(BDDTC)^{2-}$ linkers, or whether **3** is constructed from multinuclear $Fe^{2+/3+}$ nodes. Since single-crystal X-ray structural data remained elusive, EXAFS was used for the characterization of **3** to investigate the local environment around each Fe center in **3** to aid in further understanding of the observed magnetic coupling effects in **3**. A simulation of EXAFS data (Figure 11) revealed a closest Fe−Fe distance of 3.16 Å, which is slightly longer than reported values for carboxylate-bridged Fe paddlewheel complexes, but a clear indication for multinuclear metal nodes in **3**.[68,69] Also, the modeling fits very well for both S and O atoms (from coordinated OH^-, H_2O, or DMF) being coordinated to the Fe ions, going along with small Debye-Waller factors (below 10^{-3} $Å^2$) that indicate a very well ordered local environment in the first coordination shell.

In summary, despite the elusive SC-XRD analysis of CP **3**, the comprehensive analysis of the new material allows the following description: The as-synthesized CP **3** has the sum formula $[Fe_2(BDDTC)_2(OH)]\cdot 5$ DMF (elemental analysis & TGA) and possesses a permanent porosity after vacuum treatment (BET surface area 237 $m^2\ g^{-1}$). CP **3** is constructed from multinuclear metal nodes (Fe−Fe distance 3.16 Å, EXAFS), containing Fe^{2+} and Fe^{3+} ions (EPR activity, XPS and IVCT band in UV/VIS) in a 1:1 ratio (Mössbauer). Even with this detailed information at hand, an exhaustive literature analysis of structural databases revealed no satisfactory agreement with any reported structure of known coordination polymers (Table S3), thus, emphasizing the complexity of accessible structural diversity of iron−sulfur coordination compounds.

■ CONCLUSIONS

We have synthesized and fully characterized three CPs (**1**−**3**) constructed from the benzene-1,4-di(dithiocarboxylate) $(BDDTC^{2-})$ linker and Mn-, Zn-, and Fe-based inorganic building units. Single-crystal X-ray analysis revealed interesting structural features. While **1** forms 1D extended chains, **2** crystallizes in a 2D sheet structure, consisting of anionic $[Zn_2BDDTC_3]^{2-}$ subunits. For **2**, two different phases were observed, which show either pure tetrahedral coordination (phase **2a**) or a mix of tetrahedral and octahedral coordination environment (phase **2b**) around the Zn atom. This demonstrates the diverse coordination behavior of the $BDDTC^{2-}$ linker and its potential to form CPs of higher dimensionality. To date, this is the first example of a transition-metal-based 2D CP which is exclusively linked via bridging RCS_2 coordination. Although rigorous structural determination was not possible in the case of **3**, partial oxidation inducing $Fe^{2+/3+}$ mixed valency could be revealed via comprehensive analysis, including ^{57}Fe Mössbauer and EPR as well as SQUID magnetization and XAS studies. Overall, these investigations demonstrate that for the construction of electrically conductive CPs, it is beneficial to switch from classically employed hard O-donor linkers to softer and more covalent S-donor. In this study, we further illustrated that it is equally important to also engineer the inorganic metal nodes of a CP, given that metal centers with fully (Zn^{2+}) or half-filled (Mn^{2+}) d-orbitals led to the formation of nonconductive materials. In contrast, the mixed-valent $Fe^{2+/3+}$ material **3** was found to be electrically conductive within the range of semiconducting materials (5×10^{-3} S cm^{-1} in van der Pauw measurements).

https://doi.org/10.1021/acs.inorgchem.3c02471
Inorg. Chem. 2024, 63, 129−140

Further research will focus on the elucidation of the structure of **3** to perform an in-depth analysis of the underlying charge transport mechanism and derive a comprehensive understanding of related structure–property relationships.

■ ASSOCIATED CONTENT

Supporting Information

The Supporting Information is available free of charge at https://pubs.acs.org/doi/10.1021/acs.inorgchem.3c02471.

Experimental infrared spectra, thermogravimetric analysis data, solid-state UV/VIS-NIR spectra, PXRD studies for air stability, SQUID magnetometry spectra, EXAFS analysis data, XPS spectra and analysis, scanning electron microscopy images and structural details, tables for comparison of coordination motifs and electrical conductivities, and crystallographic information (PDF)

Adsorption information (PDF)

Accession Codes

CCDC 2249203–2249205 contain the supplementary crystallographic data for this paper. These data can be obtained free of charge via www.ccdc.cam.ac.uk/data_request/cif, or by emailing data_request@ccdc.cam.ac.uk, or by contacting The Cambridge Crystallographic Data Centre, 12 Union Road, Cambridge CB2 1EZ, UK; fax: +44 1223 336033.

■ AUTHOR INFORMATION

Corresponding Authors

Roland A. Fischer – *Chair of Inorganic and Metal–Organic Chemistry, Department of Chemistry, TUM School of Natural Sciences and Catalysis Research Center (CRC), Technical University of Munich, 85747 Garching, Germany;* orcid.org/0000-0002-7532-5286; Email: roland.fischer@tum.de

Alexander Pöthig – *Chair of Inorganic and Metal–Organic Chemistry, Department of Chemistry, TUM School of Natural Sciences and Catalysis Research Center (CRC), Technical University of Munich, 85747 Garching, Germany;* orcid.org/0000-0003-4663-3949; Email: alexander.poethig@tum.de

Authors

Margit Aust – *Chair of Inorganic and Metal–Organic Chemistry, Department of Chemistry, TUM School of Natural Sciences and Catalysis Research Center (CRC), Technical University of Munich, 85747 Garching, Germany*

Marina I. Schönherr – *Department of Chemistry and Center for NanoScience (CeNS), Ludwig-Maximilians-Universität (LMU), 81377 Munich, Germany*

Dominik P. Halter – *Chair of Inorganic and Metal–Organic Chemistry, Department of Chemistry, TUM School of Natural Sciences and Catalysis Research Center (CRC), Technical University of Munich, 85747 Garching, Germany;* orcid.org/0000-0003-0733-8955

Lena Schröck – *Chair of Inorganic and Metal–Organic Chemistry, Department of Chemistry, TUM School of Natural Sciences and Catalysis Research Center (CRC), Technical University of Munich, 85747 Garching, Germany*

Thomas Pickl – *Chair of Inorganic and Metal–Organic Chemistry, Department of Chemistry, TUM School of Natural Sciences and Catalysis Research Center (CRC), Technical University of Munich, 85747 Garching, Germany*

Simon N. Deger – *Chair of Inorganic and Metal–Organic Chemistry, Department of Chemistry, TUM School of Natural Sciences and Catalysis Research Center (CRC), Technical University of Munich, 85747 Garching, Germany*

Mian Z. Hussain – *Chair of Inorganic and Metal–Organic Chemistry, Department of Chemistry, TUM School of Natural Sciences and Catalysis Research Center (CRC), Technical University of Munich, 85747 Garching, Germany*

Andreas Jentys – *Chair of Industrial Chemistry and Heterogeneous Catalysis, Department of Chemistry, TUM School of Natural Sciences and Catalysis Research Center (CRC), Technical University of Munich, 85747 Garching, Germany*

Raphael Bühler – *Chair of Inorganic and Metal–Organic Chemistry, Department of Chemistry, TUM School of Natural Sciences and Catalysis Research Center (CRC), Technical University of Munich, 85747 Garching, Germany*

Zihan Zhang – *Department of Chemistry and Pharmacy, Inorganic Chemistry, Friedrich-Alexander-Universität Erlangen-Nürnberg (FAU), 91058 Erlangen, Germany*

Karsten Meyer – *Department of Chemistry and Pharmacy, Inorganic Chemistry, Friedrich-Alexander-Universität Erlangen-Nürnberg (FAU), 91058 Erlangen, Germany;* orcid.org/0000-0002-7844-2998

Matthias Kuhl – *Walter Schottky Institute, Physics Department, TUM School of Natural Sciences, Technical University of Munich, 85747 Garching, Germany*

Johanna Eichhorn – *Walter Schottky Institute, Physics Department, TUM School of Natural Sciences, Technical University of Munich, 85747 Garching, Germany*

Dana D. Medina – *Department of Chemistry and Center for NanoScience (CeNS), Ludwig-Maximilians-Universität (LMU), 81377 Munich, Germany*

Complete contact information is available at: https://pubs.acs.org/10.1021/acs.inorgchem.3c02471

Author Contributions

The manuscript was written through contributions of all authors. All authors have given approval to the final version of the manuscript.

Funding

German Research Foundation (DFG).

Notes

The authors declare no competing financial interest.

■ ACKNOWLEDGMENTS

The German Research Foundation (DFG) is gratefully acknowledged for funding this research as a part of the COORNETs (SPP 1928) and the e-conversion (EXC 2089) program as well as the funding for the easyXAFS300+ device (451579122). D.H. thanks the Fonds der Chemischen Industrie for a Liebig Fellowship. J.E. acknowledges support from the Bavarian Academy of Sciences and Humanities. D.M. is grateful for financial support from the Free State of Bavaria through the Research Network "Solar Technologies go Hybrid". The authors thank the TUM School of Natural Sciences for supporting this project. Oksana Storcheva is acknowledged for conducting EPR measurements.

■ REFERENCES

(1) Long, J. R.; Yaghi, O. M. The pervasive chemistry of metal-organic frameworks. *Chem. Soc. Rev.* **2009**, *38* (5), 1213–1214.

(2) Furukawa, H.; Cordova, K. E.; O'Keeffe, M.; Yaghi, O. M. The Chemistry and Applications of Metal-Organic Frameworks. *Science* **2013**, *341* (6149), 1230444.
(3) Fromm, K. M. Coordination Polymers. Design, Analysis and Application. *Angew. Chem., Int. Ed.* **2009**, *48*, 4890.
(4) Zhou, H. C.; Long, J. R.; Yaghi, O. M. Introduction to metal-organic frameworks. *Chem. Rev.* **2012**, *112* (2), 673−674.
(5) Ghasempour, H.; Wang, K.-Y.; Powell, J. A.; ZareKarizi, F.; Lv, X.-L.; Morsali, A.; Zhou, H.-C. Metal-organic frameworks based on multicarboxylate linkers. *Coord. Chem. Rev.* **2021**, *426*, 213542.
(6) Baumann, A. E.; Burns, D. A.; Liu, B.; Thoi, V. S. Metal-organic framework functionalization and design strategies for advanced electrochemical energy storage devices. *Commun. Chem.* **2019**, *2* (1), 86.
(7) Sun, L.; Campbell, M. G.; Dincă, M. Electrically Conductive Porous Metal-Organic Frameworks. *Angew. Chem., Int. Ed.* **2016**, *55* (11), 3566−3579.
(8) Ding, B.; Solomon, M. B.; Leong, C. F.; D'Alessandro, D. M. Redox-active ligands: Recent advances towards their incorporation into coordination polymers and metal-organic frameworks. *Coord. Chem. Rev.* **2021**, *439*, 213891.
(9) Nidamanuri, N.; Maity, K.; Saha, S. Electrically Conductive Metal-Organic Frameworks. *Elaboration and Applications of Metal-Organic Frameworks*; World Scientific, 2017; Vol. 2, pp 655−686.
(10) Ko, M.; Mendecki, L.; Mirica, K. A. Conductive two-dimensional metal-organic frameworks as multifunctional materials. *Chem. Commun.* **2018**, *54* (57), 7873−7891.
(11) He, Y.; Talin, A. A.; Allendorf, M. D. Thermoelectric Properties of 2D Ni3(hitp)2 and 3D Cu3(btc)2 MOFs: First-Principles Studies. *ECS J. Solid State Sci. Technol.* **2017**, *6* (12), N236−N242.
(12) Clough, A. J.; Skelton, J. M.; Downes, C. A.; de la Rosa, A. A.; Yoo, J. W.; Walsh, A.; Melot, B. C.; Marinescu, S. C. Metallic Conductivity in a Two-Dimensional Cobalt Dithiolene Metal-Organic Framework. *J. Am. Chem. Soc.* **2017**, *139* (31), 10863−10867.
(13) Kambe, T.; Sakamoto, R.; Kusamoto, T.; Pal, T.; Fukui, N.; Hoshiko, K.; Shimojima, T.; Wang, Z.; Hirahara, T.; Ishizaka, K.; Hasegawa, S.; Liu, F.; Nishihara, H. Redox Control and High Conductivity of Nickel Bis(dithiolene) Complex π-Nanosheet: A Potential Organic Two-Dimensional Topological Insulator. *J. Am. Chem. Soc.* **2014**, *136* (41), 14357−14360.
(14) Kambe, T.; Sakamoto, R.; Hoshiko, K.; Takada, K.; Miyachi, M.; Ryu, J.-H.; Sasaki, S.; Kim, J.; Nakazato, K.; Takata, M.; Nishihara, H. π-Conjugated Nickel Bis(dithiolene) Complex Nanosheet. *J. Am. Chem. Soc.* **2013**, *135* (7), 2462−2465.
(15) Dong, R.; Han, P.; Arora, H.; Ballabio, M.; Karakus, M.; Zhang, Z.; Shekhar, C.; Adler, P.; Petkov, P. S.; Erbe, A.; Mannsfeld, S. C. B.; Felser, C.; Heine, T.; Bonn, M.; Feng, X.; Cánovas, E. High-mobility band-like charge transport in a semiconducting two-dimensional metal-organic framework. *Nat. Mater.* **2018**, *17* (11), 1027−1032.
(16) Huang, X.; Sheng, P.; Tu, Z.; Zhang, F.; Wang, J.; Geng, H.; Zou, Y.; Di, C.-a.; Yi, Y.; Sun, Y.; Xu, W.; Zhu, D. A two-dimensional π-d conjugated coordination polymer with extremely high electrical conductivity and ambipolar transport behaviour. *Nat. Commun.* **2015**, *6*, 7408.
(17) Mensforth, E. J.; Hill, M. R.; Batten, S. R. Coordination polymers of sulphur-donor ligands. *Inorg. Chim. Acta* **2013**, *403*, 9−24.
(18) Piovesana, O.; Bellitto, C.; Flamini, A.; Zanazzi, P. F. Metal-metal interactions in one dimension. 1. Synthesis and structural and spectroscopic properties of dithioacetic acid derivatives of palladium(II). *Inorg. Chem.* **1979**, *18* (8), 2258−2265.
(19) Bellitto, C.; Dessy, G.; Fares, V.; Flamini, A. Two polymorphic forms of the tetrakis(dithioisobutanoato)diplatinum(II) complex: X-ray crystal structure and spectroscopic evidence of intermolecular interactions in the solid state. *J. Chem. Soc., Chem. Commun.* **1981**, No. 9, 409−411.
(20) Schuerman, J. A.; Fronczek, F. R.; Selbin, J. Synthesis and structure of [Au6(o-CH3C6H4CS2)6], a novel gold cluster compound. *J. Am. Chem. Soc.* **1986**, *108* (2), 336−337.
(21) Bellitto, C.; Bonamico, M.; Dessy, G.; Fares, V.; Flamini, A. Linear-chain platinum(II) dithiocarboxylates: crystal structure of tetrakis(phenyldithioacetato)diplatinum(II). *J. Chem. Soc., Dalton Trans.* **1987**, No. 1, 35−40.
(22) Mitsumi, M.; Ueda, H.; Furukawa, K.; Ozawa, Y.; Toriumi, K.; Kurmoo, M. Constructing Highly Conducting Metal-Metal Bonded Solids by Electrocrystallization of [PtII2(RCS2)4] (RCS2- = Dithiocarboxylato, R = Methyl or Ethyl). *J. Am. Chem. Soc.* **2008**, *130* (43), 14102−14104.
(23) Ball, S. C.; Cragg-Hine, I.; Davidson, M. G.; Davies, R. P.; Raithby, P. R.; Snaith, R. The mechanisms of dilithiation reactions in organic syntheses: a case study based on the syntheses of ketene dithioacetals. *Chem. Commun.* **1996**, No. 13, 1581−1582.
(24) Ma, C.; Han, Y.; Zhang, R. Investigation on the coordination modes: Syntheses, characterization and crystal structures of diorganotin (IV) dichloride with 4(5)-imidazoledithiocarboxylic acid. *Inorg. Chim. Acta* **2005**, *358* (11), 3084−3092.
(25) Li, M.-Q.; Zhao, M.; Bi, L.-Y.; Hu, Y.-Q.; Gou, G.; Li, J.; Zheng, Y.-Z. Two-Dimensional Silver(I)-Dithiocarboxylate Coordination Polymer Exhibiting Strong Near-Infrared Photothermal Effect. *Inorg. Chem.* **2019**, *58* (10), 6601−6608.
(26) Pathak, A.; Shen, J.-W.; Usman, M.; Wei, L.-F.; Mendiratta, S.; Chang, Y.-S.; Sainbileg, B.; Ngue, C.-M.; Chen, R.-S.; Hayashi, M.; Luo, T.-T.; Chen, F.-R.; Chen, K.-H.; Tseng, T.-W.; Chen, L.-C.; Lu, K.-L. Integration of a (-Cu-S-)n plane in a metal-organic framework affords high electrical conductivity. *Nat. Commun.* **2019**, *10* (1), 1721.
(27) Calzolari, A.; Alexandre, S. S.; Zamora, F.; Di Felice, R. Metallicity in Individual MMX Chains. *J. Am. Chem. Soc.* **2008**, *130* (16), 5552−5562.
(28) Kitagawa, H.; Onodera, N.; Sonoyama, T.; Yamamoto, M.; Fukawa, T.; Mitani, T.; Seto, M.; Maeda, Y. Charge Ordering with Lattice Distortions in a Conductive MMX-Chain Complex, Pt2(dta)-4I (dta = CH3CS2-). *J. Am. Chem. Soc.* **1999**, *121* (43), 10068−10080.
(29) Mitsumi, M.; Murase, T.; Kishida, H.; Yoshinari, T.; Ozawa, Y.; Toriumi, K.; Sonoyama, T.; Kitagawa, H.; Mitani, T. Metallic Behavior and Periodical Valence Ordering in a MMX Chain Compound, Pt2(EtCS2)4I. *J. Am. Chem. Soc.* **2001**, *123* (45), 11179−11192.
(30) Mitsumi, M.; Kitamura, K.; Morinaga, A.; Ozawa, Y.; Kobayashi, M.; Toriumi, K.; Iso, Y.; Kitagawa, H.; Mitani, T. Valence-Ordering Structures and Magnetic Behavior of Metallic MMX Chain Compounds. *Angew. Chem., Int. Ed.* **2002**, *41* (15), 2767−2771.
(31) Manotti Lanfredi, A. M.; Ugozzoli, F.; Camus, A.; Marsich, N. New synthesis and X-ray diffraction study of a polymeric form of Ag(I) dithio-o-toluato, [Ag4(S2C-o-C6H4CH3)4]n. *J. Chem. Crystallogr.* **1995**, *25* (1), 37−41.
(32) Gallego, M. L.; Guijarro, A.; Castillo, O.; Parella, T.; Mas-Balleste, R.; Zamora, F. Nuclearity control in gold dithiocarboxylato compounds. *CrystEngComm* **2010**, *12* (8), 2332−2334.
(33) Neuba, A.; Ortmeyer, J.; Konieczna, D. D.; Weigel, G.; Flörke, U.; Henkel, G.; Wilhelm, R. Synthesis of new copper(i) based linear 1-D-coordination polymers with neutral imidazolinium-dithiocarboxylate ligands. *RSC Adv.* **2015**, *5* (12), 9217−9220.
(34) Neofotistou, E.; Malliakas, C. D.; Trikalitis, P. N. Novel Coordination Polymers Based on the Tetrathioterephthalate Dianion as the Bridging Ligand. *Inorg. Chem.* **2007**, *46* (21), 8487−8489.
(35) Aust, M.; Herold, A. J.; Niederegger, L.; Schneider, C.; Mayer, D. C.; Drees, M.; Warnan, J.; Pöthig, A.; Fischer, R. A. Introducing Benzene-1,3,5-tri(dithiocarboxylate) as a Multidentate Linker in Coordination Chemistry. *Inorg. Chem.* **2021**, *60* (24), 19242−19252.
(36) Neese, F. *University of Konstanz*, 1993.
(37) Bill, E. *Mössbauer Program Mfit*, 2019.
(38) Bill, E. *Mössbauer Program Mcal*, 2019.
(39) Newville, M. Larch: An Analysis Package for XAFS and Related Spectroscopies. *J. Phys.: Conf. Ser.* **2013**, *430* (430), 012007.
(40) *APEX Suite of Crystallographic Software, APEX 3, Version 2015.5−2*. Bruker AXS Inc.: Madison, WI, USA, 2015.

https://doi.org/10.1021/acs.inorgchem.3c02471
Inorg. Chem. 2024, 63, 129−140

(41) SAINT. *Version 7.56 a and SADABS Version 2008/1*; Bruker AXS Inc.: Madison, WI, USA, 2008; pp 435−436.
(42) Hübschle, C. B.; Sheldrick, G. M.; Dittrich, B. ShelXle: a Qt graphical user interface for SHELXL. *J. Appl. Crystallogr.* **2011**, *44* (6), 1281−1284.
(43) Sheldrick, G. M. *SHELXL-2014/7: Program for the Solution of Crystal Structures*; University of Göttingen: Göttingen, Germany, 2014.
(44) Sheldrick, G. M. *SHELXL-97 (Release 97−2)*; University of Göttingen: Germany, 1998.
(45) *International Tables for Crystallography, Vol. C. Mathematical, Physical and Chemical Tables*; Wilson, A. J. C., Prince, E., Eds.; Springer, 1992.
(46) Macrae, C. F.; Bruno, I. J.; Chisholm, J. A.; Edgington, P. R.; McCabe, P.; Pidcock, E.; Rodriguez-Monge, L.; Taylor, R.; Van de Streek, J.; Wood, P. A. Mercury CSD 2.0 - new features for the visualization and investigation of crystal structures. *J. Appl. Crystallogr.* **2008**, *41* (2), 466−470.
(47) Kratzert, D.; Krossing, I. Recent improvements in DSR. *J. Appl. Crystallogr.* **2018**, *51* (3), 928−934.
(48) Kratzert, D.; Holstein, J. J.; Krossing, I. DSR: enhanced modelling and refinement of disordered structures with SHELXL. *J. Appl. Crystallogr.* **2015**, *48* (3), 933−938.
(49) Spek, A. L. PLATON SQUEEZE: a tool for the calculation of the disordered solvent contribution to the calculated structure factors. *Acta Crystallogr., Sect. C: Struct. Chem.* **2015**, *71* (1), 9−18.
(50) Beltrán, T. F.; Zaragoza, G.; Delaude, L. Synthesis and characterization of cationic manganese-carbonyl complexes bearing imidazole(in)ium-2-dithiocarboxylate ligands. *Polyhedron* **2021**, *197*, 115055.
(51) Mace, W. J.; Main, L.; Nicholson, B. K.; Hagyard, M. Reactions of cyclomanganated complexes with carbon disulfide: routes to η2-aryldithiocarboxylate-Mn(CO)4 complexes and to the trithiocarbonate complex (μ3-CS3)2Mn4(CO)16. *J. Organomet. Chem.* **2002**, *664* (1−2), 288−293.
(52) Sun, L.; Hendon, C. H.; Minier, M. A.; Walsh, A.; Dincă, M. Million-Fold Electrical Conductivity Enhancement in Fe2(DEBDC) versus Mn2(DEBDC) (E = S, O). *J. Am. Chem. Soc.* **2015**, *137* (19), 6164−6167.
(53) Sun, L.; Hendon, C. H.; Park, S. S.; Tulchinsky, Y.; Wan, R.; Wang, F.; Walsh, A.; Dincă, M. Is iron unique in promoting electrical conductivity in MOFs? *Chem. Sci.* **2017**, *8* (6), 4450−4457.
(54) Grosso, G.; Parravicini, G. P. Chapter 11 - Optical and Transport Properties of Metals. In *Solid State Physics*, 2nd ed.; Grosso, G., Parravicini, G. P., Eds.; Academic Press: Amsterdam, 2014, pp 483−528.
(55) Pyrasch, M.; Toutianoush, A.; Jin, W.; Schnepf, J.; Tieke, B. Self-assembled Films of Prussian Blue and Analogues: Optical and Electrochemical Properties and Application as Ion-Sieving Membranes. *Chem. Mater.* **2003**, *15* (1), 245−254.
(56) Zhang, Y.; Wen, Y.; Liu, Y.; Li, D.; Li, J. Functionalization of single-walled carbon nanotubes with Prussian blue. *Electrochem. Commun.* **2004**, *6* (11), 1180−1184.
(57) Farah, A.; Billing, C.; Dikio, C. W.; DiboforOrji, A. N.; Oyedeji, O.; Donbebe, W.; Mtunzi, F.; Dikio, E. Synthesis of Prussian Blue and its Electrochemical detection of Hydrogen Peroxide Based on Cetyltrimethylammonium Bromide (CTAB) Modified Carbon Electrode. *Int. J. Electrochem. Sci.* **2013**, *8*, 12132−12146.
(58) Cheng, M.; Peng, W.; Hua, P.; Chen, Z.; Sheng, J.; Yang, J.; Wu, Y. In situ formation of pH-responsive Prussian blue for photoacoustic imaging and photothermal therapy of cancer. *RSC Adv.* **2017**, *7*, 18270−18276.
(59) Nath, A.; Asha, K. S.; Mandal, S. Conductive Metal-Organic Frameworks: Electronic Structure and Electrochemical Applications. *Chem.—Eur. J.* **2021**, *27* (45), 11482−11538.
(60) Gütlich, P.; Gaspar, A. B.; Garcia, Y. Spin state switching in iron coordination compounds. *Beilstein J. Org. Chem.* **2013**, *9* (9), 342−391.
(61) Frank, E.; Abeledo, C. R. Mössbauer Effect in Iron(III) Dithiocarbamates. *Inorg. Chem.* **1966**, *5* (8), 1453−1455.
(62) Douglas, T.; Dickson, D. P. E.; Betteridge, S.; Charnock, J.; Garner, C. D.; Mann, S. Synthesis and Structure of an Iron(III) Sulfide-Ferritin Bioinorganic Nanocomposite. *Science* **1995**, *269* (5220), 54−57.
(63) Brown, A. C.; Thompson, N. B.; Suess, D. L. M. Evidence for Low-Valent Electronic Configurations in Iron-Sulfur Clusters. *J. Am. Chem. Soc.* **2022**, *144* (20), 9066−9073.
(64) Pandelia, M.-E.; Lanz, N. D.; Booker, S. J.; Krebs, C. Mössbauer spectroscopy of Fe/S proteins. *Biochim. Biophys. Acta, Mol. Cell Res.* **2015**, *1853* (6), 1395−1405.
(65) Hartman, J. A. R.; Rardin, R. L.; Chaudhuri, P.; Pohl, K.; Wieghardt, K.; Nuber, B.; Weiss, J.; Papaefthymiou, G. C.; Frankel, R. B.; Lippard, S. J. Synthesis and characterization of (.mu.-hydroxo)-bis(.mu.-acetato)diiron(II) and (.mu.-oxo)bis(.mu.-acetato)diiron-(III) 1,4,7-trimethyl-1,4,7-triazacyclononane complexes as models for binuclear iron centers in biology; properties of the mixed valence diiron(II,III) species. *J. Am. Chem. Soc.* **1987**, *109* (24), 7387−7396.
(66) Mukherjee, R. N.; Stack, T. D. P.; Holm, R. H. Angle dependence of the properties of the [Fe2X]4+ bridge unit (X = O, S): structures, antiferromagnetic coupling, and properties in solution. *J. Am. Chem. Soc.* **1988**, *110* (6), 1850−1861.
(67) Wollmann, R. G.; Hendrickson, D. N. Preparation and physical properties of oxidation products of oxo-bridged binuclear iron(III) complexes. Mixed-valence diiron(III, IV) complexes. *Inorg. Chem.* **1977**, *16* (4), 723−733.
(68) Eremenko, I. L.; Kiskin, M. A.; Fomina, I. G.; Sidorov, A. A.; Aleksandrov, G. G.; Ikorskii, V. N.; Shvedenkov, Y. G.; Rakitin, Y. V.; Novotortsev, V. M. Pivalate Bridged High Spin Manganese(II) and Iron(II) Polymers. *J. Cluster Sci.* **2005**, *16* (3), 331−351.
(69) Friedle, S.; Kodanko, J. J.; Fornace, K. L.; Lippard, S. J. 9-Triptycenecarboxylate-bridged diiron(II) complexes: Capture of the paddlewheel geometric isomer. *J. Mol. Struct.* **2008**, *890* (1−3), 317−327.

https://doi.org/10.1021/acs.inorgchem.3c02471
Inorg. Chem. 2024, 63, 129−140

4. CONCLUSION

Within the research associated with this thesis, the novel dithiocarboxylate ligand benzene-1,3,5-tri(dithiocarboxylate) (BTDTC) was synthesized and characterized regarding its composition, properties and crystal structure. As sulfur-substituted analogue to the well-established benzene-1,3,5-tricarboxylate (BTC), this ligand motif offers unique properties for derived coordination compounds, introducing electronic and electrochemical effects to promote charge carrier mobility, electronic communication and electrical conductivity. To complement the investigation of sulfur analogues of multivalent carboxylates, also the previously known ditopic ligand benzene-1,4-di(dithiocarboxylate) (BDDTC) was structurally investigated for the first time. Synthesis and thorough investigation of two model complexes, $[Cu(Xantphos)]_3(BTDTC)$ and $[Mo_2(DAniF)_3]_3(BTDTC)$, provide in-depth insights into the versatile coordination behavior of BTDTC, ranging from chelating to bridging conformation. Furthermore, electrochemical investigation of the Mo compound confirmed that S-substitution of the linker improves electronic communication between single metal moieties. This finding demonstrates the concept of redox matching with respect to improved ligand–metal orbital overlap resulting from the introduction of softer sulfur-donor atoms.

To further expand this ligand class toward extended coordination polymers, three crystalline materials were prepared from manganese, zinc and iron metal precursors. Single crystal structural analysis of the resulting $[Mn(BDDTC)(DMF)_2]$ and $[Zn_2(BDDTC)_3][Zn(DMF)_5(H_2O)]$ CPs revealed a one-dimensional chain structure for the Mn compound, whereas the Zn Polymer consists of two-dimensional honeycomb sheets with intercalated $[Zn(DMF)_5(H_2O)]$ complexes to achieve charge neutrality. Interestingly, two different crystal phases were found for the Zn(BDDTC) material, showing disparate coordination numbers around the central Zn atoms. In summary, these two polymers demonstrate the structural versatility of the CS_2 ligand family and showcase their potential to build structurally extended materials showing high crystallinity and good stability. In the case of the Fe-based material, solvothermal synthesis did not yield crystals suitable for structural analysis, but a microcrystalline powder was obtained. Extensive analytical characterization evidenced the stoichiometric composition $[Fe_2(BDDTC)_2(OH)]$. By means of magnetic and spectroscopic methods, a 1:1 Fe^{2+}/Fe^{3+} mixed valence was resolved with Fe atoms being located in close proximity. From this, it can be deduced that multinuclear mixed-valence metal nodes are present in the

Fe-BDDTC material. Remarkable electrical conductivity of $5 \cdot 10^{-3}$ S cm^{-1}, which is substantially higher than typical values for CPs, confirms the presence of free charge carriers, as expected for mixed-valence compounds. At this point, however, the detailed structure of $[Fe_2(BDDTC)_2(OH)]$ could not be fully resolved.

In future research, it will be interesting to further elucidate the structure of this Fe^{2+}/Fe^{3+} polymer, to reveal its connectivity, the nature of included building blocks and the underlying mechanism of its conductivity. Therefore, structural analysis using a synchrotron radiation source or emerging techniques such as electron diffraction might be suitable methods for determining the structure from microcrystals.

To access three-dimensionally extended structures, the incorporation of the tritopic ligand BTDTC into CPs will be highly interesting, opening the door to many novel structures. As demonstrated in the present work, substituting O or N ligator atoms with S can substantially improve electronic properties, leading to enhanced electronic coupling and conductivity. If this approach is applied to three-dimensional materials with intrinsic porosity, electrically conductive MOFs could be utilized as porous electrode materials or selective electrochemical sensing devices.

Finally, further steps are necessary to expand the utilization of dithiocarboxylate linkers to other transition metals. Specifically, metals such as Cr, Co and Ni, which are already investigated for electrically conductive 2D materials, are highly interesting in this regard. Along this roadmap, the next steps require exploring optimized synthesis conditions or alternative synthesis strategies to control the reaction kinetics and enable the preparation of well-defined materials.

5. REFERENCES

[1] B. D. Fahlman, *Materials Chemistry*, Springer Dordrecht, **2018**.

[2] E. Hatzikraniotis, T. Kyratsi, in *Iterative Design of Teaching-Learning Sequences: Introducing the Science of Materials in European Schools* (Eds.: D. Psillos, P. Kariotoglou), Springer Netherlands, Dordrecht, **2016**, pp. 75-100.

[3] W. D. Callister, D. G. Rethwisch, *Materials science and engineering : an introduction*, 10th edition. Australia custom edition ed., Wiley Milton, Qld, Milton, Qld, **2018**.

[4] R. P. Feynman, *Engineering and Science* **1960**, *23*, 22-36.

[5] D. R. Askeland, P. P. Fulay, *The science and engineering of materials*, 5th ed ed., Nelson ; Thomson Toronto, London, Toronto, London, **2006**.

[6] C. Ferguson, *Historical introduction to the development of material science and engineering as a teaching discipline*, **2006**.

[7] M. Bengisu, M. Ferrara, *Materials that Move: Smart Materials, Intelligent Design*, Springer International Publishing, **2018**.

[8] S. Bahl, H. Nagar, I. Singh, S. Sehgal, *Materials Today: Proceedings* **2020**, *28*, 1302-1306.

[9] S. R. Batten, N. R. Champness, X.-M. Chen, J. Garcia-Martinez, S. Kitagawa, L. Öhrström, M. O'Keeffe, M. Paik Suh, J. Reedijk, **2013**, *85*, 1715-1724.

[10] S. R. Batten, N. R. Champness, X.-M. Chen, J. Garcia-Martinez, S. Kitagawa, L. Öhrström, M. O'Keeffe, M. P. Suh, J. Reedijk, *CrystEngComm* **2012**, *14*, 3001-3004.

[11] S. N. Kitagawa, Shin-ichiro, *Comprehensive Coordination Chemistry II, Vol. 7*, **2003**.

[12] D. J. Tranchemontagne, J. L. Mendoza-Cortés, M. O'Keeffe, O. M. Yaghi, *Chemical Society Reviews* **2009**, *38*, 1257-1283.

[13] M. Safaei, M. M. Foroughi, N. Ebrahimpoor, S. Jahani, A. Omidi, M. Khatami, *TrAC Trends in Analytical Chemistry* **2019**, *118*, 401-425.

[14] O. M. Yaghi, M. O'Keeffe, N. W. Ockwig, H. K. Chae, M. Eddaoudi, J. Kim, *Nature* **2003**, *423*, 705-714.

[15] H. Furukawa, K. E. Cordova, M. O'Keeffe, O. M. Yaghi, *Science* **2013**, *341*, 1230444.

[16] W.-X. Zhang, P.-Q. Liao, R.-B. Lin, Y.-S. Wei, M.-H. Zeng, X.-M. Chen, *Coordination Chemistry Reviews* **2015**, *293-294*, 263-278.

[17] S. R. Batten, S. M. Neville, D. R. Turner, **2009**.

[18] L. E. Kreno, K. Leong, O. K. Farha, M. Allendorf, R. P. Van Duyne, J. T. Hupp, *Chemical Reviews* **2012**, *112*, 1105-1125.

[19] S. Bureekaew, S. Shimomura, S. Kitagawa, *Science and Technology of Advanced Materials* **2008**, *9*, 014108.

[20] J. J. V. Wei Lee Leong, *Chemical Reviews* **2011**, *111*, 688-764.

[21] M. Tran, K. Kline, Y. Qin, Y. Shen, M. D. Green, S. Tongay, *Applied Physics Reviews* **2019**, *6*, 041311.

[22] M. O'Keeffe, M. A. Peskov, S. J. Ramsden, O. M. Yaghi, *Accounts of Chemical Research* **2008**, *41*, 1782-1789.

[23] M. O'Keeffe, O. M. Yaghi, *Chemical Reviews* **2012**, *112*, 675-702.

[24] H. Deng, C. J. Doonan, H. Furukawa, R. B. Ferreira, J. Towne, C. B. Knobler, B. Wang, O. M. Yaghi, *Science* **2010**, *327*, 846-850.

[25] K. Koh, A. G. Wong-Foy, A. J. Matzger, *Journal of the American Chemical Society* **2009**, *131*, 4184-4185.

[26] A. D. Burrows, *CrystEngComm* **2011**, *13*, 3623-3642.

[27] J. A. Botas, G. Calleja, M. Sánchez-Sánchez, M. G. Orcajo, *Langmuir* **2010**, *26*, 5300-5303.

[28] S. Furukawa, K. Hirai, K. Nakagawa, Y. Takashima, R. Matsuda, T. Tsuruoka, M. Kondo, R. Haruki, D. Tanaka, H. Sakamoto, S. Shimomura, O. Sakata, S. Kitagawa, *Angewandte Chemie International Edition* **2009**, *48*, 1766-1770.

[29] J. R. Long, O. M. Yaghi, *Chemical Society Reviews* **2009**, *38*, 1213-1214.

[30] E. Loukopoulos, G. Kostakis, *Journal of Coordination Chemistry* **2018**, *71*, 1-40.
[31] S. Horike, S. Shimomura, S. Kitagawa, *Nature Chemistry* **2009**, *1*, 695-704.
[32] H. Furukawa, O. M. Yaghi, *Journal of the American Chemical Society* **2009**, *131*, 8875-8883.
[33] I. M. Hönicke, I. Senkovska, V. Bon, I. A. Baburin, N. Bönisch, S. Raschke, J. D. Evans, S. Kaskel, *Angewandte Chemie International Edition* **2018**, *57*, 13780-13783.
[34] J. Rouquerol, D. Avnir, C. W. Fairbridge, D. H. Everett, J. M. Haynes, N. Pernicone, J. D. F. Ramsay, K. S. W. Sing, K. K. Unger, **1994**, *66*, 1739-1758.
[35] M. Eddaoudi, J. Kim, N. Rosi, D. Vodak, J. Wachter, M. Keeffe, O. M. Yaghi, *Science* **2002**, *295*, 469.
[36] J. E. Mondloch, O. Karagiaridi, O. K. Farha, J. T. Hupp, *CrystEngComm* **2013**, *15*, 9258-9264.
[37] A. J. Howarth, A. W. Peters, N. A. Vermeulen, T. C. Wang, J. T. Hupp, O. K. Farha, *Chemistry of Materials* **2017**, *29*, 26-39.
[38] S. Kitagawa, M. Kondo, *Bulletin of the Chemical Society of Japan* **1998**, *71*, 1739-1753.
[39] J. Liu, L. Chen, H. Cui, J. Zhang, L. Zhang, C.-Y. Su, *Chemical Society reviews* **2014**, *43*.
[40] M. Kondo, T. Yoshitomi, H. Matsuzaka, S. Kitagawa, K. Seki, *Angewandte Chemie International Edition in English* **1997**, *36*, 1725-1727.
[41] D. Zhao, X. Wang, L. Yue, Y. He, B. Chen, *Chemical Communications* **2022**, *58*, 11059-11078.
[42] A. Li, *Journal of Physics: Conference Series* **2022**, *2403*, 012022.
[43] A. Ahmed, S. Seth, J. Purewal, A. G. Wong-Foy, M. Veenstra, A. J. Matzger, D. J. Siegel, *Nature Communications* **2019**, *10*, 1568.
[44] P. L. Llewellyn, S. Bourrelly, C. Serre, A. Vimont, M. Daturi, L. Hamon, G. De Weireld, J.-S. Chang, D.-Y. Hong, Y. Kyu Hwang, S. Hwa Jhung, G. Férey, *Langmuir* **2008**, *24*, 7245-7250.
[45] N. L. Rosi, J. Eckert, M. Eddaoudi, D. T. Vodak, J. Kim, M. O'Keeffe, O. M. Yaghi, *Science* **2003**, *300*, 1127-1129.
[46] J.-R. Li, R. J. Kuppler, H.-C. Zhou, *Chemical Society Reviews* **2009**, *38*, 1477-1504.
[47] B. Wang, A. P. Côté, H. Furukawa, M. O'Keeffe, O. M. Yaghi, *Nature* **2008**, *453*, 207-211.
[48] R. Banerjee, H. Furukawa, D. Britt, C. Knobler, M. O'Keeffe, O. M. Yaghi, *Journal of the American Chemical Society* **2009**, *131*, 3875-3877.
[49] K. Schlichte, T. Kratzke, S. Kaskel, *Microporous and Mesoporous Materials* **2004**, *73*, 81-88.
[50] A. Henschel, K. Gedrich, R. Kraehnert, S. Kaskel, *Chemical Communications* **2008**, 4192-4194.
[51] L. Alaerts, E. Séguin, H. Poelman, F. Thibault-Starzyk, P. A. Jacobs, D. E. De Vos, *Chemistry – A European Journal* **2006**, *12*, 7353-7363.
[52] K. Barthelet, J. Marrot, D. Riou, G. Férey, *Angewandte Chemie International Edition* **2002**, *41*, 281-284.
[53] A. Phan, A. U. Czaja, F. Gándara, C. B. Knobler, O. M. Yaghi, *Inorganic Chemistry* **2011**, *50*, 7388-7390.
[54] M. H. Alkordi, Y. Liu, R. W. Larsen, J. F. Eubank, M. Eddaoudi, *Journal of the American Chemical Society* **2008**, *130*, 12639-12641.
[55] B. Yuan, Y. Pan, Y. Li, B. Yin, H. Jiang, *Angewandte Chemie International Edition* **2010**, *49*, 4054-4058.
[56] Y. K. Hwang, D.-Y. Hong, J.-S. Chang, S. H. Jhung, Y.-K. Seo, J. Kim, A. Vimont, M. Daturi, C. Serre, G. Férey, *Angewandte Chemie International Edition* **2008**, *47*, 4144-4148.
[57] P. Horcajada, T. Chalati, C. Serre, B. Gillet, C. Sebrie, T. Baati, J. F. Eubank, D. Heurtaux, P. Clayette, C. Kreuz, J.-S. Chang, Y. K. Hwang, V. Marsaud, P.-N. Bories, L. Cynober, S. Gil, G. Férey, P. Couvreur, R. Gref, *Nature Materials* **2010**, *9*, 172-178.
[58] Y. Chen, P. Li, J. A. Modica, R. J. Drout, O. K. Farha, *Journal of the American Chemical Society* **2018**, *140*, 5678-5681.
[59] H. An, M. Li, J. Gao, Z. Zhang, S. Ma, Y. Chen, *Coordination Chemistry Reviews* **2019**, *384*, 90-106.
[60] X. Lian, Y. Fang, E. Joseph, Q. Wang, J. Li, S. Banerjee, C. Lollar, X. Wang, H.-C. Zhou, *Chemical Society Reviews* **2017**, *46*, 3386-3401.
[61] S. J. Weishäupl, Y. Cui, S. N. Deger, H. Syed, A. Ovsianikov, J. Hauer, A. Pöthig, R. A. Fischer, *Chemistry of Materials* **2022**, *34*, 7402-7411.

[62] S. J. Weishäupl, D. C. Mayer, Y. Cui, P. Kumar, H. Oberhofer, R. A. Fischer, J. Hauer, A. Pöthig, *Journal of Materials Chemistry C* **2022**, *10*, 6912-6934.
[63] S. J. Weishäupl, D. C. Mayer, E. Thyrhaug, J. Hauer, A. Pöthig, R. A. Fischer, *Dyes and Pigments* **2021**, *186*, 109012.
[64] P. M. Stanley, A. Y. Su, V. Ramm, P. Fink, C. Kimna, O. Lieleg, M. Elsner, J. A. Lercher, B. Rieger, J. Warnan, R. A. Fischer, *Advanced Materials* **2023**, *35*, 2207380.
[65] P. M. Stanley, F. Sixt, J. Warnan, *Advanced Materials* **2023**, *35*, 2207280.
[66] P. M. Stanley, K. Hemmer, M. Hegelmann, A. Schulz, M. Park, M. Elsner, M. Cokoja, J. Warnan, *Chemical Science* **2022**, *13*, 12164-12174.
[67] P. M. Stanley, J. Haimerl, N. B. Shustova, R. A. Fischer, J. Warnan, *Nature Chemistry* **2022**, *14*, 1342-1356.
[68] P. M. Stanley, J. Haimerl, C. Thomas, A. Urstoeger, M. Schuster, N. B. Shustova, A. Casini, B. Rieger, J. Warnan, R. A. Fischer, *Angewandte Chemie International Edition* **2021**, *60*, 17854-17860.
[69] P. M. Stanley, C. Thomas, E. Thyrhaug, A. Urstoeger, M. Schuster, J. Hauer, B. Rieger, J. Warnan, R. A. Fischer, *ACS Catalysis* **2021**, *11*, 871-882.
[70] H.-J. Son, S. Jin, S. Patwardhan, S. J. Wezenberg, N. C. Jeong, M. So, C. E. Wilmer, A. A. Sarjeant, G. C. Schatz, R. Q. Snurr, O. K. Farha, G. P. Wiederrecht, J. T. Hupp, *Journal of the American Chemical Society* **2013**, *135*, 862-869.
[71] J. Zhang, Y. Huang, D. Yue, Y. Cui, Y. Yang, G. Qian, *Journal of Materials Chemistry B* **2018**, *6*, 5174-5180.
[72] A. Karmakar, B. Joarder, A. Mallick, P. Samanta, A. V. Desai, S. Basu, S. K. Ghosh, *Chemical Communications* **2017**, *53*, 1253-1256.
[73] M. Zhang, G. Feng, Z. Song, Y.-P. Zhou, H.-Y. Chao, D. Yuan, T. T. Y. Tan, Z. Guo, Z. Hu, B. Z. Tang, B. Liu, D. Zhao, *Journal of the American Chemical Society* **2014**, *136*, 7241-7244.
[74] Z. Hu, W. P. Lustig, J. Zhang, C. Zheng, H. Wang, S. J. Teat, Q. Gong, N. D. Rudd, J. Li, *Journal of the American Chemical Society* **2015**, *137*, 16209-16215.
[75] W. P. Lustig, S. Mukherjee, N. D. Rudd, A. V. Desai, J. Li, S. K. Ghosh, *Chemical Society Reviews* **2017**, *46*, 3242-3285.
[76] D. Sheberla, J. C. Bachman, J. S. Elias, C.-J. Sun, Y. Shao-Horn, M. Dincă, *Nature Materials* **2016**, *16*, 220.
[77] L. Guo, J. Sun, W. Zhang, L. Hou, L. Liang, Y. Liu, C. Yuan, *ChemSusChem* **2019**, *12*, 5051-5058.
[78] J. Sun, L. Guo, X. Sun, J. Zhang, Y. Liu, L. Hou, C. Yuan, *Journal of Materials Chemistry A* **2019**, *7*, 24788-24791.
[79] L. Guo, J. Sun, X. Sun, J. Zhang, L. Hou, C. Yuan, *Nanoscale Advances* **2019**, *1*, 4688-4691.
[80] C. Dong, L. Xu, *ACS Applied Materials & Interfaces* **2017**, *9*, 7160-7168.
[81] J. Park, M. Lee, D. Feng, Z. Huang, A. C. Hinckley, A. Yakovenko, X. Zou, Y. Cui, Z. Bao, *Journal of the American Chemical Society* **2018**, *140*, 10315-10323.
[82] Y. Liu, X. Zhao, C. Fang, Z. Ye, Y.-B. He, D. Lei, J. Yang, Y. Zhang, Y. Li, Q. Liu, Y. Huang, R. Zeng, L. Kang, J. Liu, Y.-H. Huang, *Chem* **2018**, *4*, 2463-2478.
[83] A. A. Talin, A. Centrone, A. C. Ford, M. E. Foster, V. Stavila, P. Haney, R. A. Kinney, V. Szalai, F. El Gabaly, H. P. Yoon, F. Léonard, M. D. Allendorf, *Science* **2014**, *343*, 66.
[84] L. Sun, M. G. Campbell, M. Dincă, *Angewandte Chemie International Edition* **2016**, *55*, 3566-3579.
[85] N. Nidamanuri, K. Maity, S. Saha, in *Elaboration and Applications of Metal-Organic Frameworks, Vol. 2*, World Scientific, **2017**, pp. 655-686.
[86] B. J. Holliday, T. M. Swager, *Chemical Communications* **2005**, 23-36.
[87] T. C. Narayan, T. Miyakai, S. Seki, M. Dincă, *Journal of the American Chemical Society* **2012**, *134*, 12932-12935.
[88] S. S. Park, E. R. Hontz, L. Sun, C. H. Hendon, A. Walsh, T. Van Voorhis, M. Dincă, *Journal of the American Chemical Society* **2015**, *137*, 1774-1777.
[89] S. Takaishi, M. Hosoda, T. Kajiwara, H. Miyasaka, M. Yamashita, Y. Nakanishi, Y. Kitagawa, K. Yamaguchi, A. Kobayashi, H. Kitagawa, *Inorganic Chemistry* **2009**, *48*, 9048-9050.

[90] Y. Kobayashi, B. Jacobs, M. D. Allendorf, J. R. Long, *Chemistry of Materials* **2010**, *22*, 4120-4122.
[91] M. D. Allendorf, M. E. Foster, F. Léonard, V. Stavila, P. L. Feng, F. P. Doty, K. Leong, E. Y. Ma, S. R. Johnston, A. A. Talin, *The Journal of Physical Chemistry Letters* **2015**, *6*, 1182-1195.
[92] C. Schneider, D. Ukaj, R. Koerver, A. A. Talin, G. Kieslich, S. P. Pujari, H. Zuilhof, J. Janek, M. D. Allendorf, R. A. Fischer, *Chemical Science* **2018**, *9*, 7405-7412.
[93] M. Rivera-Torrente, M. Filez, C. Schneider, E. C. van der Feltz, K. Wolkersdörfer, D. H. Taffa, M. Wark, R. A. Fischer, B. M. Weckhuysen, *Physical Chemistry Chemical Physics* **2019**, *21*, 25678-25689.
[94] K. Thürmer, C. Schneider, V. Stavila, R. W. Friddle, F. Léonard, R. A. Fischer, M. D. Allendorf, A. A. Talin, *ACS Applied Materials & Interfaces* **2018**, *10*, 39400-39410.
[95] L. Sun, T. Miyakai, S. Seki, M. Dincă, *Journal of the American Chemical Society* **2013**, *135*, 8185-8188.
[96] L. Sun, C. H. Hendon, M. A. Minier, A. Walsh, M. Dincă, *Journal of the American Chemical Society* **2015**, *137*, 6164-6167.
[97] E. Cerrada, M. C. Diaz, C. Diaz, M. Laguna, A. Sabater, *Synthetic Metals* **2001**, *119*, 91-92.
[98] L. F. Szczepura, C. P. Galloway, Y. Zheng, P. Han, S. R. Wilson, T. B. Rauchfuss, A. L. Rheingold, *Angewandte Chemie International Edition in English* **1995**, *34*, 1890-1892.
[99] K.-H. Low, V. A. L. Roy, S. S.-Y. Chui, S. L.-F. Chan, C.-M. Che, *Chemical Communications* **2010**, *46*, 7328-7330.
[100] E. J. Mensforth, M. R. Hill, S. R. Batten, *Inorganica Chimica Acta* **2013**, *403*, 9-24.
[101] R. D. Shannon, *Acta Crystallographica Section A* **1976**, *32*, 751-767.
[102] Y. Kamakura, D. Tanaka, *Chemistry Letters* **2020**, *50*, 523-533.
[103] C. Lin, J. D. Protasiewicz, E. T. Smith, T. Ren, *Inorganic Chemistry* **1996**, *35*, 6422-6428.
[104] F. Albert Cotton, L. M. Daniels, C. Lin, C. A. Murillo, *Inorganic Chemistry Communications* **2001**, *4*, 130-133.
[105] F. A. Cotton, J. P. Donahue, C. A. Murillo, *Journal of the American Chemical Society* **2003**, *125*, 5436-5450.
[106] F. A. Cotton, C. Y. Liu, C. A. Murillo, D. Villagrán, X. Wang, *Journal of the American Chemical Society* **2003**, *125*, 13564-13575.
[107] X. Xiao, C. Y. Liu, Q. He, M. J. Han, M. Meng, H. Lei, X. Lu, *Inorganic Chemistry* **2013**, *52*, 12624-12633.
[108] M. J. Han, C. Y. Liu, P. F. Tian, *Inorganic Chemistry* **2009**, *48*, 6347-6349.
[109] M. H. Chisholm, N. J. Patmore, *Dalton Transactions* **2006**, 3164-3169.
[110] H. Lei, X. Xiao, M. Meng, T. Cheng, Y. Shu, Y. N. Tan, C. Y. Liu, *Inorganica Chimica Acta* **2015**, *424*, 63-74.
[111] M. T. Kang, M. Meng, Y. N. Tan, T. Cheng, C. Y. Liu, *Chemistry – A European Journal* **2016**, *22*, 3115-3126.
[112] N. E. Horwitz, J. Xie, A. S. Filatov, R. J. Papoular, W. E. Shepard, D. Z. Zee, M. P. Grahn, C. Gilder, J. S. Anderson, *Journal of the American Chemical Society* **2019**, *141*, 3940-3951.
[113] J. Cui, Z. Xu, *Chemical Communications* **2014**, *50*, 3986-3988.
[114] R. Dong, P. Han, H. Arora, M. Ballabio, M. Karakus, Z. Zhang, C. Shekhar, P. Adler, P. S. Petkov, A. Erbe, S. C. B. Mannsfeld, C. Felser, T. Heine, M. Bonn, X. Feng, E. Cánovas, *Nature Materials* **2018**, *17*, 1027-1032.
[115] R. Dong, M. Pfeffermann, H. Liang, Z. Zheng, X. Zhu, J. Zhang, X. Feng, *Angewandte Chemie International Edition* **2015**, *54*, 12058-12063.
[116] R. Dong, Z. Zheng, D. C. Tranca, J. Zhang, N. Chandrasekhar, S. Liu, X. Zhuang, G. Seifert, X. Feng, *Chemistry – A European Journal* **2017**, *23*, 2255-2260.
[117] A. J. Clough, J. W. Yoo, M. H. Mecklenburg, S. C. Marinescu, *Journal of the American Chemical Society* **2015**, *137*, 118-121.
[118] A. J. Clough, J. M. Skelton, C. A. Downes, A. A. de la Rosa, J. W. Yoo, A. Walsh, B. C. Melot, S. C. Marinescu, *Journal of the American Chemical Society* **2017**, *139*, 10863-10867.

[119] T. Kambe, R. Sakamoto, K. Hoshiko, K. Takada, M. Miyachi, J.-H. Ryu, S. Sasaki, J. Kim, K. Nakazato, M. Takata, H. Nishihara, *Journal of the American Chemical Society* **2013**, *135*, 2462-2465.
[120] T. Kambe, R. Sakamoto, T. Kusamoto, T. Pal, N. Fukui, K. Hoshiko, T. Shimojima, Z. Wang, T. Hirahara, K. Ishizaka, S. Hasegawa, F. Liu, H. Nishihara, *Journal of the American Chemical Society* **2014**, *136*, 14357-14360.
[121] X. Huang, P. Sheng, Z. Tu, F. Zhang, J. Wang, H. Geng, Y. Zou, C.-a. Di, Y. Yi, Y. Sun, W. Xu, D. Zhu, *Nature Communications* **2015**, *6*, 7408.
[122] O. Piovesana, C. Bellitto, A. Flamini, P. F. Zanazzi, *Inorganic Chemistry* **1979**, *18*, 2258-2265.
[123] C. Bellitto, G. Dessy, V. Fares, A. Flamini, *Journal of the Chemical Society, Chemical Communications* **1981**, 409-411.
[124] C. Bellitto, M. Bonamico, G. Dessy, V. Fares, A. Flamini, *Journal of the Chemical Society, Dalton Transactions* **1987**, 35-40.
[125] M. Mitsumi, H. Ueda, K. Furukawa, Y. Ozawa, K. Toriumi, M. Kurmoo, *Journal of the American Chemical Society* **2008**, *130*, 14102-14104.
[126] C. Bellitto, A. Flamini, L. Gastaldi, L. Scaramuzza, *Acta Crystallographica Section A* **1981**, *37*, C172-C173.
[127] C. Bellitto, A. Flamini, L. Gastaldi, L. Scaramuzza, *Inorganic Chemistry* **1983**, *22*, 444-449.
[128] C. Bellitto, G. Dessy, V. Fares, *Inorganic Chemistry* **1985**, *24*, 2815-2820.
[129] M. Mitsumi, Y. Yoshida, A. Kohyama, Y. Kitagawa, Y. Ozawa, M. Kobayashi, K. Toriumi, M. Tadokoro, N. Ikeda, M. Okumura, M. Kurmoo, *Inorganic Chemistry* **2009**, *48*, 6680-6691.
[130] H. Kitagawa, S. Nakagami, T. Mitani, *Synthetic Metals* **2001**, *116*, 401-404.
[131] H. Kitagawa, N. Onodera, T. Sonoyama, M. Yamamoto, T. Fukawa, T. Mitani, M. Seto, Y. Maeda, *Journal of the American Chemical Society* **1999**, *121*, 10068-10080.
[132] M. Mitsumi, T. Murase, H. Kishida, T. Yoshinari, Y. Ozawa, K. Toriumi, T. Sonoyama, H. Kitagawa, T. Mitani, *Journal of the American Chemical Society* **2001**, *123*, 11179-11192.
[133] M. Mitsumi, K. Kitamura, A. Morinaga, Y. Ozawa, M. Kobayashi, K. Toriumi, Y. Iso, H. Kitagawa, T. Mitani, *Angewandte Chemie International Edition* **2002**, *41*, 2767-2771.
[134] A. Calzolari, S. S. Alexandre, F. Zamora, R. Di Felice, *Journal of the American Chemical Society* **2008**, *130*, 5552-5562.
[135] M. Mitsumi, T. Yamashita, Y. Aiga, K. Toriumi, H. Kitagawa, T. Mitani, M. Kurmoo, *Inorganic Chemistry* **2011**, *50*, 4368-4377.
[136] C. Ma, Y. Han, R. Zhang, *Inorganica Chimica Acta* **2005**, *358*, 3084-3092.
[137] M.-Q. Li, M. Zhao, L.-Y. Bi, Y.-Q. Hu, G. Gou, J. Li, Y.-Z. Zheng, *Inorganic Chemistry* **2019**, *58*, 6601-6608.
[138] M. L. Gallego, A. Guijarro, O. Castillo, T. Parella, R. Mas-Balleste, F. Zamora, *CrystEngComm* **2010**, *12*, 2332-2334.
[139] A. M. Manotti Lanfredi, F. Ugozzoli, A. Camus, N. Marsich, *Journal of Chemical Crystallography* **1995**, *25*, 37-41.
[140] E. Neofotistou, C. D. Malliakas, P. N. Trikalitis, *Inorganic Chemistry* **2007**, *46*, 8487-8489.
[141] W. Bauer, D. Döpp, H. Döpp, T. Eicher, C. Grundmann, B. Irmisch-Pielartzik, H. G. Korth, G. Krüger, K. Kühlein, R. Mayer, H. Pielartzik, S. Scheithauer, D. Schumann, G. Simchen, R. Sustmann*, Vol. 5*, 4th Edition ed. (Ed.: J. Falbe), Georg Thieme Verlag KG, Stuttgart, **1985**.
[142] J. Grote, F. Friedrich, K. Berthold, L. Hericks, B. Neumann, H.-G. Stammler, N. W. Mitzel, *Chemistry – A European Journal* **2018**, *24*, 2626-2633.
[143] J. Houben, *Berichte der deutschen chemischen Gesellschaft* **1906**, *39*, 3219-3233.
[144] J. Houben, H. Pohl, *Berichte der deutschen chemischen Gesellschaft* **1907**, *40*, 1303-1307.
[145] A. R. Paital, J. Zhan, R. Kim, J. Kampf, P. Collins, D. Coucouvanis, *Polyhedron* **2013**, *64*, 328-338.
[146] S. Scheithauer, (Ed.: R. Mayer), Thieme, Stuttgart :, **1979**.
[147] U. Mikloweit, R. Mattes, *Zeitschrift für anorganische und allgemeine Chemie* **1986**, *532*, 145-149.
[148] A. K. Cheetham, G. Kieslich, H. H. M. Yeung, *Accounts of Chemical Research* **2018**, *51*, 659-667.
[149] R. S. Forgan, *Chemical Science* **2020**, *11*, 4546-4562.

[150] S. Rizzato, M. Moret, M. Merlini, A. Albinati, F. Beghi, *CrystEngComm* **2016**, *18*, 2455-2462.
[151] T. Zheng, Z. Yang, D. Gui, Z. Liu, X. Wang, X. Dai, S. Liu, L. Zhang, Y. Gao, L. Chen, D. Sheng, Y. Wang, J. Diwu, J. Wang, R. Zhou, Z. Chai, T. E. Albrecht-Schmitt, S. Wang, *Nature Communications* **2017**, *8*, 15369.
[152] M. E. M. Abel Moreno, **2015**, 1277-1315.
[153] D. Zacher, O. Shekhah, C. Wöll, R. A. Fischer, *Chemical Society Reviews* **2009**, *38*, 1418-1429.
[154] B. Liu, R. A. Fischer, *Science China Chemistry* **2011**, *54*, 1851-1866.
[155] R. Makiura, S. Motoyama, Y. Umemura, H. Yamanaka, O. Sakata, H. Kitagawa, *Nature Materials* **2010**, *9*, 565-571.
[156] R. A. Fischer, C. Wöll, *Angewandte Chemie International Edition* **2009**, *48*, 6205-6208.
[157] O. Shekhah, in *Materials, Vol. 3*, **2010**, pp. 1302-1315.
[158] O. Shekhah, J. Liu, R. A. Fischer, C. Wöll, *Chemical Society Reviews* **2011**, *40*, 1081-1106.
[159] M. Aust, A. J. Herold, L. Niederegger, C. Schneider, D. C. Mayer, M. Drees, J. Warnan, A. Pöthig, R. A. Fischer, *Inorganic Chemistry* **2021**, *60*, 19242-19252.
[160] M. Aust, M. I. Schönherr, D. P. Halter, L. Schröck, T. Pickl, S. N. Deger, M. Z. Hussain, A. Jentys, R. Bühler, Z. Zhang, K. Meyer, M. Kuhl, J. Eichhorn, D. D. Medina, A. Pöthig, R. A. Fischer, *Inorganic Chemistry* **2024**, *63*, 129-140.

6. SUPPORTING INFORMATION

6.1 Supporting Information Manuscript I

Supplementary Information

Introducing Benzene-1,3,5-tri(dithiocarboxylate) as a Multidentate Linker in Coordination Chemistry

Margit Aust[a], Anna J. Herold[a], Lukas Niederegger[b], Christian Schneider[a], David C. Mayer[a], Markus Drees[a], Julien Warnan[a], Alexander Pöthig[a]*, Roland A. Fischer[a]**

[a]Chair of Inorganic and Metal-Organic Chemistry, Department of Chemistry & Catalysis Research Center, Technical University of Munich, Lichtenbergstraße 4, 85748 Garching, Germany

[b]Assistant Professorship of Bioinorganic Chemistry, Catalysis Research Center, Technical University of Munich, Ernst-Otto-Fischer Straße 1, 85748 Garching, Germany

*E-mail: roland.fischer@tum.de (R.A.F.), alexander.poethig@tum.de (A.P.), julien.warnan@tum.de (J.W.)

Table of Content

NMR spectroscopic data

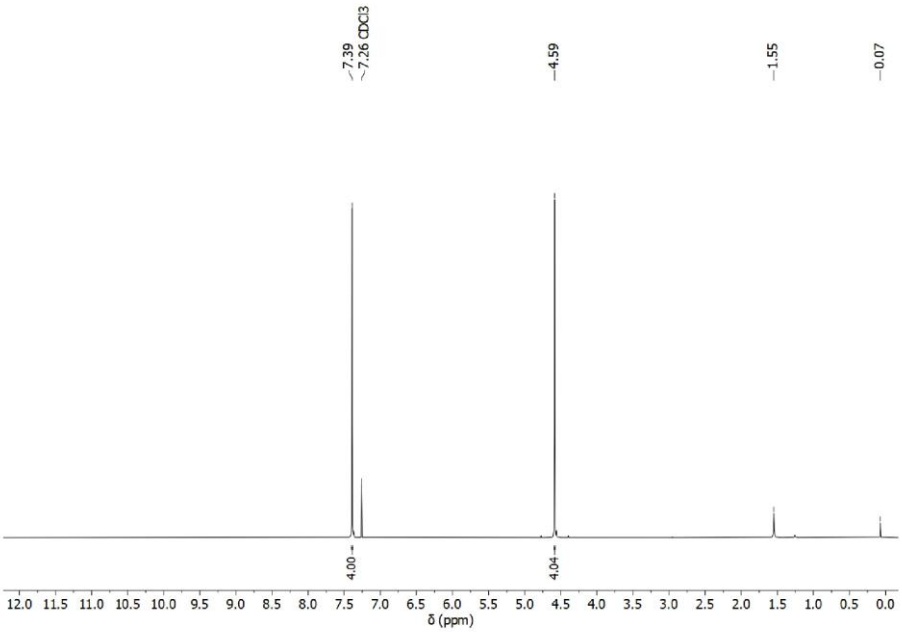

Figure S 1: ^{1}H NMR spectrum of 1,4-di(chloromethyl)benzene (400 MHz, $CDCl_3$, 298 K).

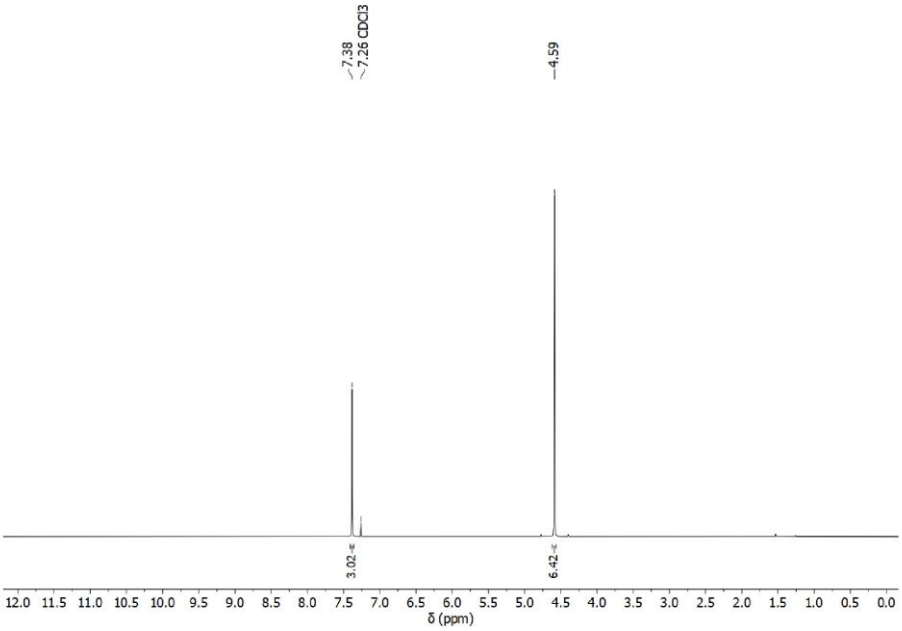

Figure S 2: ^{1}H NMR spectrum of 1,3,5-tri(chloromethyl)benzene (400 MHz, $CDCl_3$, 298 K).

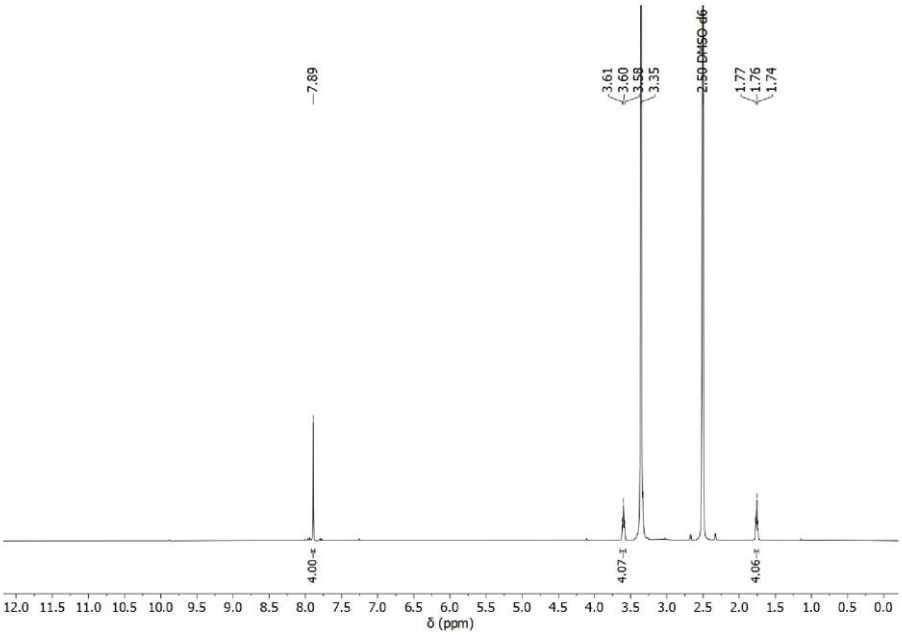

Figure S 3: ^{1}H NMR spectrum of Na_2BDDTC (**1**) (400 MHz, DMSO-d_6, 298 K).

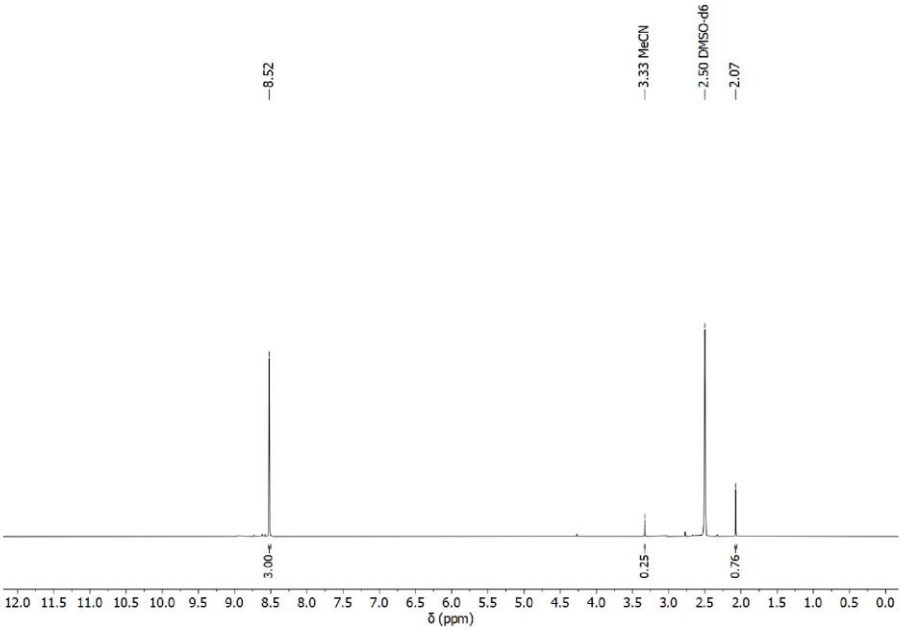

Figure S 4: ^{1}H NMR spectrum of Na_3BTDTC (**2**) (400 MHz, DMSO-d_6, 298 K).

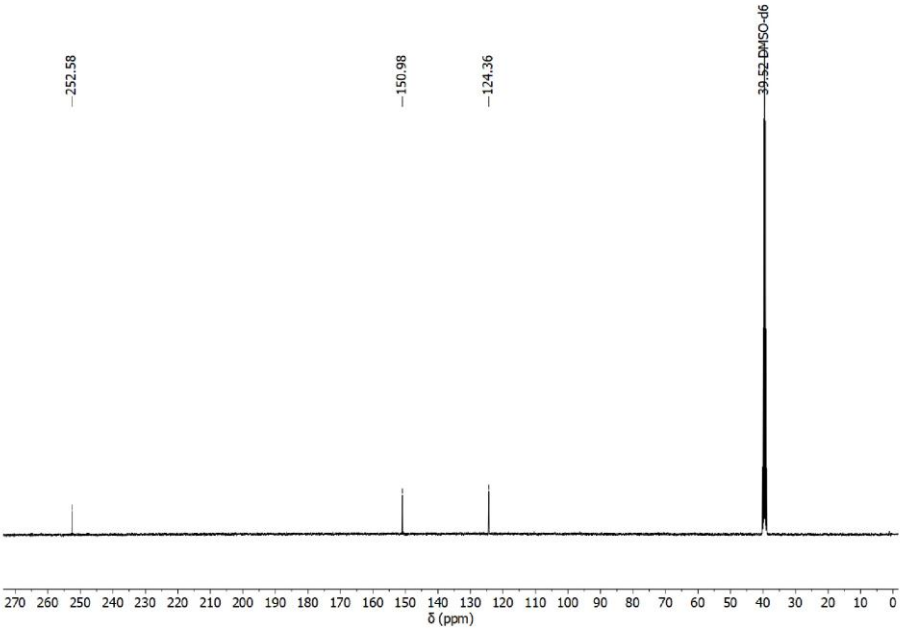

Figure S 5: ^{13}C NMR spectrum of Na_3BTDTC (**2**) (100 MHz, DMSO-d_6, 298 K).

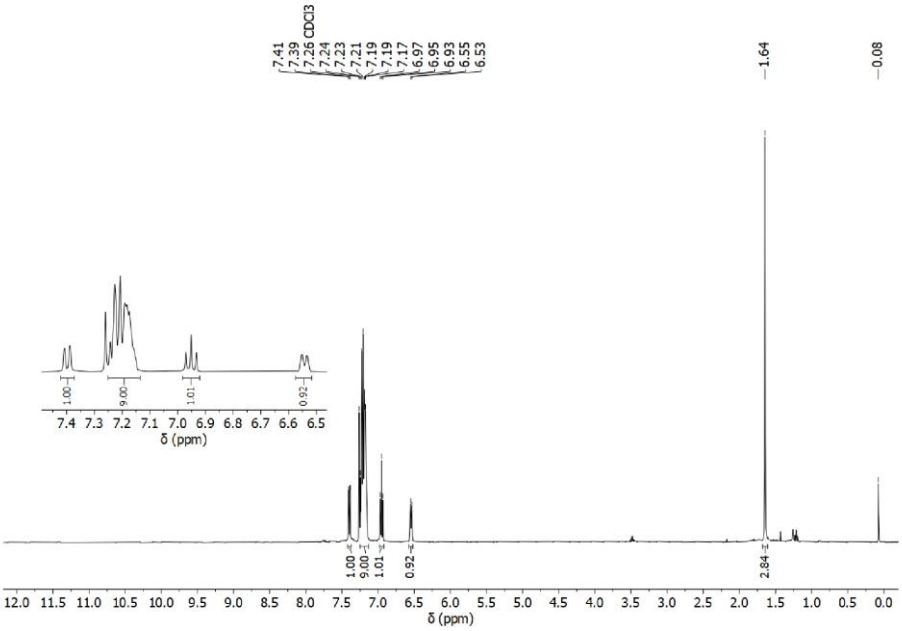

Figure S 6: ^{1}H NMR spectrum of Xantphos (400 MHz, $CDCl_3$, 298 K).

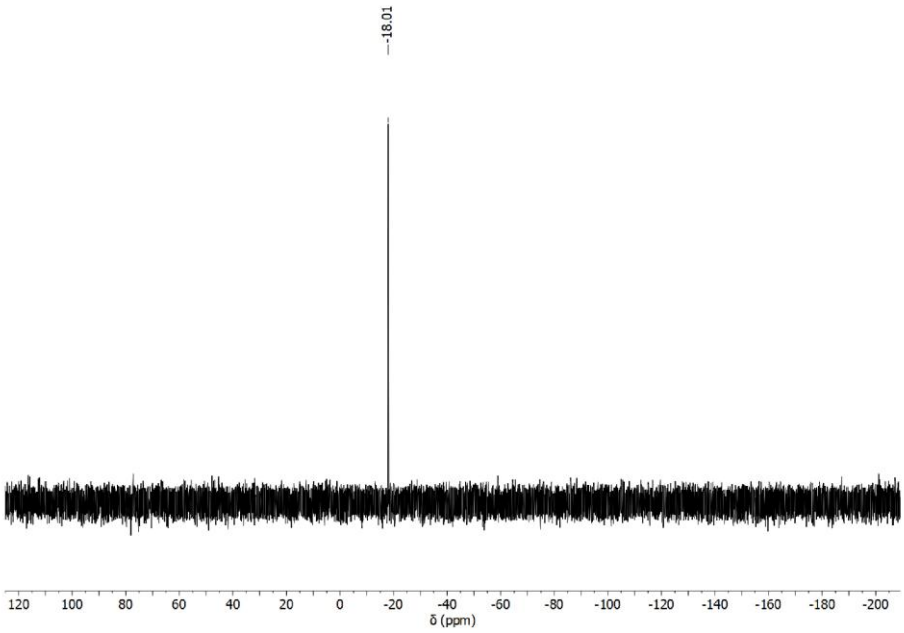

Figure S 7: ^{31}P NMR spectrum of Xantphos (160 MHz, $CDCl_3$, 298 K).

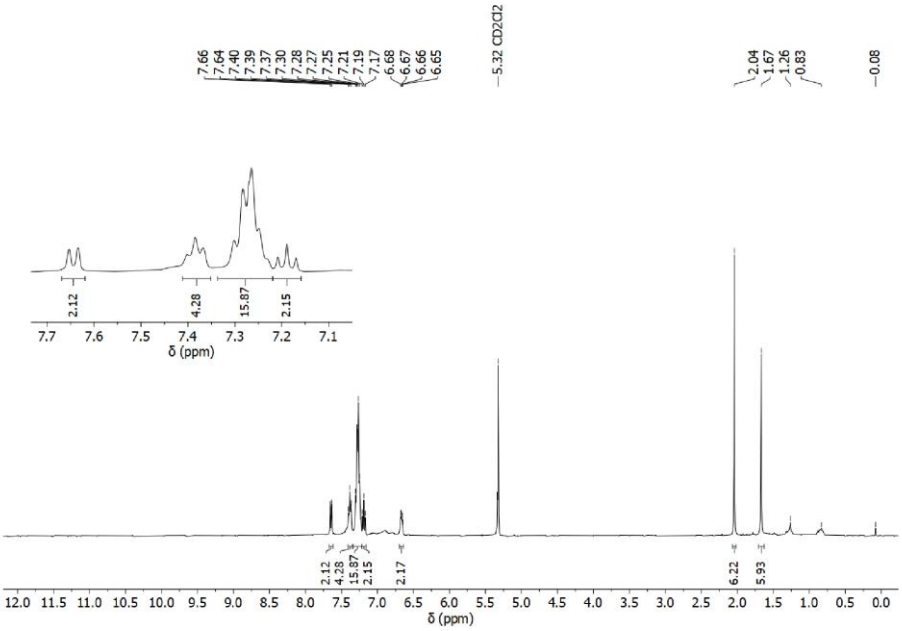

Figure S 8: ^{1}H NMR spectrum of [Cu(Xantphos)(MeCN)$_2$][PF$_6$] (**3**) (400 MHz, CD_2Cl_2, 298 K).

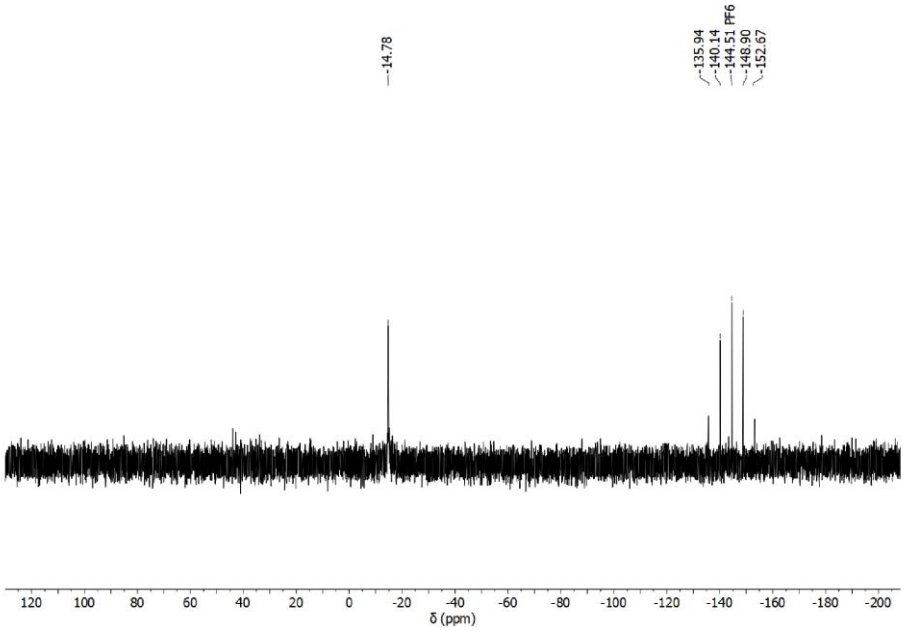

Figure S 9: ^{31}P NMR spectrum of $[Cu(Xantphos)(MeCN)_2][PF_6]$ (**3**) (160 MHz, CD_2Cl_2, 298 K).

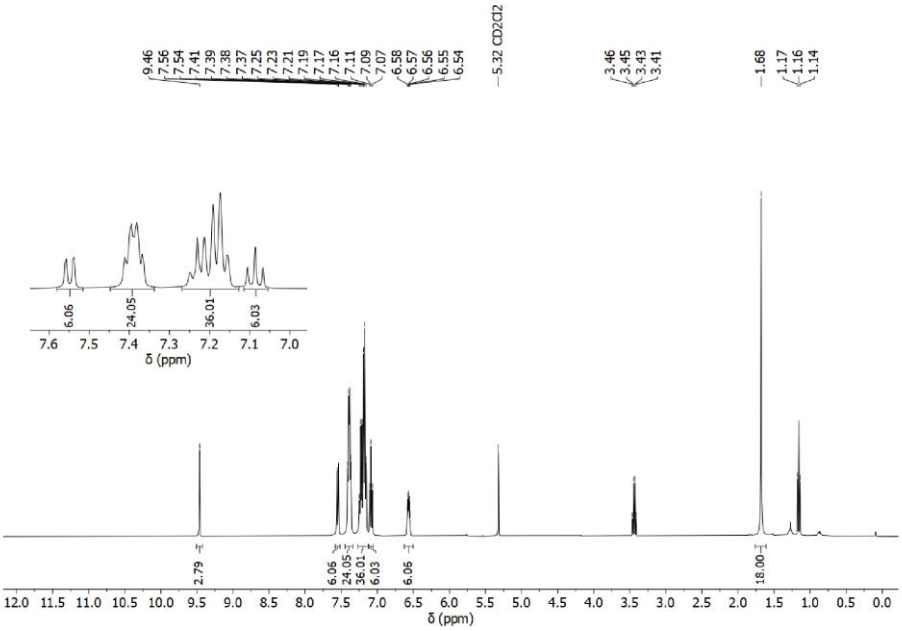

Figure S 10: ^{1}H NMR spectrum of [Cu(Xantphos)]$_3$(BTDTC) (**4**) (400 MHz, CD_2Cl_2, 298 K).

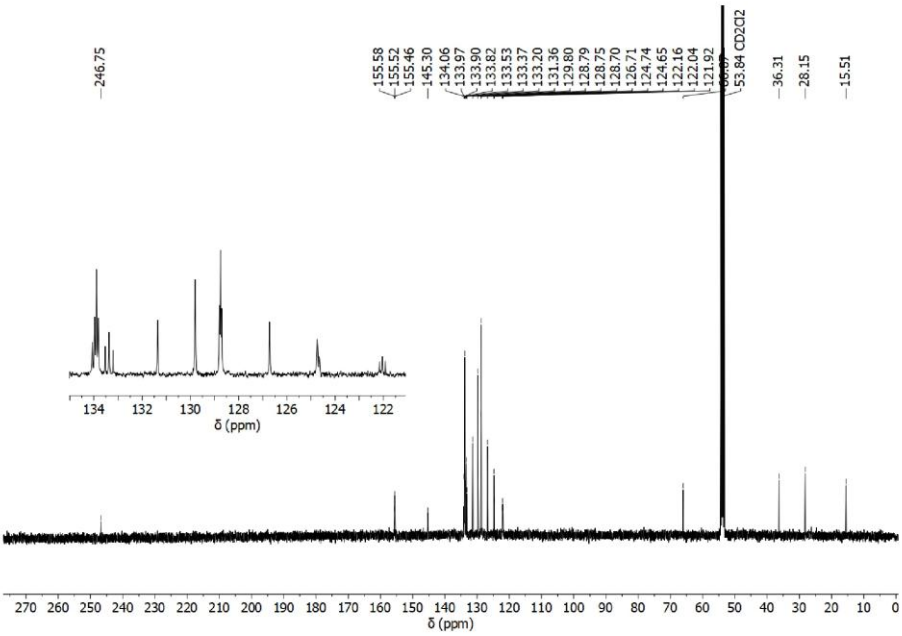

Figure S 11: ^{13}C NMR spectrum of $[Cu(Xantphos)]_3(BTDTC)$ (**4**) (100 MHz, CD_2Cl_2, 298 K).

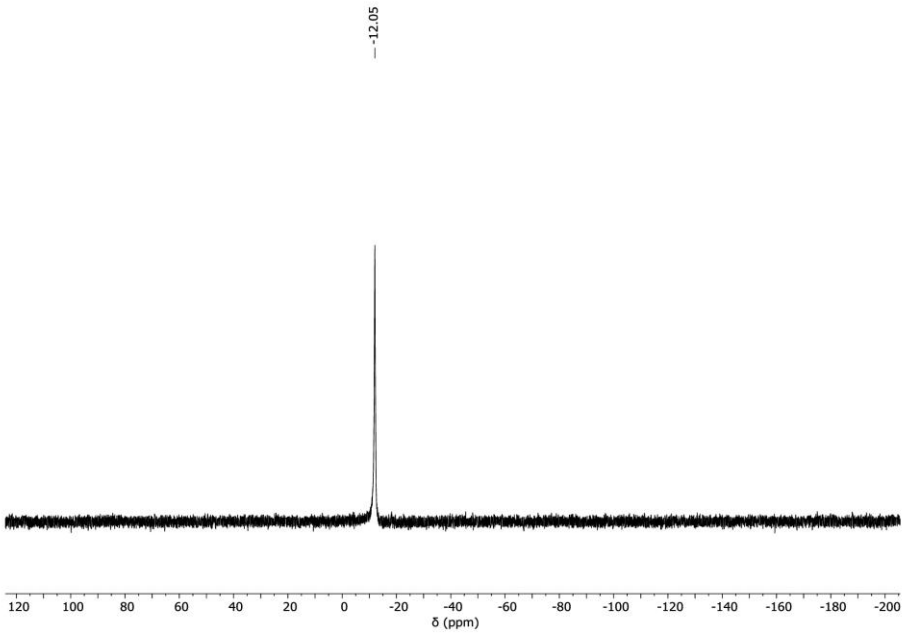

Figure S 12: ^{31}P NMR spectrum of $[Cu(Xantphos)]_3(BTDTC)$ (**4**) (160 MHz, CD_2Cl_2, 298 K).

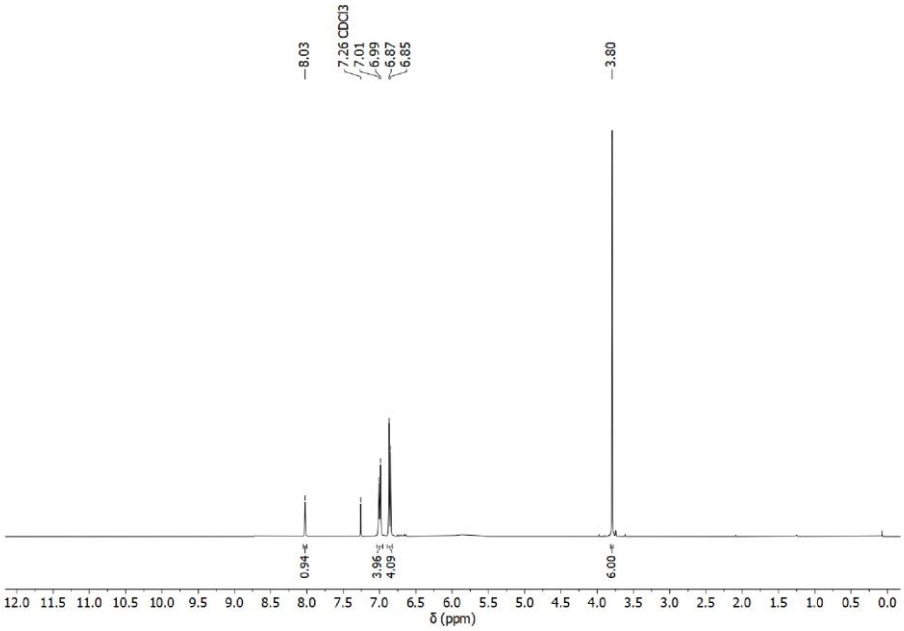

Figure S 13: ^{1}H NMR spectrum of N,N'-di-p-anisylformamidine (DAniF) (400 MHz, $CDCl_3$, 298 K).

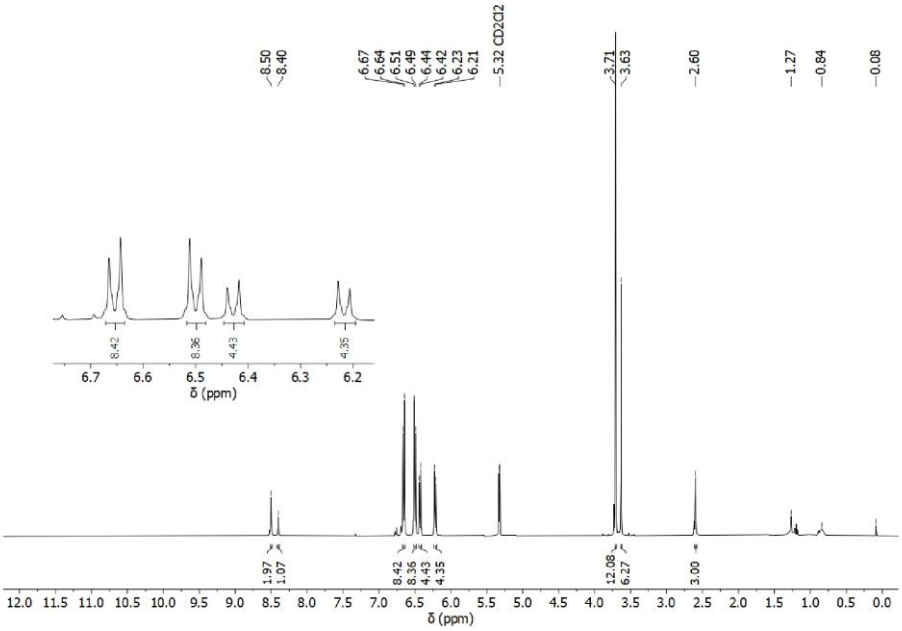

Figure S 14: ^{1}H NMR spectrum of $Mo_2(DAniF)_3(OAc)$ (**5**) (400 MHz, CD_2Cl_2, 298 K).

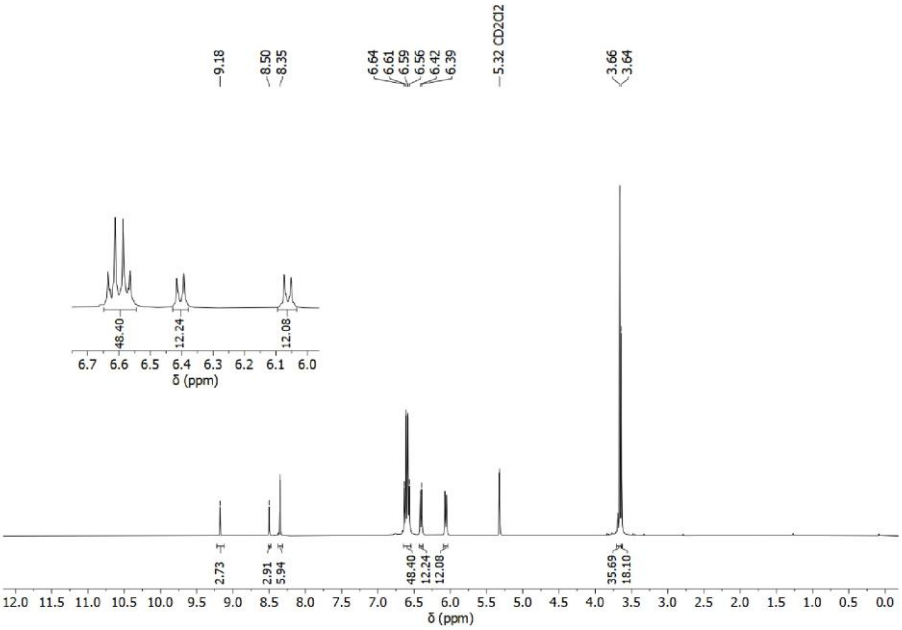

Figure S 15: ^{1}H NMR spectrum of $[Mo_2(DAniF)_3]_3(BTDTC)$ (**6**) (400 MHz, CD_2Cl_2, 298 K).

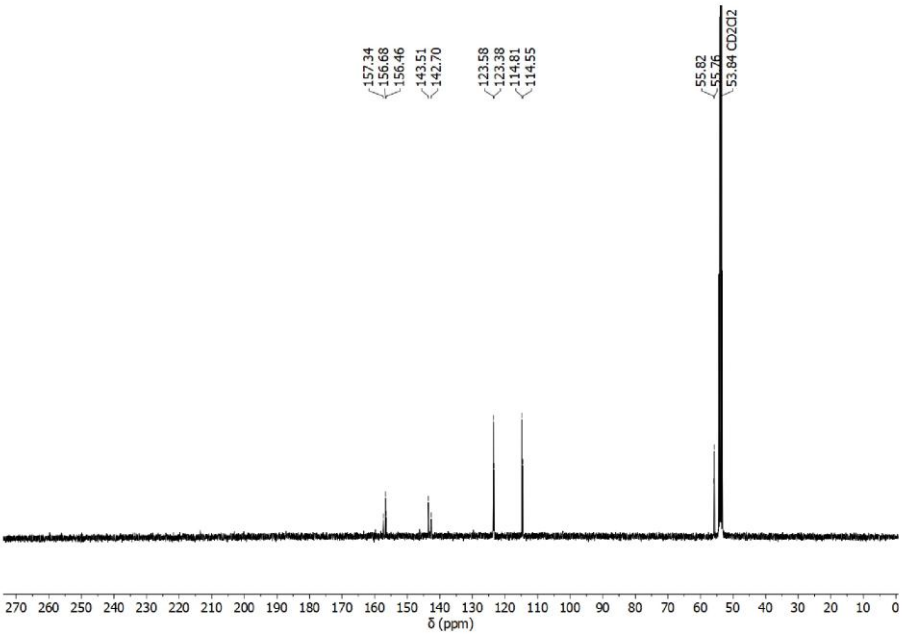

Figure S 16: ^{13}C NMR spectrum of $[Mo_2(DAniF)_3]_3(BTDTC)$ (**6**) (100 MHz, CD_2Cl_2, 298 K).

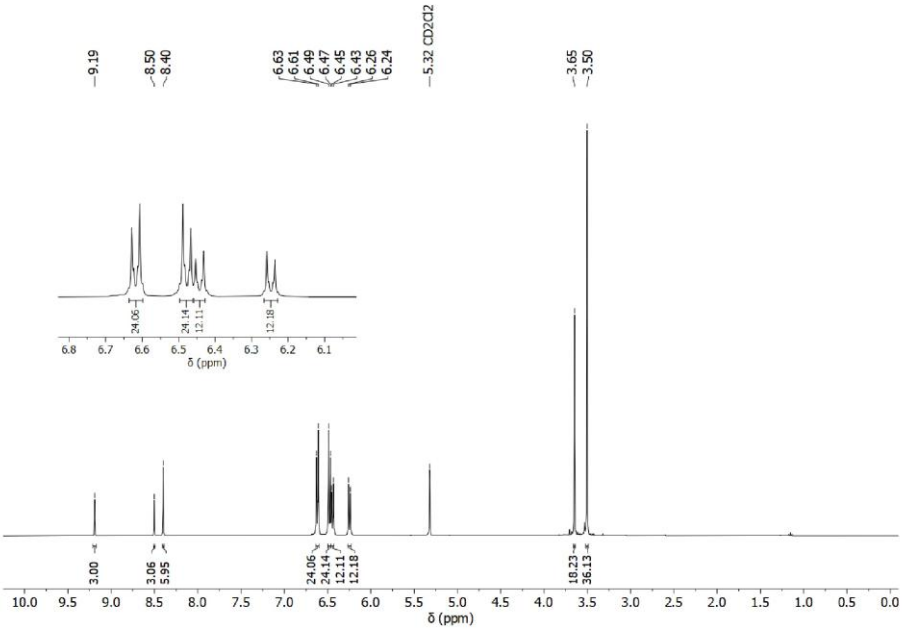

Figure S 17: ^{1}H NMR spectrum of $[Mo_2(DAniF)_3]_3(BTC)$ (**7**) (400 MHz, CD_2Cl_2, 298 K).

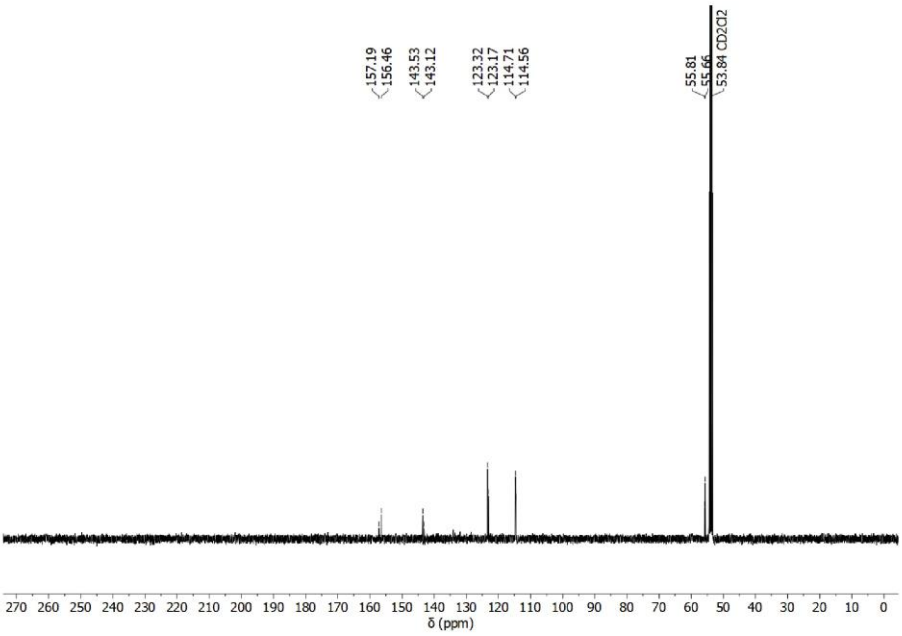

Figure S 18: ^{13}C NMR spectrum of $[Mo_2(DAniF)_3]_3(BTC)$ (7) (100 MHz, CD_2Cl_2, 298 K).

High resolution mass spectra

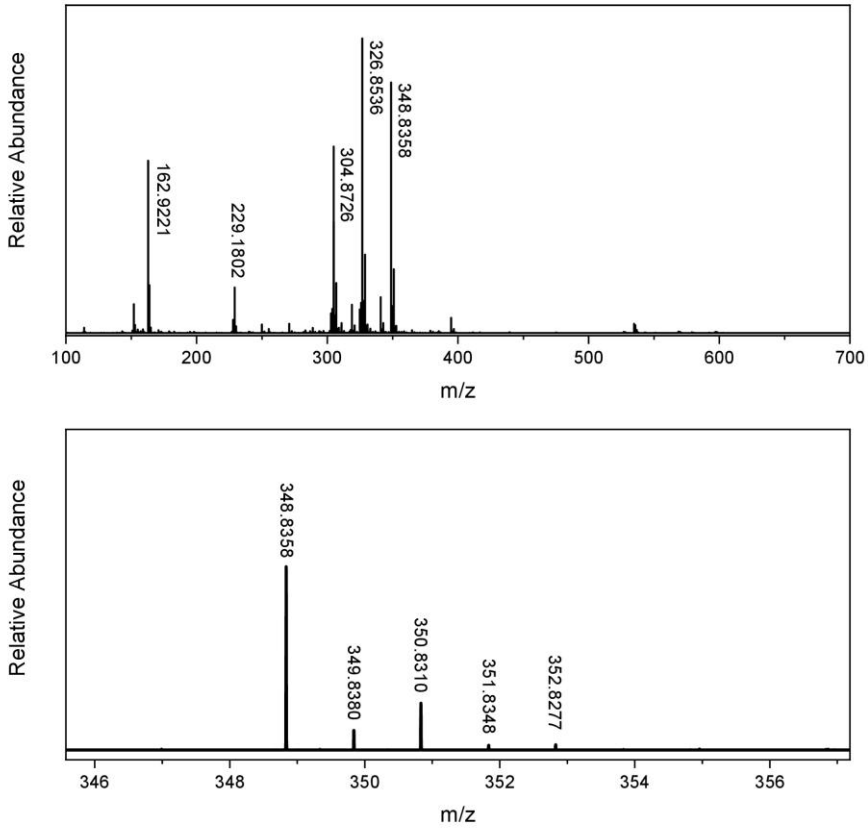

Figure S 19: Full ESI-MS of Na_3BTDTC (**2**) in the negative ionization mode (top) and isotopic pattern of Na_2BTDTC^- (bottom).

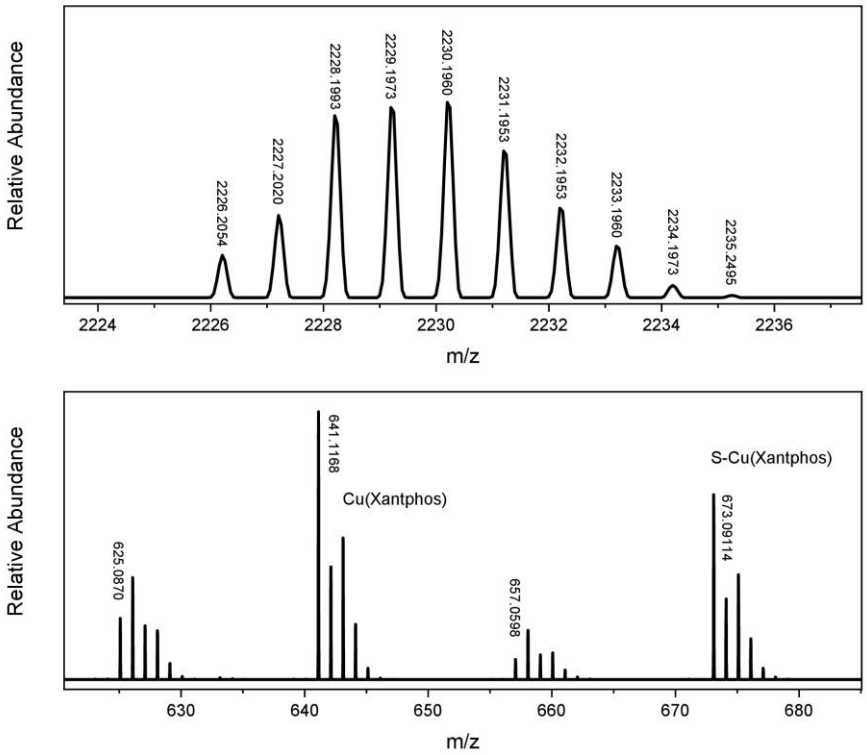

Figure S 20: Isotopic pattern of $[Cu(Xantphos)]_3(BTDTC)$ (**4**) (top) and related fragmentation products Cu(Xantphos) and S-Cu(Xantphos) (bottom). M/z values of 625 and 657 correspond to Cu(Xantphos) and S-Cu(Xantphos) after release of the oxygen atom.

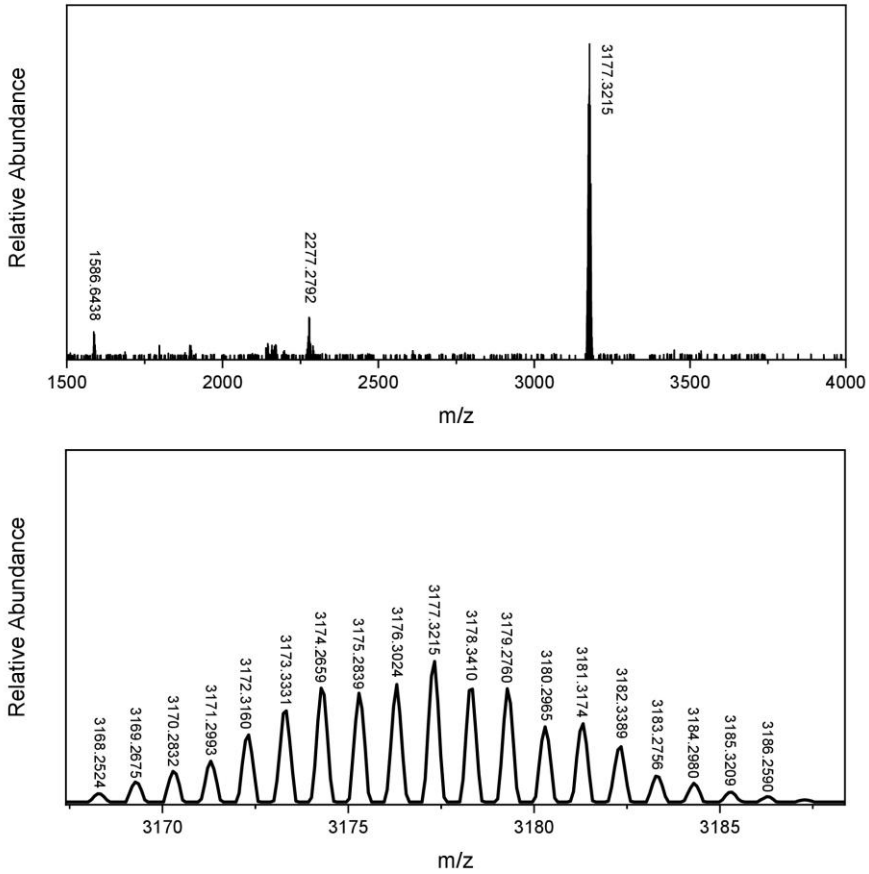

Figure S 21: Full LIFDI-MS of $[Mo_2(DAniF)_3]_3(BTDTC)$ (**6**) in the positive ionization mode (top) and isotopic pattern (bottom).

FT-IR spectra

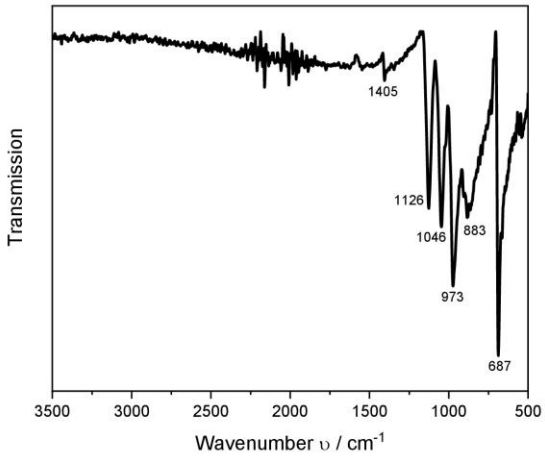

Figure S 22: FT-IR spectra of Na_3BTDTC (**2**).

Thermogravimetric analysis

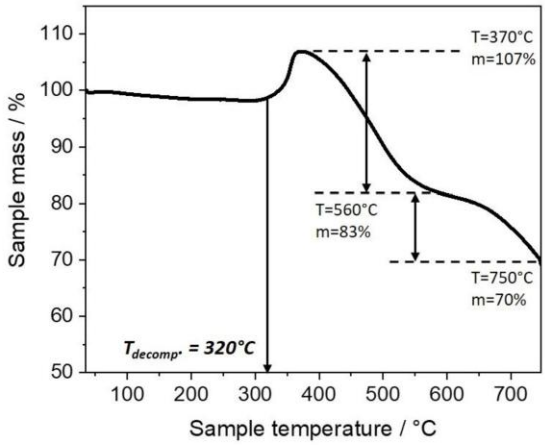

Figure S 23: TGA curve of $Na_3BTDTC \cdot 0.25MeCN$ (**2**) under synthetic air in the range between 35°C and 750°C with a heating rate of 10°C/min.

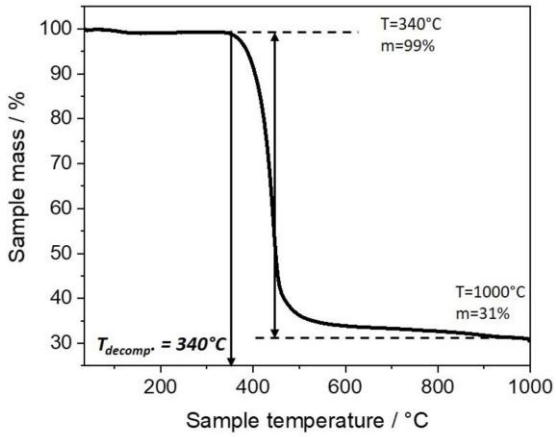

Figure S 24: TGA curve of $[Cu(Xantphos)]_3(BTDTC)$ (**4**) under N_2 atmosphere in the range between 35°C and 1000°C with a heating rate of 10°C/min.

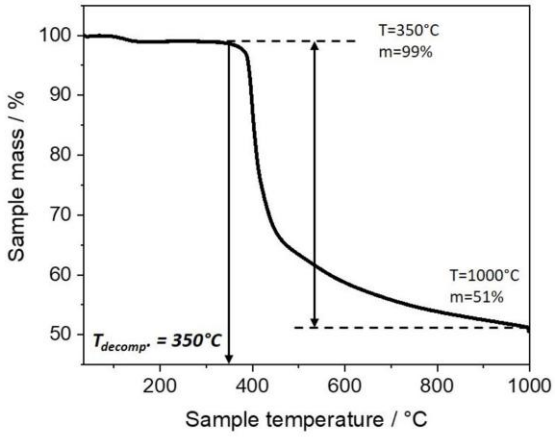

Figure S 25: TGA curve of $[Mo_2(DAniF)_3]_3(BTDTC)$ (**6**) under N_2 atmosphere in the range between 35°C and 1000°C with a heating rate of 10°C/min.

UV/VIS absorption spectra

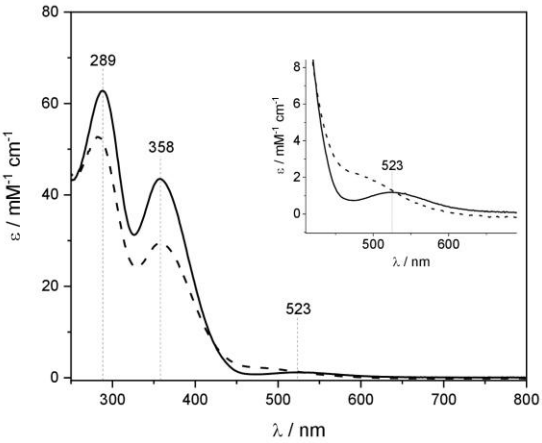

Figure S 26: Electronic absorption spectrum of **2** in MeCN solution under inert conditions (plain line) and after exposure to air for 10 h (dashed line) at room temperature.

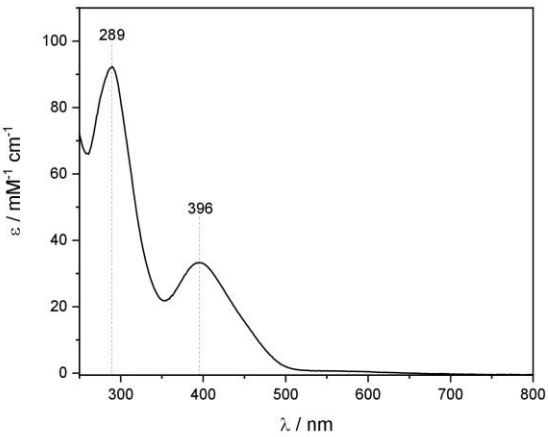

Figure S 27: Electronic absorption spectrum of **4** in CH_2Cl_2 solution at room temperature.

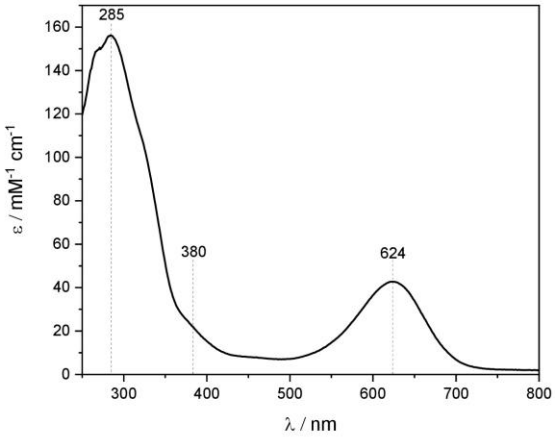

Figure S 28: Electronic absorption spectrum of **6** in CH_2Cl_2 solution at room temperature.

Structural analysis data

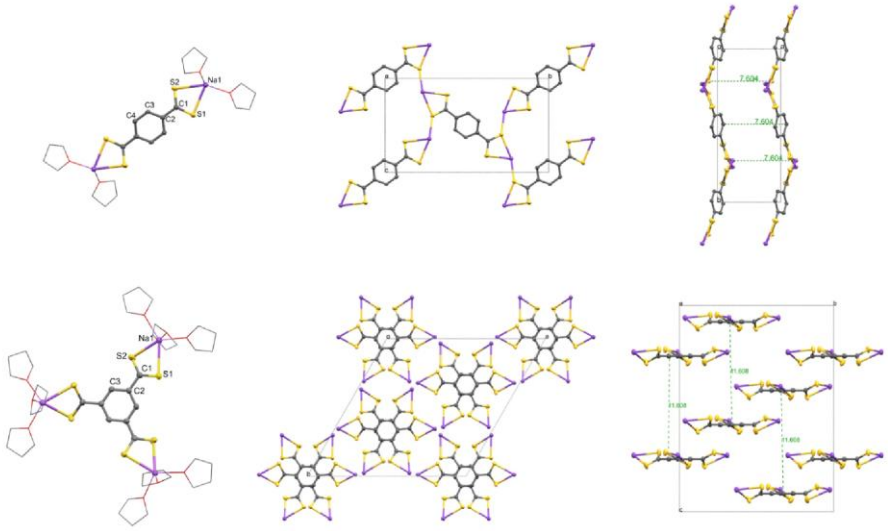

Figure S 29: Molecular structure and extended unit of $Na_2BDDTC \cdot 4$ THF (top) and $Na_3BTDTC \cdot 9$ THF (bottom) in the solid determined by SC-XRD. Ellipsoids are shown at the 50% probability level. Hydrogen atoms and THF molecules are omitted or depicted as wireframes for clarity. Color code: C (grey), S (yellow), O (red), Na (purple).

Table S 1: Selected angles and bond distances of dithiocarboxylate ligands and derived complexes as determined from SC-XRD analysis.

	Na_2BDDTC	Na_3BTDTC	$[Cu(Xantphos)]_3(BTDTC)$	$[Mo_2(DAniF)_3]_3(BTDTC)$
Crystal color	Red	red	yellow	dark blue
Space group	$P2_1/c$	R3c	P1	$P2_1/c$
a (Å)	7.6045(14)	20.0408(10)	17.802(3)	14.6685(13)
b (Å)	17.946(3)	20.0408(10)	17.846(3)	39.059(4)
c (Å)	10.5244(18)	23.2063(10)	19.891(4)	24.918(2)
α (°)	90	90	91.373(6)	90
β (°)	102.499(8)	90	92.037(6)	91.280(3)
γ (°)	90	120	106.493(6)	90
S1–C1–S2 (°)	122.80	123.42(19)	-	-
S1–Na–S2 (°)	61.64	63.00(4)	-	-
S1–C1 (Å)	1.688(3)	1.691(3)	-	-
S2–C1 (Å)	1.683(3)	1.689(3)	-	-
S1–C7 (Å)	-	-	1.689(7)	1.698(5)
S2–C7 (Å)	-	-	1.697(6)	1.704(5)
S3–C8 (Å)	-	-	1.699(7)	1.701(4)
S4–C8 (Å)	-	-	1.686(7)	1.685(5)
S5–C9 (Å)	-	-	1.700(7)	1.702(5)
S6–C9 (Å)	-	-	1.674(7)	1.683(5)
S7–C207 (Å)	-	-	1.681(5)	-
S8–C207 (Å)	-	-	1.696(5)	-
S9–C209 (Å)	-	-	1.693(5)	-
S10–C209 (Å)	-	-	1.694(6)	-

Na1–S1 (Å)	2.8488(14)	2.8793(15)	-	-
Na1–S2 (Å)	2.9327(15)	2.8153(16)	-	-
Cu1–S1 (Å)	-	-	2.337(2)	-
Cu1–S2 (Å)	-	-	2.3898(18)	-
Cu2–S3 (Å)	-	-	2.4022(17)	-
Cu2–S4 (Å)	-	-	2.3728(17)	-
Cu3–S5 (Å)	-	-	2.413(2)	-
Cu3–S6 (Å)	-	-	2.3729(18)	-
Cu4–S7 (Å)	-	-	2.411(16)	-
Cu4–S8 (Å)	-	-	2.3694(16)	-
Cu5–S9 (Å)	-	-	2.3741(16)	-
Cu5–S10 (Å)	-	-	2.4073(16)	-
Cu6–S11 (Å)	-	-	2.4004(15)	-
Cu6–S12 (Å)	-	-	2.3751(16)	-
Mo1–S1 (Å)	-	-	-	2.4734(12)
Mo2–S2 (Å)	-	-	-	2.4200(12)
Mo3–S3 (Å)	-	-	-	2.4271(12)
Mo4–S4 (Å)	-	-	-	2.4435(12)
Mo5–S5 (Å)	-	-	-	2.4481(12)
Mo6–S6 (Å)	-	-	-	2.4459(12)

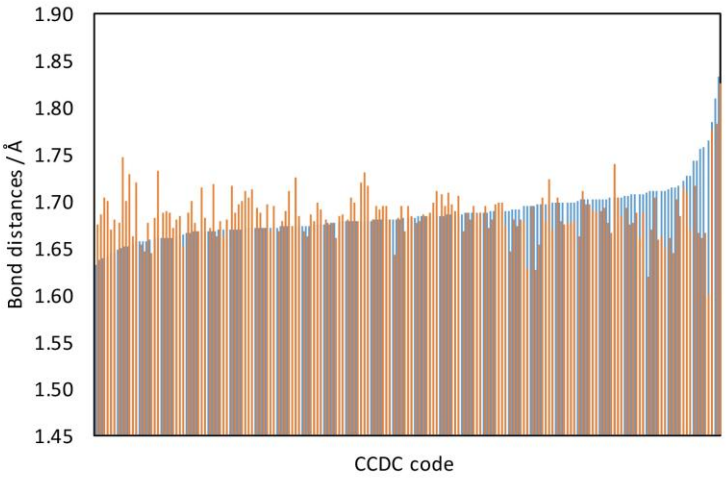

Figure S 30: Overview of observed C–S bond distances for dithiocarboxylate compounds listed in the Cambridge Crystallographic Data Centre (CCDC). C–S1 (orange) and C–S2 (blue) bond distances of each CCDC entry are plotted against the respective CCDC number.

Computational data

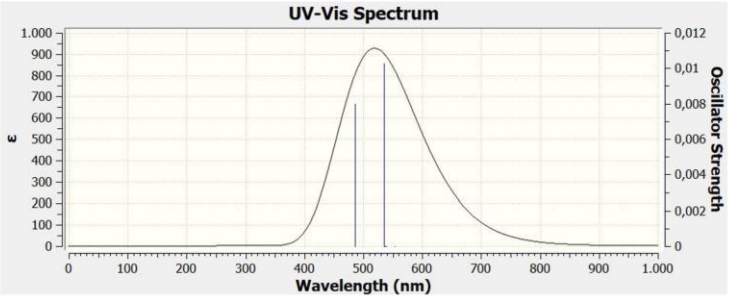

Figure S 31: Simulated UV/VIS absorption spectrum of Na_3BTDTC (**2**) obtained from time-dependent DFT calculations at the O3LYP/6-31G*-aug-cc-pVDZ level of theory.

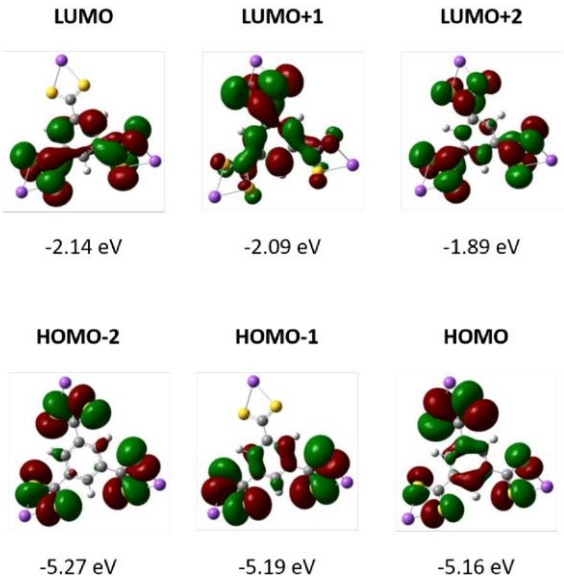

Figure S 32: Computed Kohn-Sham orbitals of the sodium salt Na_3BTDTC (**2**) with an isocontour value of 0.02 at the O3LYP/6-31G*-aug-cc-pVDZ level of theory, including PCM solvent calculations for acetonitrile.

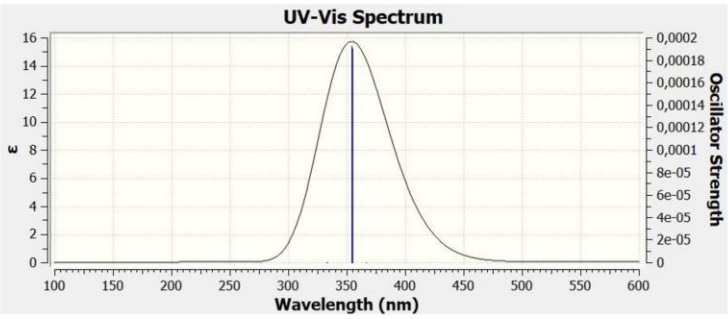

Figure S 33: Simulated UV/VIS absorption spectrum of Na_3BTC obtained from time-dependent DFT calculations at the O3LYP/6-31G*-aug-cc-pVDZ level of theory.

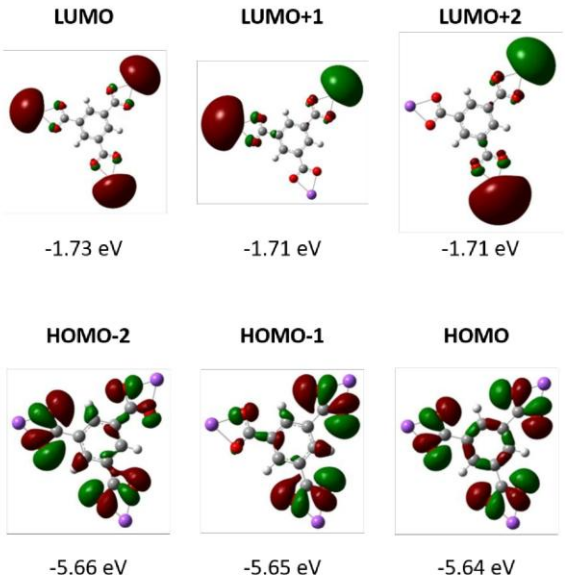

Figure S 34: Computed Kohn-Sham orbitals of the sodium salt Na_3BTC with an isocontour value of 0.02 at the O3LYP/6-31G*-aug-cc-pVDZ level of theory, including PCM solvent calculations for acetonitrile.

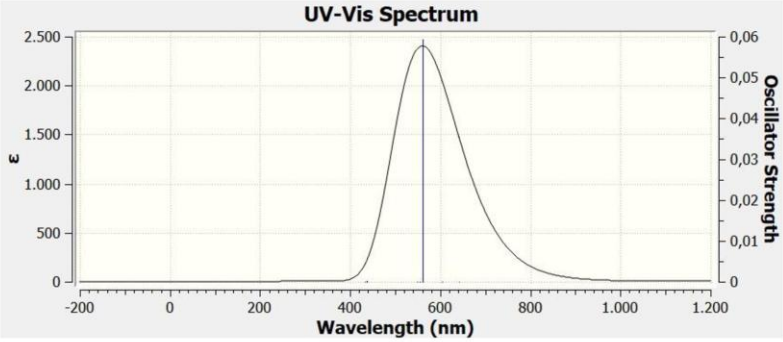

Figure S 35: Simulated UV/VIS absorption spectrum of Na_2BDDTC (**1**) obtained from time-dependent DFT calculations at the O3LYP/6-31G*-aug-cc-pVDZ level of theory.

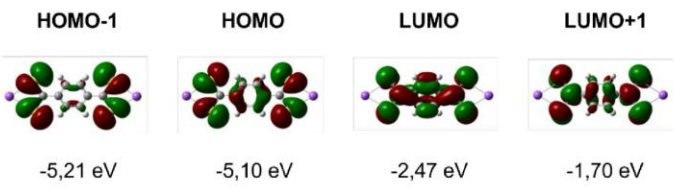

Figure S 36: Computed Kohn-Sham orbitals of the sodium salt Na_2BDDTC (**1**) with an isocontour value of 0.02 at the O3LYP/6-31G*-aug-cc-pVDZ level of theory, including PCM solvent calculations for acetonitrile.

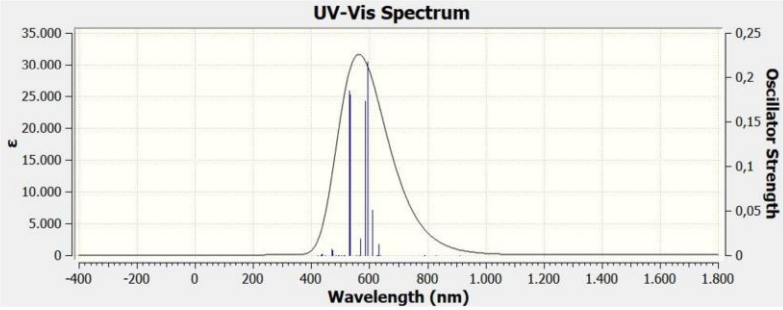

Figure S 37: Simulated UV/VIS absorption spectrum of $[Mo_2(DAniF)_3]_3(BTDTC)$ (**6**) obtained from time-dependent DFT calculations at the O3LYP/6-31G*-aug-cc-pVDZ level of theory for C,H and N and SDD ECP for Mo.

Coordinates and absolute energy of the calculated complexes:

Na_2BDC

Center Number	Atomic Number	Atomic Type	Coordinates (Angstroms) X	Y	Z
1	6	0	1.203876	0.696876	0.000184
2	6	0	1.203876	-0.696876	0.000184
3	6	0	0.000000	-1.418020	0.000188
4	6	0	-1.203876	-0.696876	0.000184
5	6	0	-1.203876	0.696876	0.000184
6	6	0	0.000000	1.418020	0.000188
7	1	0	2.143329	1.240422	0.000088
8	1	0	2.143329	-1.240422	0.000088
9	1	0	-2.143329	-1.240422	0.000088
10	1	0	-2.143329	1.240422	0.000088
11	6	0	0.000000	2.939946	0.000043
12	6	0	0.000000	-2.939946	0.000043
13	8	0	-1.119317	3.533901	-0.000012
14	8	0	1.119317	3.533901	-0.000012
15	8	0	1.119317	-3.533901	-0.000012
16	8	0	-1.119317	-3.533901	-0.000012
17	11	0	0.000000	5.642216	-0.000326
18	11	0	0.000000	-5.642216	-0.000326

HF=-932. 8018946

Na_2BDDTC

Center Number	Atomic Number	Atomic Type	Coordinates (Angstroms) X	Y	Z
1	6	0	0.695210	-1.008254	-0.609336
2	6	0	-0.695259	-1.008232	-0.609307
3	6	0	-1.423056	0.009865	0.034940
4	6	0	-0.695406	1.028315	0.678879
5	6	0	0.695443	1.028283	0.678884
6	6	0	1.423026	0.009819	0.034902
7	1	0	1.231358	-1.797076	-1.127095
8	1	0	-1.231436	-1.797028	-1.127068
9	1	0	-1.231528	1.817451	1.196374
10	1	0	1.231610	1.817410	1.196353
11	6	0	2.916543	0.007633	0.031884
12	6	0	-2.916605	0.007710	0.031959
13	16	0	3.723134	1.491382	-0.226835
14	16	0	3.716451	-1.480825	0.284337
15	16	0	-3.716482	-1.480786	0.284291
16	16	0	-3.723166	1.491511	-0.226592
17	11	0	-6.196160	-0.037907	-0.164579
18	11	0	6.196308	-0.037741	-0.164384

HF=-2224.661332

Na_3BTC

Center Number	Atomic Number	Atomic Type	Coordinates (Angstroms) X	Y	Z
1	6	0	-1.373173	0.307002	0.000038
2	6	0	-0.944411	-1.026473	0.000083
3	6	0	0.420363	-1.341848	0.000137
4	6	0	1.360786	-0.303732	0.000179
5	6	0	0.951539	1.035860	0.000104
6	6	0	-0.417721	1.331324	0.000019
7	1	0	-1.677530	-1.823656	0.000067
8	1	0	2.417752	-0.539935	0.000250
9	1	0	-0.741794	2.364774	-0.000075
10	6	0	-2.849292	0.636396	-0.000021
11	8	0	-3.682011	-0.325591	0.000210
12	8	0	-3.194261	1.861064	-0.000242
13	6	0	0.873009	-2.784928	0.000099
14	8	0	-0.015038	-3.696084	-0.000225
15	8	0	2.122481	-3.025056	0.000358
16	6	0	1.975460	2.148920	0.000065
17	8	0	1.559695	3.351376	-0.000204
18	8	0	3.208311	1.834371	0.000314
19	11	0	-5.298144	1.182207	0.000004
20	11	0	3.675163	3.994264	-0.000225
21	11	0	1.625600	-5.178014	-0.000338

HF=-1282.9936364

Na_3BTDTC

Center Number	Atomic Number	Atomic Type	Coordinates (Angstroms) X	Y	Z
1	6	0	-0.319220	1.376193	0.003181
2	6	0	-1.335089	0.407148	-0.001649
3	6	0	-1.030054	-0.962209	0.041492
4	6	0	0.315712	-1.357320	0.000063
5	6	0	1.349330	-0.409021	-0.039669
6	6	0	1.019913	0.954711	0.007274
7	1	0	-2.371281	0.721628	-0.007014
8	1	0	0.561338	-2.411885	-0.001548
9	1	0	1.811248	1.693962	0.014295
10	6	0	-0.658998	2.833696	0.003248
11	6	0	-2.118375	-1.984775	0.124408
12	6	0	2.776543	-0.847616	-0.125032
13	11	0	-1.324571	5.726932	-0.010373
14	11	0	5.609796	-1.716446	-0.309947
15	11	0	-4.282238	-4.008910	0.307447
16	16	0	-3.562681	-1.680182	-0.743874
17	16	0	-1.823820	-3.371587	1.087386
18	16	0	-2.026767	3.327348	-0.902591
19	16	0	0.349489	3.882154	0.907680
20	16	0	3.939694	0.052811	0.752178
21	16	0	3.122039	-2.215911	-1.097281

HF=-3220.7852649

$[Mo_2(DAniF)_3]_3(BTDTC)$

Center Number	Atomic Number	Atomic Type	Coordinates (Angstroms) X	Y	Z
1	6	0	1.384337	0.155782	0.031955
2	6	0	0.836562	-1.138180	0.021631
3	6	0	-0.561172	-1.280131	-0.002375
4	6	0	-1.407811	-0.158842	-0.025873
5	6	0	-0.831614	1.122844	-0.035486
6	6	0	0.562604	1.295249	-0.001631
7	1	0	2.460627	0.277028	0.037514
8	1	0	-1.474533	1.994469	-0.039519
9	6	0	1.157083	2.656091	-0.000095
10	1	0	-0.994226	-2.272848	-0.002484
11	6	0	1.718353	-2.333365	0.022354
12	6	0	-2.883599	-0.325690	-0.025092
13	42	0	-6.226443	0.190963	-0.608318
14	42	0	-6.028205	-1.566832	0.572885
15	42	0	4.369932	-4.431509	0.611426
16	42	0	2.950601	-5.481342	-0.574974
17	42	0	3.266716	5.293401	0.608430
18	42	0	1.668839	5.994483	-0.608049
19	7	0	0.494924	6.532907	1.105554
20	1	0	-0.442361	6.918787	1.119409
21	7	0	2.214341	5.782561	2.413789
22	1	0	2.514319	5.626801	3.369478
23	7	0	4.457389	4.791765	-1.104559
24	1	0	5.375645	4.362572	-1.118108
25	7	0	2.741804	5.549977	-2.413231
26	1	0	2.424347	5.665142	-3.369031
27	7	0	2.470769	7.987189	-0.654839
28	1	0	2.089043	8.799099	-1.126370
29	7	0	4.191074	7.232599	0.653154
30	1	0	5.047342	7.501487	1.124077
31	6	0	3.599446	8.221408	-0.001244
32	1	0	4.040098	9.224996	-0.001815
33	6	0	1.003403	6.311885	2.309760
34	1	0	0.425081	6.553344	3.208384
35	6	0	3.950767	5.016266	-2.308880
36	1	0	4.519912	4.753374	-3.207348
37	7	0	5.392574	-3.691934	-1.123975
38	7	0	3.870156	-4.825481	-2.400121
39	7	0	4.175482	-7.245680	-0.624224
40	7	0	1.950607	-6.251354	1.159953
41	7	0	5.704028	-6.115027	0.650437
42	7	0	3.479457	-5.126591	2.436076
43	6	0	4.931179	-4.034933	-2.318586
44	1	0	5.414407	-3.660401	-3.227730
45	6	0	5.337756	-7.216747	0.011657
46	1	0	5.990784	-8.097022	0.009350
47	6	0	2.414517	-5.911894	2.354536
48	1	0	1.916868	-6.266912	3.263690
49	1	0	3.751026	-4.899481	3.385957

50	1	0	1.121957	-6.834390	1.191208
51	1	0	6.605773	-6.181953	1.108293
52	1	0	3.976924	-8.126516	-1.084618
53	1	0	3.572695	-5.017813	-3.349919
54	1	0	6.191741	-3.069076	-1.155099
55	7	0	-8.154371	-1.869733	0.623887
56	7	0	-8.368019	0.023429	-0.644802
57	7	0	-6.132954	-0.929472	-2.436230
58	7	0	-5.913319	-2.818631	-1.165797
59	7	0	-6.377551	1.438766	1.130597
60	7	0	-6.170790	-0.451496	2.401417
61	1	0	-8.664060	-2.616017	1.082744
62	1	0	-9.031298	0.639922	-1.100050
63	6	0	-8.925084	-0.996617	-0.008342
64	1	0	-10.014464	-1.117291	-0.004884
65	1	0	-6.107761	-0.802845	3.350187
66	1	0	-6.464861	2.448131	1.164525
67	6	0	-6.313055	0.864164	2.323567
68	1	0	-6.365778	1.470767	3.234376
69	1	0	-5.776056	-3.822404	-1.200084
70	1	0	-6.152891	-0.573264	-3.385087
71	6	0	-5.982743	-2.244340	-2.358650
72	1	0	-5.905357	-2.847944	-3.269654
73	16	0	2.602790	2.928604	0.869909
74	16	0	0.377137	3.904593	-0.868854
75	16	0	3.200628	-2.270028	0.870530
76	16	0	1.222842	-3.732239	-0.826012
77	16	0	-3.570432	-1.643116	0.820383
78	16	0	-3.847353	0.805378	-0.869148

HF= -4488.3694796

Electrochemical data

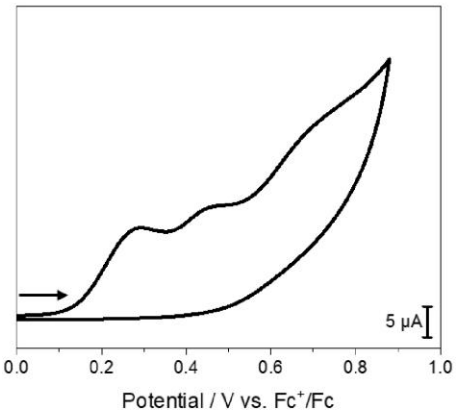

Figure S 38: Cyclic voltammogram of **4**. Conditions: 1 mM solution of **4** in CH_2Cl_2, scan rate = 100 mV/s, 0.1 M NBu_4PF_6/CH_2Cl_2 electrolyte-solvent system, room temperature, Ar atmosphere, glassy carbon WE, Pt CE, Ag wire RE, $E_{1/2}(Fc^+/Fc) = 0.621$ V.

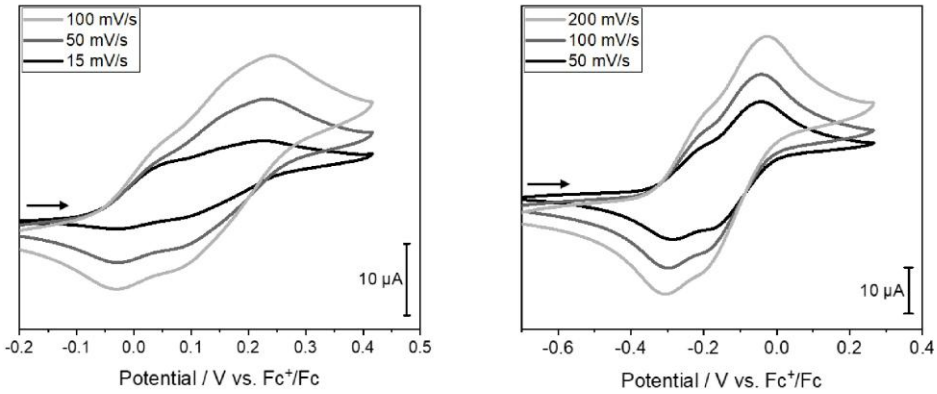

Figure S 39: Cyclic voltammograms of **6** (left) and **7** (right) in a 1 mM CH_2Cl_2 solution at different scan rates. Conditions: 0.1 M NBu_4PF_6/CH_2Cl_2 electrolyte-solvent system, room temperature, Ar atmosphere, glassy carbon WE, Pt CE, $Ag/AgNO_3$ RE, $E_{1/2}(Fc^+/Fc) = 0.234$ V.

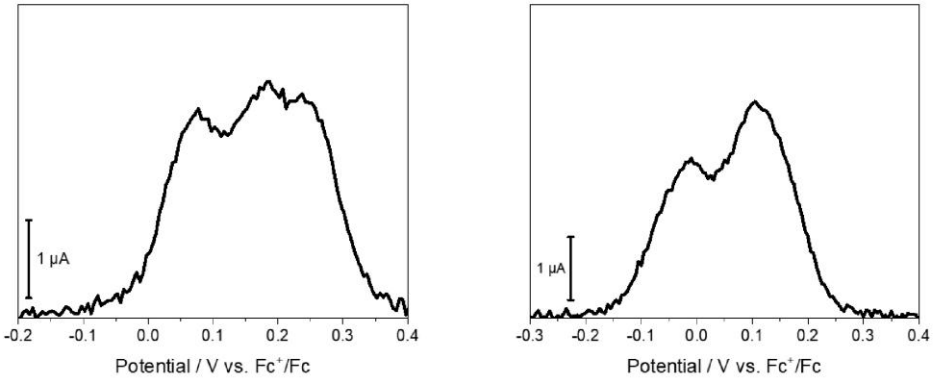

Figure S 40: Differential pulse voltammograms of **6** (left) and **7** (right) in a 1 mM CH_2Cl_2 solution. Conditions: 0.1 M NBu_4PF_6/CH_2Cl_2 electrolyte solvent system, room temperature, Ar atmosphere, glassy carbon WE, Pt CE, $Ag/AgNO_3$ RE, $E_{1/2}(Fc^+/Fc) = 0.234$ V, step size 5 mV, pulse size 15 mV, pulse time 0.2 s, sample period 1 s.

6.2 Supporting Information Manuscript II

Supplementary Information

Benzene-1,4-di(dithiocarboxylate) Linker-based Coordination Polymers of Mn^{2+}, Zn^{2+} and Mixed-Valence $Fe^{2+/3+}$

Margit Aust,[a] Marina I. Schönherr,[b] Dominik P. Halter,[a] Lena Schröck,[a] Thomas Pickl,[a] Simon N. Deger,[a] Mian Z. Hussain,[a] Andreas Jentys,[c] Raphael Bühler,[a] Zihan Zhang,[d] Karsten Meyer,[d] Matthias Kuhl,[e] Johanna Eichhorn,[e] Dana D. Medina,[b] Alexander Pöthig,[a] Roland A. Fischer[a]**

[a] Technical University of Munich, TUM School of Natural Sciences, Department of Chemistry Chair of Inorganic and Metal-Organic Chemistry; Catalysis Research Center (CRC), 85747 Garching, Germany.

[b] Ludwig-Maximilians-Universität (LMU), Department of Chemistry and Center for Nanoscience (CeNS), Butenandtstraße 11, 81377 Munich Germany.

[c] Technical University of Munich, TUM School of Natural Sciences, Department of Chemistry, Chair of Industrial Chemistry and Heterogeneous Catalysis; Catalysis Research Center (CRC), 85747 Garching, Germany.

[d] Friedrich-Alexander-Universität Erlangen-Nürnberg (FAU), Department of Chemistry and Pharmacy, Inorganic Chemistry, Egerlandstr. 1, 91058 Erlangen, Germany.

[e] Technical University of Munich, Walter Schottky Institute, 85747 Garching, Germany; TUM School of Natural Sciences, Physics Department, Technical University of Munich, 85747 Garching, Germany.

TABLE OF CONTENT

FT-IR Spectra

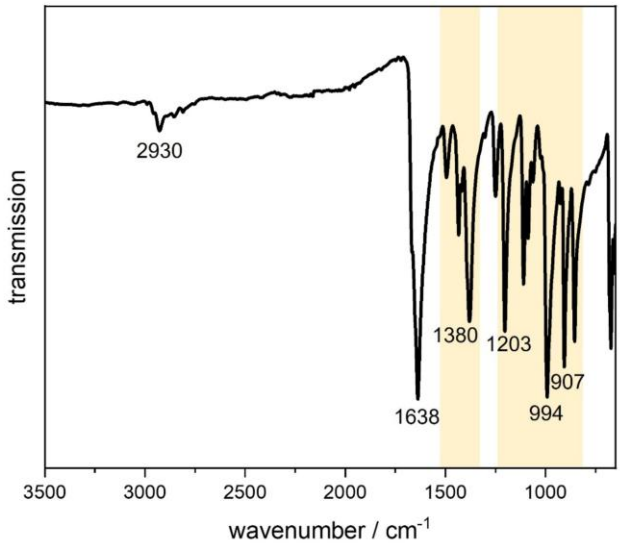

Figure S 1. FT-IR spectrum of **1**. Bands resulting from the $BDDTC^{2-}$ linker are marked in yellow.

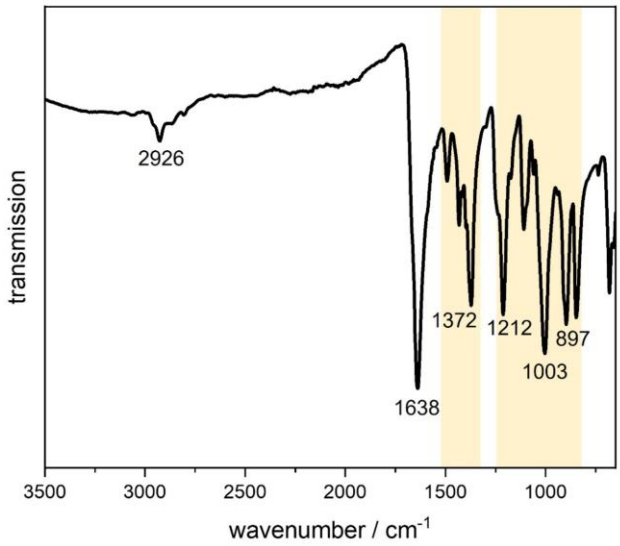

Figure S 2. FT-IR spectrum of **2**. Bands resulting from the $BDDTC^{2-}$ linker are marked in yellow.

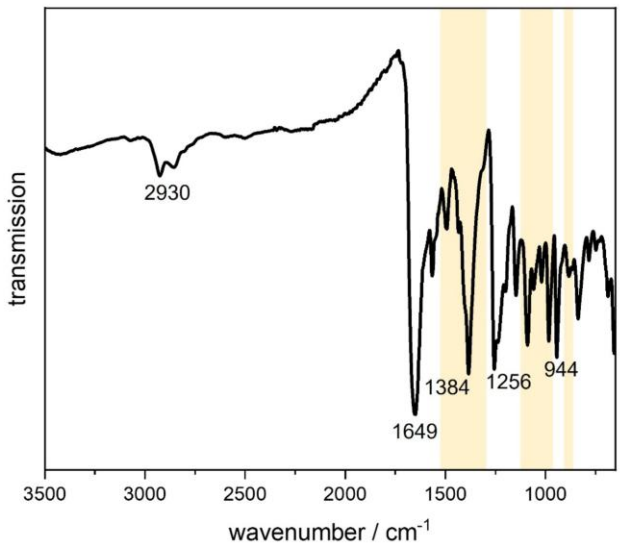

Figure S 3. FT-IR spectrum of **3**. Bands resulting from the $BDDTC^{2-}$ linker are marked in yellow.

Thermogravimetric analysis

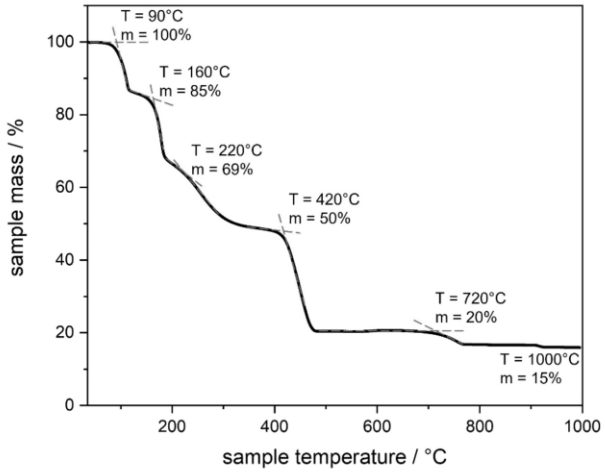

Figure S 4. TGA curve of **1** measured under a constant flow of synthetic air with a heating rate of 10°C/min. Temperature and mass percentage are determined at the crossing point of the respective trend lines (orange).

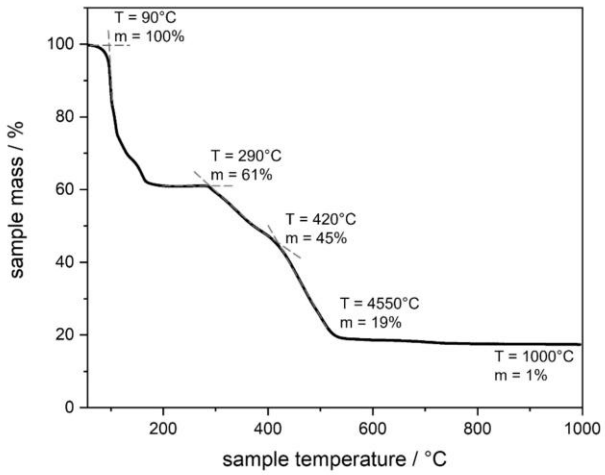

Figure S 5. TGA curve of **2** measured under a constant flow of synthetic air with a heating rate of 10°C/min. Temperature and mass percentage are determined at the crossing point of the respective trend lines (orange).

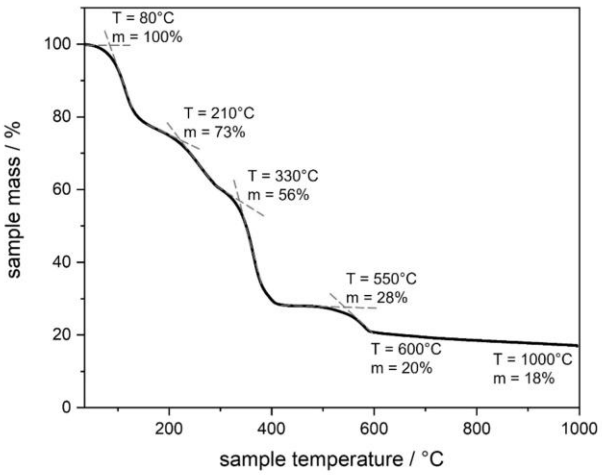

Figure S 6. TGA curve of **3** measured under a constant flow of synthetic air with a heating rate of 10°C/min. Temperature and mass percentage are determined at the crossing point of the respective trend lines (orange).

Additional PXRD data for stability of **1** and **2** in air

In contrast to CP **3** materials **1** and **2** do not show pronounced air sensitivity as evidenced by PXRD analysis (Figure S 7). For CP **1** even after four weeks in air no significant differences are visible in the PXRD pattern, suggesting air stability over the monitored time.

Since CP **2** consists of the two phases **2a** and **2b**, we opted to monitor air stability on a batch that contained both phases, which allows to study air stability of the two phases over time more easily. The synthesis procedure described in the main text of the manuscript afforded CP **2** materials with **2b** as the majority phase with traces of **2a**. By scaling up the batch size for a synthesis procedure described below, a much higher content of phase **2a** was achieved as shown in Figure S 7, right.

A Pawley fit was performed on the PXRD pattern of the as synthesized sample of CP **2** with phases **2a** and **2b** simultaneously, which produced a fit in good agreement with the experimental data. Even after four weeks in air the Pawley fitting is in still in good agreement (Figure S 8), suggesting that both phases **2a** and **2b** are generally air stable. With respect to the minor changes in the PXRD pattern of CP **2** over time, we like to note that all characterizations mentioned in the main text were conducted immediately after the synthesis as described.

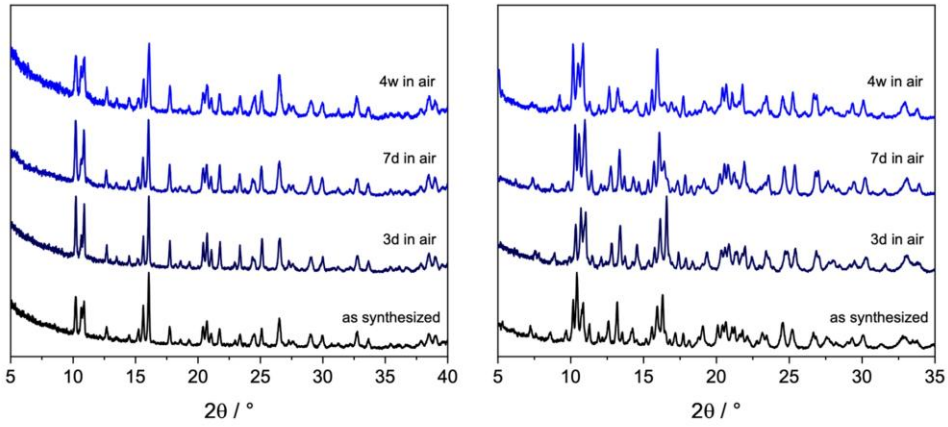

Figure S 7. PXRD pattern of **1** (left) and **2** (right) experimentally obtained after synthesis and after three days, seven days and four weeks in air.

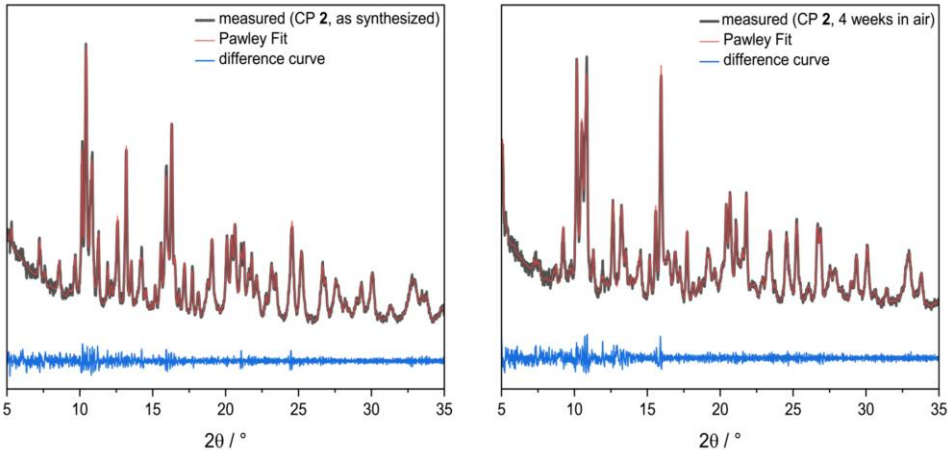

Figure S 8. Pawley fitting of CP **2** as synthesized (left) and after 4 weeks in air (right). Phases **2a** and **2b** were fitted simultaneously. Phase **2a**: space group=$P2_1/n$, a=14.769(5) Å, b=31.629(10) Å, c=16.161(5) Å, α=γ=90°, β=94.841(12)°, V=7522(4) Å^3; Phase **2b**: space

group=$P2_1/n$, a=12.836(5) Å, b=33.188(13) Å, c=16.207(6) Å, α=γ=90°, β=97.120(12)°, V=6851(5) Å3, R_{wp}(as synthesized)=3.51306326, GoF(as synthesized)=3.62978705, R_{wp}(4 weeks in air)=3.40986969, GoF(4 weeks in air)=3.62321046.

Synthetic procedure for upscaling of **2**:

Separate solutions of Na_2BDDTC (100 mg, 0.36 mmol) and $Zn(OTf)_2$ (130.4 mg, 0.38 mmol) where prepared in DMF (20 mL each) and combined in a 100 mL screw cap Schott bottle. After vigorous shaking, the resulting suspension was placed in a pre-heated oven and reacted under solvothermal conditions at 60°C for 24 h to form a dark red crystalline powder at the bottom of the glass bottle. The reaction container was then removed from the oven without cooling and the crystalline powder was collected via centrifugation of the hot mixture. After washing with DMF (3x40 mL) and Et_2O (3x40 mL) the red powder was dried on air for 1 hour and transferred to an argon filled glovebox (yield: 159.3 mg, 31%).

N_2 Physisorption

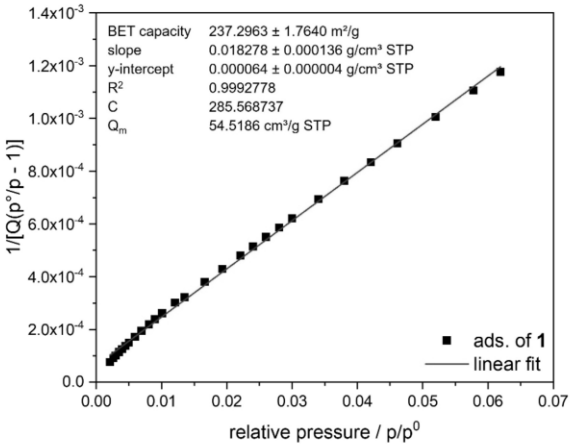

Figure S 9. BET plot for **3** with linear fit, control parameters and calculated monolayer capacity (Q_m).

Solid-state UV/VIS-NIR spectra

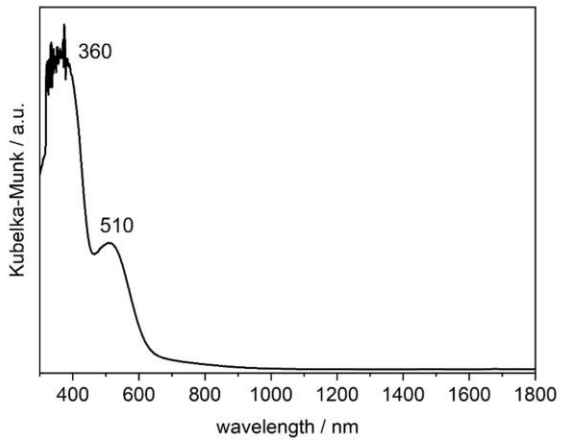

Figure S 10. Normalized UV/VIS-NIR absorption spectrum of the Na_2BDDTC linker. Measurement was performed on powder at room temperature.

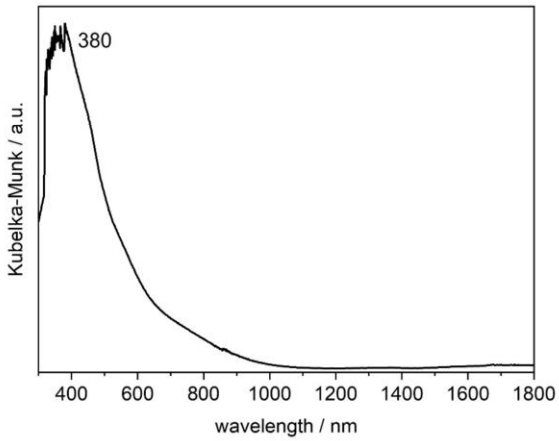

Figure S 11. Normalized UV/VIS-NIR absorption spectrum of **1**. Measurement was performed on crystalline powder at room temperature.

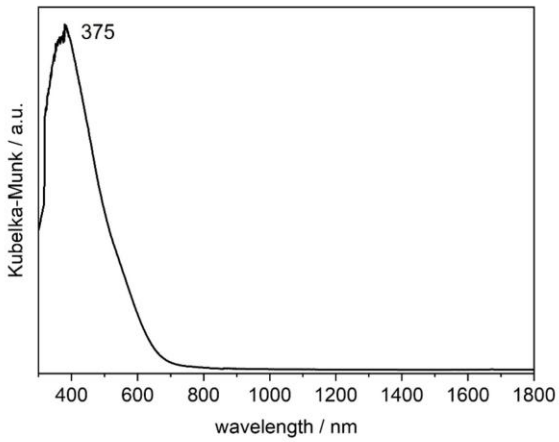

Figure S 12. Normalized UV/VIS-NIR absorption spectrum of **2**. Measurement was performed on crystalline powder at room temperature.

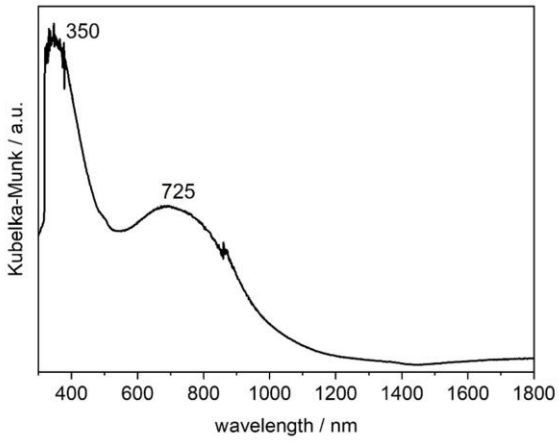

Figure S 13. Normalized UV/VIS-NIR absorption spectrum of **3**. Measurement was performed on crystalline powder at room temperature.

SQUID Magnetometry

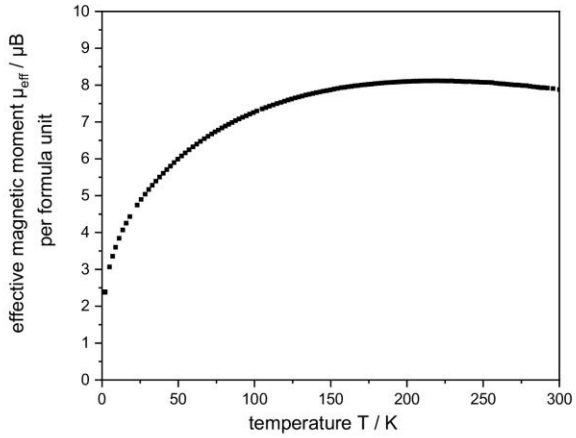

Figure S 14. Temperature dependent effective magnetic moment of **3** as determined by SQUID magnetometry.

The slight decrease in magnetic moment at temperatures above 250 K arises from slight inaccuracy of the applied diamagnetic correction with respect to residual solvent adsorbed inside the porous coordination polymer. The sample composition $[Fe_2C_{16}H_9S_8O]\cdot 5$ DMF based on which the diamagnetic correction was applied, was derived from elemental analysis data of the same batch used for SQUID magnetometry. Upon introducing the porous solvated coordination polymer to the dynamic vacuum of the SQUID magnetometer is likely to remove some of the DMF solvent; thus, causing slight deviations of sample composition during the experiment. We are convinced that this situation is not problematic for the overall interpretation we present for our magnetometry results.

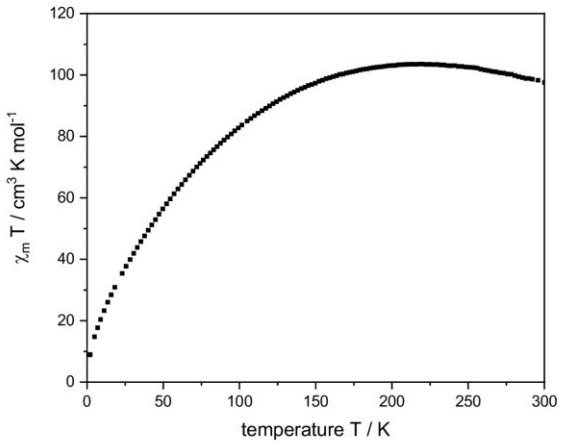

Figure S 15. $\chi_m \cdot T$ vs. T plot for **3** suggesting antiferromagnetic coupling between Fe atoms.

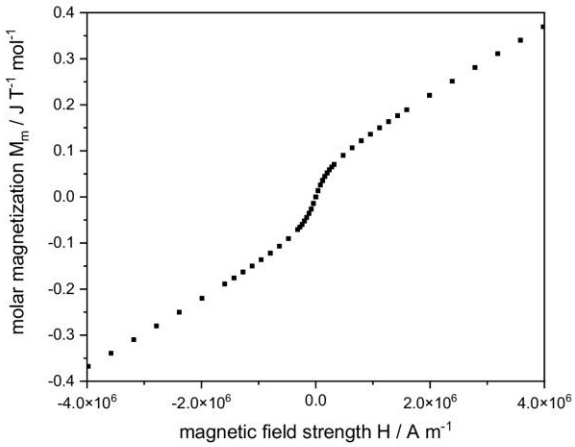

Figure S 16. Molar magnetization of **3** plotted against the applied magnetic field strength. Non-linearity indicates coupling effects between Fe atoms.

SEM Images of CPs

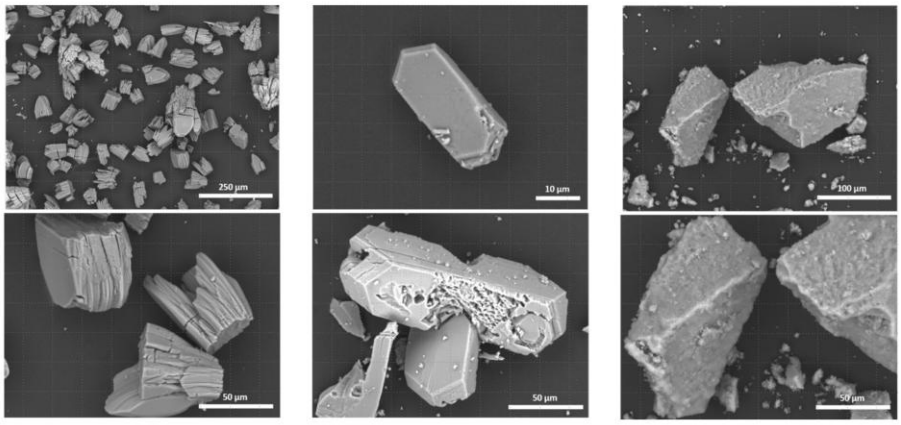

Figure S 17. SEM images of **1** (left), **2** (middle) and **3** (right).

EXAFS analysis data

Table S 1. Results of the EXAFS analysis for **3** [$Fe_2(BDDTC)_2(OH)$] with S_0^2=1.0 (fixed) and E_0=1.12 eV (varied in the fitting)

Scattering contribution	Coordination number, N	Distance r, Å	Debye-Waller factor $\Delta\sigma^2$, Å^2
Fe-O	1.6	1.92	0.0005
Fe-S	1.5	2.27	0.0003
Fe-Fe	1.0	3.16	0.007

Structural analysis data

Table S 2. Selected bond angles and bond lengths of CPs **1** and **2a-b** as determined from SC XRD analysis.

CP1	
CCDC number	2249203
Crystal color	dark red
Crystal system	triclinic
Space group	$P\overline{1}$
a /Å	7.0353(6)
b /Å	9.7532(8)
c /Å	16.9183(15)
α /°	94.259(4)
β /°	98.676(3)
γ /°	92.975(3)
Volume /Å^3	1142.08(17)
Atom–Atom	**Length /Å**
Mn1–S1	2.5601(12)
Mn1–S2	2.6638(12)
Mn1–S3	2.6002(12)
Mn1–S4	2.5691(12)
Mn1–O1	2.130(3)
Mn1–O2	2.176(3)
S1–C1	1.690(4)
S2–C1	1.689(4)

S3–C5	1.690(4)
S4–C5	1.698(4)
O1–C9	1.241(5)
O2–C12	1.244(5)
N1–C9	1.310(6)
N1–C10	1.462(6)
N1–C11	1.465(6)
N2–C12	1.314(6)
N2–C13	1.468(7)
N2–C14	1.446(7)
O3–C15	1.224(7)
N3–C15	1.324(6)
N3–C16	1.444(8)
N3–C17	1.443(7)
Atom–Atom–Atom	**Angle /°**
S1–Mn1–S2	68.52(4)
S1–Mn1–S3	167.68(4)
S1–Mn1–S4	103.23(4)
S1–Mn1–O1	96.15(8)
S1–Mn1–O2	93.58(8)
S2–Mn1–S3	100.81(4)
S2–Mn1–S4	88.27(4)
S2–Mn1–O1	164.66(9)
S2–Mn1–O2	90.01(9)
S3–Mn1–S4	69.37(4)

S3–Mn1–O1	94.34(8)
S3–Mn1–O2	92.55(8)
S4–Mn1–O1	94.88(9)
S4–Mn1–O2	161.13(8)
O1–Mn1–O2	91.73(11)
Mn1–S1–C1	86.87(13)
Mn1–S2–C1	83.55(13)
Mn1–S3–C5	84.66(14)
Mn1–S4–C5	85.50(13)
Mn1–O1–C9	122.4(3)
Mn1–O2–C12	122.1(3)
C9–N1–C10	121.6(4)
C9–N1–C11	121.1(4)
C10–N1–C11	117.3(4)
C12–N2–C13	121.7(4)
C12–N2–C14	120.9(4)
C13–N2–C14	117.4(4)
S1–C1–S2	121.0(2)
S1–C1–C2	119.2(3)
S2–C1–C2	119.8(3)
S3–C5–S4	120.5(2)
S3–C5–C6	119.7(3)
S4–C5–C6	119.8(3)
O1–C9–N1	123.8(4)
O2–C12–N2	124.2(4)
C15–N3–C16	122.7(4)

C15–N3–C17	120.2(5)
C16–N3–C17	117.2(5)
O3–C15–N3	125.1(5)
CP 2a	
CCDC number	2249205
Crystal colour	dark red
Crystal system	monoclinic
Space group	$P2_1/n$
a /Å	14.769(5)
b /Å	31.629(10)
c /Å	16.161(5)
α /°	90
β /°	94.841(12)
γ /°	90
Volume /Å^3	7522(4)
Atom–Atom	**Length /Å**
Zn1–S4	2.2821(16)
Zn1–S5	2.2914(16)
Zn1–S1$^{\#1}$	2.4352(16)
Zn1–S2$^{\#1}$	2.4338(17)
Zn2–S7	2.3003(16)
Zn2–S9	2.3038(16)
Zn2–S11$^{\#2}$	2.4231(16)

Zn2–S12$^{\#2}$	2.4338(16)
Zn3–O1_17	2.128(4)
Zn3–O1_14	2.22(4)
Zn3–O1_1	2.084(3)
Zn3–O1_2	2.080(3)
Zn3–O1_4	2.142(3)
Zn3–O1_5	2.070(4)
Zn3–O1_15	2.057(18)
Zn3–O1_16	2.07(4)
S1–C1	1.680(5)
S2–C1	1.701(5)
S3–C8	1.658(5)
S4–C8	1.717(5)
S5–C9	1.720(5)
S6–C9	1.658(5)
S7–C16	1.722(5)
S8–C16	1.666(5)
S9–C17	1.714(5)
S10–C17	1.665(5)
S11–C24	1.697(5)
S12–C24	1.681(5)
O1_1–C1_1	1.242(6)
O1_2–C1_2	1.237(7)
O1_4–C1_4	1.247(5)
O1_5–C1_5	1.242(6)
O1_14–C1_14	1.24(3)

O1_15–C1_15	1.216(19)
O1_16–C1_16	1.24(5)
N1_1–C1_1	1.324(7)
N1_1–C2_1	1.455(6)
N1_1–C3_1	1.457(7)
N1_2–C2_2	1.466(8)
N1_2–C3_2	1.440(7)
N1_2–C1_2	1.320(7)
N1_4–C2_4	1.456(7)
N1_4–C3_4	1.457(7)
N1_4–C1_4	1.318(6)
N1_5–C1_5	1.321(7)
N1_5–C3_5	1.461(8)
N1_5–C2_5	1.449(7)
N1_14–C3_14	1.44(3)
N1_14–C1_14	1.32(3)
N1_14–C2_14	1.47(4)
N1_15–C2_15	1.453(15)
N1_15–C3_15	1.480(15)
N1_15–C1_15	1.313(14)
N1_16–C2_16	1.44(3)
N1_16–C1_16	1.31(2)
N1_16–C3_16	1.48(3)
O1_3–C1_3	1.210(14)
N1_3–C3_3	1.442(12)
N1_3–C1_3	1.343(14)

N1_3–C2_3	1.411(13)
O1_7–C1_7	1.224(16)
N1_7–C1_7	1.303(19)
N1_7–C2_7	1.453(18)
N1_7–C3_7	1.448(18)
O1_8–C1_8	1.228(11)
N1_8–C1_8	1.321(12)
N1_8–C2_8	1.465(12)
N1_8–C3_8	1.455(14)
O1_10–C1_10	1.26(2)
N1_10–C1_10	1.31(2)
N1_10–C2_10	1.47(2)
N1_10–C3_10	1.439(19)
O1_12–C1_12	1.216(8)
N1_12–C1_12	1.305(8)
N1_12–C2_12	1.459(10)
N1_12–C3_12	1.442(10)
O1_6–C1_6	1.23(2)
N1_6–C1_6	1.32(3)
N1_6–C2_6	1.45(3)
N1_6–C3_6	1.45(3)
O1_9–C1_9	1.23(4)
N1_9–C1_9	1.32(5)
N1_9–C2_9	1.45(4)
N1_9–C3_9	1.44(5)
O1_11–C1_11	1.24(2)

N1_11–C1_11	1.32(2)
N1_11–C2_11	1.45(3)
N1_11–C3_11	1.45(3)
O1_13–C1_13	1.24(5)
N1_13–C1_13	1.33(5)
N1_13–C2_13	1.44(6)
N1_13–C3_13	1.45(6)
O1_18–C1_18	1.27(5)
N1_18–C1_18	1.33(4)
N1_18–C2_18	1.44(4)
N1_18–C3_18	1.48(4)
Atom–Atom–Atom	**Angle /°**
S4–Zn1–S5	127.08(5)
S1$^{\#1}$–Zn1–S4	118.76(5)
S2$^{\#1}$–Zn1–S4	112.43(5)
S1$^{\#1}$–Zn1–S5	103.13(5)
S2$^{\#1}$–Zn1–S5	108.93(5)
S1$^{\#1}$–Zn1–S2$^{\#1}$	74.04(5)
S7–Zn2–S9	119.45(5)
S7–Zn2–S11$^{\#2}$	116.04(5)
S7–Zn2–S12$^{\#2}$	110.48(5)
S9–Zn2–S11$^{\#2}$	114.07(5)
S9–Zn2–S12$^{\#2}$	114.14(5)
S11$^{\#2}$–Zn2–S12$^{\#2}$	74.06(5)
O1_4–Zn3–O1_15	88.8(6)

O1_4–Zn3–O1_17	89.18(13)
O1_4–Zn3–O1_14	98.5(7)
O1_4–Zn3–O1_16	88.9(12)
O1_5–Zn3–O1_15	95.3(5)
O1_5–Zn3–O1_17	177.39(15)
O1_5–Zn3–O1_14	85.0(12)
O1_5–Zn3–O1_16	90.5(11)
O1_15–Zn3–O1_17	82.4(5)
O1_14–Zn3–O1_17	92.9(12)
O1_16–Zn3–O1_17	87.2(11)
O1_2–Zn3–O1_15	95.4(6)
O1_2–Zn3–O1_17	89.51(14)
O1_2–Zn3–O1_14	86.0(7)
O1_2–Zn3–O1_16	95.4(12)
O1_4–Zn3–O1_5	89.53(13)
O1_1–Zn3–O1_16	175.9(11)
O1_1–Zn3–O1_2	87.51(14)
O1_1–Zn3–O1_4	88.10(12)
O1_1–Zn3–O1_5	92.31(14)
O1_1–Zn3–O1_15	171.7(5)
O1_1–Zn3–O1_17	89.91(14)
O1_1–Zn3–O1_14	172.9(8)
O1_2–Zn3–O1_4	175.42(13)
O1_2–Zn3–O1_5	91.96(15)
$Zn1^{\#3}$–S1–C1	82.78(17)
$Zn1^{\#3}$–S2–C1	82.42(16)

Zn1–S4–C8	99.60(17)
Zn1–S5–C9	99.86(17)
Zn2–S7–C16	98.39(17)
Zn2–S9–C17	99.55(17)
Zn2$^{\#4}$–S11–C24	82.99(16)
Zn2$^{\#4}$–S12–C24	82.96(17)
S2–C1–C2	118.5(3)
S1–C1–C2	121.2(3)
S1–C1–S2	120.2(3)
Zn3–O1_1–C1_1	128.1(3)
Zn3–O1_2–C1_2	123.1(4)
Zn3–O1_4–C1_4	119.6(3)
Zn3–O1_5–C1_5	122.8(3)
S3–C8–C5	121.3(3)
S4–C8–C5	114.2(3)
S3–C8–S4	124.5(3)
S5–C9–S6	123.4(3)
S5–C9–C10	115.4(3)
S6–C9–C10	121.3(3)
Zn3–O1_14–C1_14	112(3)
Zn3–O1_15–C1_15	127.4(14)
S7–C16–S8	123.0(3)
S7–C16–C13	115.7(4)
S8–C16–C13	121.3(4)
Zn3–O1_16–C1_16	139(3)
S9–C17–C18	114.9(3)

S10–C17–C18	120.6(3)
S9–C17–S10	124.5(3)
S11–C24–S12	120.0(3)
S11–C24–C21	119.5(3)
S12–C24–C21	120.6(3)
C1_1–N1_1–C3_1	120.5(4)
C1_1–N1_1–C2_1	121.9(4)
C2_1–N1_1–C3_1	117.6(4)
C1_2–N1_2–C2_2	120.8(5)
C2_2–N1_2–C3_2	117.5(5)
C1_2–N1_2–C3_2	121.4(5)
C1_4–N1_4–C3_4	121.2(4)
C1_4–N1_4–C2_4	121.9(4)
C2_4–N1_4–C3_4	116.8(4)
C1_5–N1_5–C3_5	120.9(5)
C2_5–N1_5–C3_5	117.3(5)
C1_5–N1_5–C2_5	121.8(5)
C1_14–N1_14–C3_14	122(3)
C2_14–N1_14–C3_14	116(3)
C1_14–N1_14–C2_14	122(2)
C1_15–N1_15–C3_15	122.3(10)
C1_15–N1_15–C2_15	120.9(10)
C2_15–N1_15–C3_15	116.8(10)
C1_16–N1_16–C2_16	131.9(18)
C2_16–N1_16–C3_16	113.6(18)
C1_16–N1_16–C3_16	114.5(18)

O1_1–C1_1–N1_1	123.8(4)
O1_2–C1_2–N1_2	125.1(5)
O1_4–C1_4–N1_4	125.3(4)
O1_5–C1_5–N1_5	124.5(5)
O1_14–C1_14–N1_14	138(3)
O1_15–C1_15–N1_15	124.7(13)
O1_16–C1_16–N1_16	125(3)
C1_3–N1_3–C3_3	118.6(9)
C2_3–N1_3–C3_3	120.3(9)
C1_3–N1_3–C2_3	121.0(9)
O1_3–C1_3–N1_3	126.1(10)
C2_7–N1_7–C3_7	117.3(12)
C1_7–N1_7–C2_7	120.2(13)
C1_7–N1_7–C3_7	122.1(12)
O1_7–C1_7–N1_7	126.1(14)
C1_8–N1_8–C3_8	120.3(8)
C2_8–N1_8–C3_8	117.8(7)
C1_8–N1_8–C2_8	121.8(8)
O1_8–C1_8–N1_8	125.1(9)
C1_10–N1_10–C3_10	122.7(14)
C2_10–N1_10–C3_10	116.6(13)
C1_10–N1_10–C2_10	120.6(13)
O1_10–C1_10–N1_10	121.4(15)
C1_12–N1_12–C3_12	121.3(6)
C2_12–N1_12–C3_12	116.2(6)
C1_12–N1_12–C2_12	122.2(6)

O1_12–C1_12–N1_12	126.7(7)
C1_6–N1_6–C3_6	120.3(17)
C2_6–N1_6–C3_6	117.3(19)
C1_6–N1_6–C2_6	122.0(19)
O1_6–C1_6–N1_6	127.9(17)
C1_9–N1_9–C3_9	123(3)
C2_9–N1_9–C3_9	118(3)
C1_9–N1_9–C2_9	119(3)
O1_9–C1_9–N1_9	126(3)
C1_11–N1_11–C3_11	117.9(17)
C2_11–N1_11–C3_11	118.1(16)
C1_11–N1_11–C2_11	123.9(17)
O1_11–C1_11–N1_11	122.8(17)
C1_13–N1_13–C3_13	117(4)
C2_13–N1_13–C3_13	116(4)
C1_13–N1_13–C2_13	127(4)
O1_13–C1_13–N1_13	119(3)
C1_18–N1_18–C3_18	108(2)
C2_18–N1_18–C3_18	113(2)
C1_18–N1_18–C2_18	139(3)
O1_18–C1_18–N1_18	114(3)
CP 2b	
CCDC number	2249204
Crystal colour	red

Crystal system	monoclinic
Space group	$P2_1/n$
a /Å	12.836(5)
b /Å	33.188(13)
c /Å	16.207(6)
α /°	90
β /°	97.120(12)
γ /°	90
Volume /Å^3	6851(5)
Atom–Atom	**Length /Å**
Zn2–S7	2.288(5)
Zn2–S10	2.296(5)
Zn2–S11$^{\#1}$	2.436(5)
Zn2–S12$^{\#1}$	2.418(6)
Zn3–S3	2.522(6)
Zn3–S4	2.464(5)
Zn3–S5	2.529(5)
Zn3–S6	2.519(5)
Zn3–S1$^{\#2}$	2.494(5)
Zn3–S2$^{\#2}$	2.536(5)
Zn1–O5	2.085(11)
Zn1–O1_2	2.075(13)
Zn1–O1	2.096(12)
Zn1–O1_1	2.073(13)
Zn1–O3	2.072(13)

Zn1–O1_3	2.153(10)
S1–C1	1.698(17)
S2–C1	1.674(17)
S3–C8	1.680(17)
S4–C8	1.691(19)
S5–C9	1.682(19)
S6–C9	1.689(18)
S7–C16	1.713(17)
S8–C16	1.691(17)
S9–C17	1.642(17)
S10–C17	1.707(18)
S11–C24	1.707(19)
S12–C24	1.669(18)
O1–C28	1.25(2)
O1_1–C1_1	1.20(2)
O1_2–C1_2	1.19(2)
O3–C40	1.24(2)
O5–C31	1.22(2)
N1_1–C1_1	1.34(2)
N1_1–C2_1	1.44(3)
N1_1–C3_1	1.43(3)
N2–C31	1.34(3)
N2–C33	1.43(3)
N2–C32	1.46(3)
N1_2–C2_2	1.42(3)
N1_2–C3_2	1.42(3)

N1_2–C1_2	1.34(2)
N3–C29	1.46(2)
N3–C30	1.47(2)
N3–C28	1.32(2)
N5–C40	1.29(2)
N5–C42	1.47(2)
N5–C41	1.45(2)
O7–C37	1.26(2)
N6–C37	1.34(3)
N6–C38	1.48(3)
N6–C39	1.38(3)
O8–C43	1.25(3)
N7–C44	1.50(3)
N7–C45	1.41(3)
N7–C43	1.36(3)
O9–C46	1.27(3)
N9–C46	1.33(3)
N9–C47	1.45(3)
N9–C48	1.45(3)
Atom–Atom–Atom	**Angle /°**
S7–Zn2–S10	121.7(2)
S7–Zn2–S11$^{\#1}$	114.49(19)
S7–Zn2–S12$^{\#1}$	121.43(19)
S10–Zn2–S11$^{\#1}$	105.15(19)
S10–Zn2–S12$^{\#1}$	108.95(19)

S11$^{\#1}$–Zn2–S12$^{\#1}$	74.59(18)
S3–Zn3–S4	72.05(17)
S3–Zn3–S5	102.80(18)
S3–Zn3–S6	172.08(18)
S1$^{\#2}$–Zn3–S3	96.55(17)
S2$^{\#2}$–Zn3–S3	93.26(18)
S4–Zn3–S5	103.69(17)
S4–Zn3–S6	104.43(18)
S1$^{\#2}$–Zn3–S4	163.31(17)
S2$^{\#2}$–Zn3–S4	96.91(17)
S5–Zn3–S6	70.83(17)
S1$^{\#2}$–Zn3–S5	90.53(16)
S2$^{\#2}$–Zn3–S5	156.93(18)
S1$^{\#2}$–Zn3–S6	88.34(17)
S2$^{\#2}$–Zn3–S6	94.22(18)
S1$^{\#2}$–Zn3–S2$^{\#2}$	71.05(16)
O3–Zn1–O1_3	93.0(5)
O3–Zn1–O5	173.6(5)
O1_3–Zn1–O5	93.4(5)
O1_1–Zn1–O3	92.2(5)
O1–Zn1–O1_1	92.4(5)
O1–Zn1–O1_2	91.8(5)
O1–Zn1–O3	83.6(5)
O1–Zn1–O1_3	176.5(5)
O1–Zn1–O5	90.1(5)
O1_1–Zn1–O1_2	173.4(5)

O1_2–Zn1–O3	93.3(5)
O1_1–Zn1–O1_3	87.1(4)
O1_1–Zn1–O5	89.5(5)
O1_2–Zn1–O1_3	89.0(5)
O1_2–Zn1–O5	85.5(5)
Zn3$^{\#3}$–S1–C1	84.8(6)
Zn3$^{\#3}$–S2–C1	83.9(6)
Zn3–S3–C8	82.3(7)
Zn3–S4–C8	83.9(6)
Zn3–S5–C9	83.3(6)
Zn3–S6–C9	83.5(6)
Zn2–S7–C16	97.1(6)
Zn2–S10–C17	101.3(6)
Zn2$^{\#4}$–S11–C24	81.3(6)
Zn2$^{\#4}$–S12–C24	82.6(6)
S1–C1–S2	120.2(10)
S1–C1–C2	118.5(12)
S2–C1–C2	121.3(12)
Zn1–O1–C28	128.2(12)
Zn1–O1_1–C1_1	122.5(12)
Zn1–O1_2–C1_2	134.5(13)
Zn1–O3–C40	130.9(13)
Zn1–O5–C31	121.5(12)
S3–C8–S4	120.9(10)
S3–C8–C7	119.8(13)
S4–C8–C7	119.2(12)

S5–C9–S6	120.3(10)
S5–C9–C10	119.4(13)
S6–C9–C10	120.3(13)
S8–C16–C15	120.4(12)
S7–C16–S8	122.5(10)
S7–C16–C15	117.1(12)
S9–C17–C18	120.0(13)
S9–C17–S10	126.5(10)
S10–C17–C18	113.5(12)
S11–C24–C23	118.0(13)
S12–C24–C23	120.8(13)
S11–C24–S12	121.2(10)
C2_1–N1_1–C3_1	118.5(16)
C1_1–N1_1–C2_1	123.3(17)
C1_1–N1_1–C3_1	118.1(16)
C31–N2–C32	119.7(17)
C31–N2–C33	121.3(17)
C32–N2–C33	119.0(17)
C1_2–N1_2–C2_2	118.9(17)
C1_2–N1_2–C3_2	122.0(17)
C2_2–N1_2–C3_2	119.0(17)
C28–N3–C29	123.1(15)
C28–N3–C30	120.9(15)
C29–N3–C30	116.0(14)
C40–N5–C41	122.2(16)
C41–N5–C42	117.1(16)

C40–N5–C42	120.6(16)
O1_1–C1_1–N1_1	126.9(18)
O1_2–C1_2–N1_2	127.6(18)
O1–C28–N3	121.1(17)
O5–C31–N2	124.1(18)
O3–C40–N5	126.9(17)
C37–N6–C39	127.1(17)
C38–N6–C39	116.9(17)
C37–N6–C38	115.8(17)
O7–C37–N6	121.5(18)
C44–N7–C45	119.1(17)
C43–N7–C44	116.8(19)
C43–N7–C45	124.1(19)
O8–C43–N7	124(2)
C46–N9–C48	122(2)
C47–N9–C48	114.0(18)
C46–N9–C47	124(2)
O9–C46–N9	125(2)

Literature known coordination motifs for potential comparison with CP **3**

Literature research for similar compounds was done in order to identify possible coordination environments in CP **3** based on known compounds. In this table some examples with similar sum formulas to our suggested one $[Fe_2(BDDTC)_2(OH)]$ (CP **3**), other iron compounds containing -OH groups, or possible iron environments and a compound with mixed-valency Fe, S, O environment, are shown.

Table S 3. Overview on potentially related literature of known iron coordination compounds (compound: name and sum formula, specifications: similarities and differences compared to CP **3**, structure: sketch of the coordination environment, references). Color code for crystal structures: orange for Fe, gray for C, red for O, white for H, light blue for N).

Compound	**Specifications**	**Structure**	**Ref**
MIL-187(Fe) **($Fe(OH)(C_9O_6H_5)_2(C_2H_5OH)_{0.5}$)**	- similarity: composition of sum formula, (μ_2-OH group) - difference: carboxylate linker	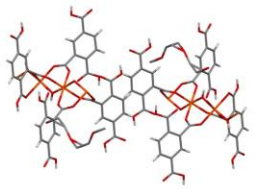	1
MIL-53(Fe) **(Fe(OH)BDC)**	- similarity: composition of sum formula (μ_2-OH group) - difference: carboxylate linker	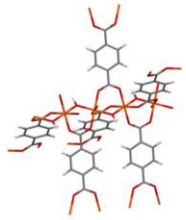	2

MIL-101(Fe) **($[Fe_3O(BDC)_3(OH)_2R]$** **(e.g. R=OH^-, Cl^-))**	- similarity: multinuclear metal center, terminal -OH group possible for "R" - difference: carboxylate linker	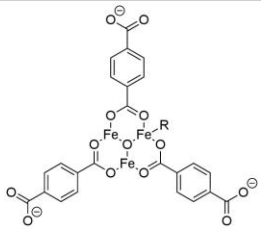	2
$Fe_2(DSBDC)(DMF)_2$ **(DSBDC=2,5-disulfhydrylbenzene-1,4-dicarboxylate)**	- similarity: $Fe^{2+/3+}$ mixed-valency (Fe, S, O environment) - difference: carboxylate linker (with coordinating SH groups)	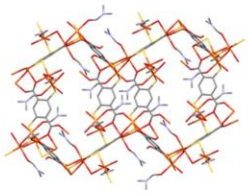	3
$[Fe(AnErytH_{-2})_2(OH)]$ **$\cdot$ 0.5 $NaNO_3$ $\cdot$ 3.5 H_2O** **(AnEryt=1,4-anhydroerythritol)**	- similarity: composition of sum formula → here: FeL_2OH complex - difference: non-polymeric structure (no sulfur)	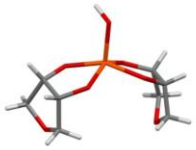 $[Fe(AnErytH_{-2})_2(OH)]^{2-}$ ion	4
$Fe(OC_4H_8dtc)_2(DMF)$ **(dtc=dialkyldithiocarbamate)**	- similarity: FeS_4O environment (FeL_2OR_1) ($R_1=C_3H_7N$) - difference: non-polymeric structure, DMF coordinating through oxygen	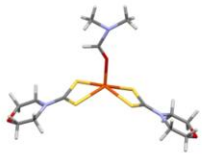	5
$[C_7H_7(C_6H5)_3P_2]Fe[S_2CC(COOC_2H_5)_2]_3$	- similarity: FeS_6 environment (distorted octahedron) - difference: non-polymeric structure	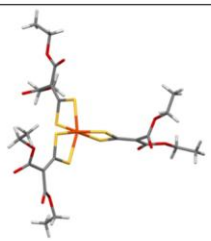 $Fe[S_2CC(COOC_2H_5)_2]_3^{2-}$ ion	6

$[(C_6H_5)_4P]_2[Fe(S_2C_4O_2)_2]$	- similarity: FeS_4 environment - difference: non-polymeric structure	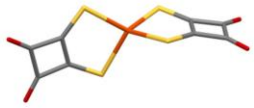 $Fe(S_2C_4O_2)_2^{2-}$ ion	7
$[Fe_4S_4(BDT)_2][TMA]_2$	- similarity: iron/sulfur containing compound with similar Mössbauer signal - difference: iron-sulfur clusters, linker	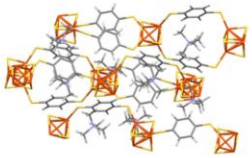	8

Overview of selected literature known values for electrical conductivity in CPs

Table S 4. Overview of selected reported literature values of electrically conductive coordination polymers.

Material	Method	Sample	El. conductivity [S cm^{-1}]	Ref
Fe-DSBDC	Two-probe	Pellet	$3.9 \cdot 10^{-6}$	9
Fe-THBQ	Four-probe	Pellet	$2.7 \cdot 10^{-4}$	10
Fe-HHTP	Van der Pauw	Pellet	$5.6 \cdot 10^{-3}$	11
Fe-DHBQ	Two-probe	Pellet	$1.2 \cdot 10^{-2}$	12
Fe-DHBQ	Two-probe	Pellet	0.16	13
Co-THT	Van der Pauw	Pellet	$1.4 \cdot 10^{-3}$	14
Cu-HITP	Two-probe	Pellet	0.2	15
Cu-BHT	Four-probe	Film	1580	16
Ho-HHTP	Two-probe	Single-crystal	0.05	17
Cu-TAPT	Two-probe	Single-crystal	4.0	18
Cu-CAT-1	Four-probe	Single-crystal	0.1	19

XPS measurement of **3**

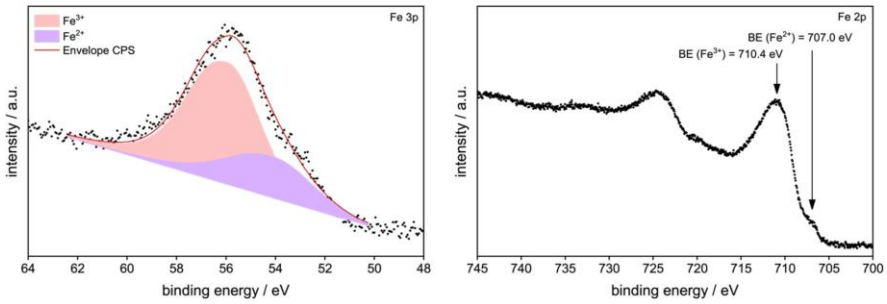

Figure S 18. High resolution XPS spectra of **3**. Fe 3p spectrum including the fitted linear background function and the Fe^{2+} and Fe^{3+} components (left); Fe 2p spectrum and associated peak positions (right).

The ratio of Fe^{2+} to Fe^{3+} was determined using the methodology developed by Yamashita and Hayes[20], which utilizes the Fe 3p high-resolution spectrum rather than the more commonly employed Fe 2p spectrum. The primary reason for this choice is that the 2p spectrum exhibits more pronounced satellite peaks and multiplet splitting features, rendering it more challenging to fit compared to the 3p spectrum. We adopted the same fit parameters (GL(40), linear background) as Yamashita and Hayes[20], albeit with an asymmetry parameter of 2 instead of 0.4, to achieve an appropriate fit, representing a more symmetric peak shape for our sample.

From fitting the 3p spectrum we obtained an Fe^{2+}/Fe^{3+} ratio of 3:7. The disparity with the Mössbauer spectroscopy results (1:1) can be attributed to the surface sensitivity of XPS. In the presence of air and water, Fe^{3+} is typically the more stable oxidation state, whereas Fe^{2+} compounds are often oxidized to Fe^{3+}. Consequently, a higher concentration of Fe^{3+} is expected at the surface of **3** due to inevitable sample storage and transfer to the XPS instrument. We therefore consider

the 1:1 ratio (Fe^{2+}/Fe^{3+}) obtained by bulk sensitive Mössbauer spectroscopy measurements to be more reliable.

It is worth noting that the employed fitting method represents a significant simplification of the actual complex Fe 3p line shape, and results should therefore be interpreted with caution[21], despite its frequent use by other researchers. Further evidence for the presence of Fe^{2+} and Fe^{3+} states is provided by the Fe 2p spectrum. Higher binding energies (BE) are typically associated with Fe^{3+} states, while lower BE peaks correspond to Fe^{2+} states. Although exceptions exist due to substantial shifts dependent on the chemical environment, the research of Grosvenor *et al.*[22] and Biesinger *et al.*[23] indicates that this trend is applicable to most standard Fe compounds. The primary Fe 2p 3/2 peak exhibits a binding energy of 710.4 eV, consistent with other Fe^{3+}-containing compounds.[22, 23] On the lower BE side, a minor shoulder at 707.0 eV can be attributed to Fe^{2+}.[22, 23] The relative peak intensities suggest a higher prevalence of Fe^{3+} states. However, fitting these components was not possible due to the necessity of knowledge regarding the positions of associated multiplet and satellite peaks. These positions not only differ among various Fe oxidation states but also vary depending on the specific compound and chemical environment in which the Fe atom is situated[22, 23], and are unknown in the case of **3**. Altogether we conclude that XPS does support a substantial mixed-valence nature of the compound, however the method is not really suitable to exactly determine the bulk stoichiometry of our material under the available conditions.

Experimental

The sample was prepared for XPS measurements by preparing an ink with Et_2O and drop casting it on a highly doped Si substrate (Siegert, n-type (As), <0.005 Ωcm) to provide sufficient electrical contact to the sample holder.

XPS measurements were carried out on a homemade system, equipped with an XR-50 X-ray source (SPECS), a PHOIBOS 100 hemispherical electron analyzer (SPECS) and a MCD-5 multichannel detector (SPECS). During the measurement, the sample was irradiated with non-monochromatized X-rays from an $Al_{K\alpha}$ source (E= 1486.61 eV). Data evaluation was carried out using the Casa XPS software. Due to the complex shape of the C 1s spectrum in organic compounds, in addition to the uncertainty associated with charge referencing to the adventitious C 1s C-C peak[24, 25]we did not do a post-measurement charge correction but used the measured data directly with their internal instrument calibration.

References

1. Benzaqui, M.; Wahiduzzaman, M.; Zhao, H.; Hasan, M. R.; Steenhaut, T.; Saad, A.; Marrot, J.; Normand, P.; Grenèche, J.-M.; Heymans, N.; De Weireld, G.; Tissot, A.; Shepard, W.; Filinchuk, Y.; Hermans, S.; Carn, F.; Manlankowska, M.; Téllez, C.; Coronas, J.; Maurin, G.; Steunou, N.; Serre, C., A robust eco-compatible microporous iron coordination polymer for CO2 capture. *Journal of Materials Chemistry A* **2022,** *10* (15), 8535-8545.

2. Bara, D.; Meekel, E. G.; Pakamorė, I.; Wilson, C.; Ling, S.; Forgan, R. S., Exploring and expanding the Fe-terephthalate metal–organic framework phase space by coordination and oxidation modulation. *Materials Horizons* **2021,** *8* (12), 3377-3386.

3. Sun, L.; Hendon, C. H.; Park, S. S.; Tulchinsky, Y.; Wan, R.; Wang, F.; Walsh, A.; Dincă, M., Is iron unique in promoting electrical conductivity in MOFs? *Chemical Science* **2017,** *8* (6), 4450-4457.

4. Burger, J.; Klüfers, P., Polyol Metal Complexes. 17. Crystalline Iron(III) Complexes with Twofold Deprotonated Anhydroerythritol Ligands. *Zeitschrift für anorganische und allgemeine Chemie* **1996,** *622* (10), 1740-1748.

5. Deng, Y.; Wen, T.; Liu, Q.; Zhu, H.; Chen, C.; Wu, D., Structure and characterization of a mononuclear FeII dialkyldithiocarbamate complex Fe(OC4H8dtc)2(DMF). *Inorganica Chimica Acta* **1999,** *293* (1), 95-99.

6. Coucouvanis, D.; Hollander, F. J.; Pedelty, R., Transition metal ions in high formal oxidation states. Synthesis and structural characterization of the six-coordinate iron(IV) complex of the 1,1-dicarboethoxy-2,2-ethylenedithiolate chelating ligand. *Inorganic Chemistry* **1977,** *16* (11), 2691-2696.

7. Coucouvanis, D.; Swenson, D.; Baenziger, N. C.; Murphy, C.; Holah, D. G.; Sfarnas, N.; Simopoulos, A.; Kostikas, A., Tetrahedral complexes containing the Fe(II)S4 core. The syntheses, ground-state electronic structures and crystal and molecular structures of the bis(tetraphenylphosphonium) tetrakis (thiophenolato)ferrate (II) and bis (tetrapheny lphosphonium) bis(dithiosquarato)ferrate (II) complexes. An analog for the active site in reducd rubredoxins (Rdred). *Journal of the American Chemical Society* **1981,** *103* (12), 3350-3362.

8. Horwitz, N. E.; Xie, J.; Filatov, A. S.; Papoular, R. J.; Shepard, W. E.; Zee, D. Z.; Grahn, M. P.; Gilder, C.; Anderson, J. S., Redox-Active 1D Coordination Polymers of Iron–Sulfur Clusters. *Journal of the American Chemical Society* **2019,** *141* (9), 3940-3951.

9. Sun, L.; Hendon, C. H.; Minier, M. A.; Walsh, A.; Dincă, M., Million-Fold Electrical Conductivity Enhancement in Fe2(DEBDC) versus Mn2(DEBDC) (E = S, O). *Journal of the American Chemical Society* **2015,** *137* (19), 6164-6167.

10. Chen, G.; Gee, L. B.; Xu, W.; Zhu, Y.; Lezama-Pacheco, J. S.; Huang, Z.; Li, Z.; Babicz, J. T., Jr.; Choudhury, S.; Chang, T.-H.; Reed, E.; Solomon, E. I.; Bao, Z., Valence-

Dependent Electrical Conductivity in a 3D Tetrahydroxyquinone-Based Metal–Organic Framework. *Journal of the American Chemical Society* **2020,** *142* (51), 21243-21248.

11. Mähringer, A.; Döblinger, M.; Hennemann, M.; Gruber, C.; Fehn, D.; Scheurle, P. I.; Hosseini, P.; Santourian, I.; Schirmacher, A.; Rotter, J. M.; Wittstock, G.; Meyer, K.; Clark, T.; Bein, T.; Medina, D. D., An Electrically Conducting Three-Dimensional Iron–Catecholate Porous Framework. *Angewandte Chemie International Edition* **2021,** *60* (33), 18065-18072.

12. Gupta, S.; Tanaka, H.; Fuku, K.; Uchida, K.; Iguchi, H.; Sakamoto, R.; Kobayashi, H.; Gambe, Y.; Honma, I.; Hirai, Y.; Hayami, S.; Takaishi, S., Quinoid-Based Three-Dimensional Metal–Organic Framework Fe2(dhbq)3: Porosity, Electrical Conductivity, and Solid-State Redox Properties. *Inorganic Chemistry* **2023,** *62* (16), 6306-6313.

13. Darago, L. E.; Aubrey, M. L.; Yu, C. J.; Gonzalez, M. I.; Long, J. R., Electronic Conductivity, Ferrimagnetic Ordering, and Reductive Insertion Mediated by Organic Mixed-Valence in a Ferric Semiquinoid Metal–Organic Framework. *Journal of the American Chemical Society* **2015,** *137* (50), 15703-15711.

14. Clough, A. J.; Skelton, J. M.; Downes, C. A.; de la Rosa, A. A.; Yoo, J. W.; Walsh, A.; Melot, B. C.; Marinescu, S. C., Metallic Conductivity in a Two-Dimensional Cobalt Dithiolene Metal–Organic Framework. *Journal of the American Chemical Society* **2017,** *139* (31), 10863-10867.

15. Campbell, M. G.; Sheberla, D.; Liu, S. F.; Swager, T. M.; Dincă, M., Cu3(hexaiminotriphenylene)2: An Electrically Conductive 2D Metal–Organic Framework for Chemiresistive Sensing. *Angewandte Chemie International Edition* **2015,** *54* (14), 4349-4352.

16. Huang, X.; Sheng, P.; Tu, Z.; Zhang, F.; Wang, J.; Geng, H.; Zou, Y.; Di, C.-a.; Yi, Y.; Sun, Y.; Xu, W.; Zhu, D., A two-dimensional π–d conjugated coordination polymer with extremely high electrical conductivity and ambipolar transport behaviour. *Nature Communications* **2015,** *6* (1), 7408.

17. Skorupskii, G.; Trump, B. A.; Kasel, T. W.; Brown, C. M.; Hendon, C. H.; Dincă, M., Efficient and tunable one-dimensional charge transport in layered lanthanide metal–organic frameworks. *Nature Chemistry* **2020,** *12* (2), 131-136.

18. Fan, K.; Li, J.; Xu, Y.; Fu, C.; Chen, Y.; Zhang, C.; Zhang, G.; Ma, J.; Zhai, T.; Wang, C., Single Crystals of a Highly Conductive Three-Dimensional Conjugated Coordination Polymer. *Journal of the American Chemical Society* **2023,** *145* (23), 12682-12690.

19. Hmadeh, M.; Lu, Z.; Liu, Z.; Gándara, F.; Furukawa, H.; Wan, S.; Augustyn, V.; Chang, R.; Liao, L.; Zhou, F.; Perre, E.; Ozolins, V.; Suenaga, K.; Duan, X.; Dunn, B.; Yamamto, Y.; Terasaki, O.; Yaghi, O. M., New Porous Crystals of Extended Metal-Catecholates. *Chemistry of Materials* **2012,** *24* (18), 3511-3513.

20. Yamashita, T.; Hayes, P., Analysis of XPS spectra of Fe2+ and Fe3+ ions in oxide materials. *Applied Surface Science* **2008,** *254* (8), 2441-2449.

21. Paparazzo, E., On the quantitative XPS analysis of Fe2O3 and Fe1−xO oxides. *Journal of Electron Spectroscopy and Related Phenomena* **2006,** *154* (1), 38-40.

22. Grosvenor, A. P.; Kobe, B. A.; Biesinger, M. C.; McIntyre, N. S., Investigation of multiplet splitting of Fe 2p XPS spectra and bonding in iron compounds. *Surface and Interface Analysis* **2004,** *36* (12), 1564-1574.

23. Biesinger, M. C.; Payne, B. P.; Grosvenor, A. P.; Lau, L. W. M.; Gerson, A. R.; Smart, R. S. C., Resolving surface chemical states in XPS analysis of first row transition metals, oxides and hydroxides: Cr, Mn, Fe, Co and Ni. *Applied Surface Science* **2011,** *257* (7), 2717-2730.

24. Greczynski, G.; Hultman, L., X-ray photoelectron spectroscopy: Towards reliable binding energy referencing. *Progress in Materials Science* **2020,** *107*, 100591.

25. Greczynski, G.; Hultman, L., Compromising Science by Ignorant Instrument Calibration—Need to Revisit Half a Century of Published XPS Data. *Angewandte Chemie International Edition* **2020,** *59* (13), 5002-5006.

```
data_raw2aif
_exptl_operator 'n.n.'
_exptl_date 2023-02-24T10:04:07
_exptl_instrument '3Flex 5.01'
_exptl_adsorptive N2
_exptl_temperature 76.868
_exptl_sample_mass 0.0496
_sample_id 'N2_77K'
_sample_material_id 'Fe-BDDTC'
_units_temperature K
_units_pressure mbar
_units_mass g
_units_loading 'cm³/g STP'
_audit_aif_version 6acf6ef

loop_
_adsorp_pressure
_adsorp_p0
_adsorp_amount
0.0570575096848011 956.5263510543563 9.178102590385544
0.3132988979076147 956.4640439853516 17.890205458585974
1.280323334980488 955.9670144326172 25.044255260169855
1.4876185219402314 955.8118351010742 25.929489707210234
1.9895133220539092 955.8701799257811 27.557672098634693
2.497926428412437 955.235222230957 29.000721674510217
2.8462386936779023 955.0192568686523 29.85770041933178
3.3345495171318054 954.9377205864257 30.86239702970503
3.777280671340942 954.8401537177733 31.683007646164338
4.267587689329147 954.9907761313477 32.53895619420537
4.746071069086074 954.854556833496 33.35687333838449
5.657697829845429 954.7572340854492 34.642257454308435
6.617147753643036 954.6138539165039 35.88048944707169
7.68588297088623 954.4202662763672 37.06256632905186
8.586476306728363 953.8491054331054 38.019074285134025
9.62098568793869 953.5972989284675 39.00295116312947
11.49 953.5359780738096 40.49894365587717
12.91626611705017 953.8651360195312 42.65999335557245
15.844536009338379 953.8775861704102 44.49865741629928
18.415610411750794 954.0222683159179 45.89224005340021
21.06016130202484 954.0535971269532 47.05364440736751
22.89571303477478 953.9689686503905 47.82316073518141
24.81485700297546 953.9600989350586 48.51429933197917
26.721082922470092 953.893698130371 49.17271773232479
28.611936872589112 953.8585447631837 49.774072709058025
32.47045376124573 953.8722155170899 50.78885656964898
36.22733256156921 953.8416190678711 51.70496724161265
40.118373435058594 953.8641595371093 52.604694091390925
43.99922481619262 953.9479742783202 53.4107563830871
49.59537945996094 953.901509989746 54.50992461346467
55.12838315460205 953.957169487793 55.47052174055942
59.05451890805053 953.957250861328 56.11781381998982
62.97738446255493 953.8345395703126 56.768351728214206
66.91695193515014 953.714025364746 57.36907188604451
70.45118765744019 953.7640700888672 57.878925026665236
```

74.42033949591064	953.7097939409178	58.412484689514606
81.92928080044555	953.5105915268554	59.30156357129111
89.69291109832763	953.5774805727539	60.158040673581134
95.41016481994629	953.6534590127931	60.80166571138595
103.0810242019043	953.7998744443361	61.54097125808706
110.48718564569091	953.714025364746	62.20586355385954
118.0957739298706	953.7203725004883	62.86584436969907
125.825232428833	953.8883274770508	63.4806031812912
133.65887956787108	953.7116655322264	64.10910165449465
141.46431043359374	953.7266382626951	64.72400709920173
148.96225105334472	953.6767562856444	65.27038126938507
156.2004982073364	953.8675772255858	65.78439876671767
163.88289228790282	954.1521404780274	66.26232826174713
171.7457626977539	954.5220645688474	66.77649266025882
179.2629685019531	954.8659491284179	67.24567712120056
186.91629188708495	955.1447348598633	67.7002950888292
202.07050568261718	955.2477537553711	68.52706648373396
213.7267153223877	955.2702942246093	69.1835944432911
225.26477058911132	955.3808808588867	69.80182782316393
236.54053860864258	955.4161969731446	70.35288792885875
247.9250013277588	955.5557525859376	70.91719712452895
259.5440029185791	955.4607896704101	71.52577227568064
270.97584537854004	955.5267022338868	72.11063071228006
282.91492976989747	955.5298758017578	72.71597269190985
293.90515805456545	955.5959511123048	73.27918525003662
305.24293270788576	955.7075142290039	73.844560253883
316.72207353515626	955.814845921875	74.3868991010124
328.22637912817385	955.7527579145509	74.96481888817509
340.1660941644287	955.8777476645507	75.56863026623816
351.032655019043	955.8921507802735	76.16522488593333
362.4920424206543	956.0361005639647	76.74614890217127
374.06108066088865	956.1504303808593	77.32062109025188
385.4331949460449	956.1541735634765	77.89685524422532
396.9727759665527	956.0946895092773	78.51507409055067
408.3848039707031	956.1687394262696	79.0996957768734
419.82299356640624	956.1473381865234	79.72630162695503
431.5645843879394	956.2580061943358	80.36698805735728
442.8650899621582	956.2194351386719	80.99304410348797
455.23988894750977	956.255483614746	81.69540748356803
466.7550985942383	956.2147968471679	82.39843313436369
477.26750148046875	956.2414873666991	83.05789801046751
500.05099278149413	956.1768767797852	84.47570171111371
523.2993710888671	956.1805385888671	86.00138633131323
547.4703625378418	956.3352296791991	87.68605803794462
570.4085449291993	956.3161068984375	89.48173670532779
593.3324462651367	956.4128600317381	91.38826904772347
615.5978729545898	956.3379150058591	93.51384460858209
639.0919586513671	956.350772024414	95.9696307284441
661.5656609040527	956.4472810371093	98.63497966027872
683.895494746582	956.5557519594727	101.73669732239385
707.3788391367187	956.6102722280274	105.41040889811367
729.6642023422852	956.6234547407228	109.66
752.7582557402344	956.7703339716797	115.10948389894365
775.6330888344727	956.8591938720703	121.78534894716454

```
798.346558208496 957.075159234375 130.59067317927335
821.2504416547852 957.2997501914062 142.74069806924604
843.8783874433593 957.2068216142577 160.2875373757405
865.75712709375 957.1689015468751 186.48671959689716
887.223628415039 957.3266848315429 227.49427337079496
909.9333546064453 957.3082944125975 286.58068032223713
954.6565750224609 957.3977239277343 330.06756186983876

loop_
_desorp_pressure
_desorp_p0
_desorp_amount
908.8715113461914 957.4493147490234 314.0829654638387
877.6335945498047 957.6280110322265 311.83830930146473
854.8876571352539 957.6413562919922 300.7294357985953
839.8193941362305 957.78083053125 277.5939458539282
809.5103562436523 957.8880808505858 224.7091014562753
783.0242470327148 957.9692102651368 179.6439050949765
753.2931239868163 957.9584689584959 148.21691373550172
732.409745418457 958.0966412211914 134.35171974512198
704.2442491889648 958.1751666826171 121.42614418716413
676.8379680424805 958.2632128476563 112.89816198444798
650.1033847419434 958.3082124125975 106.75195267572867
622.6913667612305 958.3210694311523 101.87214976780692
595.7860210971679 958.3468648417967 98.02651658170966
569.16 958.4033804812055 94.81313292521583
542.2225832556152 958.263619715332 92.07870526897207
515.134065763916 958.2643520771485 89.66344501445256
488.325310486084 958.4063488959961 87.53314542458881
478.65520506225585 958.503671644043 86.80665993853468
458.8847723342285 958.4758418950194 85.11476842834912
437.04509198071287 958.4222981088866 82.37162066872538
414.71647874121095 958.3475158300782 80.84959466079098
394.8062869665527 958.3515845068359 79.82136499646911
373.51518630029295 958.2559706030272 78.72953219304118
352.4346803430176 958.2744423955078 77.73265083090357
331.3285010354004 958.3252194814452 76.75864954532273
310.28502003662106 958.4681114091796 75.78509920604027
289.37956889685057 958.3855986445312 74.83767603235427
268.27574942175295 958.4168460820314 73.85538121818594
247.22557544970704 958.4474425312501 72.89128575084986
226.22143855517578 958.438572815918 71.89167727816076
205.5232864962158 958.4799919453123 70.86014750614228
191.7612518269043 958.6365785877745 70.1286372772706
176.5238335916748 958.5114835034179 69.30794997702573
161.1978911218872 958.4554171376953 68.44113321716856
145.83279780999754 958.4976500024413 67.49459787774185
130.55875131225585 958.37200926416 66.47422379831166
115.30086763293457 958.3595591132813 65.34013267608672
100.15407917248535 958.3310783759765 64.09449071855465
88.50052434429931 958.2143887265624 63.027051705045054
80.80481551904296 958.2768836015625 62.20335573939968
73.15455889901733 958.2436018256835 61.30736306483415
65.52891777337646 958.2686648745116 60.353492720433756
```

```
57.888044539123534 958.3167566337892 59.305296787242206
50.26982366271972 958.2725708041992 58.098433209412576
42.59165846305847 958.2230956948242 56.74316000204586
35.03453131109619 958.3017839033203 55.13951917826822
27.402929574005125 958.202752311035 53.21786800249073
19.716179466384887 958.2075533496093 50.62248805919293
12.53288233493042 958.2236653095704 45.41665803145053
10.390764708709716 958.1698774028318 44.761487499071904
3.873150456773758 958.0898058442383 37.439427685836684
1.4480957773532868 958.0033057763671 31.74273616385541
0.3128653096740246 958.2135749912109 23.65169698203166
0.06550363960915803 960.8600865117829 14.47390651413334
```

7. APPENDIX

7.1 List of Figures

7.2 List of Publications

7.2.1 Publications Related to This Thesis

[1] M. Aust; A. J. Herold; L. Niederegger; C. Schneider; D. C. Mayer; M. Drees; J. Warnan; A. Pöthig; R. A. Fischer, Introducing Benzene-1,3,5-tri(dithiocarboxylate) as a Multidentate Linker in Coordination Chemistry. *Inorganic Chemistry* **2021,** *60* (24), 19242-19252.

[2] M. Aust; M. I Schönherr; D. P. Halter; L. Schröck; T. Pickl; S. N. Deger; M. Z Hussain; A. Jentys; R. Bühler; Z. Zhang; K. Meyer; M. Kuhl; J. Eichhorn; D. D. Medina; A. Pöthig; R. A. Fischer, Benzene-1,4-Di(dithiocarboxylate) Linker-Based Coordination Polymers of Mn^{2+}, Zn^{2+}, and Mixed-Valence $Fe^{2+/3+}$. *Inorganic Chemistry* **2024,** 63 (1), 129-140.

7.2.2 Other Publications

[1] A. Wimmer; A. Urstoeger; T. Hinke; M. Aust; P. J. Altmann; M. Schuster, Separating dissolved silver from nanoparticulate silver is the key: Improved cloud-point-extraction hyphenated to single particle ICP-MS for comprehensive analysis of silver-based nanoparticles in real environmental samples down to single-digit nm particle sizes. *Analytica Chimica Acta* **2021,** *1150*, 238198.

7.3 Reprint Permissions

AAAS permits the use of content published in its journals *Science*, *Science Immunology*, *Science Robotics*, *Science Signaling*, and *Science Translational Medicine* to be used in a thesis or dissertation, but only provided the following criteria are met:

1. If you are using figure(s)/table(s), permission is granted for use in print and electronic versions of your dissertation or thesis.
2. A full-text article may be used only in print versions of a dissertation or thesis. AAAS does not permit the reproduction of full-text articles in electronic versions of theses or dissertations.
3. The following credit line must be printed along with the AAAS material: "From [Full Reference Citation]. Reprinted with permission from AAAS."
4. All required credit lines and notices must be visible any time a user accesses any part of the AAAS material and must appear on any printed copies that an authorized user might make.
5. The AAAS material may not be modified or altered, with the exception that figures and tables may be modified with permission from the author. Author permission for any such changes must be secured prior to your use.
6. AAAS must publish the full paper prior to your use of any of its text or figures.
7. If the AAAS material covered by this permission was published in *Science* during the years 1974–1994, you must also obtain permission from the author, who may grant or withhold permission, and who may or may not charge a fee if permission is granted. See original article for author's address. This condition does not apply to news articles.
8. If you are an original author of the AAAS article being reproduced, please refer to your License to Publish for rules on reproducing your paper in a dissertation or thesis.
9. Permission covers the distribution of your dissertation or thesis on demand by a third-party distributor (e.g., ProQuest/UMI), provided the AAAS material covered by this permission remains in situ and is not distributed by that third party outside of the context of your thesis/dissertation.
10. Permission does not apply to figures/photos/artwork or any other content or materials included in your work that are credited to non-AAAS sources. If the requested material is sourced to or references non-AAAS sources, you must obtain authorization from that source as well before using that material. You agree to hold harmless and indemnify AAAS against any claims arising from your use of any content in your work that is credited to non-AAAS sources.
11. By using the AAAS material identified in your request, you agree to abide by all the terms and conditions herein.
12. AAAS makes no representations or warranties as to the accuracy of any information contained in the AAAS material covered by this permission, including any warranties of merchantability or fitness for a particular purpose.

JOHN WILEY AND SONS LICENSE
TERMS AND CONDITIONS

Apr 21, 2024

This Agreement between Technical University of Munich -- Margit Aust ("You") and John Wiley and Sons ("John Wiley and Sons") consists of your license details and the terms and conditions provided by John Wiley and Sons and Copyright Clearance Center.

License Number	5773670661637
License date	Apr 21, 2024
Licensed Content Publisher	John Wiley and Sons
Licensed Content Publication	Angewandte Chemie International Edition
Licensed Content Title	Electrically Conductive Porous Metal–Organic Frameworks
Licensed Content Author	Mircea Dincă, Michael G. Campbell, Lei Sun
Licensed Content Date	Jan 8, 2016
Licensed Content Volume	55
Licensed Content Issue	11
Licensed Content Pages	14
Type of use	Dissertation/Thesis
Requestor type	University/Academic
Format	Print and electronic

Portion	Figure/table
Number of figures/tables	3
Will you be translating?	No
Title of new work	Dithiocarboxylate-Based Ligands as Linkers for Metal-Organic Coordination Polymers
Institution name	Technical University of Munich
Expected presentation date	Aug 2024
Order reference number	4
Portions	Figure 2, Figure 5, Figure 6
Requestor Location	Technical University of Munich Lichtenbergstraße 4 Garching, 85748 Germany Attn: Technical University of Munich
Publisher Tax ID	EU826007151
Total	0.00 EUR

Terms and Conditions

TERMS AND CONDITIONS

This copyrighted material is owned by or exclusively licensed to John Wiley & Sons, Inc. or one of its group companies (each a"Wiley Company") or handled on behalf of a society with which a Wiley Company has exclusive publishing rights in relation to a particular work (collectively "WILEY"). By clicking "accept" in connection with completing this licensing transaction, you agree that the following terms and conditions apply to this transaction (along with the billing and payment terms and conditions established by the Copyright Clearance Center Inc., ("CCC's Billing and Payment terms and conditions"), at the time that you opened your RightsLink account (these are available at any time at http://myaccount.copyright.com).

Terms and Conditions

- The materials you have requested permission to reproduce or reuse (the "Wiley Materials") are protected by copyright.

- You are hereby granted a personal, non-exclusive, non-sub licensable (on a stand-alone basis), non-transferable, worldwide, limited license to reproduce the Wiley Materials for the purpose specified in the licensing process. This license, **and any CONTENT (PDF or image file) purchased as part of your order,** is for a one-time use only and limited to any maximum distribution number specified in the license. The first instance of republication or reuse granted by this license must be completed within two years of the date of the grant of this license (although copies prepared before the end date may be distributed thereafter). The Wiley Materials shall not be used in any other manner or for any other purpose, beyond what is granted in the license. Permission is granted subject to an appropriate acknowledgement given to the author, title of the material/book/journal and the publisher. You shall also duplicate the copyright notice that appears in the Wiley publication in your use of the Wiley Material. Permission is also granted on the understanding that nowhere in the text is a previously published source acknowledged for all or part of this Wiley Material. Any third party content is expressly excluded from this permission.

- With respect to the Wiley Materials, all rights are reserved. Except as expressly granted by the terms of the license, no part of the Wiley Materials may be copied, modified, adapted (except for minor reformatting required by the new Publication), translated, reproduced, transferred or distributed, in any form or by any means, and no derivative works may be made based on the Wiley Materials without the prior permission of the respective copyright owner.**For STM Signatory Publishers clearing permission under the terms of the STM Permissions Guidelines only, the terms of the license are extended to include subsequent editions and for editions in other languages, provided such editions are for the work as a whole in situ and does not involve the separate exploitation of the permitted figures or extracts,** You may not alter, remove or suppress in any manner any copyright, trademark or other notices displayed by the Wiley Materials. You may not license, rent, sell, loan, lease, pledge, offer as security, transfer or assign the Wiley Materials on a stand-alone basis, or any of the rights granted to you hereunder to any other person.

- The Wiley Materials and all of the intellectual property rights therein shall at all times remain the exclusive property of John Wiley & Sons Inc, the Wiley Companies, or their respective licensors, and your interest therein is only that of having possession of and the right to reproduce the Wiley Materials pursuant to Section 2 herein during the continuance of this Agreement. You agree that you own no right, title or interest in or to the Wiley Materials or any of the intellectual property rights therein. You shall have no rights hereunder other than the license as provided for above in Section 2. No right, license or interest to any trademark, trade name, service mark or other branding ("Marks") of WILEY or its licensors is granted hereunder, and you agree that you shall not assert any such right, license or interest with respect thereto

- NEITHER WILEY NOR ITS LICENSORS MAKES ANY WARRANTY OR REPRESENTATION OF ANY KIND TO YOU OR ANY THIRD PARTY, EXPRESS, IMPLIED OR STATUTORY, WITH RESPECT TO THE MATERIALS OR THE ACCURACY OF ANY INFORMATION CONTAINED IN THE MATERIALS, INCLUDING, WITHOUT LIMITATION, ANY IMPLIED WARRANTY OF MERCHANTABILITY, ACCURACY, SATISFACTORY QUALITY, FITNESS FOR A PARTICULAR PURPOSE, USABILITY, INTEGRATION OR NON-INFRINGEMENT AND ALL SUCH WARRANTIES ARE HEREBY EXCLUDED BY WILEY AND ITS LICENSORS AND WAIVED

BY YOU.

- WILEY shall have the right to terminate this Agreement immediately upon breach of this Agreement by you.
- You shall indemnify, defend and hold harmless WILEY, its Licensors and their respective directors, officers, agents and employees, from and against any actual or threatened claims, demands, causes of action or proceedings arising from any breach of this Agreement by you.
- IN NO EVENT SHALL WILEY OR ITS LICENSORS BE LIABLE TO YOU OR ANY OTHER PARTY OR ANY OTHER PERSON OR ENTITY FOR ANY SPECIAL, CONSEQUENTIAL, INCIDENTAL, INDIRECT, EXEMPLARY OR PUNITIVE DAMAGES, HOWEVER CAUSED, ARISING OUT OF OR IN CONNECTION WITH THE DOWNLOADING, PROVISIONING, VIEWING OR USE OF THE MATERIALS REGARDLESS OF THE FORM OF ACTION, WHETHER FOR BREACH OF CONTRACT, BREACH OF WARRANTY, TORT, NEGLIGENCE, INFRINGEMENT OR OTHERWISE (INCLUDING, WITHOUT LIMITATION, DAMAGES BASED ON LOSS OF PROFITS, DATA, FILES, USE, BUSINESS OPPORTUNITY OR CLAIMS OF THIRD PARTIES), AND WHETHER OR NOT THE PARTY HAS BEEN ADVISED OF THE POSSIBILITY OF SUCH DAMAGES. THIS LIMITATION SHALL APPLY NOTWITHSTANDING ANY FAILURE OF ESSENTIAL PURPOSE OF ANY LIMITED REMEDY PROVIDED HEREIN.
- Should any provision of this Agreement be held by a court of competent jurisdiction to be illegal, invalid, or unenforceable, that provision shall be deemed amended to achieve as nearly as possible the same economic effect as the original provision, and the legality, validity and enforceability of the remaining provisions of this Agreement shall not be affected or impaired thereby.
- The failure of either party to enforce any term or condition of this Agreement shall not constitute a waiver of either party's right to enforce each and every term and condition of this Agreement. No breach under this agreement shall be deemed waived or excused by either party unless such waiver or consent is in writing signed by the party granting such waiver or consent. The waiver by or consent of a party to a breach of any provision of this Agreement shall not operate or be construed as a waiver of or consent to any other or subsequent breach by such other party.
- This Agreement may not be assigned (including by operation of law or otherwise) by you without WILEY's prior written consent.
- Any fee required for this permission shall be non-refundable after thirty (30) days from receipt by the CCC.
- These terms and conditions together with CCC's Billing and Payment terms and conditions (which are incorporated herein) form the entire agreement between you and WILEY concerning this licensing transaction and (in the absence of fraud) supersedes all prior agreements and representations of the parties, oral or written. This Agreement may not be amended except in writing signed by both parties. This Agreement shall be binding upon and inure to the benefit of the parties' successors, legal representatives, and authorized assigns.
- In the event of any conflict between your obligations established by these terms and conditions and those established by CCC's Billing and Payment terms and conditions, these terms and conditions shall prevail.

- WILEY expressly reserves all rights not specifically granted in the combination of (i) the license details provided by you and accepted in the course of this licensing transaction, (ii) these terms and conditions and (iii) CCC's Billing and Payment terms and conditions.

- This Agreement will be void if the Type of Use, Format, Circulation, or Requestor Type was misrepresented during the licensing process.

- This Agreement shall be governed by and construed in accordance with the laws of the State of New York, USA, without regards to such state's conflict of law rules. Any legal action, suit or proceeding arising out of or relating to these Terms and Conditions or the breach thereof shall be instituted in a court of competent jurisdiction in New York County in the State of New York in the United States of America and each party hereby consents and submits to the personal jurisdiction of such court, waives any objection to venue in such court and consents to service of process by registered or certified mail, return receipt requested, at the last known address of such party.

WILEY OPEN ACCESS TERMS AND CONDITIONS

Wiley Publishes Open Access Articles in fully Open Access Journals and in Subscription journals offering Online Open. Although most of the fully Open Access journals publish open access articles under the terms of the Creative Commons Attribution (CC BY) License only, the subscription journals and a few of the Open Access Journals offer a choice of Creative Commons Licenses. The license type is clearly identified on the article.

The Creative Commons Attribution License

The Creative Commons Attribution License (CC-BY) allows users to copy, distribute and transmit an article, adapt the article and make commercial use of the article. The CC-BY license permits commercial and non-

Creative Commons Attribution Non-Commercial License

The Creative Commons Attribution Non-Commercial (CC-BY-NC)License permits use, distribution and reproduction in any medium, provided the original work is properly cited and is not used for commercial purposes.(see below)

Creative Commons Attribution-Non-Commercial-NoDerivs License

The Creative Commons Attribution Non-Commercial-NoDerivs License (CC-BY-NC-ND) permits use, distribution and reproduction in any medium, provided the original work is properly cited, is not used for commercial purposes and no modifications or adaptations are made. (see below)

Use by commercial "for-profit" organizations

Use of Wiley Open Access articles for commercial, promotional, or marketing purposes requires further explicit permission from Wiley and will be subject to a fee.

Further details can be found on Wiley Online Library
http://olabout.wiley.com/WileyCDA/Section/id-410895.html

Other Terms and Conditions:

v1.10 Last updated September 2015

Questions? customercare@copyright.com.

CCC | RightsLink

MA

ACS Publications
Most Trusted. Most Cited. Most Read.

Control of the Charge Distribution and Modulation of the Class II–III Transition in Weakly Coupled Mo2–Mo2 Systems

Author: Xuan Xiao, Chun Y. Liu, Qiao He, et al
Publication: Inorganic Chemistry
Publisher: American Chemical Society
Date: Nov 1, 2013

Copyright © 2013, American Chemical Society

PERMISSION/LICENSE IS GRANTED FOR YOUR ORDER AT NO CHARGE

This type of permission/license, instead of the standard Terms and Conditions, is sent to you because no fee is being charged for your order. Please note the following:

- Permission is granted for your request in both print and electronic formats, and translations.
- If figures and/or tables were requested, they may be adapted or used in part.
- Please print this page for your records and send a copy of it to your publisher/graduate school.
- Appropriate credit for the requested material should be given as follows: "Reprinted (adapted) with permission from {COMPLETE REFERENCE CITATION}. Copyright {YEAR} American Chemical Society." Insert appropriate information in place of the capitalized words.
- One-time permission is granted only for the use specified in your RightsLink request. No additional uses are granted (such as derivative works or other editions). For any uses, please submit a new request.

If credit is given to another source for the material you requested from RightsLink, permission must be obtained from that source.

BACK CLOSE WINDOW

CCC | RightsLink

MA

ACS Publications
Most Trusted. Most Cited. Most Read.

Introducing Benzene-1,3,5-tri(dithiocarboxylate) as a Multidentate Linker in Coordination Chemistry

Author: Margit Aust, Anna J. Herold, Lukas Niederegger, et al
Publication: Inorganic Chemistry
Publisher: American Chemical Society
Date: Dec 1, 2021

Copyright © 2021, American Chemical Society

PERMISSION/LICENSE IS GRANTED FOR YOUR ORDER AT NO CHARGE

This type of permission/license, instead of the standard Terms and Conditions, is sent to you because no fee is being charged for your order. Please note the following:

- Permission is granted for your request in both print and electronic formats, and translations.
- If figures and/or tables were requested, they may be adapted or used in part.
- Please print this page for your records and send a copy of it to your publisher/graduate school.
- Appropriate credit for the requested material should be given as follows: "Reprinted (adapted) with permission from {COMPLETE REFERENCE CITATION}. Copyright {YEAR} American Chemical Society." Insert appropriate information in place of the capitalized words.
- One-time permission is granted only for the use specified in your RightsLink request. No additional uses are granted (such as derivative works or other editions). For any uses, please submit a new request.

If credit is given to another source for the material you requested from RightsLink, permission must be obtained from that source.

BACK CLOSE WINDOW

CCC | RightsLink

MA

ACS Publications
Most Trusted. Most Cited. Most Read.

Benzene-1,4-Di(dithiocarboxylate) Linker-Based Coordination Polymers of Mn2 , Zn2 , and Mixed-Valence Fe2 /3

Author: Margit Aust, Marina I. Schönherr, Dominik P. Halter, et al
Publication: Inorganic Chemistry
Publisher: American Chemical Society
Date: Jan 1, 2024

Copyright © 2024, American Chemical Society

PERMISSION/LICENSE IS GRANTED FOR YOUR ORDER AT NO CHARGE

This type of permission/license, instead of the standard Terms and Conditions, is sent to you because no fee is being charged for your order. Please note the following:

- Permission is granted for your request in both print and electronic formats, and translations.
- If figures and/or tables were requested, they may be adapted or used in part.
- Please print this page for your records and send a copy of it to your publisher/graduate school.
- Appropriate credit for the requested material should be given as follows: "Reprinted (adapted) with permission from {COMPLETE REFERENCE CITATION}. Copyright {YEAR} American Chemical Society." Insert appropriate information in place of the capitalized words.
- One-time permission is granted only for the use specified in your RightsLink request. No additional uses are granted (such as derivative works or other editions). For any uses, please submit a new request.

If credit is given to another source for the material you requested from RightsLink, permission must be obtained from that source.

BACK | CLOSE WINDOW